

Iron Hysteresis and Enhanced Kalman Filtering for Sensorless Position Detection of Synchronous Motors

THÈSE N° 5630 (2013)

PRÉSENTÉE LE 18 JANVIER 2013

À LA FACULTÉ DES SCIENCES ET TECHNIQUES DE L'INGÉNIEUR
LABORATOIRE D'ACTIONNEURS INTÉGRÉS
PROGRAMME DOCTORAL EN SYSTÈMES DE PRODUCTION ET ROBOTIQUE

ÉCOLE POLYTECHNIQUE FÉDÉRALE DE LAUSANNE

POUR L'OBTENTION DU GRADE DE DOCTEUR ÈS SCIENCES

PAR

Omar SCAGLIONE

acceptée sur proposition du jury:

Prof. M.-O. Hongler, président du jury
Prof. Y. Perriard, directeur de thèse
Dr S. Biwersi, rapporteur
Prof. B. Dehez, rapporteur
Dr F. Mondada, rapporteur



ÉCOLE POLYTECHNIQUE
FÉDÉRALE DE LAUSANNE

Suisse
2013

What I cannot create,
I do not understand.
— Richard Feynman

A Rita e Loreto

Remerciements

LA réussite d'un travail de longue haleine ne serait pas possible sans l'aide précieuse de beaucoup de personnes. Avec ces quelques lignes j'espère transmettre ma gratitude à tous ceux qui m'ont aidé pendant ces années de thèse.

En premier lieu, j'aimerais remercier Yves, pour m'avoir donné la possibilité d'effectuer ce travail, pour son soutien et ses précieux conseils. Les années passées au laboratoire ont été une expérience énormément enrichissante, tant du point de vue professionnel que humain.

Ce travail n'aurait pas pu se réaliser sans les partenaires industriels Sonceboz SA et MMT Moving Magnet Technologies SA. Parmi tous les collaborateurs qui ont aidé d'une manière ou d'une autre à la réalisation de cette thèse, j'aimerais remercier particulièrement M. Persson et M. Wicht pour la gestion des projets, M. Rondot, M. Nita et M. Thivet pour leur aide technique ainsi que M. Gandel et M. Pfister pour leur enthousiasme sans faille.

Cette thèse m'a permis de connaître des collègues formidables avec qui j'ai eu la chance de partager des moments inoubliables. J'aimerais remercier Mika pour l'énorme contribution fournie tout au long de mon travail, Paolo pour les innombrables services rendus, Christian, André et Alain pour toutes les belles discussions eues ainsi que Magda grâce à laquelle tout fonctionne au secrétariat. J'aimerais aussi souligner ici la grande amitié qui me lie à Sebi le tessinois, Greg et Pascal les valaisans, Joël et Nicolas les sportifs, Markus le suisse-allemand et Ale le cuisinier.

Je remercie également mes copains d'études, Julien, Bastien, les deux Guillaume, Fanny, Lucas, Frédéric, Gavriilo et Laurent ainsi que Muriel et Renato de la formidable équipe Swisscube et le comité Sysmic 2006-2009. Grâce à vous toutes ces années à l'EPFL ont été si extraordinaires.

Enfin, un grand merci va à amis de Belgique, Bruno, François, Thibaud et Jonathan, et à ceux du Faubourg de la Gare. Vous m'avez si chaleureusement accueilli, je vous en suis énormément reconnaissant.

Un ringraziamento speciale va al mio compagno di molte avventure, Maggio, sempre presente, e alla mia fantastica Céline che riempie di felicità ogni nuovo giorno passato insieme. Spero che queste poche righe possano trasmettervi l'immensa stima, gratitudine ed affetto che nutro per voi.

Infine, non posso non concludere questo testo senza ringraziare la mia famiglia, ed in particolare i miei genitori, Rita e Loreto, ai quali devo ogni cosa ed a cui dedico con amore questo lavoro.

Neuchâtel, Dicembre 2012

Omar

THE auto-commutated permanent magnet synchronous motors, or brushless DC motors (BLDC), are more and more used in many different industrial low power (< 1 kW) applications. BLDC motors have the phase coils on the stator and the permanent magnet(s) on the rotor. Besides many advantages provided by this configuration, a drawback is that the position of the rotor has to be known in order to correctly drive the motor. Normally, Hall effect sensors or angular encoders are used for this purpose.

In order to increase the reliability, reduce the size, manufacturing cost and wiring, a big research effort has been done for avoiding the use of direct sensors for the position detection of the rotor, leading to sensorless (or self-sensing if the motor is designed for that purpose) position detection. Effective solutions have been proposed for the nominal and high speed operations, as well as for the standstill position detection. However, in the case of BLDC motors with non-salient rotor, classical sensorless techniques using high frequency signal injections, state estimators or back-EMF detection still fail during the low speed operations.

The objective of this thesis is therefore to propose new principles for the sensorless driving of BLDC motors with non-salient rotor, especially during low speed operations.

Thanks to the introduced research, a deeper knowledge of the magnetic phenomena influencing the motor phase inductances and resistances is provided. It is highlighted that the phase inductances and resistances of most BLDC motors are naturally dependent on the rotor position. All known phenomena, like mechanical saliency, magnetic saturation, eddy currents, magnetic anisotropy, are analyzed and no one explains the measured inductance and resistance variations. Their origin is found in the non-linearity of the BH characteristic of the stator iron and, more accurately, in the local BH hysteresis loops. Based on this knowledge, an existing BLDC motor is modified for increasing the effects of the highlighted phenomenon.

Although small, the inductance and resistance variations are successfully used for detecting the rotor position. In order to maximize the information retrieval, a simple differential measurement is proposed and an innovative ready-to-use position-dependent

Abstract

signal is provided.

On this basis, a first innovative sensorless position detection principle, naturally integrated into the classical two-phases ON supply, is introduced for the low speed operations. The principle is implemented in a prototype and extensively and successfully tested.

An innovative implementation of a Kalman filter for the sensorless position detection of BLDC motor is introduced. Thanks to the additional measurement provided by the new position-dependent signal, the working range of the Kalman filter is extended down to the low speed operations. Moreover, in order to avoid any kind of off-line calibration, an innovative on-line parameter estimation principle is introduced in the BLDC motor position detection domain. The principle is based on two interacting Kalman filters, one dedicated to the motor state estimation and a second dedicated to the parameters estimation. The principle is confirmed by simulations and with the realization of an industrial-based prototype.

The fusion of the parameter estimation principle with the Kalman filter with extended working range leads to a fully sensorless principle, adapted to most BLDC motors, robust, suitable for steady-state or dynamic operations and without any need of off-line calibration.

Finally, thanks to the understanding of the physical origin of the inductance and resistance variations, another innovative measurement principle is introduced for the rotor position estimation at standstill. A theoretical model is provided and its effectiveness is confirmed with a practical realization.

Keywords: Brushless DC (BLDC) motor, position detection, sensorless, self-sensing, iron BH hysteresis, Kalman filter, parameter estimation.

LES moteurs synchrones à aimants permanents auto-commutés, communément appelés moteurs BLDC, sont de plus en plus utilisés dans diverses applications industrielles de faible puissance (< 1 kW). Les moteurs BLDC ont les bobinages au stator et les aimants permanents au rotor. Cette configuration comporte de nombreux avantages, mais a l'inconvénient de nécessiter la connaissance de la position du rotor pour correctement actionner le moteur. Généralement, des capteurs à effet Hall ou des encodeurs angulaires sont utilisés pour cette tâche.

Afin d'accroître la fiabilité de l'entraînement, de réduire ses dimensions, son câblage et son coût de fabrication, beaucoup d'études ont été menées pour éliminer l'utilisation des capteurs directs de la position rotorique. Les électroniques fonctionnant sans l'utilisation de ces capteurs se nomment sensorless, ou self-sensing, si le moteur a spécifiquement été créé pour faciliter cette tâche.

Des solutions efficaces ont été proposées pour le fonctionnement du moteur à vitesse nominale, ainsi que à l'arrêt. Néanmoins, la détection de la position rotorique aux basses vitesses des moteurs BLDC avec rotor non-saillant reste à ce jour un problème pour ces techniques classiques basées sur l'injection de signaux à haute fréquence, sur les estimateurs ou sur la tension induite.

L'objectif de cette thèse est de proposer de nouveaux principes pour la détection de la position rotorique de moteurs BLDC à rotor non-saillant, spécialement pour les basses vitesses.

Grâce aux recherches effectuées, une connaissance accrue des phénomènes qui influencent l'inductance et la résistance des phases du moteur est apportée. Il est mis en évidence que l'inductance et la résistance des phases de la plupart des moteurs BLDC dépendent déjà de la position rotorique. Tous les phénomènes connus, comme la saillance mécanique, la saturation magnétique, les courants de Foucault ou l'anisotropie magnétique sont analysés, mais aucun n'explique les variations d'inductance et de résistance mesurées. Leur origine est trouvée dans la non-linéarité de la caractéristique BH du fer du stator, et plus précisément, dans les cycles d'hystérèse locaux.

Grâce à cette connaissance, un moteur BLDC existant est modifié afin d'amplifier les

effets de ce phénomène sur les variations d'inductance et résistance de phase.

Malgré leur faible amplitude, ces variations sont utilisées avec succès pour détecter la position rotorique. Afin de maximiser l'extraction d'information, un simple circuit de mesure différentiel est proposé et un nouveau signal, prêt à l'emploi, dépendant de la position rotorique est fourni.

Sur cette base, un premier principe innovant de détection de la position rotorique sans capteurs pour les basses vitesses est présenté. Le principe, intégré de façon naturelle dans une alimentation classique *deux-phases ON*, est implémenté sur un prototype et testé en profondeur avec succès.

L'implémentation innovante d'un filtre de Kalman pour la détection de la position rotorique sans capteurs de moteurs BLDC est ensuite présentée. Grâce à la source d'information supplémentaire fournie par le nouveau signal, la plage de fonctionnement du filtre de Kalman est étendue jusqu'aux basses vitesses. De plus, afin d'éliminer tout besoin de calibration *off-line*, un principe innovant pour l'estimation *on-line* des paramètres du modèle du moteur BLDC est proposé. Le principe est basé sur l'interaction de deux filtres de Kalman : un premier dédié à l'estimation des variables d'état du moteur, et un deuxième dédié à l'estimation des paramètres du modèle du moteur. Le fonctionnement correct du principe est confirmé par des simulations et avec la réalisation d'un prototype.

L'association de ce principe d'estimation des paramètres avec le filtre de Kalman avec plage de fonctionnement étendue donne naissance à un innovant principe de détection de la position rotorique sans capteurs, adapté à la plupart des moteurs BLDC, robuste, fonctionnant sur toute la plage de vitesses, en régime stationnaire ainsi que dynamique, sans besoin d'aucune calibration *off-line*.

Enfin, grâce à la connaissance de l'origine physique des variations d'inductance et de résistance, un autre principe innovant de mesure est proposé pour l'estimation de la position rotorique à l'arrêt. Un modèle théorique est fourni et sa pertinence est vérifiée par les mesures effectuées.

Keywords: Moteur synchrone auto-commuté (BLDC), détection de la position rotorique, sans capteurs, sensorless, self-sensing, hystérèse BH, filtre de Kalman, estimation de paramètres.

Contents

1	Introduction	1
2	State of the art	13
3	Iron BH hysteresis	29
4	Exploitation of the iron BH hysteresis effects	59
5	Sensorless position detection during normal drive	77
6	Enhanced Kalman filtering	109
7	First pulse principle	149
8	Conclusions	171
	Appendix	177
A	Demonstrators of the developed sensorless principles	179
B	Motor datasheets	183
C	Automatic measurement setups	187
D	Power bridge for BLDC motor drives	191
	List of Symbols and Acronyms	193
	Bibliography	197
	Curriculum Vitae	205

CHAPTER 1

Introduction

Contents

1.1	Electrical drive	2
1.1.1	Brushless DC motor	3
1.2	Sensorless position detection	5
1.2.1	Mechanical and electrical position	5
1.2.2	Definition	6
1.2.3	Motivations	6
1.2.4	How to do sensorless position detection	9
1.3	Research context and objectives	11
1.4	Work structure	11

1.1 Electrical drive

THIS thesis treats electrical drives, and more precisely the electronics needed for driving a family of them, the three-phase star connected brushless DC (BLDC) motors. In Fig. 1.1, an electrical drive is schematically represented. As it can be seen, an electrical motor is not a drive, but only a part of it. For driving the motor, a drive electronics is needed. The latter is composed by the command electronics, where is placed the microcontroller (μC), and the power bridge. Power supplies of those two circuits are usually independent, the first has a digital supply, V_{cc} , and the second a power supply, V_{pp} . The command electronics controls the power bridge, and the latter delivers the power needed for turning the motor. Most of the time, a position encoder is present. Through the position encoder, a feedback is given to the command electronics about the position or speed of the motor that permits to control the drive in closed loop. Finally, the motor is usually coupled to a load through a mechanical transmission, like a gearbox, a chain or a belt.

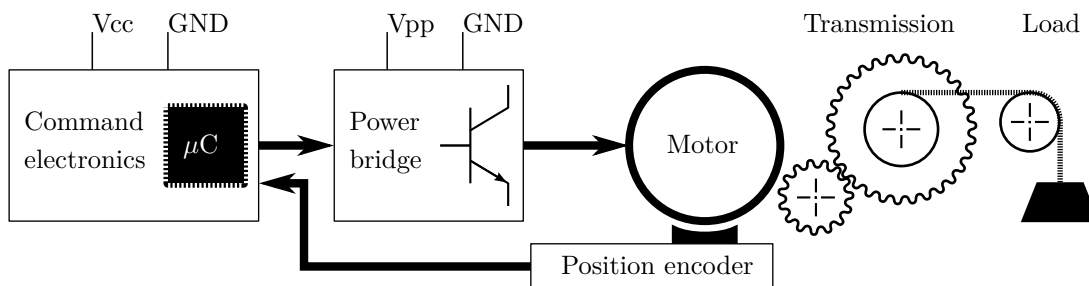


FIGURE 1.1 – Entire drive schematics.

In Fig. 1.2 a small industrial drive for an automotive application is shown. It is a perfect example of the development of an integrated drive. The motor, shown alone in Fig. 1.2a, is only a part of the drive shown in Fig. 1.2b. The motor is placed at the bottom of the drive, over it the drive electronics is visible, as well as the gear train that connect the motor to the output axis. From the customer point of view, only the electrical connection placed to the right lower corner in Fig. 1.2b and the output axis are accessible. In the case of the shown drive, an angular position is asked by a higher control unit through a data bus and the drive executes the task. It is a smart drive. The challenge of the high quality electrical motor industry is no more to sell the best motor, but to sell the best drive. The motor on its own is not enough. The development in the electrical motor domain has therefore to consider the entire drive, and not focus on the motor only.

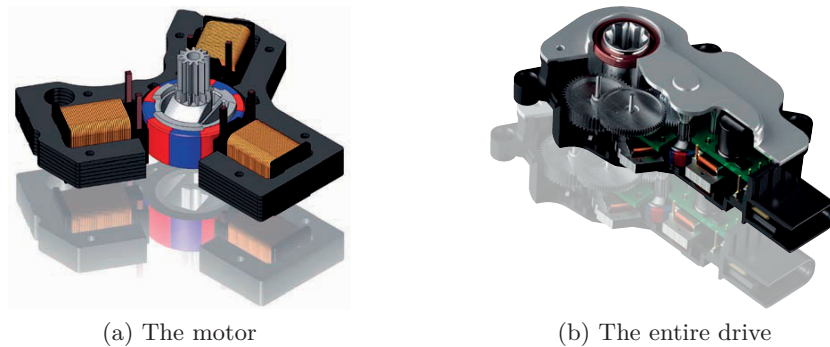


FIGURE 1.2 – Sonceboz 6466 stepper motor with integrated electronics.

Source: *75 years Sonceboz*, MTZ journal, 2011, www.sonceboz.com

1.1.1 Brushless DC motor

During the last decades, the development of the electrical drives in industrial low power applications, where variable speed and simple torque control is needed, has led to the substitution of DC motors with brushless DC motors. In order to understand this transition, it is important to highlight the differences between these two motors.

In Fig. 1.3a a DC motor is schematically represented and in Fig. 1.3b a typical commercial DC motor is shown. In this kind of electrical motors, coils are on the rotor and the permanent magnet (PM) is fixed on the stator. For creating a static magnetic field the coils are mechanically switched thanks to the collector. This means that no electronic switch is needed. For this reason DC motors appeared at the end of XIX century, much earlier compared to the BLDC motors which advent is quite recent in the history of electromechanical devices.

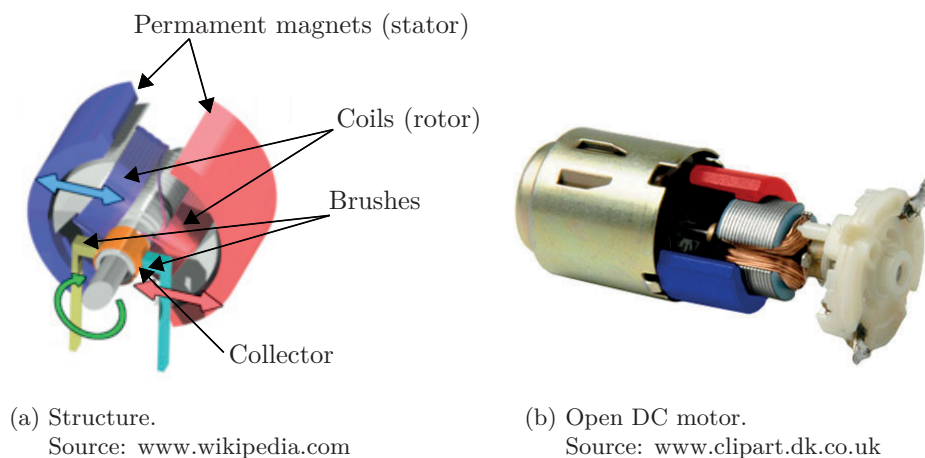


FIGURE 1.3 – DC motor.

The development of BLDC motor drives started in the sixties with the beginning of the transistor-based electronics. A classical BLDC motor structure is represented in Fig. 1.4a. An open commercial BLDC motor is shown in Fig. 1.4b. The mechanical

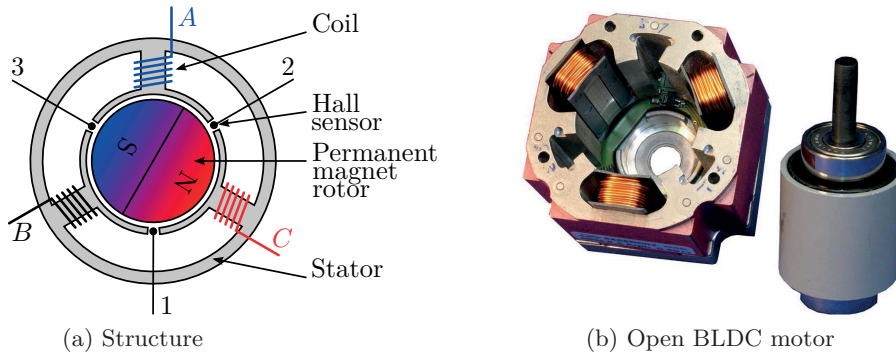


FIGURE 1.4 – BLDC motor.

realization of a BLDC motor is exactly the opposite in respect to the DC motor: the rotor is composed by the permanent magnet, mounted on an iron support. The non-moving parts are the iron stator and the phase coils. In addition, on the stator are placed the Hall sensors or another position encoder. These sensors are normally present because a particularity of the BLDC motor is that the drive electronics has to know the rotor position in order to create a rotating magnetic field and correctly drive the motor in closed loop.

Despite the need of more electronics for the realization of the rotating magnetic field, thanks to the absence of the collector, BLDC motors exhibit many advantages compared to DC motors that justify their development and massive utilisation. They are adapted for clean and explosive environment because neither dust particles nor sparks are created. They have less wear and tear, thus longer operation live. Moreover, they are easier to cool because the coils are fixed to the stator iron, which can be used as a cooler. Finally, because of their mechanical simplicity, BLDC motors are also easier to produce and their miniaturisation is simpler.

The emergence of BLDC motors doubtlessly increases the drives quality. The price to pay for all this advantages is the need of a more sophisticated drive electronics: the power bridge of a BLDC drive, introduced in Appendix D, needs more transistors and the command electronics needs to know the rotor position. After the change of motor, in order to keep on enhancing the drive quality, the need of improving the drive electronics rapidly appears. One of the most studied topics is the development of a command electronics that does not need the Hall sensors or other position encoders. This way to proceed is called sensorless or, if the motor is designed for that purpose, self-sensing position detection.

1.2 Sensorless position detection

1.2.1 Mechanical and electrical position

An important distinction has to be made when referring to BLDC motors position. In a BLDC motor, two rotor positions are defined. The first is the *mechanical* or *absolute* position which refers to the angular position of the rotor, independently from the internal motor structure. This is the position seen by the motor user on the output axis, it is the more intuitive one. If not otherwise specified, the term *rotor position* refers to its mechanical position in this thesis. The second rotor position is defined as the rotor *electrical* position that, on the other hand, refers to the angular position of the rotor in a one pole pair reference. The electrical position is the one needed in order to correctly drive a BLDC motor.

The ratio between electrical and mechanical position depends on the number of pole pairs p and is given by:

$$\theta_{elec} = p \theta_{mec} \quad (1.1)$$

For example, in Fig. 1.5, the digital signals of the three Hall sensors of a 5 pole pairs BLDC motor are plotted. Below, the electrical and mechanical positions are indicated. A complete 360° rotor electrical period is divided into 6 sectors of 60° each by the three Hall sensors signals. This is the minimum angular resolution necessary for driving a BLDC motor in closed loop. In a 5 pole pairs motor there are hence 5 complete electrical periods for one mechanical period. As the Hall sensors give the electrical position only, it is not possible to know the mechanical position without any additional information. The reference position 0° is here arbitrarily chosen to match the rising edge of the Hall sensor 1. This reference may change and not be the same in other measurements shown in this thesis.

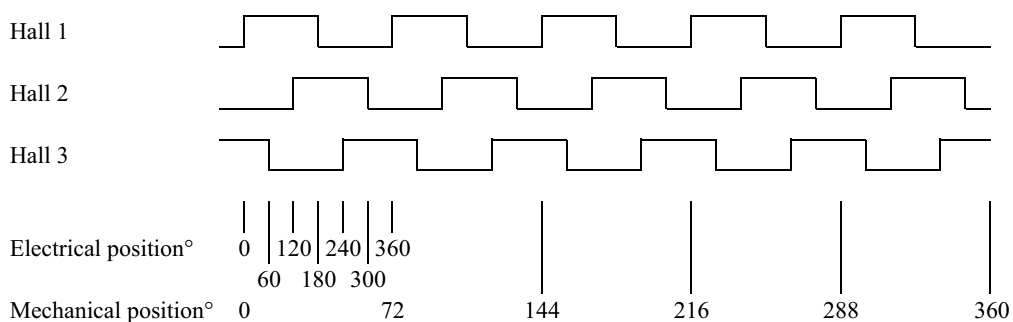


FIGURE 1.5 – Mechanical and electrical positions of a 5 pole pairs BLDC motor.

1.2.2 Definition

Sensorless position detection means that the drive electronics is used to retrieve at least the electrical position of the rotor (and in an ideal case the mechanical position) without any direct position sensor. Of course, some measurements on the motor phase voltages and currents are necessary and indeed the drive electronics has some sensors for measuring these values. But these sensors are placed into the electronics and not on the motor.

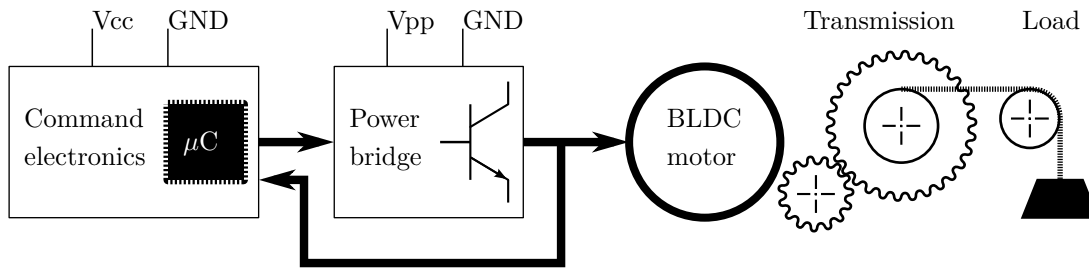


FIGURE 1.6 – Entire BLDC drive schematics, sensorless position detection

The drive schematics is slightly different that the one introduced in Fig. 1.1 and is shown in Fig. 1.6. The position encoder is suppressed, the position information comes directly from the power wires that connect the power bridge to the BLDC motor.

Finally, the term “sensorless position detection” could be resumed by: only the power wires are needed to drive the motor.

1.2.3 Motivations

Some examples introduced hereafter highlight why, in many applications, the suppression of the position sensors is suitable, leading to sensorless position detection.

Room

The first motivation for sensorless position detection has been space saving. Sensorless position detection started in fact in the eighties, in the field of floppy disk [1] and hard disk motor drives [2], where space saving was a major objective. Nowadays, sensors are still a limitation to miniaturization. As an example, in [3] a microfabricated microelectromechanical systems (MEMS) motor for watch applications is realized. The coils, printed on silicon wafer, are shown in Fig. 1.7a and the assembly of the motor and the gear train in Fig. 1.7b. Because of the reduced size and power consumption, a sensorless drive electronics is developed.

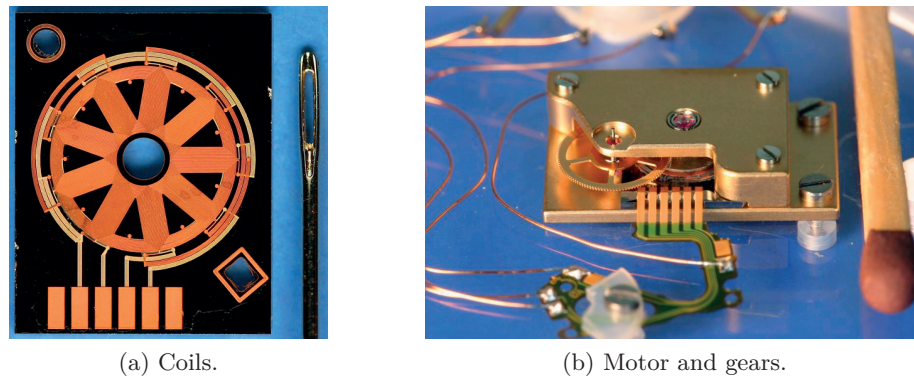
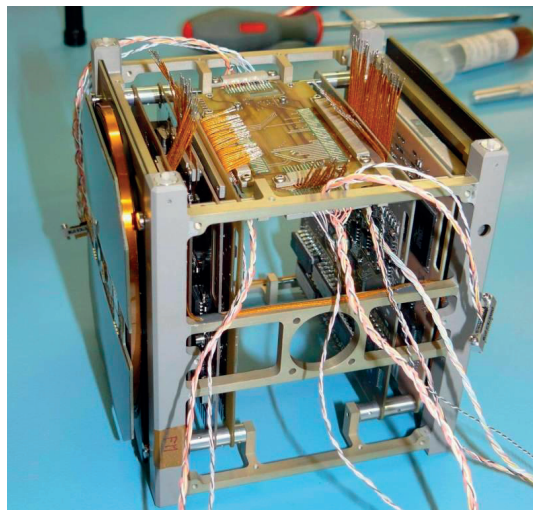


FIGURE 1.7 – Microfabricated MEMS motor [3].

Wiring

In addition to the volume occupied by an extra sensor, wiring is a second important incentive to sensorless position detection. In fact, a BLDC motor drive with Hall sensors needs five additional sensor wires (Vcc, Gnd, Hall 1, Hall 2 and Hall 3). If a resolver or a optical encoder is used, at least four extra wires are needed. As an example, for the stabilization of the pico-satellite Swisscube (100x100x100 mm, 1 kg), a drive for an inertia wheel is developed. A picture taken during the flight model assembling is shown in Fig. 1.8. In this picture, it can be appreciated how, despite a hard work for the integration optimisation, wires are still very numerous. In such a tiny volume, the integration constraints are enormous, and the five wires needed in case of Hall sensors use are absolutely to be avoided. For this reason, only the three power wires are allowed and the constraint of a sensorless electronics for the inertia BLDC motor drive is imposed.

FIGURE 1.8 – Swisscube satellite during integration.
Source: www.swisscube.ch

Robustness, Reliability

Often neglected, it is not to forget that the sensors for the direct position measurement increase failure risks. There are more cables that can broke, more electronic or electromechanical components that may fail. This is especially the case when the motor is placed in a hostile environment. So, the elimination of the position encoder intrinsically improves the mechanical reliability of the drive.

Cost

Finally, cost is another incentive to sensorless position detection. Fig. 1.9 shows an open BLDC motor and its Hall sensor module. All the components of the Hall sensor module (components from ⑧ to ⑬ in Fig. 1.9) add extra cost to the motor. Moreover, the extra permanent magnet ⑫ adds an additional constraint to the fabrication process. In fact, ⑫ is present for permitting the position detection through the Hall sensors ⑩. Therefore, the magnetisation of ⑫ has to be perfectly aligned with the one of the main permanent magnet ④.

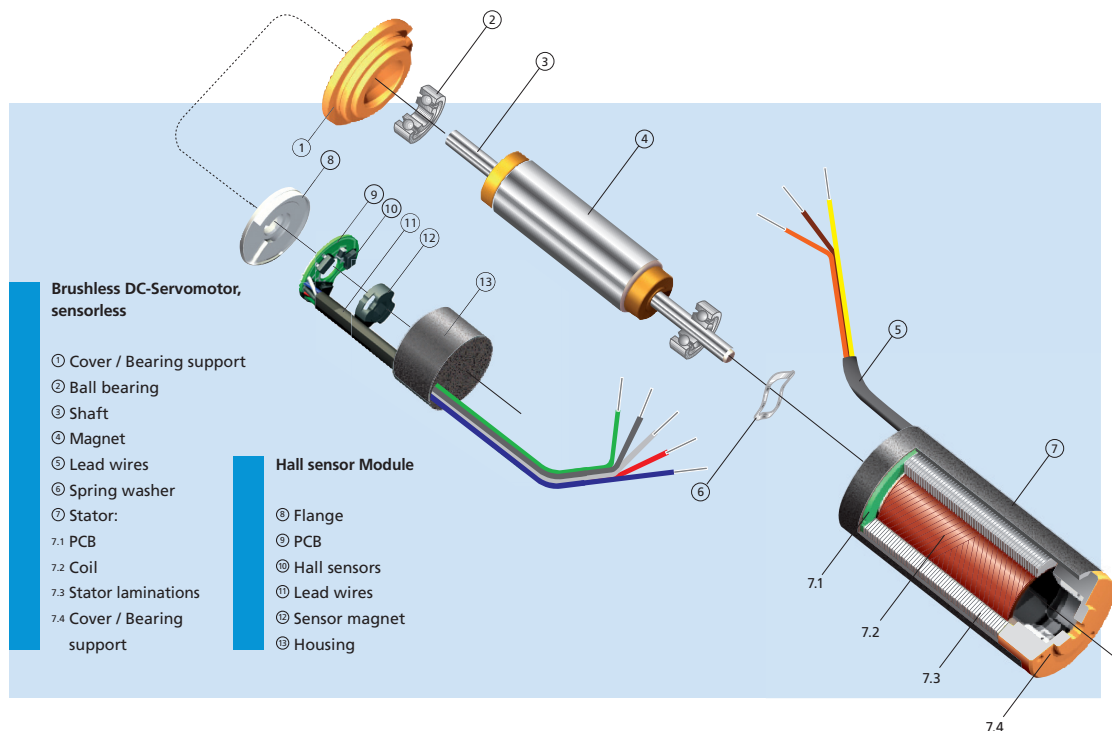


FIGURE 1.9 – Faulhaber Brushless DC-Servomotors.
 Source: Faulhaber catalogue 2012-2013. www.faulhaber.com

1.2.4 How to do sensorless position detection

A simple way for analyzing the problem is to focus on the electrical representation of a BLDC motor. The phase voltages $u_x(t)$ and the phase currents $i_x(t)$ of a BLDC motor are linked by the phase equations [4]:

$$\begin{aligned} u_A(t) &= R_A i_A(t) + L_{AA} \frac{di_A(t)}{dt} + L_{AB} \frac{di_B(t)}{dt} + L_{AC} \frac{di_C(t)}{dt} + u_{iA}(t) \\ u_B(t) &= R_B i_B(t) + L_{BB} \frac{di_B(t)}{dt} + L_{AB} \frac{di_A(t)}{dt} + L_{BC} \frac{di_C(t)}{dt} + u_{iB}(t) \\ u_C(t) &= R_C i_C(t) + L_{CC} \frac{di_C(t)}{dt} + L_{AC} \frac{di_A(t)}{dt} + L_{BC} \frac{di_B(t)}{dt} + u_{iC}(t) \end{aligned} \quad (1.2)$$

where $u_{ix}(t)$ are the back electromotive force voltages (back-EMF), R_x the phase resistances, L_{xx} the phase self inductances and L_{xy} the phase mutual inductances, with $x, y = A, B, C$.

In a star connected BLDC motor the relation

$$i_A + i_B + i_C = 0 \quad (1.3)$$

is always true. Moreover, considering the motor as symmetric, the mutual inductances may be defined as

$$L_m = L_{AB} = L_{AC} = L_{BC} \quad (1.4)$$

With (1.3) and (1.4) the relations (1.2) can be simplified as follows:

$$\begin{aligned} u_A(t) &= R_A i_A(t) + L_A \frac{di_A(t)}{dt} + u_{iA}(t) \\ u_B(t) &= R_B i_B(t) + L_B \frac{di_B(t)}{dt} + u_{iB}(t) \\ u_C(t) &= R_C i_C(t) + L_C \frac{di_C(t)}{dt} + u_{iC}(t) \end{aligned} \quad (1.5)$$

where

$$\begin{aligned} L_A &= L_{AA} - L_m \\ L_B &= L_{BB} - L_m \\ L_C &= L_{CC} - L_m \end{aligned} \quad (1.6)$$

are defined as the phase inductances.

This simplified electrical representation of a BLDC motor is shown in Fig. 1.10. From the point of view of the drive electronics, the three phase terminals, A , B and C are the access points to the motor. On everyone of these access points, the drive electronics

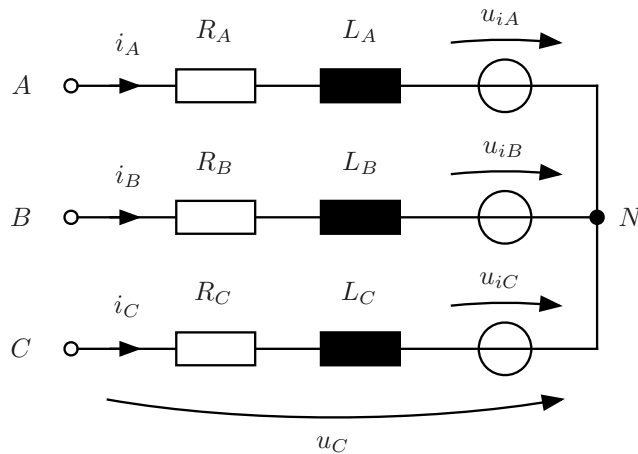


FIGURE 1.10 – Simplified electrical representation of a BLDC motor.

can measure the phase voltage $u_x(t)$ and the phase current $i_x(t)$. If a sensorless drive electronics is wanted to estimate the rotor position from these access points, the signals $u_x(t)$ and $i_x(t)$ have to be position-dependent. So, finally, the answer to the initial question is as simple as affirming that, for detecting the rotor position without additional sensors, one or more of these three terms of the phase equation (1.5) have to be position-dependent.

Nominal and high speed position detection techniques

The first term analyzed is the back-EMF voltage $u_{ix}(t)$. $u_{ix}(t)$ appears only for non-zero rotor speed and is clearly position dependent. Most of the techniques developed since the beginning of sensorless position detection are based on the direct back-EMF detection or on state-observers, which are also back-EMF dependent.

These techniques suffer nevertheless from a major drawback: at standstill and low speed the $u_{ix}(t)$ signal does not exist or is too low, and therefore the techniques may fail.

Standstill and low speed position detection techniques

Standstill and low speed position detection is only possible if an electrical characteristic of the motor, R_x and/or L_x , changes with the rotor position.

Far from being defined only by their mechanical properties, the phase resistances R_x and phase inductances L_x of a BLDC motor highly depend on the magnetic environment around them.

Some magnetic phenomena are known for producing position dependent variations in these parameters. These variations may intrinsically exist in the motor realisation, like mechanical asymmetries and magnetic anisotropy. On the other hand some variations in R_x and L_x can be created by phenomena like in iron saturation or eddy currents that are created voluntarily by the drive electronics.

1.3 Research context and objectives

Sensorless position detection of brushless DC motors is an old research topic. Many solutions have been studied for detecting the rotor position without the use of Hall effect sensors, resolvers or optical encoders. Nevertheless, the domain of sensorless position detection is still of interest, especially for the extrema operations like at standstill and low speed or, on the opposite, when high dynamics is needed.

Besides a few works like [5, 6] or [7], in the last years special attention has been brought to low speed and standstill position detection. Most of the published papers deal with salient rotor motors. In fact, the position detection of a BLDC motor at zero speed and during low speed operations is very difficult to achieve if no saliencies are present on the rotor. In order to overcome this limitation, many authors have also modified the rotor geometries for improving the sensorless position detection without affecting the torque, like in [8–17].

Following this actual trend, the main objective of this research is to propose new low speed and standstill sensorless rotor position detection principles for BLDC motors. In order to achieve this objective, it is allowed to make some modifications to existing motors, as long as the motor performances are not too much degraded.

Moreover, according to the needs of an industrial sensorless position detection drive, it is wished that the proposed sensorless position detection principle does not need neither off-line calibration nor first-use calibration time or predefined start-up sequence.

1.4 Work structure

In Chapter 2, a state-of-the-art of the known magnetic phenomena that produce position dependent variations in the electrical parameters of a BLDC motor is presented. Kalman filtering applied to synchronous motor position detection is also introduced. Particular attention is put on the algorithms for the parameters estimation of the motor model.

In Chapter 3 a particular physical phenomenon, the iron BH hysteresis, is deeply analyzed. The influence of the BH hysteresis on the electrical parameters of a BLDC

Chapter 1. Introduction

motor is highlighted by theory and attested with many measurements. A modification to an existing BLDC motor is suggested in order to increase the phenomenon influence.

In Chapter 4 a measurement schema of the motor phase inductance and resistance variations caused by the iron BH hysteresis is introduced. Thanks to the suggested method, an innovative ready-to-use position-dependent signal is obtained.

In Chapter 5 a sensorless position detection principle based on the position-dependent signal is proposed for low speed operations, down to standstill. The principle is implemented on a custom electronic drive and deeply tested.

In Chapter 6 two innovative Kalman filtering implementations are introduced in order to enhance the robustness and the overall performances of the sensorless position detection drive.

First of all, a new on-line model parameter estimation based on two interacting Kalman filters is introduced. The parameter estimation technique is theoretically proven, simulated and implemented on a demonstrator.

Thereafter, a second innovative Kalman filter implementation exploits the hysteresis effect measurements developed in Chapter 4. This implementation, combined with the parameter estimation technique, is theoretically proven and simulated, leading to a cutting edge, calibration free, full speed range Kalman filtering sensorless position detection principle.

In Chapter 7 a second innovative application of the iron BH hysteresis influence on the motor electrical characteristics is introduced. Theoretical analysis and practical measurements show the validity of the application and open the way to the development of a new promising standstill position detection principle.

In Chapter 8 some general considerations on the work are introduced. Main contributions are highlighted and some suggestions on future developments are recommended.

CHAPTER 2

State of the art

Contents

2.1	Introduction	14
2.2	Iron saturation	14
2.3	Eddy currents	17
2.4	Magnetic path asymmetries	20
2.4.1	Iron mechanical asymmetries	20
2.4.2	Permanent magnet asymmetries	21
2.4.3	Permanent magnet anisotropy	22
2.5	Kalman filtering	24
2.5.1	Kalman filtering for sensorless position detection	25
2.5.2	Parameters estimation	26
2.6	Conclusions	28

2.1 Introduction

COHERENTLY with the distinction made in Subsection 1.2.4, the state-of-the-art of sensorless position detection techniques can be divided into techniques based on the back-EMF and techniques based on the variations of the phase resistance R_x and/or phase inductance L_x .

These last need special attention and are analyzed first because they permit the stand-still and low speed position detection. In this chapter and in order to better understand, the known phenomena that modify the phase resistance and the phase inductance of a BLDC motor are enumerated and their influence on the motor electrical circuit is analyzed. These phenomena are not very numerous. Therefore, where possible, not only the references to the techniques already developed but also measurements are provided.

On the other hand, there are plenty of techniques based on back-EMF. As back-EMF detection needs a rotor speed higher than a necessary limit, these methods are not suitable for zero and low speed operations. They will therefore not be treated in detail here, as this thesis is focused on low speed operations. One may refer to [18] where a non-exhaustive list of sensorless techniques is reported. Nevertheless, a review on Kalman filtering position detection techniques is given because this method is adopted for the practical implementation in this thesis of the developed sensorless algorithm. A special attention is also paid on the estimation techniques of BLDC motor parameters, especially when coupled to a sensorless drive.

2.2 Iron saturation

Iron saturation techniques are well known since the end of the eighties [2]. The principle resides in saturating the iron of the motor by injecting high current pulses in the phases. If the PM is aligned with the phase and the flux generated by the winding has the same direction, the iron saturates and consequently the relative permeability and the phase inductance decrease. On the other hand, if the magnet flux is in the opposite direction relatively to the winding flux, the iron will desaturate and the inductance will increase. This change of inductance can be indirectly perceived analyzing the current evolution during the pulses of phase voltages.

A small hard disk BLDC motor, Fig. 2.1, is used for performing the measurements shown in Fig. 2.2. On the top of Fig. 2.2 the first measurements are shown. In this trial, as it can be seen on the left hand side, the PM north pole is aligned with phase *A*. Phase *A* is supplied by two voltage pulses of 0.8 ms, one positive and one negative. The currents generated by those pulses are superimposed in Fig. 2.2 on the right hand side. The current of the negative pulse is mirrored for a better visualization. It can be clearly

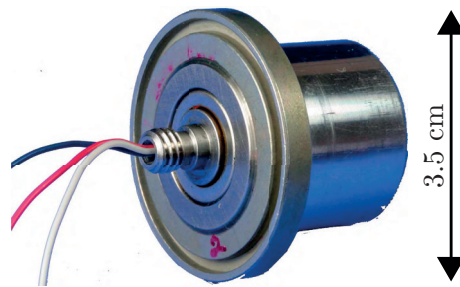


FIGURE 2.1 – Small hard disk BLDC motor used for the measurements.

noticed that the current evolution and the maximum reached value of the phase current is not the same for the two pulses. The current, when the pulse is negative, grows quicker and reaches a higher value. This happens because when the current grows in the phase, the created magnetic field is added to the PM one, the stator iron saturates and thus L_A decreases. In the second trial, in the middle, the PM pole transition is aligned with phase A . It can be noticed in the graph shown on the right hand side that this time, for both pulses, positive and negative, the current evolution is the same. As the iron does not saturate neither for the negative nor positive pulse, L_A remains the same for both current evolutions. In the last trial, shown at the bottom of Fig. 2.2, the PM south pole is now aligned with phase A . In opposition to the first trial, this time the iron saturates for the positive pulse. Hence, L_A decreases for the positive pulse, leading to a quicker current growth.

Starting from this example, the injection of a series of pulses in the three motor phases permits to detect the electrical position of the rotor without ambiguity [2].

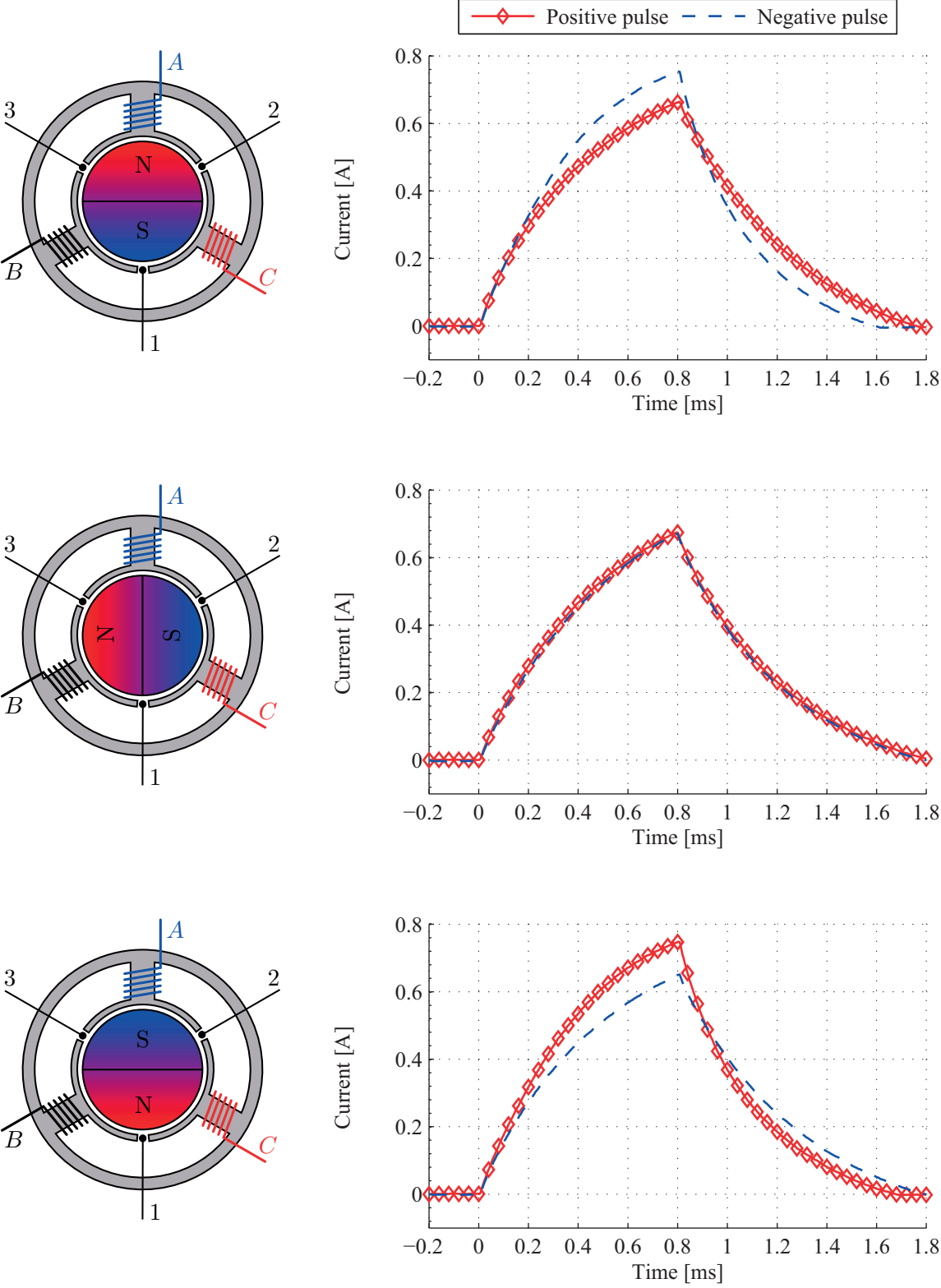


FIGURE 2.2 – Absolute value of the positive and negative pulse currents for three different rotor positions.

2.3 Eddy currents

Eddy currents in the BLDC motor are often neglected because of the complexity in their estimation and calculation. Nevertheless, eddy currents are always present when a high frequency signal is injected into a motor phase. They influence both phase resistance and inductance. Perceived phase resistance is higher compared to the DC value for compensating the additional eddy currents losses [19]. Eddy currents also generate a flux opposite to the flux which created them; thus, they indirectly influence the value of the phase inductance too, so that it lowers with increasing frequency.

As an example, an aluminium piece is simply machined so that an asymmetry is created. Aluminium is chosen as non-magnetic material, but very good electric conductor. The aluminium piece is inserted and rotated in a three-phase coil plastic support, this assembly is shown in Fig. 2.3. Reference rotor positions 0° and 90° are schematically represented in Fig. 2.4. Measurements at 40 kHz of the phase self inductance L_{AA} and

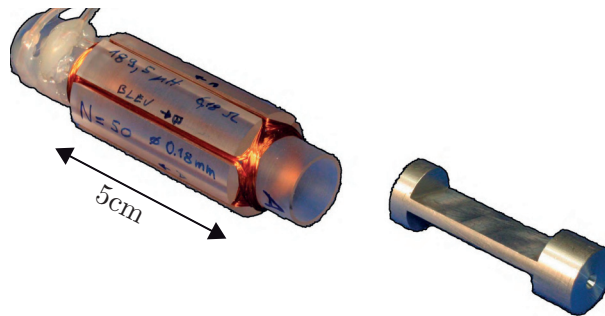


FIGURE 2.3 – Three phase coils on plastic support and the machined aluminium cylinder.

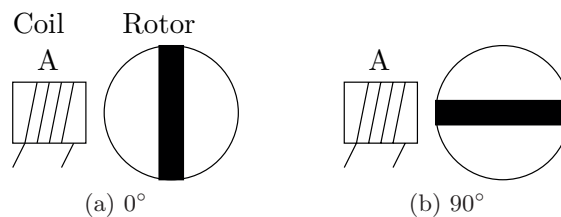
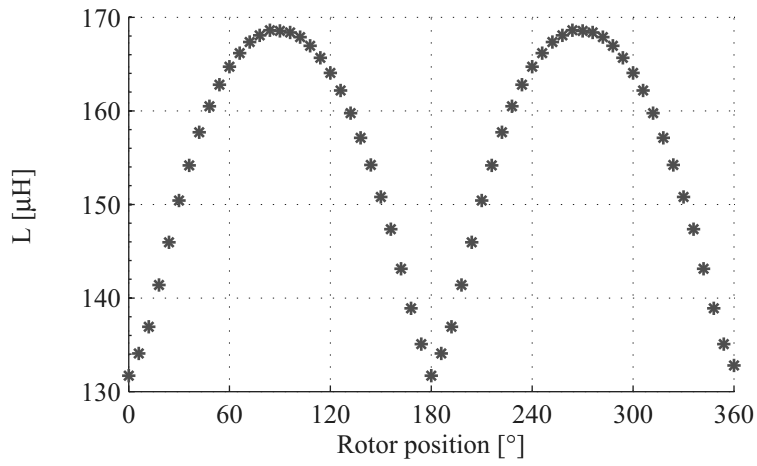
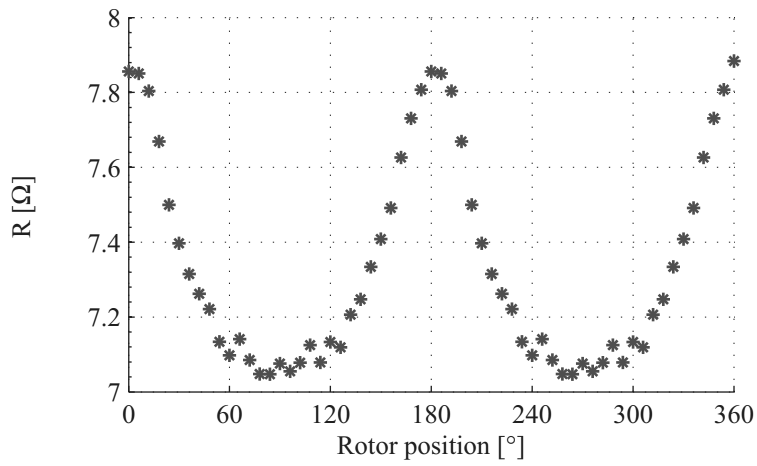


FIGURE 2.4 – Eddy currents measurements angular reference.

the resistance R_A as functions of the rotor position are shown in Fig. 2.5. As expected, at 0° , when the flat zone of the rotor faces the coil A and eddy currents are the highest, R_A is at its maximum value and L_{AA} at its minimum. At 90° , the situation is opposite. Eddy currents are at their lowest value and thus L_{AA} is at its maximum and R_A at its minimum. Clearly, as eddy currents are involved, the inductance variation depends on the excitation frequency. Fig. 2.6 shows the maximum relative induction variation (with reference to the mean value) in function of the excitation signal frequency. As expected, the variations in L_{AA} increase with the frequency of the injected signal.



(a)



(b)

FIGURE 2.5 – Measured L_{AA} (a) and R_A (b) at 40kHz.

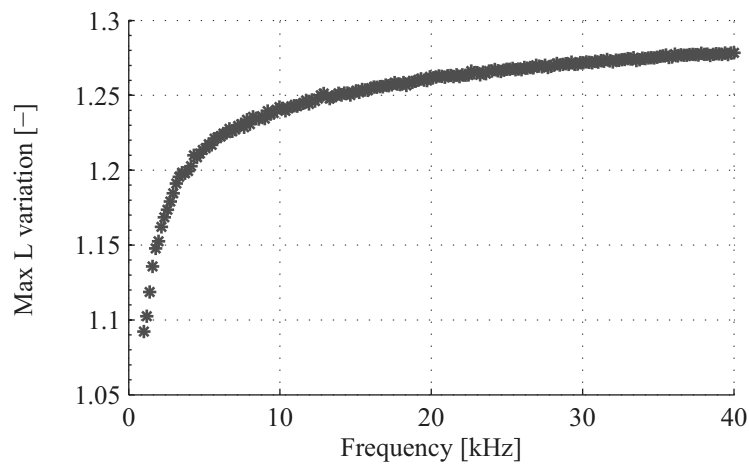


FIGURE 2.6 – Maximum variations of L_{AA} around the mean value, as a function of the signal frequency.

Starting from the basic consideration and measurements introduced above, it is therefore possible to voluntarily confine eddy currents in a selected region of a rotor and, thanks to the inductance and resistance variations, finally detect the rotor position.

Eddy currents are used in [8] and [9] where a thin film of electrical conducting non-magnetic metal is plated on the rotor at a chosen location, Fig. 2.7. Thanks to this modification, the authors are able to correctly estimate the rotor position and drive the BLDC motor.

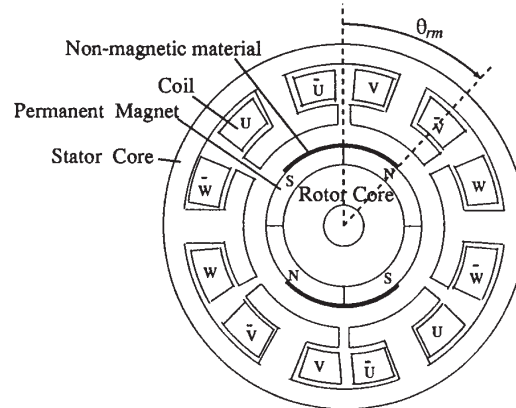


FIGURE 2.7 – Modified motor for the sensorless position detection through eddy currents detection [8].

Following the same concept, in [11–13] a copper ring is placed on the rotor, around the permanent magnets. Thanks to this special modification shown in Fig. 2.8, the rotor is made magnetically anisotropic. With the use of an high frequency signal injection the rotor position is easily retrieved by the authors.

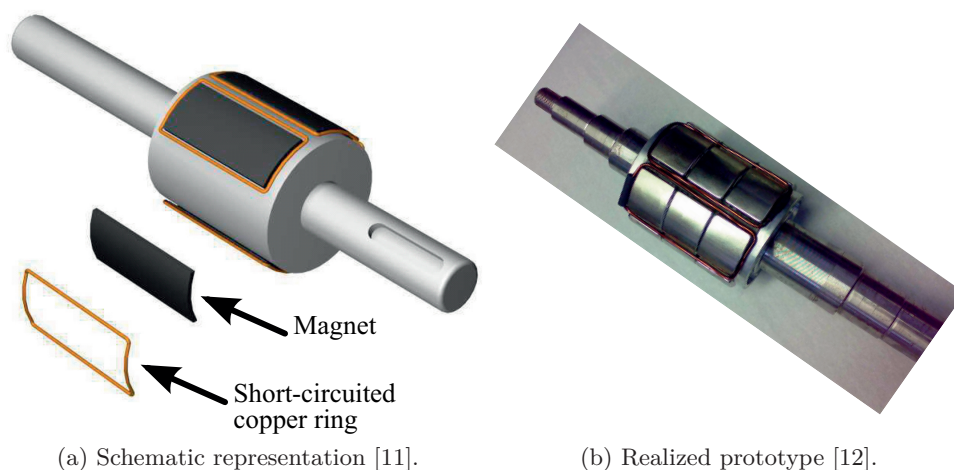


FIGURE 2.8 – Modified rotor for the sensorless position estimation through eddy currents detection.

2.4 Magnetic path asymmetries

The phase inductance is a function of the magnetic path of the flux in the motor, and thus it also depends on the relative permeance of the different materials along this path. Hereafter three cases that influence the magnetic path are analyzed. In all the cited techniques the inductance variations are normally retrieved through the injection of high frequency (500 Hz - 2 kHz) signals. The high frequency measured currents contain the information about the inductance, and thus about the rotor position too.

2.4.1 Iron mechanical asymmetries

In this first case, mechanical asymmetries in the rotor iron produce inductance variations. These mechanical saliencies can involuntarily result from the motor construction or can be voluntary introduced in the rotor structure, as in [20]. The modified rotor is shown in Fig. 2.9. The saliency is obtained by machining some slot openings, each one with different width.

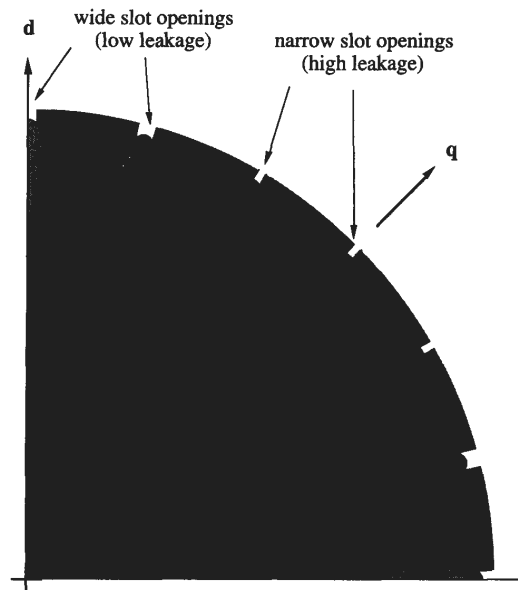


FIGURE 2.9 – Modified rotor for the sensorless position detection through iron mechanical saliency [20].

The intentional modification of the rotor has the great advantage that the absolute rotor position can be retrieved, which is not the case in most of the other techniques. The drawback is that a rotor has, obviously, to be modified.

2.4.2 Permanent magnet asymmetries

A second case is that the magnetic path may be position-dependent not only due to mechanical but also due to magnetic asymmetries. Indeed, in some motors, the phase inductance varies with the rotor position, although no mechanical saliency is present, as in a Interior Permanent Magnet (IPM) motor for example. In Fig. 2.10, an IPM rotor is shown.

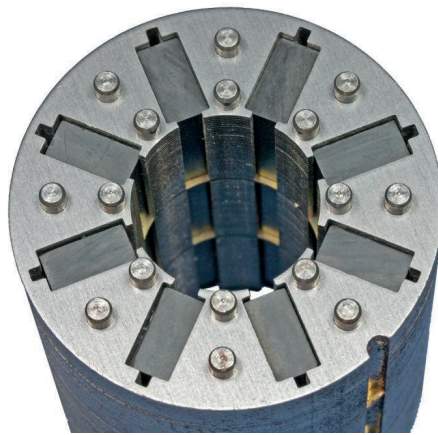


FIGURE 2.10 – Interior permanent magnet rotor.

The origin of these inductance variations is found in the magnet disposition on the rotor. Depending on the rotor position, the relative permeability of some permeances of the magnetic path change.

Already in the late nineties an IPM motor is driven thanks to these inductance variations [21]. Nevertheless, IPM structure is still very up-to-date and is the most studied for the sensorless position detection nowadays. Actually, most of the recent papers deal with IPM. In fact, as it is clearly stated in [22–25], IPM motors are suited for high-frequency signal injection techniques because the direct d -axis and the quadrature q -axis inductances are different, i.e. $L_d \neq L_q$ as the rotor is salient.

In [25–31] the position detection at standstill and in the very-low speed range is obtained with high frequency signal injection. In [32] a new tool is used to compare various sensorless techniques applied to IPM drives based on high frequency injection signals. An exhaustive list of rotor position detection techniques for IPM motors classified in different families is introduced in [33, 34].

2.4.3 Permanent magnet anisotropy

As the third case, the magnetic anisotropy method (MAM) introduced in [35] is a promising technique for detecting the rotor position. The principle consists in taking advantage of the modern rare earth magnet magnetic characteristics. In fact, magnets such as SmCo or NdFeB are intentionally made anisotropic during the production process. As a consequence of this anisotropy, the relative permeability of the magnets varies significantly between easy and hard magnetization axis. The measured magnetization curve of a NdFeB magnet is shown in Fig. 2.11. Again, the magnetic path is position-dependent because of the permeability variations in the magnetic equivalent circuit permeances. As for the eddy currents, a small setup is made in order to qualitatively estimate the

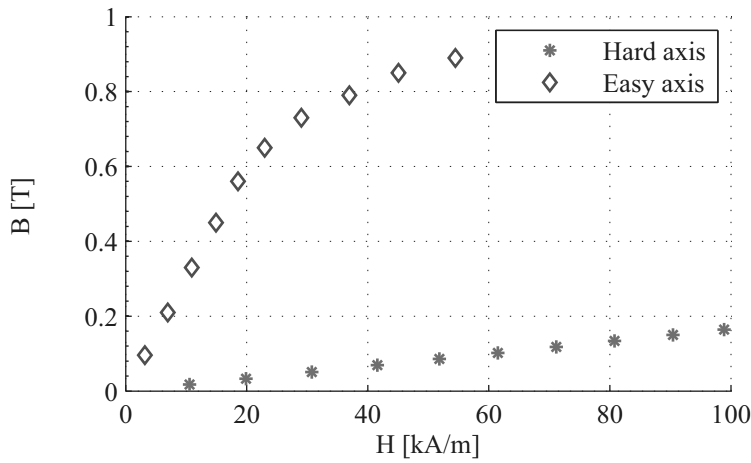


FIGURE 2.11 – Hard (*) and easy (\diamond) magnetization curve for NdFeB magnet [35].

influence of the magnetic anisotropy on the phase inductances and resistances. Fig. 2.12 shows the used hardware, a three phases coils on a plastic support and a anisotropic magnet (hold by the white plastic support). Referent rotor positions 0° and 90° are schematically represented in Fig. 2.13. Fig. 2.14 shows the measured L_{AA} as a function of the rotor position. As predicted, at 0° , when the coil A is aligned with the rotor PM easy axis, the relative permeance of the PM is the highest, and L_{AA} reaches its maximum values. At 90° , the situation is opposite. The rotor PM hard axis faces now coil A , the PM relative permeance is lower and thus L_{AA} is at its minimum. Despite the fact that the variations are noisy and in the order of 3% only, in [35] they are detected and used as a source of position information.

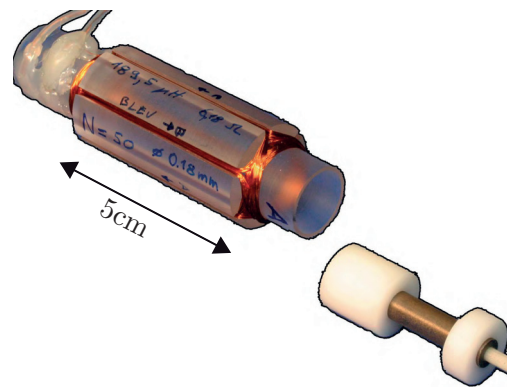


FIGURE 2.12 – Plastic coil support and SmCo magnet.

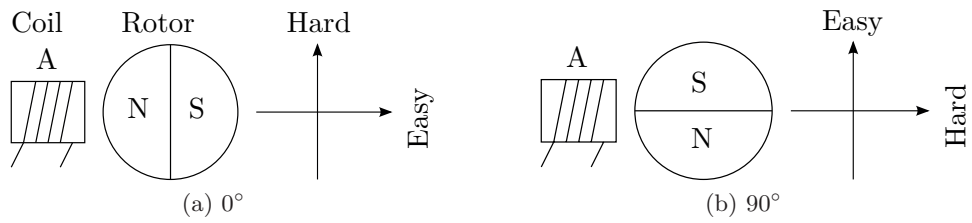


FIGURE 2.13 – Magnetic anisotropy measurements angular reference.

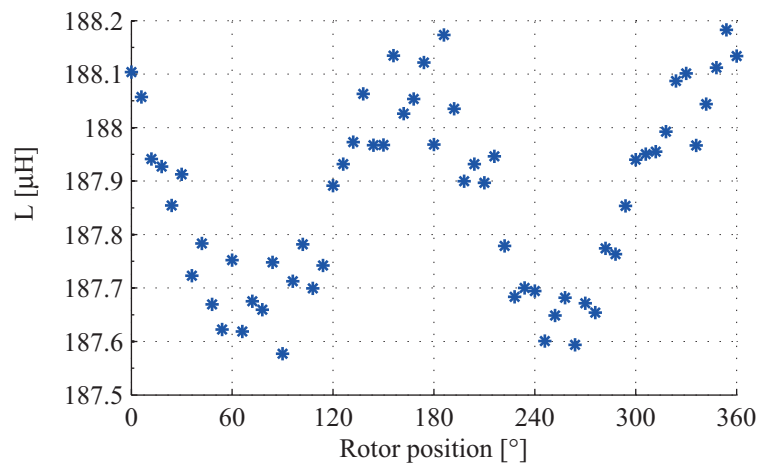


FIGURE 2.14 – Measured L_{AA} at 40kHz.

2.5 Kalman filtering

« *Theoretically* the Kalman Filter is an estimator for what is called the *linear-quadratic problem*, which is the problem of estimating the instantaneous “state” [...] of a linear dynamic system perturbed by white noise - by using measurements linearly related to the state but corrupted by white noise. The resulting estimator is statistically optimal with respect to any quadratic function of estimation error.

Practically, it is certainly one of the greater discoveries in the history of statistical estimation theory and possibly the greatest discovery in the twentieth century » [36].

Kalman filtering is a powerful mathematical tool and has been implemented in an extremely wide number of applications. Its functioning can be explained with the following example. Let Σ_{real} be a system regulated by the control vector \mathbf{u} . Σ_{real} is completely described by some physical values, the state variables x_n , contained in the state vector $\mathbf{x} = (x_1, x_2, \dots, x_m)^T$. Most of times, one or more state variables x_m are not directly accessible and may not be measured. Imagine now that it is wanted to monitor or control one or more state variables x_m . A first trial that can be done is to estimate the state of Σ_{real} by building a mathematical model of the real system, Σ_{mod} , and inject in both systems, the real and the model, same control vector \mathbf{u} . This approach is schematized in Fig. 2.15, where $\hat{\mathbf{x}}$ is the estimated state vector.

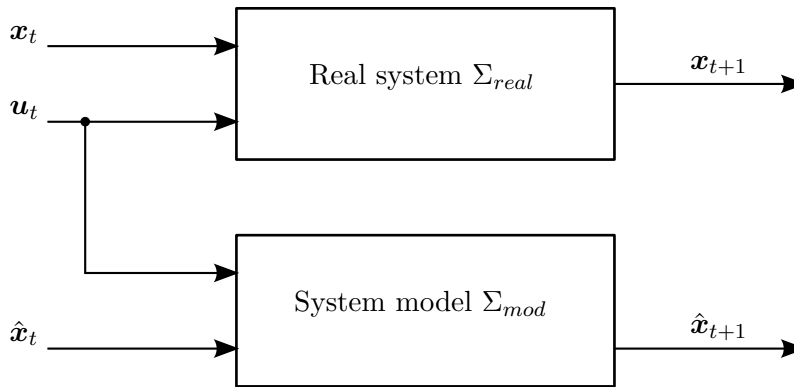


FIGURE 2.15 – Scheme of an open loop simulation.

If $\hat{\mathbf{x}} = \mathbf{x}$ at $t = 0$ s, it is expected that both systems evolve in the same manner. However, this ideal case does not exist in reality. The model is always in some way an approximation of the real system and noise is present. Because of that, the practical realization of Fig. 2.15 rapidly lead to divergence and $\hat{\mathbf{x}}_t \neq \mathbf{x}_t$ when $t \rightarrow \infty$.

A solution to this divergence is provided by the observer based estimators, to which the Kalman filter belongs to. The Kalman filter functioning is schematically represented in Fig. 2.16. As it can be noticed, in this second schema, a measurement vector \mathbf{y} connects

the real system block with the estimator block. \mathbf{y} contains the information about the real system that is available, measurable. This information coming from Σ_{real} is then merged by the Kalman filter with the information coming from Σ_{mod} and the optimal estimation $\hat{\mathbf{x}}_{t+1}$ is calculated.

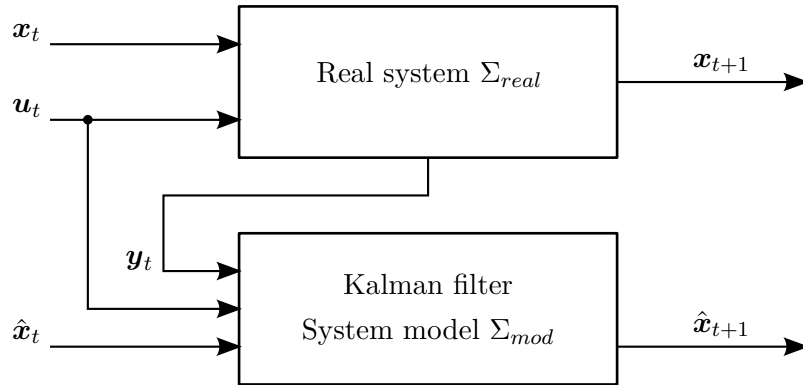


FIGURE 2.16 – Scheme of a Kalman filter functioning.

The mathematical background and the implementation of a Kalman filter are not addressed in this thesis. An extensive introduction to Kalman filtering and its practical implementation is provided in [36].

2.5.1 Kalman filtering for sensorless position detection

Although Kalman filtering has been initially developed for linear systems, its extension to non-linear application has rapidly been introduced. The most successful implementation of the Kalman filter for non-linear systems is the Extended Kalman Filter (EKF), where the non-linear state equations are linearized about the estimated trajectory. Further in this thesis, no distinction is done between the linear or non-linear implementation of the Kalman filter. The model equation of a synchronous motor are typically non-linear and the realization of a sensorless drive based on Kalman filtering has been deeply investigated in [37–47].

From these analysis, three main drawbacks of Kalman filtering based techniques applied to the sensorless position detection are highlighted.

Matrices choice

First of all, these techniques exhibit high dependence on the choice of the matrices needed for algorithm implementation, as the system covariance matrix \mathbf{Q}_n , the noise covariance matrix \mathbf{R}_n and the initial covariance matrix of state estimation uncertainty \mathbf{P} . Elegant

solutions for this problem are introduced by [44, 47], where methodical procedures for the matrices choice are suggested.

Low speed operations

A second major limitation of these techniques is the motor operation at low speed. This topic has been addressed for example in [45, 48] where the motor is driven in open loop, or in [46] where the proposed solution uses substitutive techniques at low speed. In [49] a Hall sensor is used as a low resolution sensor for the low speed operations. Although this last solution really extends the working range of the Kalman filter down to the low speed operations, its implementation needs a Hall sensor and thus is not sensorless. Finally, these few works do not really solve the problem, and a fix to this drawback has not been found.

Parameters quality dependence

In [40, 46, 50] another weakness of observer based techniques is highlighted. Kalman filtering exhibit high dependence on the parameter model accuracy. Poor quality model parameters lead to poor quality estimations. This weakness is not important in case of steady state operations, but it affects considerably the high dynamic operations. For overcoming this last drawback, parameter estimation techniques are investigated. This special research topic is detailed in the following subsection.

2.5.2 Parameters estimation

The field of synchronous motor parameter estimation has widely been studied in order to increase the drive control performance. In [46] the electrical and mechanical parameters of the Kalman filter synchronous motor model are estimated with an off-line optimisation algorithm. Thanks to this fitting, the drive performance increases and a very high dynamical performance is obtained. In [51], a powerful off-line technique is introduced for the synchronous motor electrical parameters estimation, even in presence of space harmonics. These calibration methods need nevertheless to be applied off-line, and therefore they still suffer from a major drawback: the drive parameters are not static in time, they evolve. The torque constant changes with the motor temperature, as well as the phase resistances, which may also change because of the connections wear-out. In addition, the load is unknown. Even if its inertia may not change in time, the friction constant is highly dependent on the bearings health, lubrication and changes extremely during the drive lifetime. Moreover, because the calibration is performed off-line, every new drive electronics-motor pair has to be calibrated before its first use.

For an industrial application, an on-line parameter estimation is preferable. On-line techniques have also been widely studied for improving the performance and the robustness of the drive regulator, like in [52–54]. In [53] the author use a recursive least square algorithm to estimate the stator resistance, the rotor magnetic flux and d - and q -axis coil inductances. A fast algorithm estimates the inductances, and its results are used by a slower algorithm for estimating resistance and magnetic flux. In [54], the identifiability of synchronous motor parameters is deeply analyzed. It is shown that it is not possible to identify R , L and K_m at steady state, and therefore, because of the limits imposed by the application, it is chosen to assume K_m as constant and known. Three identifications methods are compared: the first and the second are based on output error cancellation on a normal and on a decoupled system [55] respectively. The third method is an Extended Kalman Filter. The second method results to be the best as it shows a rapid convergence and is less time-consuming than the EKF. Results show that all three techniques converge towards the correct values of R and L only if K_m is exact, and that small uncertainty on K_m leads to important estimation errors on R . The parameter estimations in [52–54] are nevertheless obtained using a mechanical transducer for the rotor position and speed measurement. In [53] the authors claim that the technique could be coupled with a sensorless position and speed drive, but it should be minimally dependent on the motor parameter.

On-line parameter estimation and sensorless control is addressed in the following papers. In [56], the estimation of the stator resistance for improving the sensorless Matsui's method [57], based on the back-EMF reconstruction, is introduced. In [58], stator resistance and back-EMF coefficient are identified, but a constant speed is needed. In [59], the stator resistance and d - and q -axis coil inductances, but not the torque constant, are estimated in a sensorless drive. In [60], R , L are estimated at standstill and K_m during normal drive. However, if speed variations are imposed to the drive, position estimation errors during the transient still persist.

The on-line estimation of the electrical parameters of a synchronous motor model for a sensorless drive based on a Kalman filter is introduced in [40]. The technique is based on a recursive parameter identification. Results, shown for a speed step from 0 to 200 rad/s, are very interesting, but only when the motor has attained the reference speed. Again, during the transient, a quite big difference of more than 1000 rpm appears between the real motor speed and the estimated one. The reason can be found in the fact that the mechanical characteristics of the drive are not studied in that work. In [61] a BLDC motor is driven with a Kalman filter and the state estimation accuracy, especially at low speeds, is increased thanks to the additional estimation of the phase resistance. The others parameters are however not estimated.

2.6 Conclusions

The literature on sensorless position detection of BLDC motors is copious and only a small sample of it is introduced here. However, at the end of this chapter some conclusions, that may help to focus the present research, can be drawn.

In the domain of the standstill and low speed operations many phenomena that influence the phase impedance have already been studied: iron saturation, eddy currents, mechanical or magnetic asymmetries present on the rotor and magnetic anisotropy of the permanent magnets. However, an important characteristic of a BLDC motor has been neglected so far: the BH characteristic of the iron composing the motor structure. This property of the iron influences the magnetic field and therefore a deep analysis of this phenomenon is needed for improving the motor modeling.

From the literature it also appears that practically all developed techniques for the position detection need a sort of calibration of the algorithm. This point is often neglected, sometimes briefly mentioned and rarely analyzed into detail. In case of an industrial utilisation, the need of a calibration step can be most of the time inadequate. For this reason, in this thesis an eventual need for calibration will be analyzed and a solution proposed.

Another important point missing in many papers is the testing of the sensorless algorithm in harsh environments. Many papers limit the trials to steady state operations, eventually testing the motor under constant load conditions. However, again in the optic of an industrial application, less information is provided on the behaviour of the drive neither in case of variable load and dynamic operations nor during long-time utilization that may lead to the change of the motor characteristics because of heating and wear and tear. The influence of the environment around the drive like the electromagnetic noise, the wiring between drive electronics and motor, the temperature variations and the robustness against load and speed variations have to be analyzed for ensuring the correct position estimation in all situations.

Contents

3.1	Introduction	30
3.2	Iron BH local hysteresis	32
3.2.1	Measurement setup	32
3.2.2	Measurements	33
3.3	Influence of the hysteresis on L_{xx} and R_x	37
3.3.1	Measurement of L_x	37
3.3.2	Measurement of R_x	40
3.3.3	Comments	40
3.4	Proof of the hysteresis influence on L_{xx} and R_x	40
3.4.1	Iron saturation	41
3.4.2	Rotor saliency	41
3.4.3	Eddy currents	43
3.4.4	Magnetic anisotropy	45
3.4.5	Empirical proof of the hysteresis influence on L_{xx} and R_x	46
3.4.6	FEM simulations	50
3.5	Motor modification	53
3.5.1	Measurements and comparison	53
3.6	Conclusions	54

3.1 Introduction

A LONG with the coils made of copper and the permanent magnet, iron is one of the three basic materials needed for the construction of a BLDC motor. Iron is necessary for conducting the magnetic flux and is normally present both at the stator and at the rotor.

The magnetic characteristic of iron is sometimes simplified to a linear relationship between the magnetic field H and the magnetic induction B . The parameter linking these two values is defined as its permeability $\mu = \mu_0 \mu_r$, where $\mu_0 = 4\pi \cdot 10^{-7}$ H/m is the vacuum permeability and μ_r is the iron relative permeability. It is:

$$B = \mu_0 \mu_r H \quad [T] \quad (3.1)$$

In order to improve the quality of the characterization, the phenomenon of saturation is also taken into account. Thus, every type of iron is normally qualified by its relative permeability at the origin μ_r , its saturation induction B_{sat} and its BH characteristic is represented like in Fig. 3.1. The knowledge of this curve is enough for solving most of the engineering problems.

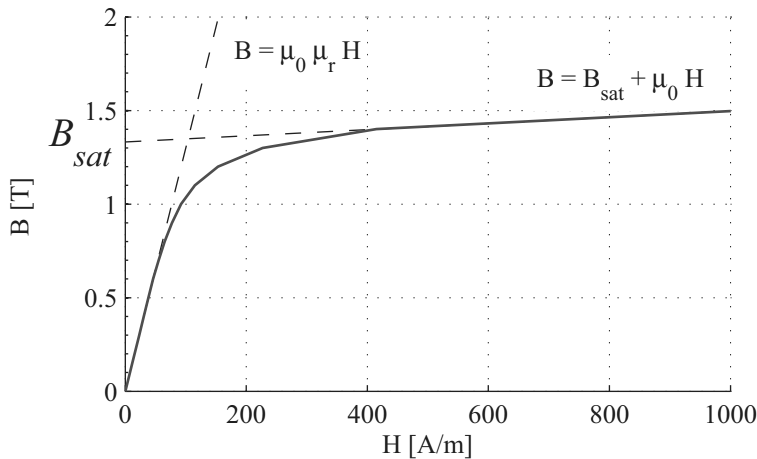


FIGURE 3.1 – Simplified iron BH characteristic.

In reality however, the magnetic characteristic of a magnetic material is much more complicated. Another non-linearity in the BH relationship exist: hysteresis. For describing the phenomenon of hysteresis in magnetism, a simplified explication based on the macroscopic interpretation of the Weiss domains can be used. A magnetic material is considered as an assembly of magnetic domains, each one of these has its own magnetic direction north-south (N-S). In a demagnetized magnetic material, the magnetic directions of the domains are chaotically oriented, misaligned. This situation is represented in Fig. 3.2 and the corresponding material working point in a BH plane is the origin (0,0).

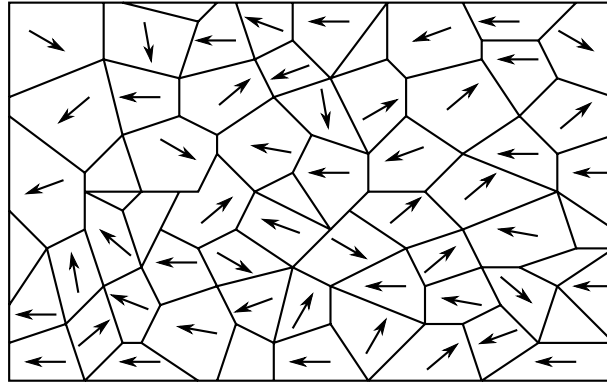


FIGURE 3.2 – Weiss domains in a non magnetised magnetic material.

Now, when the material is placed in a strong magnetic field \mathbf{H} , the domains will tend to align themselves with the external field. This situation is represented in Fig. 3.3. Because of the friction between the domain walls, the domains cannot rotate freely. The

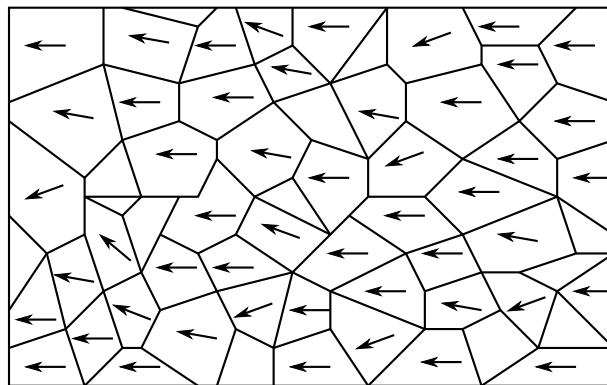


FIGURE 3.3 – Weiss domains in a magnetised magnetic material.

energy needed for the rotation of the domains creates a first difference from the idealized BH characteristic. The BH working point leaves from the origin, and only after a first bend due to the energy loss in the domain rotation, the induction field \mathbf{B} grows linearly with \mathbf{H} . This line is called first magnetization curve and is represented with the crossed line $\text{---}\times\text{---}$ in Fig. 3.4.

Now, if the magnetic field \mathbf{H} is decreased to zero the domains will start misaligning, but, again because of the friction between the walls that counter the domain rotations, the magnetic induction \mathbf{B} does not decrease linearly with \mathbf{H} and an hysteresis appears.

A main hysteresis, obtained by varying the external magnetic field strength linearly and symmetrically from a positive to a negative value is represented with the line $\text{---}\blacklozenge\text{---}$ in Fig. 3.4. The slope of the tangent to the hysteresis loop at $\mathbf{H} = 0$ A/m is usually defined as the relative permeability μ_r of the iron.

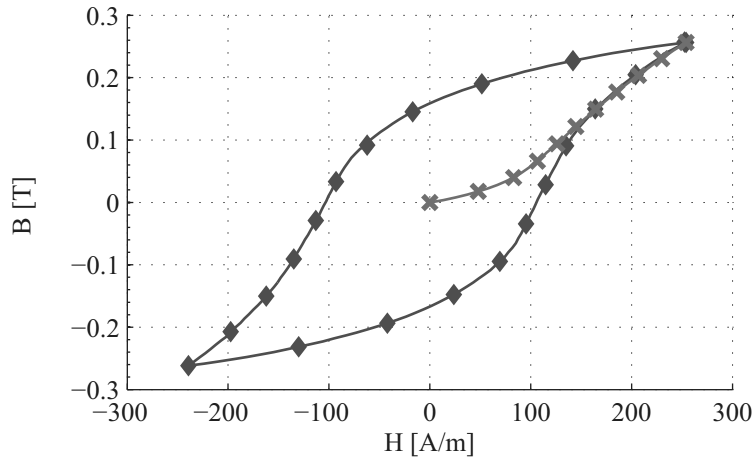


FIGURE 3.4 – Iron BH first magnetization curve and main hysteresis.

3.2 Iron BH local hysteresis

In the case of BLDC motors, the stator iron is constantly exposed to the phenomenon of hysteresis because of the permanent magnet. In fact, when the permanent magnet moves, the magnetic field seen locally by the stator iron varies between a maximum and a minimum, when the north and respectively south permanent magnet poles are aligned with the considered iron zone. During one electrical period, the working point of every zone of the stator iron makes an entire cycle along this main hysteresis.

The magnetic field created by the phase currents of the BLDC motor evidently also affect the iron BH working point. For example, the injection of high currents can lead to the iron saturation. This is exploited in the saturation techniques for the standstill position detection, as introduced in Section 2.2. However, when a small current is injected into a phase coil, the BH working point of the iron is also influenced. In order to highlight this influence and better understand the hysteresis phenomenon in a BLDC motor, an iron BH characteristic is measured and analyzed hereafter. The lecturer may refer to [62–64] or Chapter 11 in [65] for more details on the hysteresis in magnetic materials.

3.2.1 Measurement setup

For performing the measurements of the magnetic characteristic of the iron, a torus with airgap is used, Fig. 3.5. The torus iron is the one used in the construction of the motor shown in Fig. 1.4b. A current I is injected into a winding which is wound around the torus, and a gaussmeter is placed in the airgap for measuring the induction field B . An automatized measurement test bench is realized, Appendix C.1.

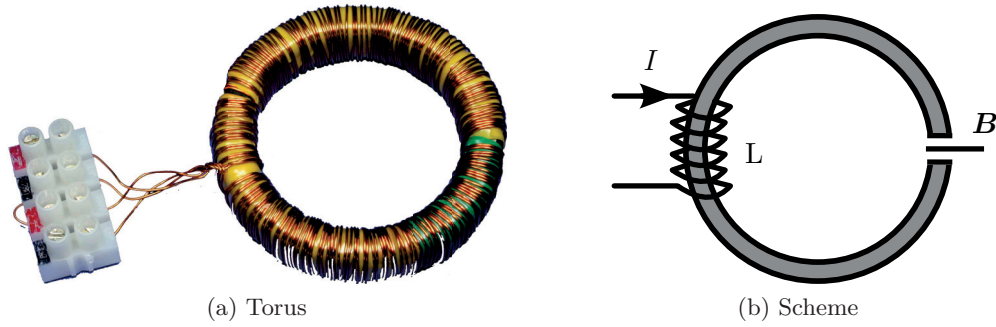


FIGURE 3.5 – Torus used for the BH measurements

Let δ be the airgap, C the medium circumference of the iron and N the number of turns of the coil, the magnetic field \mathbf{H} is calculated as follows:

$$H = \frac{NI - \frac{B\delta}{\mu_0}}{C - \delta} \left[\frac{A}{m} \right] \quad (3.2)$$

3.2.2 Measurements

The contribution of the permanent magnets to the iron magnetization in the motor is imitated by a DC current injected into the coil. By varying this current between I_{max} and $-I_{max}$, the working point in the BH plane describes a main hysteresis loop. For imitating the injection of a current into the coil, an additional current is superposed. This measurement is repeated at different levels of DC current, i.e. at different positions of the main hysteresis. By this way the injection of current into a phase coil for different rotor positions is simulated.

It is found that, because of the current injected into the coil, the working point in the BH plane is led to follow local hysteresis loops. The resulting loops (the main and the local ones) are shown in Fig. 3.6.

Local hysteresis slopes

For enabling a comparison between the local loops slopes, 8 local loops are superimposed in Fig. 3.7. It is interesting to note that the small loops have different slopes compared to each other. In fact, it is normally assumed that the local hysteresis, that are often neglected and simplified with a straight line, have an unique slope. A classical approach is to consider that the latter is the same as the slope of the tangent to the main hysteresis loop at $\mathbf{H} = 0$ A/m [4].

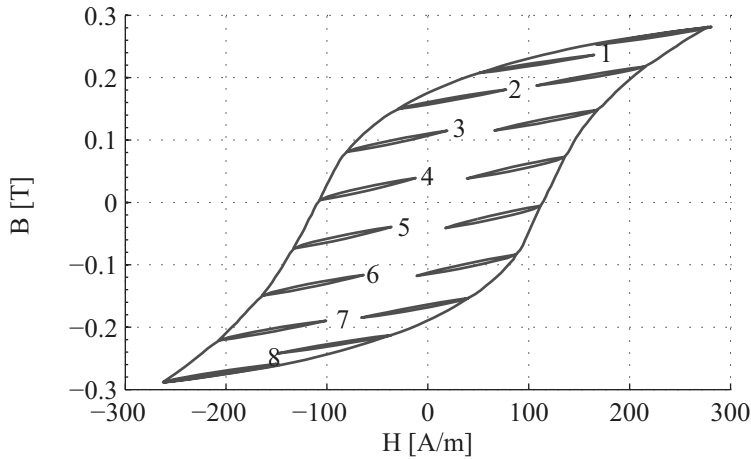


FIGURE 3.6 – Iron BH main and local hysteresis.

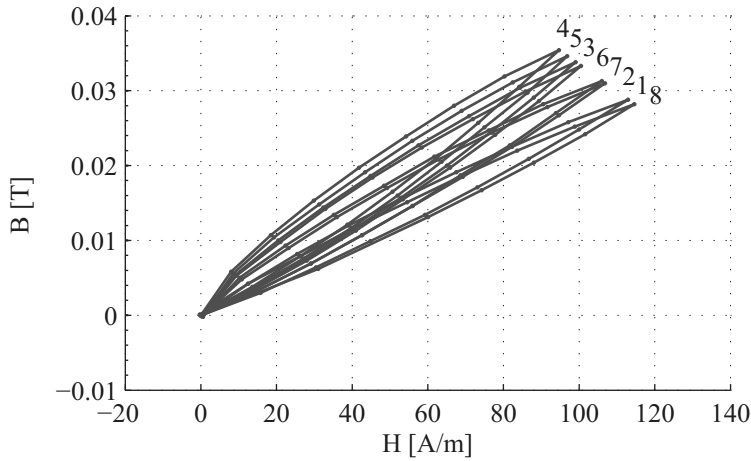
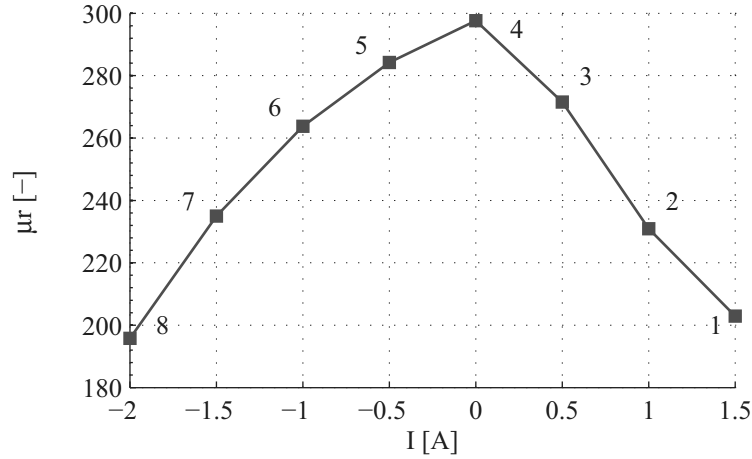


FIGURE 3.7 – Local hysteresis superimposed

However, this experiment shows that the relative permeability μ_r of the stator iron varies locally depending on its corresponding point on the main hysteresis. The value of μ_r of the local loops is shown in Fig. 3.8. This phenomenon has a mayor influence on the coil inductance. As the relative permeability μ_r of the iron is directly related to the inductance, the latter varies as a function of the position of the iron BH working point on the hysteresis loop. In the case of a BLDC motor, that means that for different rotor positions the coil self inductance will vary too. Coherently with the loops slopes shown in Fig. 3.8, the highest L_{xx} value should be found for the q positions, $L_{xx} = L_q$, where a pole transition is opposite to the phase (the respective Hall sensor changes between 0 and 1). On the other hand, the lowest L_{xx} value should be found for the d positions, $L_{xx} = L_d$, where an N or S pole is opposite to the corresponding phase (the respective Hall sensor value is 0 or 1).

The mutual inductance L_m is also influenced by this effect, but their contribution to


 FIGURE 3.8 – μ_r versus injected current.

the variation of the phase inductance L_A depend on the magnetic configuration of the BLDC motor.

Local hysteresis areas

Another important consequence of hysteresis in magnetic material is the appearance of the hysteresis losses. That means that whenever the magnetic field \mathbf{H} vary in time, some energy is lost because of the hysteresis phenomenon.

From [4] it is known that the hysteresis losses are proportional to the area of the BH hysteresis loops. The energy per volume unit lost during one hysteresis loop is given by:

$$w_h = \oint H dB \quad \left[\frac{J}{m^3} \right] \quad (3.3)$$

Multiplying (3.3) by a frequency f and a volume V , the power losses P are found:

$$P = w_h f V \quad [W] \quad (3.4)$$

For quantifying these losses, the energy per volume unit w_h created by each of the presented 8 local hysteresis loops is calculated and presented in Fig. 3.9. Surprisingly, it is found that w_h of the local hysteresis loops is not constant, but varies depending on the working point on the main BH hysteresis.

The influence of this phenomenon on a BLDC motor is highlighted in [19]. Based on the observation that the value of the resistance R of a coil measured at a high frequency is higher than the same resistance measured with an ohmmeter, it is proven that one part of this difference is due to the eddy current losses, and that another part is due to the

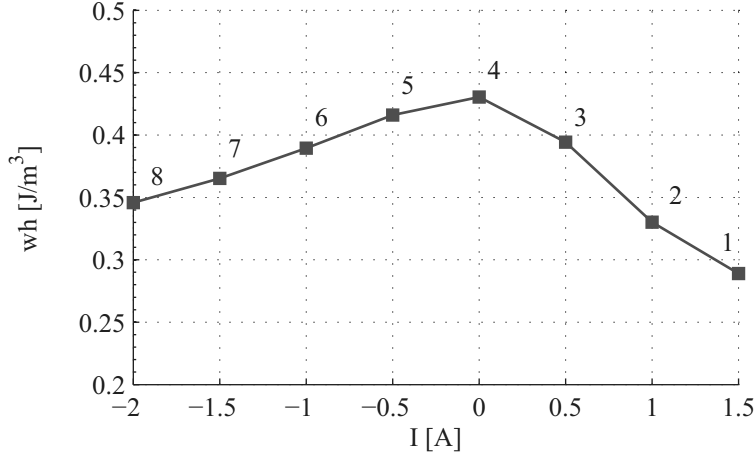


FIGURE 3.9 – Energy per volume unit losses w_h versus injected current.

iron hysteresis losses.

The power losses in an electrical circuit can be quantified by

$$P = \frac{1}{2} R I^2 \quad [W] \quad (3.5)$$

where I is the amplitude of the AC current and R the coil resistance. Equalling (3.4) and (3.5), P is eliminated and it follows that

$$R = \frac{w_h f V}{\frac{1}{2} I^2} = \frac{2 w_h f V}{I^2} \quad [\Omega] \quad (3.6)$$

Now we can define a resistivity parameter ρ , independent from the volume V and the frequency f , which is a physical constant like μ_r .

$$\rho = \frac{R}{2 V f} = \frac{w_h}{I^2} \left[\frac{J/m^3}{A^2} \right] \quad (3.7)$$

Starting from the measurements of w_h and the current amplitude needed for creating the local loops, ρ for the 8 local loops is calculated and presented in Fig. 3.10.

It can be noticed that ρ behaves like μ_r . As for μ_r , ρ has its maximum value for the local loop 4, and the minima for the loops 1 and 8. As a consequence of the hysteresis effect, it can be stated that the resistance R of the coil also varies depending on the iron working point in the BH plane. In a BLDC motor that means that, as for the coil inductance, the coil resistance varies with the rotor position. Furthermore, as for L_{xx} and coherently with the ρ values shown in Fig. 3.10, the highest R_x value should be found for the q positions, $R_x = R_q$, where a pole transition is opposite to the phase (the respective Hall sensor changes between 0 and 1). The lowest R_x value should be found

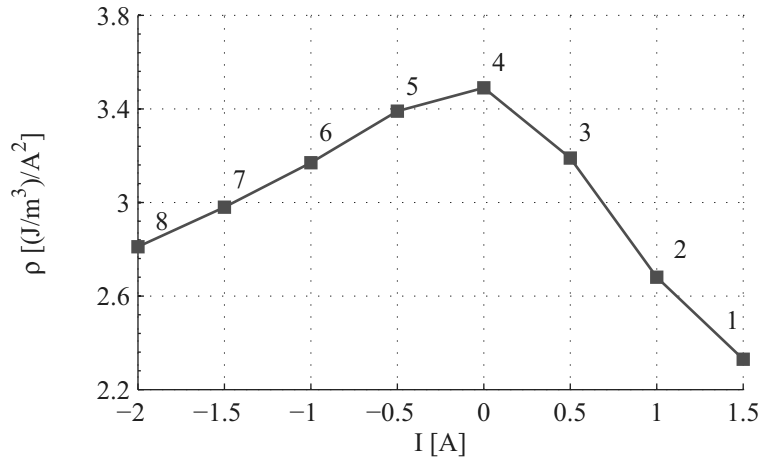


FIGURE 3.10 – ρ versus injected current.

again for the d positions, $R_x = R_d$, where an N or S pole is opposite to the corresponding phase (the respective Hall sensor value is 0 or 1).

Finally, from the performed measurements it is seen that the relative variations of μ_r and ρ around their respective mean values are very similar, 15 ~ 20%. It follows that the relative variations of L_{xx} and R_x during the rotor rotation should also have the same range.

3.3 Influence of the hysteresis on L_{xx} and R_x

In order to verify the results introduced in the previous section, the coil inductances L_{xx} and resistances R_x of a small industrial BLDC motor are measured. A picture of the motor is shown in Fig. 1.4b and a cut of the same motor is presented in Fig. 3.11. The motor nominal power is 100 W, it has 3 phases and 5 pole pairs. Its datasheet is given in Appendix B.1.

3.3.1 Measurement of L_x

Measurement of L_{xx}

The self inductance L_{xx} of each motor phase is measured at 20 kHz at standstill in function of the rotor angular position. Measurement is performed by injecting a sinusoidal voltage and detecting the current, using a precision impedance analyzer. The rotor is coupled with an actuator controlled from the PC that imposes the angular position. The three Hall sensors of the motor are also used to give an information about the

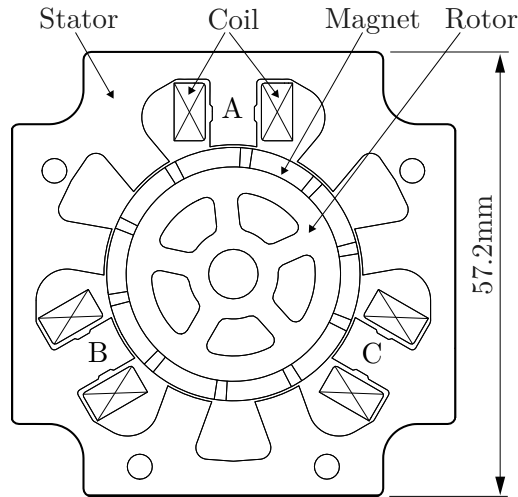


FIGURE 3.11 – Analyzed BLDC motor horizontal cut.

rotor position. Hall sensors give at their outputs a digital 0 or 1 and those signals are superimposed on the next figures at the bottom. The measurement setup is shown in Appendix C.2.

The measurements for an entire mechanical turn are plotted in Fig. 3.12. It clearly appears that the self inductances of the motor phases are dependent on the rotor position, although the variations are only about 1%. There are two complete oscillations of L_{xx} during one electrical period.

A zoom of two electrical periods only, shown in Fig. 3.13, highlights that the minima $L_{xx} = L_d$ are measured for the d positions, where an N or S pole is opposite to the corresponding phase (the respective Hall sensor value is 0 or 1), and the maxima $L_{xx} = L_q$ for the q positions, where a pole transition is opposite to the phase (the respective Hall sensor changes between 0 and 1). The p and q positions of the analyzed motor are illustrated in Fig. 3.14.

Measurement of L_m

Mutual inductances of the motor are measured manually as it is not possible to use the precision impedance analyzer for this purpose. The measured values are around $18 \mu\text{H}$ at 20 kHz. Because of the noise in the measurements, it is not possible to clearly state that they are position-dependent. Nevertheless, in the considered motor, the measured mean value of L_m is more than 20 times smaller than L_{xx} , and thus, its influence on the L_x variations can be neglected.

3.3. Influence of the hysteresis on L_{xx} and R_x

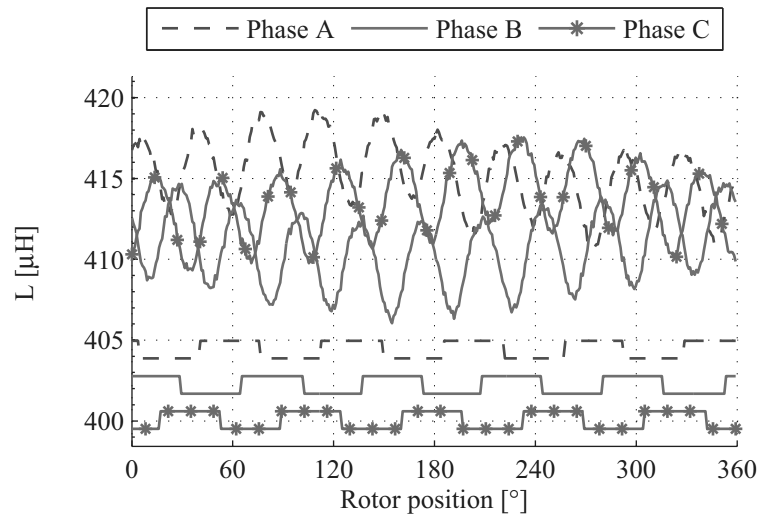


FIGURE 3.12 – L_{AA} , L_{BB} and L_{CC} versus the rotor position, measured at 20 kHz.

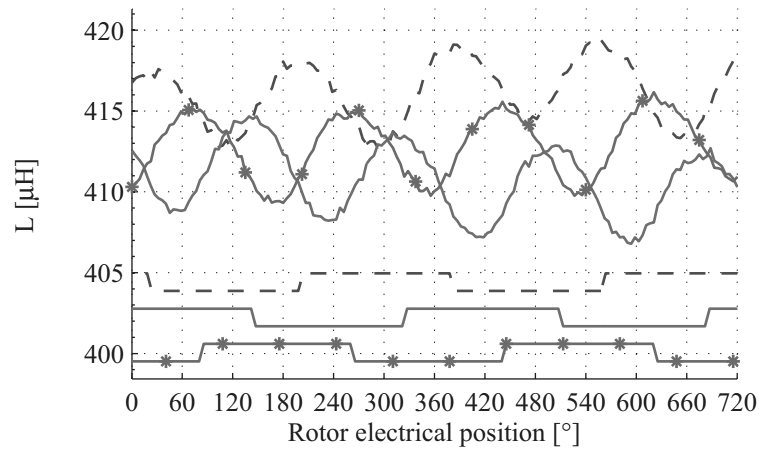
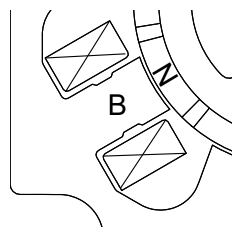
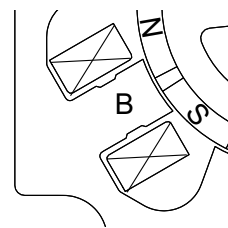


FIGURE 3.13 – L_{AA} , L_{BB} and L_{CC} versus the rotor position, measured at 20 kHz. Two electrical periods zoomed.



(a) Rotor d position.
 L_{xx} and R_x are minimum



(b) Rotor q position.
 L_{xx} and R_x are maximum

FIGURE 3.14 – Rotor d (a) and q (b) positions for the phase B .

3.3.2 Measurement of R_x

The phase resistances are now measured with the same technique and instrumentation shown in Appendix C.2. The performed measurements are shown in Fig. 3.15. Note that the phase DC resistance measured with a precision ohmmeter is 0.533Ω , which is approximately 20 times less than the measured AC values.

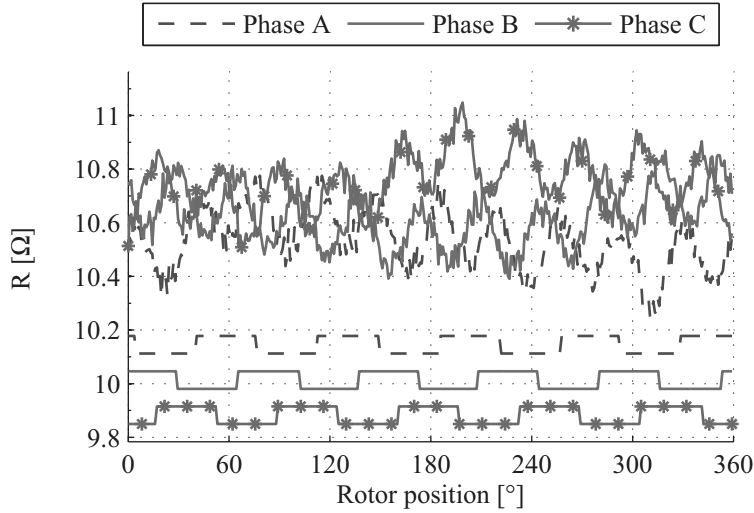


FIGURE 3.15 – R_A , R_B and R_C versus the rotor position, measured at 20 kHz.

As for the inductance L_{xx} , the resistance R_x is slightly position-dependent too and the variations are also about 1%. Furthermore, as for the inductance, the minima of the resistances are measured in the d positions and the maxima in the q positions.

3.3.3 Comments

As predicted by the measurements on the iron hysteresis, both L_{xx} and R_x show a position dependence. The relative variations are in the same range, about 1%, coherently with the local hysteresis measurements. Furthermore, the L_{xx} and R_x behave as predicted, with the maximum values for q positions and the minima in the d positions.

3.4 Proof of the hysteresis influence on L_{xx} and R_x

Many magnetic phenomena lead to position-dependent variations in L_{xx} and R_x . It is therefore required to prove that the variations measured in Section 3.3 are really caused by the iron BH hysteresis and not by another phenomenon. In the next subsections the different candidates that could be at the origin of the observed inductance and resistance

variations are analyzed. As in Chapter 2, for every candidate, if possible, measurements that confirm or exclude their influence to the observed phenomenon are provided.

3.4.1 Iron saturation

The flux density in the stator teeth, due to the permanent magnets only, is analyzed. As suggested in [66], the permanent magnets can cause local iron saturation in the stator teeth, thus modifying the local permeance and finally the phase inductance. That means that it would be possible to see some inductance variations depending on the rotor position due to saturation, without injecting any currents.

A Finite Elements Method (FEM) simulation of the analyzed motor is performed. The iron is modeled by its first BH magnetization curve, Fig. 3.16, and the phase currents are not injected. Fig. 3.17 shows that the maximal flux density in the stator is about 0.9 T,

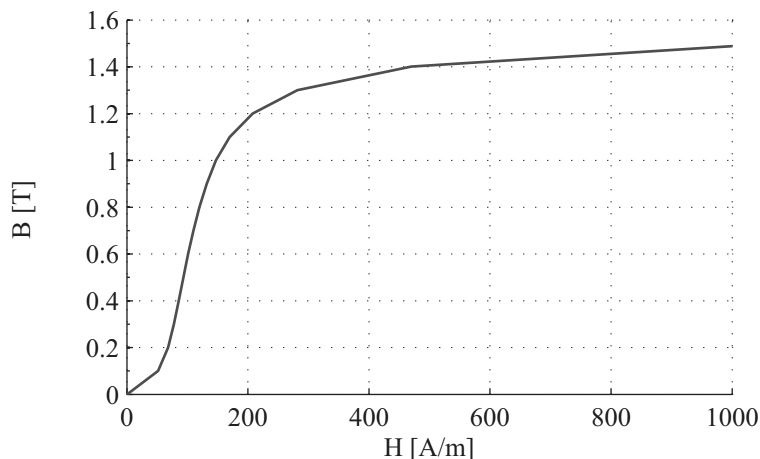


FIGURE 3.16 – Analyzed motor BH first magnetization.

higher values exist only in small areas. It can be concluded that in our case the iron is far from saturation. Moreover, the manufacturer of the analyzed motor confirms this result by its own measurements and simulations. As expected, the motor designer has taken for sure the important fact that the saturation deteriorates the motor performances. Hence, the influence of iron saturation on the measured L_{xx} and R_x variations is to be excluded.

3.4.2 Rotor saliency

The magnetic flux path in the motor, and therefore also the relative permeability of the different materials in the path, determines the inductance of the phase coil. Mechanical saliencies in the rotor introduce variations in the magnetic path and are consequently

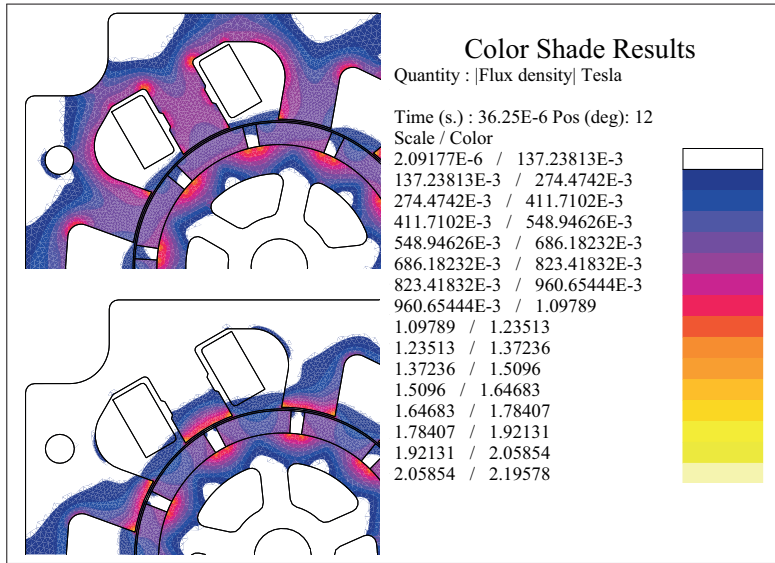


FIGURE 3.17 – Flux density in the stator iron for the d (top) and q (bottom) positions.

source of inductance variations. As stated in Chapter 2, these mechanical saliencies can result from the fabrication process or be voluntary introduced in the rotor by adapting its iron structure. Finally, permanent magnet asymmetries in the rotor can lead to inductance variations, as for example in buried permanent magnet synchronous motors. In the analyzed motor, mechanical saliency is rapidly excluded. In fact, as it can be noticed in Fig. 3.11, the rotor is symmetric (non-salient) by its construction. The rotor eccentricity is nevertheless measured. The measurement test bench is shown in Appendix C.3 and the results are plotted in Fig. 3.18.

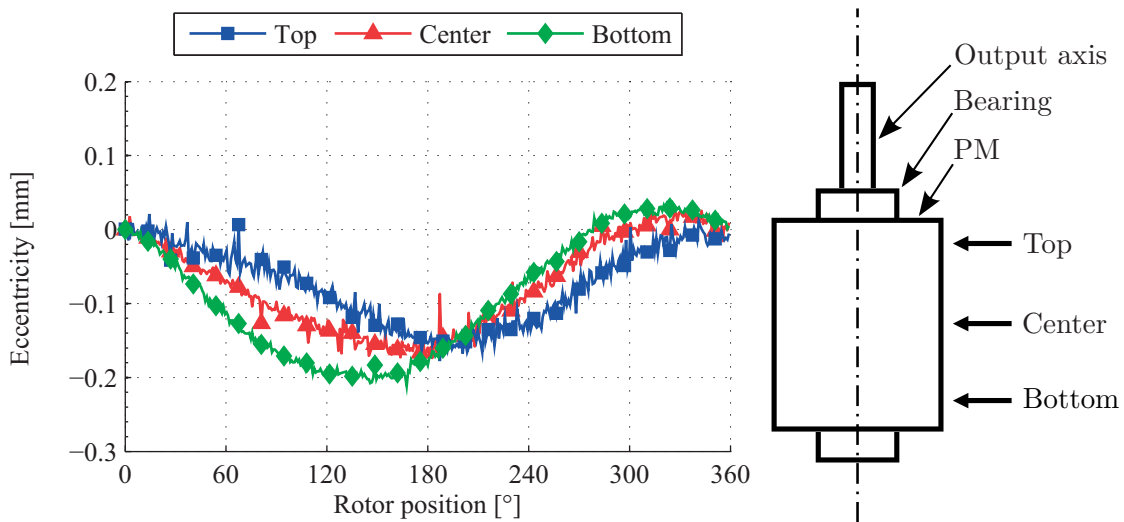


FIGURE 3.18 – Eccentricity (left) and measurement locations on the rotor (right).

3.4. Proof of the hysteresis influence on L_{xx} and R_x

The rotor permanent magnet is a unique plastic molded piece, magnetized when the rotor is already built. Its mechanical construction does not present any saliency neither.

Based on all these considerations, the influence of mechanical saliency on the measured L_{xx} and R_x variations is to be excluded.

3.4.3 Eddy currents

Eddy currents are always present in the motor iron and permanent magnets despite the facts that the electrical conductivity of the magnets is quite poor, $\rho = 56 \mu\Omega m$ for the analyzed motor, and the iron is laminated.

Fig. 3.19 shows L_{xx} and R_x of one motor phase, measured at frequencies varying from 1 kHz up to 40 kHz for a fixed rotor position. Obviously, L_{xx} decreases and R_x increases as the frequency increases. This is the well known effect of eddy currents. The skin and proximity effects in the conductor are also involved as the frequency increases and their effect is added to the eddy currents one.

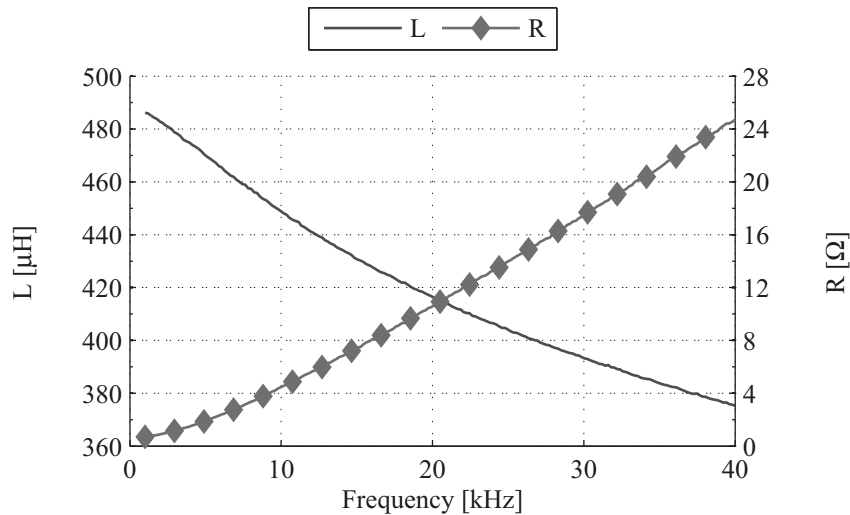
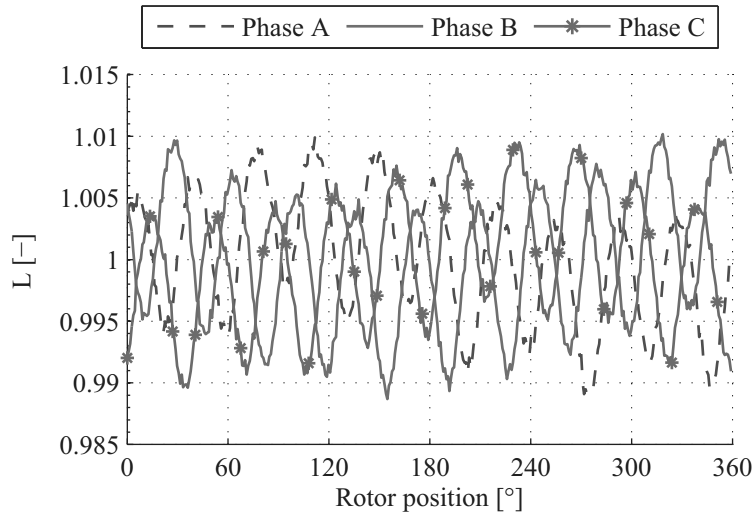
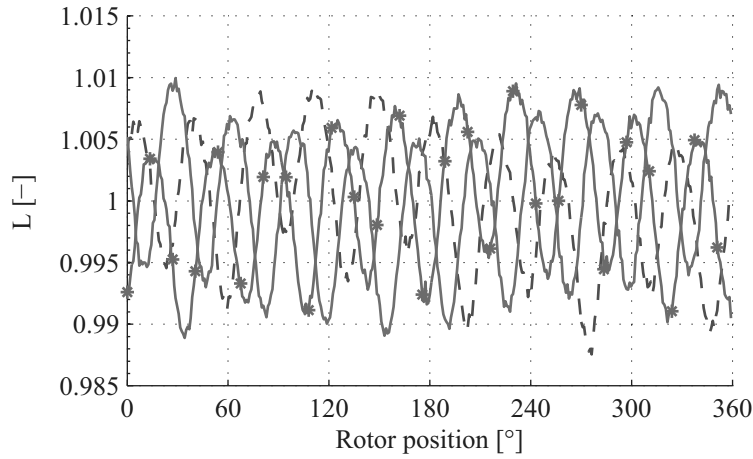


FIGURE 3.19 – L_{xx} (left axis) and R_x (right axis) of a motor phase versus the injected signal frequency for a fixed rotor position.

The inductance is then measured at 20 kHz and 40 kHz for different rotor positions. The measured values are normalized around the respective mean value in order to highlight relative variations. The normalized values for both frequencies are presented in Fig. 3.20. No difference can be seen between them. If the influence of the eddy currents in the phase inductance were position dependent, as they are stronger at 40 kHz, relative variations would be higher at 40 kHz and this is not the case. So, it can be concluded that the eddy currents do not participate to the position dependence of the inductance variations.



(a)



(b)

FIGURE 3.20 – Relative value of L_{xx} for the three motor phases versus the rotor position, measured at 20 kHz (a) and 40 kHz (b).

In the same way, phase resistances are analyzed. The values are measured for different rotor positions at 20 kHz and 40 kHz and the normalized values are presented in Fig. 3.21. For the resistance too, the amplitude of the relative variations is quite constant. We conclude that for the resistance variations, eddy currents seem not to be involved for the same reason as for the inductance.

3.4. Proof of the hysteresis influence on L_{xx} and R_x

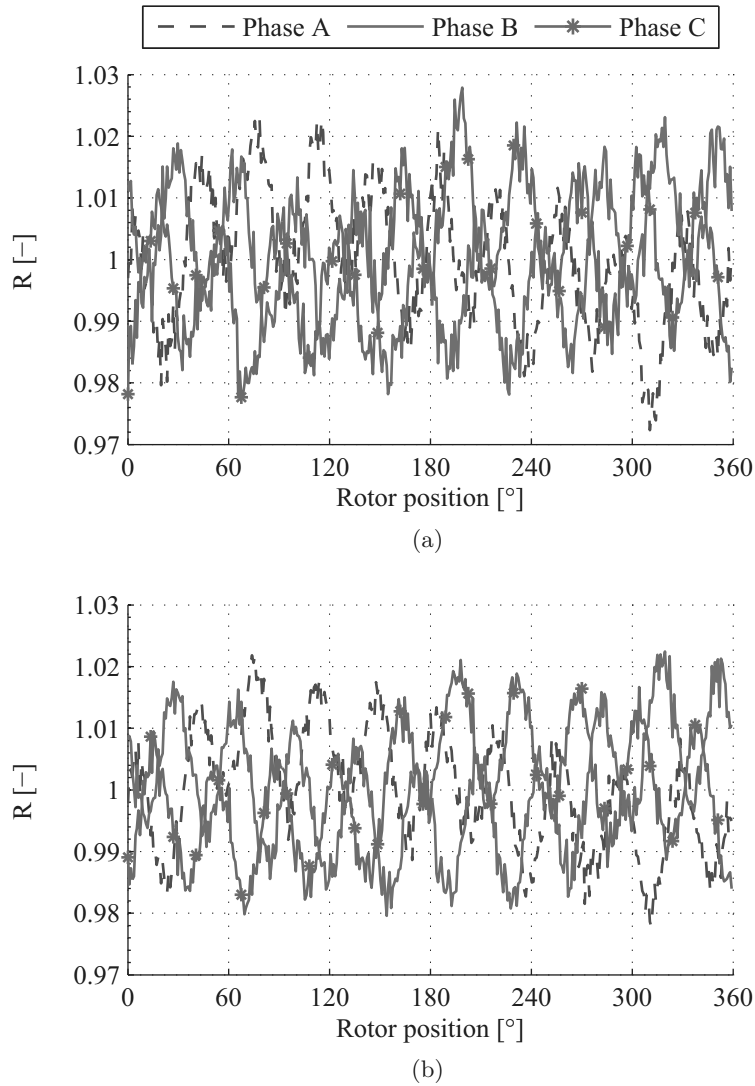


FIGURE 3.21 – Relative value of R_x for the three motor phases versus the rotor position, measured at 20 kHz (a) and 40 kHz (b).

3.4.4 Magnetic anisotropy

Magnetic anisotropy is also source of small inductance variations [9, 35]. Modern rare earth permanent magnets such as SmCo or NdFeB are intentionally made anisotropic during the production process and the relative permeability of these permanent magnets varies significantly between easy and hard magnetization axis. The magnetic path can therefore be position dependent and consequently some inductance variations may appear. However, in the analyzed motor, permanent magnets are isotropic by construction. As already written, the magnetic poles are created by magnetizing a unique cylindrical piece of plastic compression molded permanent magnet. For proving this fact, both L_{xx} and R_x are measured in a special motor in which the rotor permanent magnets are not

magnetized. Measurements are shown in Fig. 3.22. Clearly, no position variation due to the permanent magnet is detected, only a drift due to the mechanical eccentricity appears. Based on these considerations, magnetic anisotropy can be excluded as the source of the variations too.

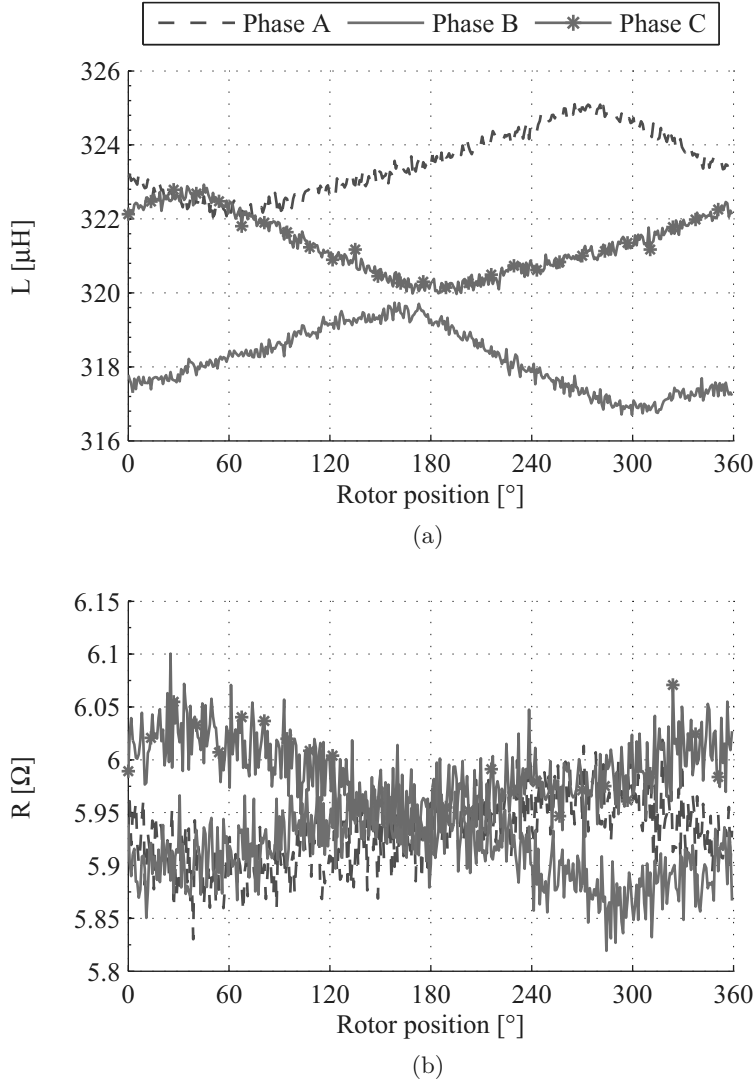


FIGURE 3.22 – L_{xx} (a) and R_x (b) measured at 20 kHz on a special motor with plastic rotor and non-magnetised permanent magnets.

3.4.5 Empirical proof of the hysteresis influence on L_{xx} and R_x

The theory introduced in Section 3.2 states that the interaction between the permanent magnets and the stator iron creates a variation in phase inductance and resistance because of the hysteresis on the iron BH plane. Hence, if the stator iron is removed,

3.4. Proof of the hysteresis influence on L_{xx} and R_x

no more hysteresis effects exists, and consequently, no more inductance and resistance variations should appear. Based on this consideration, and knowing now that all the previous phenomena are not involved in the measured L_{xx} and R_x variations, two new measurements are realized. They are performed on a special motor with a plastic stator. The rotor is one case a normal one made of iron, and in another case it is made of plastic. The permanent magnets in both cases are magnetized. A picture of the open plastic stator and plastic rotor motor is shown in Fig. 3.23.

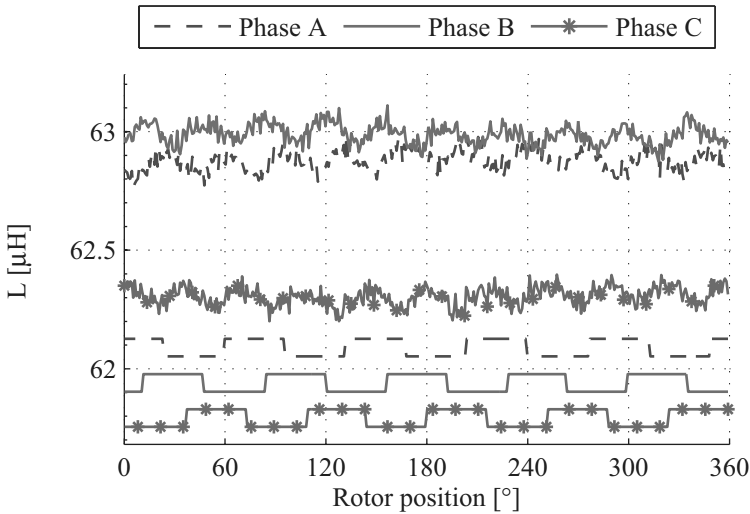


FIGURE 3.23 – Realized plastic stator and plastic rotor.

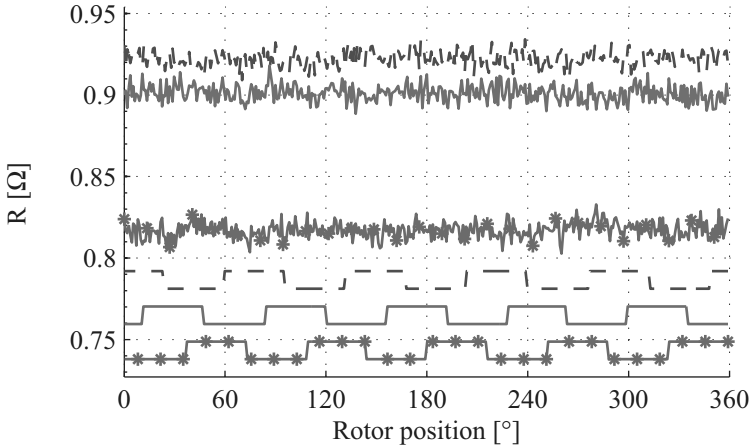
Measurements on the plastic stator, iron rotor are shown in Fig. 3.24, and the ones done on the plastic stator and plastic rotor are shown in Fig. 3.25. Surprisingly, for both motors there is a position dependency of L_{xx} ! L_{xx} variations are very small, in the order of $\sim 1\%$, which is 10 times lower than the L_{xx} variations measured on an normal iron motor. As in the measurements performed on the normal motor, the maximum values are obtained for the q positions and the minimum for the d positions. It is assumed that the origin of these small variations on L_{xx} that still appear in these two motors with no stator iron is a permanent magnet anisotropy created during the permanent magnet magnetization.

On the other hand, R_x does not vary at all. This is an expected result, as without iron there are no more hysteresis losses that are at the origin of the R_x variations.

Finally, even in presence of these very small oscillations on L_{xx} , it can be stated that without iron on the stator, the variations on L_{xx} and R_x measured in Section 3.3 disappear. Without iron the hysteresis effects cannot exist and thus, the theory developed in Section 3.2 is confirmed.



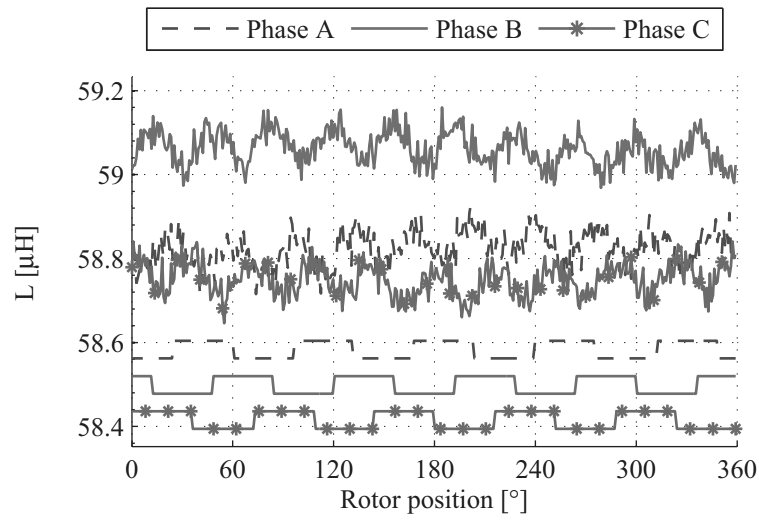
(a)



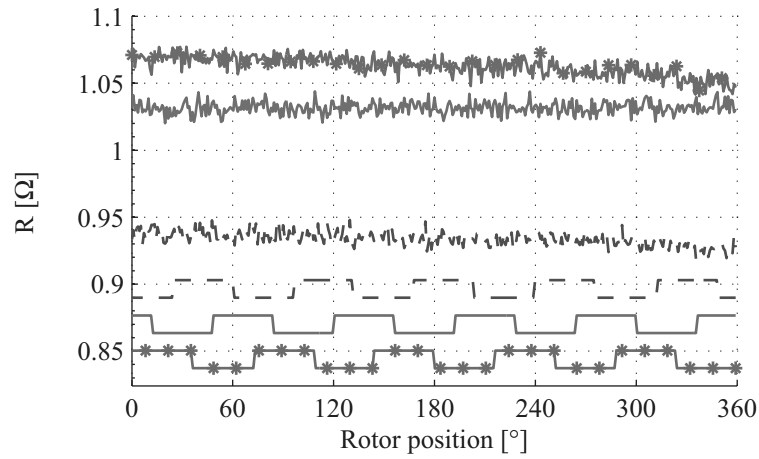
(b)

FIGURE 3.24 – L_{xx} (a) and R_x (b) measured at 20 kHz on a special motor with plastic stator, iron rotor and magnetised permanent magnets.

3.4. Proof of the hysteresis influence on L_{xx} and R_x



(a)



(b)

FIGURE 3.25 – L_{xx} (a) and R_x (b) measured at 20 kHz on a special motor with plastic stator, plastic rotor and magnetised permanent magnets.

3.4.6 FEM simulations

It is important to point out that the given explication of the phase inductance and resistance variations as a function of the position, based on empirical measurements, cannot be proven with FEM simulations. In fact, it is actually not possible to simulate by FEM the proposed theory because FEM simulation softwares cannot assign an hysteresis-type description to the iron BH characteristic [67]. As done for example in Subsection 3.4.1, FEM simulation softwares can only assign a non-linear function to the iron BH characteristic, which is normally the first magnetization curve. In order to prove the non-capability of FEM to simulate the measured phenomenon, L_{xx} is numerically calculated with a FEM software with different first magnetization BH curves. The different first magnetization BH curves used in these simulations are:

BH1, reproducing the real iron first magnetization curve, Fig. 3.26

BH2, the same curve without saturation, Fig. 3.27

BH3, a curve without starting bend but with saturation, Fig. 3.28

BH4, an linear iron, in which \mathbf{B} and \mathbf{H} are linearly dependent, Fig. 3.29

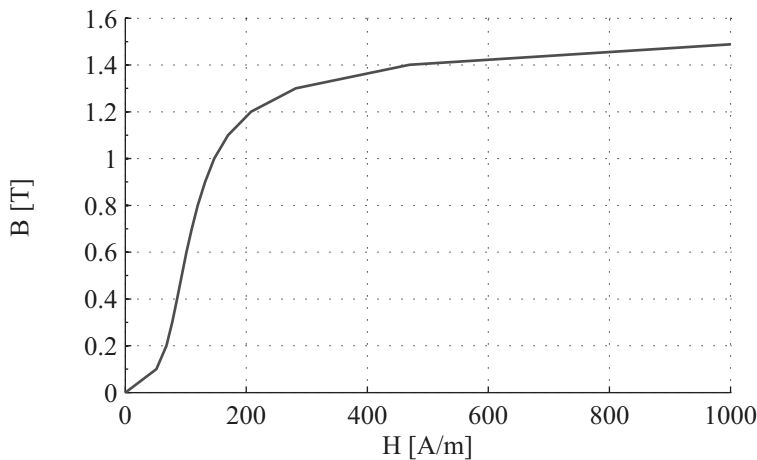


FIGURE 3.26 – First magnetization BH1 curve for FEM simulations.

3.4. Proof of the hysteresis influence on L_{xx} and R_x

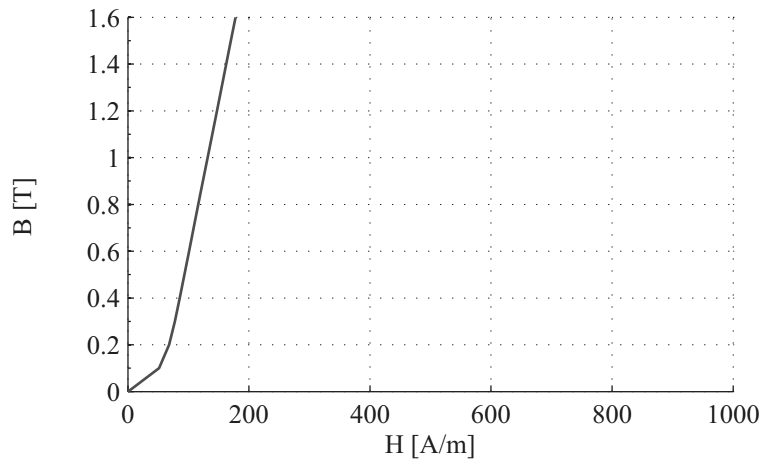


FIGURE 3.27 – First magnetization BH2 curve for FEM simulations.

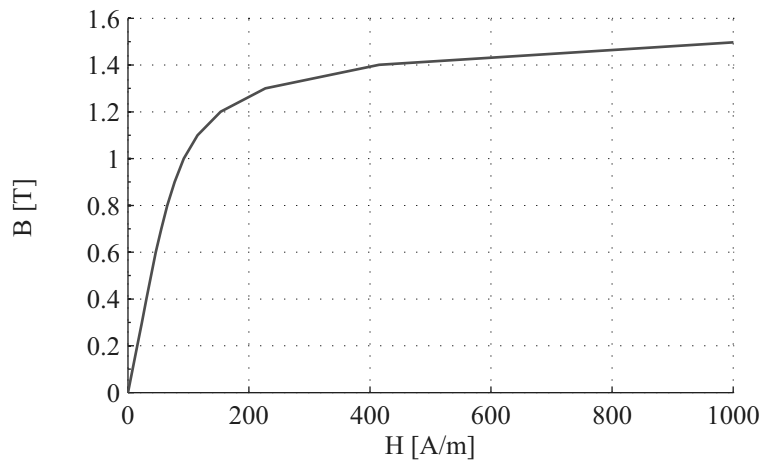


FIGURE 3.28 – First magnetization BH3 curve for FEM simulations.

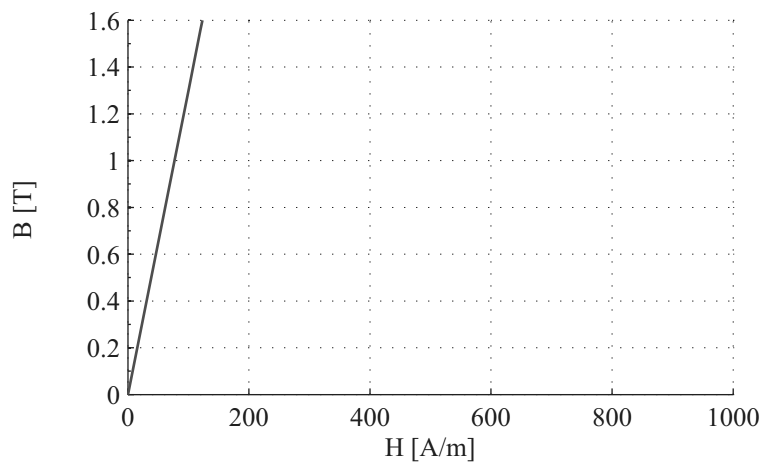


FIGURE 3.29 – First magnetization BH4 curve for FEM simulations.

L_{xx} is calculated for different rotor positions, the results of these simulations are summarized in Fig. 3.30. Position 0° corresponds to the d position and 18° corresponds to the q position.

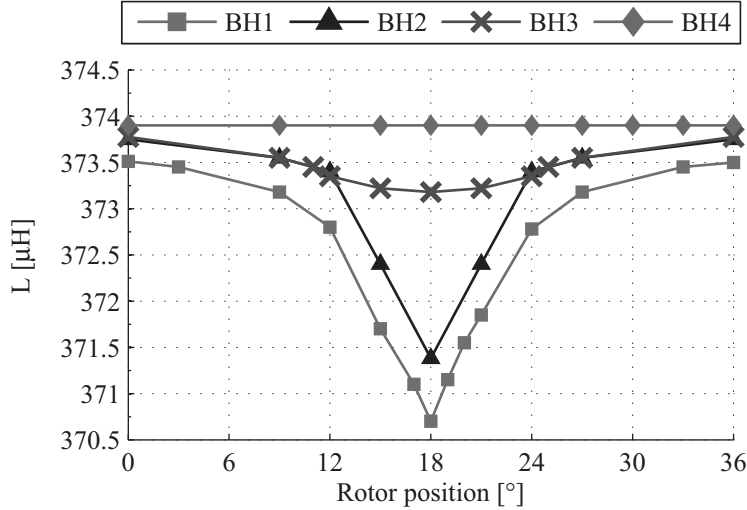


FIGURE 3.30 – L_{xx} versus rotor position for several BH magnetization curves.

As it can be noticed, for two BH curves L_{xx} vary significantly. These are the simulations performed with the curves BH1 and BH2 that have the initial bend. A small variation on L_{xx} is present in the simulation performed with BH3 too. That means that the saturation influences a little bit the L_{xx} value. Finally, if the simulation is performed with a linear iron, BH4, absolutely no variation is measured on L_{xx} .

Now, what is really important to point out, is that with the performed simulations the maximum is found for the d position and minimum is found for the q position. This is exactly the opposite of what has been measured on the real motor, where the maximum is found for the q position and the minimum is found for the d position. This example shows that not only FEM simulations cannot prove the influence of the BH hysteresis on the motor inductances and resistances, but they can moreover give completely wrong results!

So, finally, even if FEM simulations are often very helpful and are nowadays present everywhere, this small example shows that all the simulation results absolutely need to be carefully verified and analyzed.

3.5 Motor modification

Now that the physical background of the phase inductance and resistance variations is clarified, it is possible to propose some modifications to the motor, in order to amplify those variations. The objective of the modifications is to extend the size of the iron BH main loop, without leading to the teeth magnetic saturation that will affect the motor main characteristics. This can be obtained by reducing the iron section. In order to make the simplest adjustment to the motor geometry, it is chosen to shrink the three teeth that hold the three phase coils. The reduction of the iron section is obtained by cutting four slots into the tooth. A zoom on phase *A* for comparing the original and the modified stator is shown in Fig. 3.31.

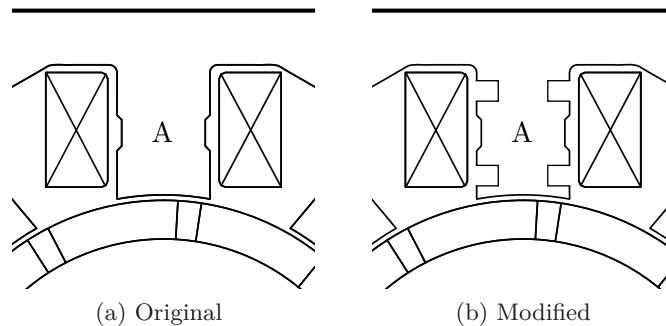


FIGURE 3.31 – Proposed stator modification.

A FEM simulation of the motor torque is performed for different slots depths Z . For the simulations, the curve BH1, Fig. 3.26, is used. The torque is calculated in a quasi-static simulation. The rotor speed is imposed to 6'500 rpm (nominal speed) and two coils are supplied by the nominal current 6.2 A. In Fig. 3.32 the saturation level at $t_{\Gamma_{max}} = T/3$ is shown. In Fig. 3.33 the results of the torque simulations during $t = T/6$ around $t_{\Gamma_{max}} = T/3$ are shown.

Based on these results, the depth of the slots is chosen at $Z = 1.5$ mm because deeper slots would lead to a mayor loss in terms of torque generated by the motor.

3.5.1 Measurements and comparison

Measurements of L_{xx} and R_x are performed on the modified motor with the same setups already used. The inductance L_{xx} of the three phases of the modified motor, measured at 20 kHz are shown in Fig. 3.34 for two electrical periods.

In Figs. 3.35 and 3.36 the relative variations on L_{xx} and R_x of the modified motor are compared to the same measurements done on the standard motor. It can clearly appre-

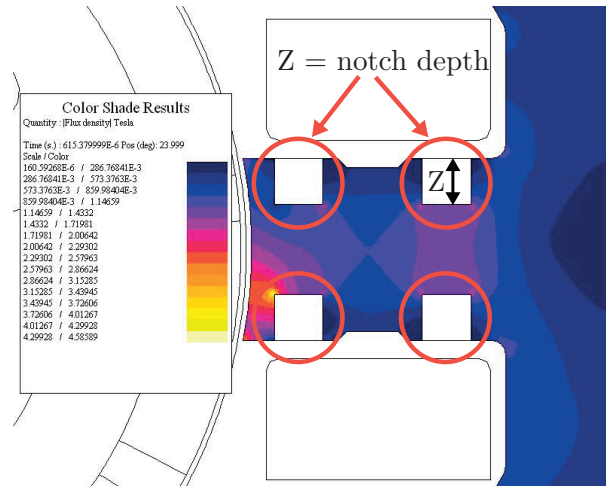


FIGURE 3.32 – Proposed stator modification. Modified motor.

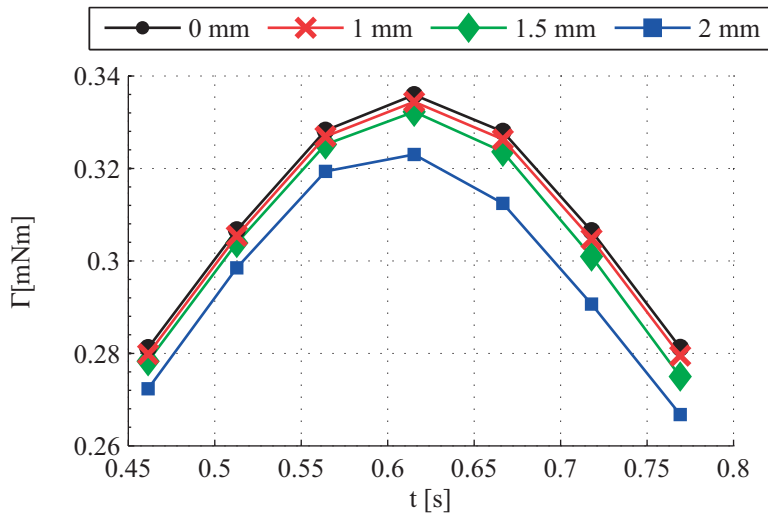


FIGURE 3.33 – Torque simulation of the modified motor for different notch deeps.

ciated how the L_{xx} and R_x variations in the modified motor are effectively increased. It can be observed that the modified motor relative variations are around five times larger than in the standard version. Moreover, some deformations on the sinusoidal shape appear. This is because of the magnetic interaction between the permanent magnets and the injected signal: the first signs of the iron teeth saturation appear.

3.6 Conclusions

In this chapter it is theoretically shown that in every BLDC motor with a stator made of iron, the interaction between the latter and the permanent magnets influences the

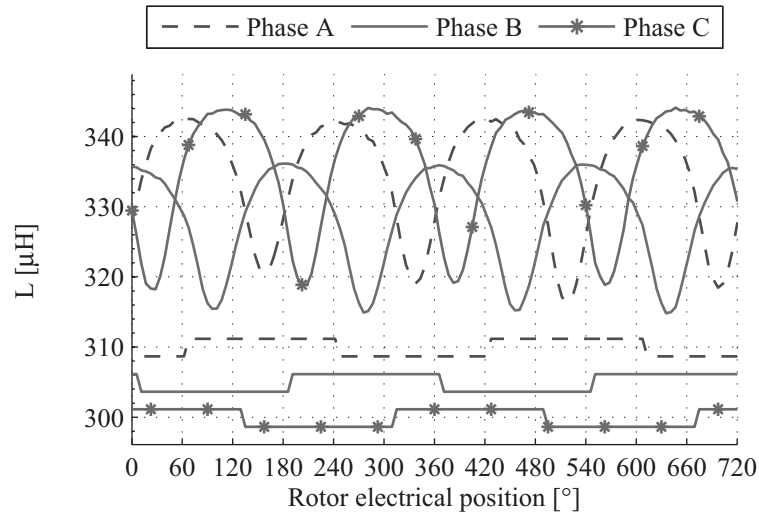


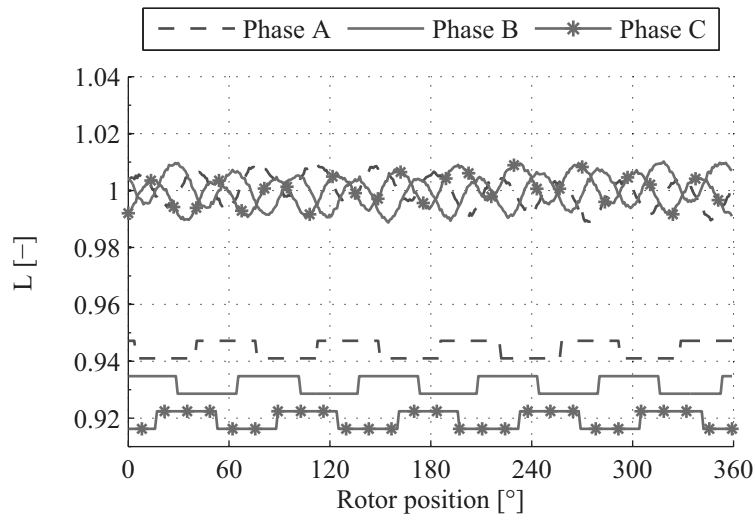
FIGURE 3.34 – L_{AA} , L_{BB} and L_{CC} versus the rotor position, measured at 20 kHz, modified motor.

motor phase inductances and resistances. The phase impedance variations are position-dependent and their origin is found in the iron BH characteristic.

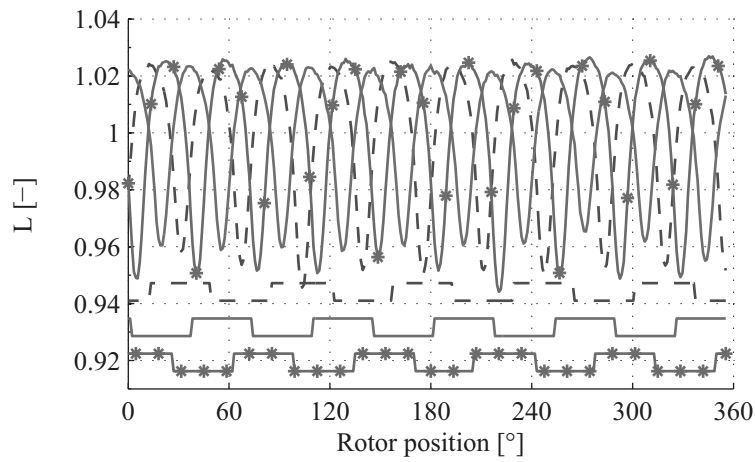
Measurements on an industrial BLDC motor confirm how the phase inductances and resistances vary with the rotor position. Variations are about 1% of the nominal value. All the classical physical phenomena related to impedance variation are analyzed and their influence is excluded. The origin of these variations is confirmed in the nonlinearities of the stator iron BH hysteresis characteristic.

Based on the acquired knowledge, a minor modification of the analyzed motor is suggested, in order to amplify the impedance variations without affecting the motor torque. In this new motor, the phase impedance variations are increased by a factor of five. However, if not otherwise specified, further in this thesis the standard motor will be used, as it is the standard, already commercialised motor.

Finally, the limits of FEM simulation are highlighted, the detected phenomenon cannot be simulated. Even more, if not used with a perfect control on the model, FEM simulation can give completely erroneous results.



(a)



(b)

FIGURE 3.35 – Relative value of L_{AA} , L_{BB} and L_{CC} versus the rotor position, measured at 20 kHz, standard (a) and modified motor (b), normalized around the mean value

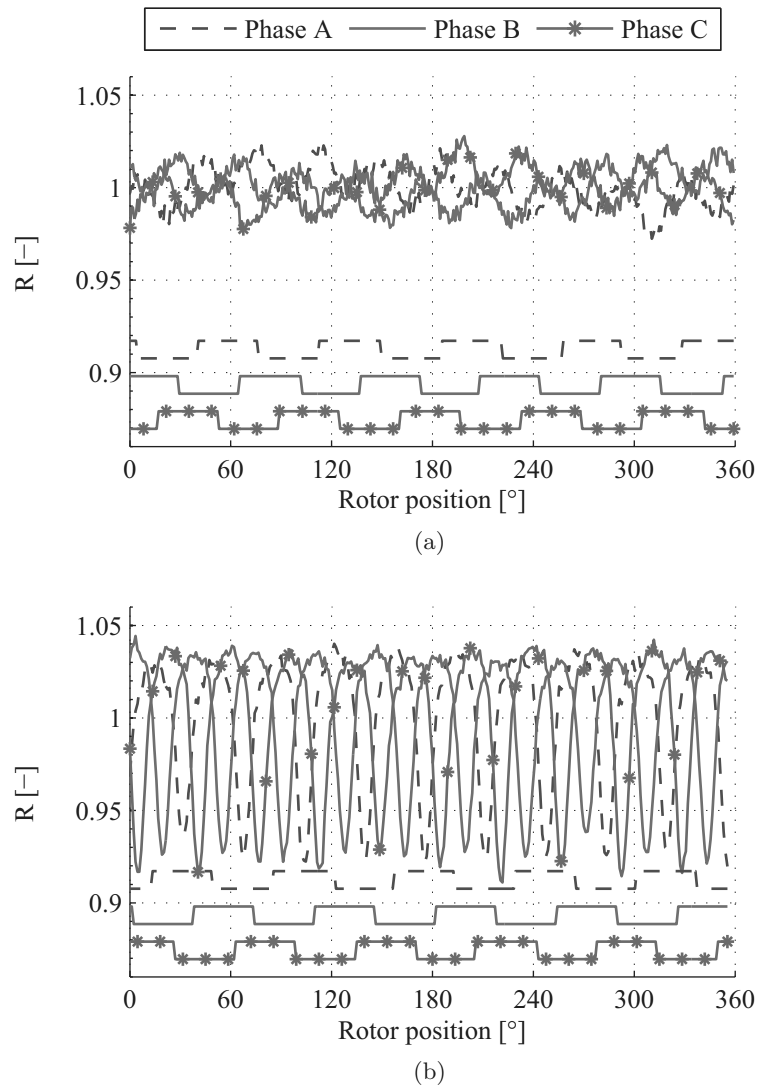


FIGURE 3.36 – Relative value of R_A , R_B and R_C versus the rotor position, measured at 20 kHz, standard (a) and modified motor (b), normalized around the mean value

 Exploitation of the iron BH hysteresis effects

 Contents

4.1	Introduction	60
4.2	Low level measurements differential circuits	60
4.2.1	Differential circuit 1	61
4.2.2	Differential circuit 1 without third resistance	63
4.2.3	Differential circuit 2	64
4.2.4	Circuit choice	66
4.3	Analytical calculations with a sinusoidal \underline{U}_{in}	66
4.4	Measurements with a sinusoidal \underline{U}_{in}	66
4.4.1	\underline{U}_{out} measurements during a mechanical turn	68
4.5	Measurements with a square U_{in}	69
4.5.1	U_{out} measurements during two electrical periods	70
4.6	Realized drive electronics	74
4.7	Conclusions	75

4.1 Introduction

IN this chapter, a way for exploiting the small position-dependent variations on the motor phase inductances, L_x , and resistances, R_x , is introduced. The method consists in the injection of an high frequency voltage into the motor phases, the input signal, and the measurement of a differential voltage, the output signal. The technique is applied on a BLDC motor, using first a sinusoidal and then a square input signal. Calculations and measurements are provided, the position dependence of the output signal is proven. Thanks to the developed measurement technique, a ready-to-use position dependent signal is provided, opening the way for the creation of a sensorless position detection drive.

4.2 Low level measurements differential circuits

From Chapter 3 it is known that the three phase inductances L_x and resistances R_x vary with the rotor position. The measured variations around the mean values are in the range of 1% for the standard motor and 5% for the modified motor. These variations are too small compared to the absolute value for being measured without a precision impedance analyzer like the one used in Chapter 3. Measurements techniques like current measurement, used for the position detection with saturation [2], are therefore not adapted.

A common way for measuring low level variations of high values consists in differential measurement techniques [68]. Let the electrical scheme of the star-coupled BLDC motor introduced in Fig. 1.10 be simplified by adopting the hypothesis that the back-EMF $u_{ix} = 0$. This is true at standstill or when the motor turns at low speed. Moreover, let consider the electrical scheme to be at steady state, no current is flowing in none of the motor phases at the beginning of the measurements. Finally, let consider the motor neutral point N as inaccessible. An artificial neutral point N' is built using three resistances $R_n \gg R_x$. This electrical representation of the motor without the three back-EMF voltages and with the artificial neutral point is shown in Fig. 4.1. The motor is electrically represented by its three phase impedances, \underline{Z}_A , \underline{Z}_B and \underline{Z}_C , which are composed by

$$\underline{Z}_x = R_x + j\omega L_x \mid_{x=A,B,C} \quad (4.1)$$

Starting from this electrical scheme, two differential measurement circuits can be used.

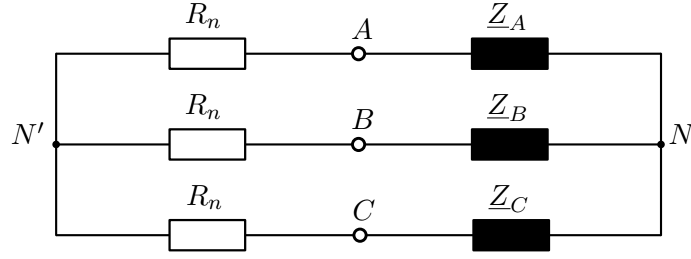


FIGURE 4.1 – BLDC motor with artificial neutral point N' .

4.2.1 Differential circuit 1

In this first circuit, already used in [35], a voltage \underline{U}_{in} is applied between two motor terminals and a voltage \underline{U}_{out} is measured over the resistance of the third, the floating phase. One possible configuration of this measurement circuit is shown in Fig. 4.2, where the phases A and B are supplied and \underline{U}_{out} is measured between the artificial neutral point N' and phase C terminal.

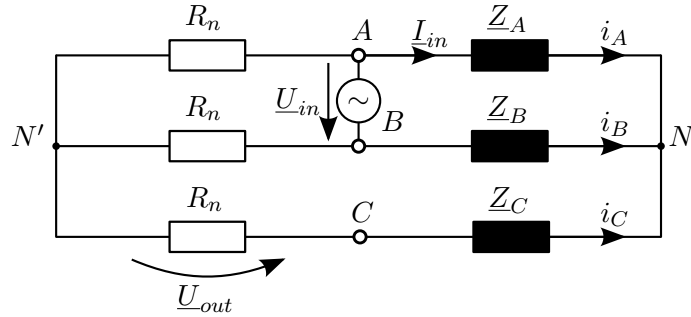


FIGURE 4.2 – Differential circuit 1.

By applying the $Y - \Delta$ transformation to the motor phases impedances, this circuit can be redrawn as in Fig. 4.3, where

$$\begin{aligned}
 \underline{Z}_{AB} &= \underline{Z}_A + \underline{Z}_B + \frac{\underline{Z}_A \underline{Z}_B}{\underline{Z}_C} \\
 \underline{Z}_{BC} &= \underline{Z}_B + \underline{Z}_C + \frac{\underline{Z}_B \underline{Z}_C}{\underline{Z}_A} \\
 \underline{Z}_{AC} &= \underline{Z}_A + \underline{Z}_C + \frac{\underline{Z}_A \underline{Z}_C}{\underline{Z}_B}
 \end{aligned} \tag{4.2}$$

The differential nature of the measurement clearly appears, a classical Wheatstone bridge can be recognized.

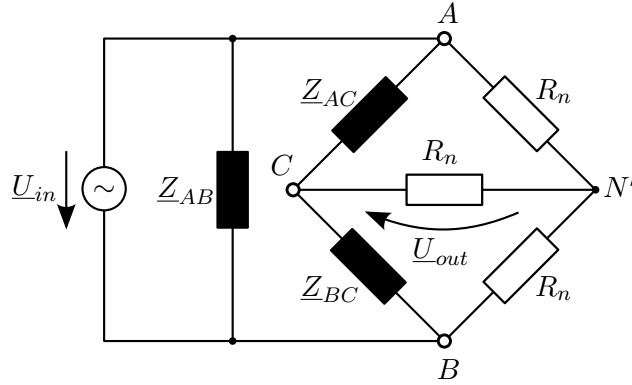


FIGURE 4.3 – Differential circuit 1 after Y – Δ transformation.

The analytical resolution of \underline{U}_{out} in circuit 1 gives:

$$\underline{U}_{out} = \frac{R_n \underline{U}_{in} (\underline{Z}_A - \underline{Z}_B)}{2 \underline{Z}_A \underline{Z}_B + 2 \underline{Z}_C \underline{Z}_A + 2 \underline{Z}_C \underline{Z}_B + 3 R_n (\underline{Z}_A + \underline{Z}_B)} \quad (4.3)$$

It can be noticed that (4.3) varies with R_n , the value of the resistance used for building the artificial neutral point N' .

In order to qualitatively evaluate the influence of R_n on \underline{U}_{out} , (4.3) is calculated with a variable R_n and a sinusoidal \underline{U}_{in} with amplitude 10 V and frequency $f = 20$ kHz. The great advantage of using a sinusoidal \underline{U}_{in} is that the analytical calculation of \underline{U}_{out} is easy because only one frequency of the system is excited. The L_x and R_x values used for the calculations are based on the measurements performed in Chapter 3 at the frequency $f = 20$ kHz. The values (4.4) are used.

$$\begin{aligned} \delta &= 1\% \\ L_A &= 410 (1 + \delta) \mu\text{H} \\ L_B &= 410 (1 - \delta) \mu\text{H} \\ L_C &= 410 \mu\text{H} \\ L_m &= 18 \mu\text{H} \\ R_A &= 10 (1 + \delta) \Omega \\ R_B &= 10 (1 - \delta) \Omega \\ R_C &= 10 \Omega \end{aligned} \quad (4.4)$$

The resulting \underline{U}_{out} absolute value, which is the amplitude of the signal, for different R_n values is shown in Fig. 4.4. It appears that the absolute value on the \underline{U}_{out} voltage approaches an upper limit for $R_n \rightarrow +\infty$. The calculation of this limit applied to (4.3)

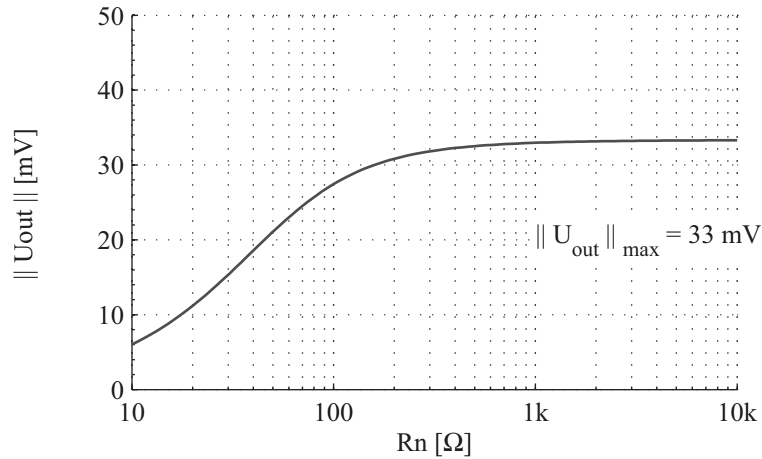


FIGURE 4.4 – Differential circuit 1: Amplitude of \underline{U}_{out} as a function of R_n .

gives:

$$\lim_{R_n \rightarrow +\infty} \underline{U}_{out} = \frac{1}{3} \frac{\underline{U}_{in} (\underline{Z}_A - \underline{Z}_B)}{(\underline{Z}_A + \underline{Z}_B)} \quad (4.5)$$

Hence, for sufficiently high values of R_n , just the variations between \underline{Z}_A and \underline{Z}_B influence \underline{U}_{out} and the R_n terms disappears. The amplitude of the \underline{U}_{out} signal in (4.5) reaches 33 mV with the values (4.4).

4.2.2 Differential circuit 1 without third resistance

A simple improvement on the differential circuit 1 can be achieved by eliminating the resistance R_n from the floating phase, as shown in Fig. 4.5. With this modification,

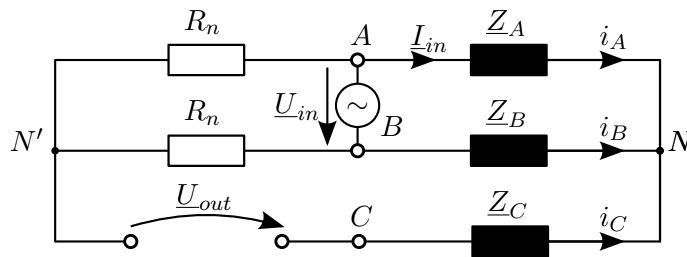


FIGURE 4.5 – Differential circuit 1 without third resistance

no current flows through phase C , $i_C = 0$ A, and thus the circuit can be simplified by eliminating \underline{Z}_C . In Fig. 4.6a the circuit 2 is simply redrawn for highlighting the differential nature of the \underline{U}_{out} voltage. In Fig. 4.6b the circuit is redrawn without \underline{Z}_C .

The \underline{U}_{out} calculation is consequently simplified:

$$\underline{U}_{out} = \frac{1}{2} \frac{\underline{U}_{in} (\underline{Z}_A - \underline{Z}_B)}{(\underline{Z}_A + \underline{Z}_B)} \quad (4.6)$$

In (4.6) R_n does not appear and the gain is slightly higher than in (4.5). With the same input values (4.4), an \underline{U}_{out} amplitude of 49 mV is obtained independently from the R_n value.

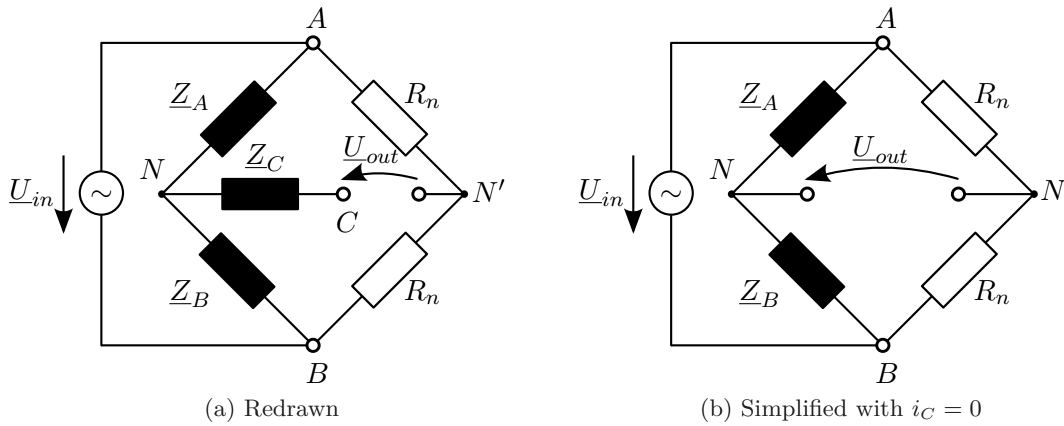


FIGURE 4.6 – Differential circuit 1 without third resistance redrawn.

4.2.3 Differential circuit 2

By inverting the positions of \underline{U}_{in} and \underline{U}_{out} in Fig. 4.2, a classical Wheatstone bridge with four impedances is created, without necessitating the Y – Δ transformation on the motor phases. One possible configuration of this measurement circuit is shown in Fig. 4.7, the source is set between the artificial neutral point N' and phase C , and \underline{U}_{out} is measured between phases A and B . In this measurement circuit, the presence or not

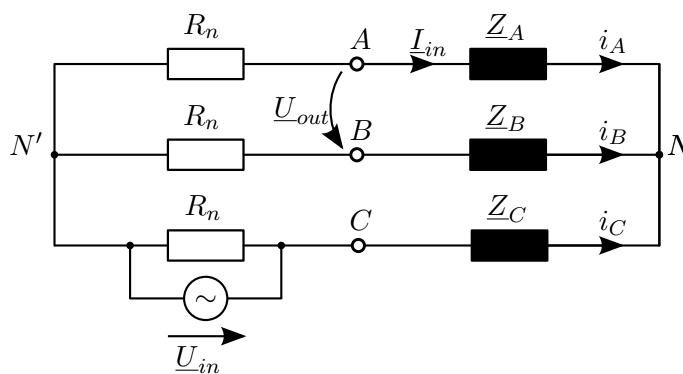


FIGURE 4.7 – Differential circuit 2.

of the third resistance R_n does not influence the resulting \underline{U}_{out} voltage, as it is in parallel

4.2. Low level measurements differential circuits

with the \underline{U}_{in} voltage source. The differential circuit 2 without the third resistance is redrawn in Fig. 4.8.

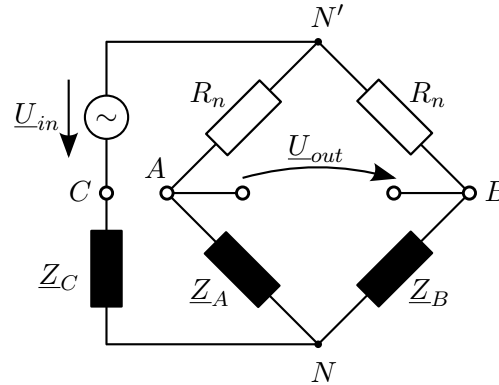


FIGURE 4.8 – Differential circuit 2 redrawn.

The analytical calculation of \underline{U}_{out} gives:

$$\underline{U}_{out} = \frac{\underline{U}_{in} R_n (\underline{Z}_A - \underline{Z}_B)}{\underline{Z}_A \underline{Z}_B + \underline{Z}_C \underline{Z}_B + \underline{Z}_C \underline{Z}_A + 2 \underline{Z}_C R_n + R_n^2 + R_n (\underline{Z}_A + \underline{Z}_B)} \quad (4.7)$$

As for the differential circuit 1, \underline{U}_{out} depends on R_n . Its absolute value for different R_n is calculated with the values (4.4). The resulting \underline{U}_{out} as a function of R_n is plotted in Fig. 4.9. It can be noticed that the maximum \underline{U}_{out} is higher than for circuit 1, it attains

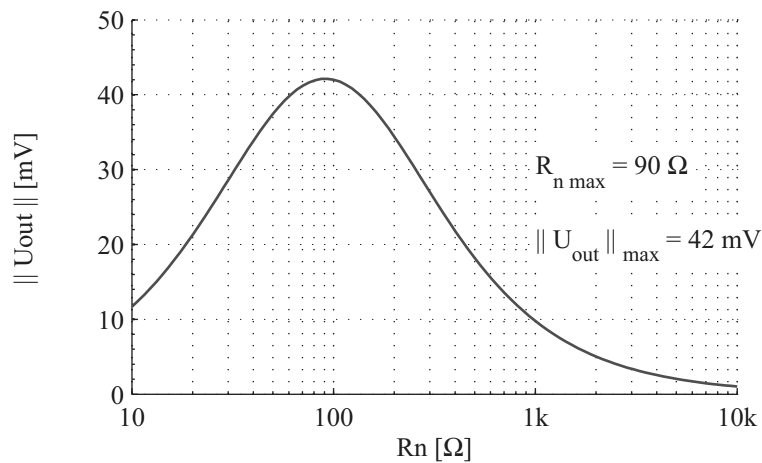


FIGURE 4.9 – Differential circuit 2: Amplitude of \underline{U}_{out} as a function of R_n .

42 mV, but the value of R_n has to be tuned. The value of R_n which gives the maximum \underline{U}_{out} amplitude is:

$$R_{n,max} = \|\sqrt{\underline{Z}_A \underline{Z}_B + \underline{Z}_C \underline{Z}_A + \underline{Z}_C \underline{Z}_B}\| \quad (4.8)$$

The analytical calculation of \underline{U}_{out} with this value is not meaningful, the expression can

not be reduced and is therefore not shown.

4.2.4 Circuit choice

Based on the shown calculations, circuit 1 is chosen due to its practical simplicity. In fact, the voltage source \underline{U}_{in} between two motor phases corresponds already to a normal motor supply created with a standard power bridge, like the one shown in Appendix D. Moreover, circuit 1 has constant gain for a sufficiently high resistance R_n . Even if circuit 1 without the third resistance has the highest gain and the latter does moreover not depend on the R_n value, this configuration is not retained. An important drawback of this circuit in a practical implementation is the need of some additional circuitry for switching between the different phase measurements. Finally, despite the fact that circuit 2 has a higher gain than the circuit 1, this choice is not considered because the R_n value has to be tuned and this is not suitable.

4.3 Analytical calculations with a sinusoidal \underline{U}_{in}

An analytical calculation over an electrical period of \underline{U}_{out} for the chosen circuit is performed. The \underline{U}_{out} voltage is calculated with (4.5) for a sinusoidal \underline{U}_{in} of amplitude 10 V, 20 kHz, using the inductance L_A and resistance R_A measured at 20 kHz in Chapter 3 and shown in Figs. 3.12 and 3.15. The calculated \underline{U}_{out} , with separated amplitude and phase, is presented in Figs. 4.10 and 4.11. From this calculation it can be seen that \underline{U}_{out} has a maximum amplitude and is in phase with \underline{U}_{in} at rotor positions 0° and 32° . On the other hand, at rotor position 15° , \underline{U}_{out} has another maximum with a maximal phase shift of a little less than π , i.e. the signal is inverted.

4.4 Measurements with a sinusoidal \underline{U}_{in}

In order to verify on a real system the previous analytical calculations, a sinusoidal voltage with amplitude 10 V and frequency 20 kHz is applied to the motor shown in Fig. 1.4b, following the scheme of the measurement circuit 1 shown in Fig. 4.2. The \underline{U}_{out} voltage is measured and two scope images are presented in Fig. 4.12 for the rotor positions 15° (a) and 32° (b). For completeness, not only \underline{U}_{in} (trace 2) and \underline{U}_{out} are shown (trace 3), but also the input current \underline{I}_{in} (trace 1) and \underline{U}_{out} after filtering and amplification (trace 4).

As predicted in the analytical calculation, \underline{U}_{out} amplitude is quite low and therefore the signal appears noisy. Amplitude and phase of \underline{U}_{out} at rotor position 32° correspond

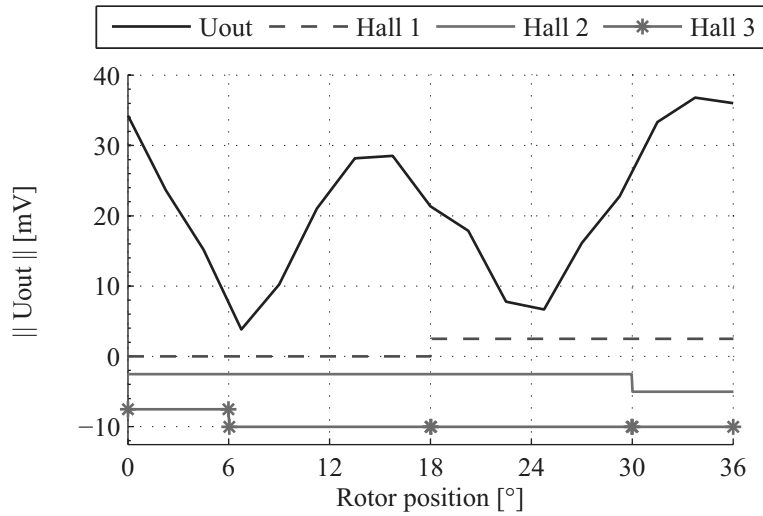


FIGURE 4.10 – \underline{U}_{out} amplitude based on analytical calculation and phase inductance and resistance measurements.

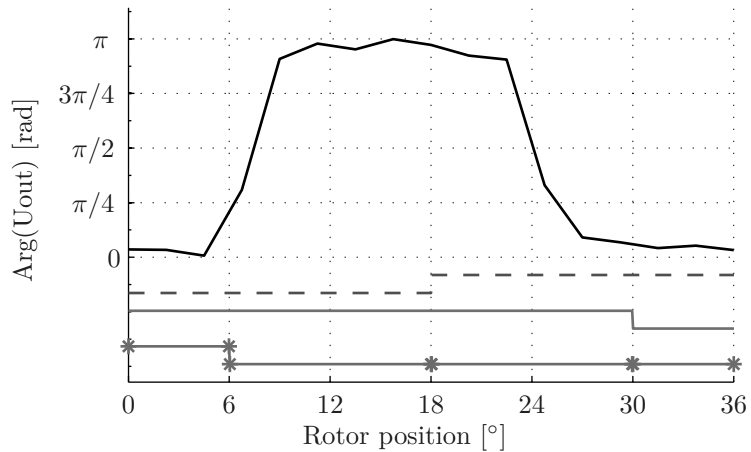


FIGURE 4.11 – \underline{U}_{out} phase based on analytical calculation and phase inductance and resistance measurements.

well to the analytical calculation, the amplitude is in the order of 40 mV and the phase shift is near zero. On the other hand, for the rotor position 15° the amplitude is a little bit smaller than calculated, ~ 20 mV, and the phase shift is clearly not as big as predicted. Nevertheless, the difference between the two positions clearly appears and could be used for rotor position detection. As it can be seen in Fig. 4.12 (trace 4), the signal is easily filtered and amplified because the frequency of the injected voltage is imposed, and thus, well known. With the measurements shown in Fig. 4.12 it is also proven that iron saturation do not participate in the presented technique because the maximum amplitude of the injected current, (trace 1), does not even reach 50 mA.

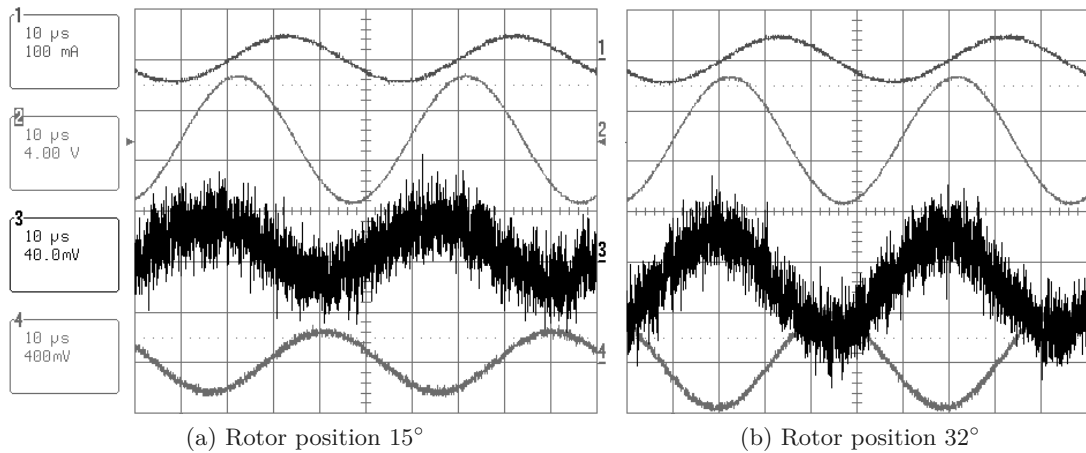


FIGURE 4.12 – I_{in} , U_{in} , U_{out} , and U_{out} after filtering and amplification.

4.4.1 U_{out} measurements during a mechanical turn

The amplitude of U_{out} for a sinusoidal U_{in} during a complete mechanical rotation is shown in Fig. 4.13. Measurements are performed on the three phases, permutating the U_{in} and U_{out} signals. It can be appreciated how the small variations in the

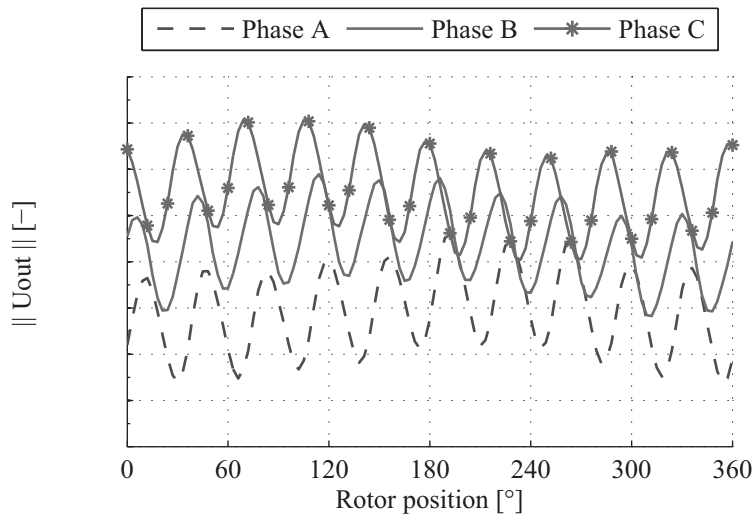


FIGURE 4.13 – U_{out} amplitude after filtering and amplification for a complete motor rotation. Measurement on the three phases.

phase impedances L_x and resistance R_x are amplified by the circuit and reflected in the oscillations on U_{out} . Thanks to this empirical demonstration it can be stated that the iron hysteresis effects on the motor electrical parameters are perfectly retrieved and can be used for the position detection.

Finally, it can be noticed how the the differential circuit highlights also the small differences in the mean values of L_x and R_x that are measured in Chapter 3. These differences appear in the U_{out} signals as a variable offset. The mechanical eccentricity of the rotor, measured in Subsection 3.4.2, is also amplified by the differential circuit and is reflected on the U_{out} signal as a periodical drift.

4.5 Measurements with a square U_{in}

In digital electronics, sinus wave is not easy to create and an alternative has to be searched. For its extremely easy implementation in a normal drive electronics it is rapidly chosen to use a square U_{in} signal instead. Clearly, if U_{out} can be measured with a sinusoidal U_{in} , a square wave will also create information because many frequencies of the system are excited.

First of all, a step is imposed to U_{in} . Fig. 4.14 shows U_{out} after filtering, amplification and offset addition of 1.5 V for two different rotor positions when a step $U_{in} = 10$ V is injected between the phases A and B . The difference in the U_{out} voltage between the two positions is clearly visible. In order to avoid all the electric transient effects, U_{out} can be measured with an Analogical to Digital (AD) converter 5-10 μ s after the rising edge without difficulty. In Fig. 4.14 it is chosen to trig the AD conversion 7 μ s after the U_{in} rising edge.

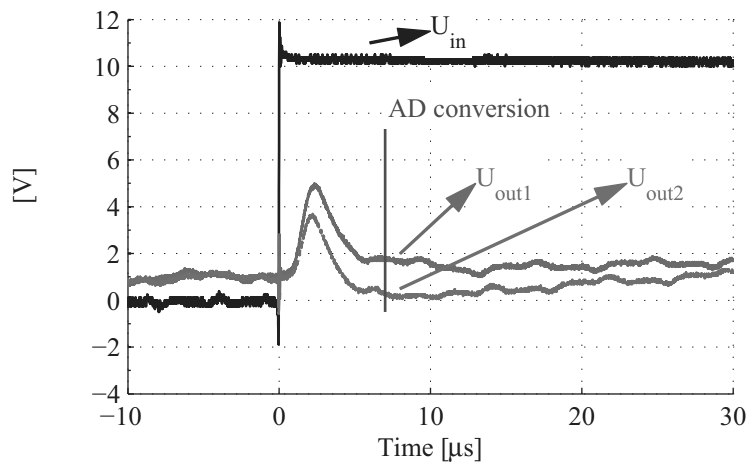


FIGURE 4.14 – U_{out} after filtering and amplification for two different positions created by a step on U_{in} .

If, instead of a step, a pulse is injected in U_{in} the U_{out} signal contains position information also on the falling edge of U_{in} . In Fig. 4.15 an example of a pulse U_{in} with $t_{on} = 10$ μ s and the voltage U_{out} after filtering and amplification for two different rotor positions is shown. The negative pulse on U_{in} after $t = 10$ μ s is not imposed but appears

because of the current extinction through the diodes of the power bridge. In this case, the AD conversion may start $7 \mu\text{s}$ after the rising edge and/or $7 \mu\text{s}$ after the falling edge.

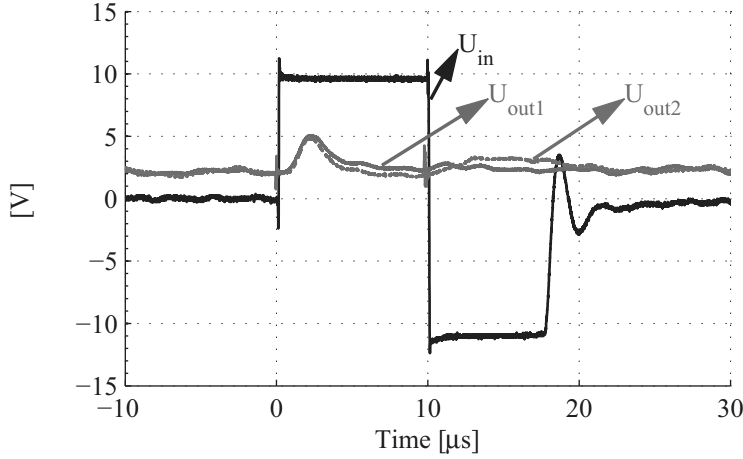


FIGURE 4.15 – U_{out} after filtering and amplification for two different positions created by a pulse on U_{in} .

4.5.1 U_{out} measurements during two electrical periods

For showing the effectiveness of the information content of U_{out} , the signal is sampled with an AD converter during two electrical periods. The aim is to prove that the information content of the U_{out} signal, even if measured with a square signal and retrieved with an AD sampling, comes from phase inductance and resistance variations. A train of U_{in} pulses is generated, as shown in Fig. 4.16. The carrier frequency $f = 1/T = 20 \text{ kHz}$ is imposed and the duty cycle $d = t_{ON}/T$ is kept small enough to not generate torque.

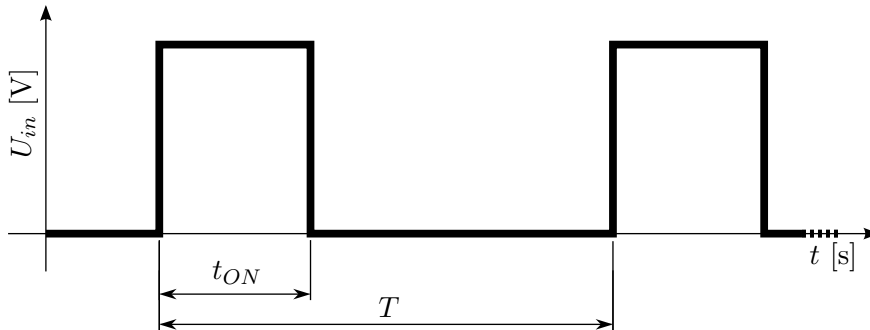


FIGURE 4.16 – Train of U_{in} pulses.

Standard motor

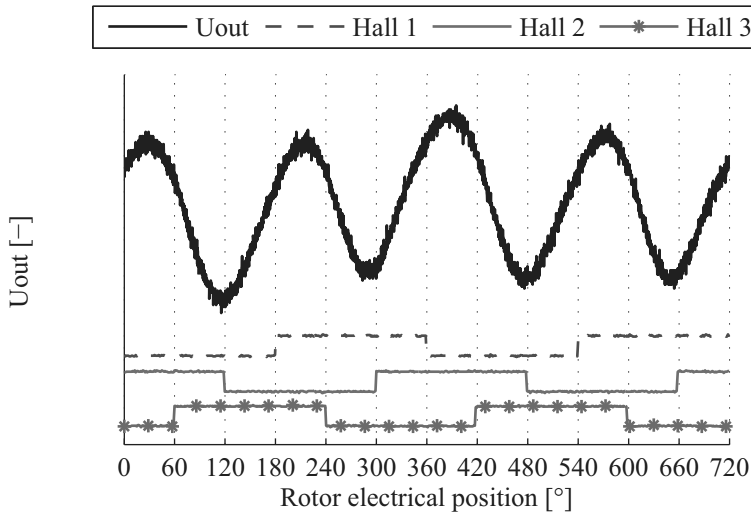
The presented U_{in} signal is applied to the standard motor following the circuit 1 scheme and the rotor is externally turned in steps. The resulting U_{out} voltage is analogically filtered, amplified, and finally sampled at $t = 7 \mu s$ after each rising edge of the voltage U_{in} . In Fig. 4.17 on the top the U_{out} signal sampled during two electrical periods is shown. For comparison, in Fig. 4.17 on the bottom, the U_{out} signal is calculated with (4.5). L_x and R_x values are taken at 20 kHz from the measurements shown in Chapter 3. As the U_{out} signal after AD sampling has been filtered and amplified in various ways, the magnitude scale of Fig. 4.17 is not shown as irrelevant.

It is very interesting to notice that the signal shape of the measured U_{out} signal corresponds well to the calculated one. This definitively proves the accuracy of the hypothesis and of the model. The U_{out} signal is highly position-dependent and two oscillations per electrical period can be seen. On the other hand, one single sample of U_{out} gives not enough information about the rotor position. It can be noticed that the same U_{out} value can be obtained from up to four different electrical positions during the same electrical period.

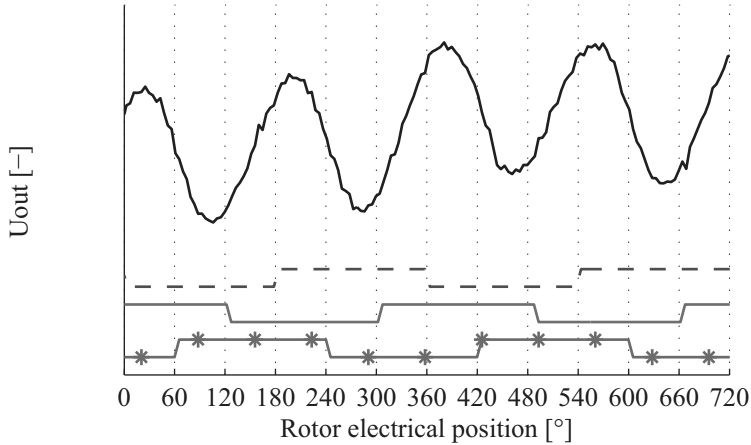
Modified motor

The same procedure is applied to the modified motor. In Fig. 4.18 the calculated and measured U_{out} signals are compared. The correspondence between calculation and measurements is even more evident than for the standard motor because of the signal non-symmetry between the rising and falling slopes. This non-symmetry is the consequence of the non-sinusoidal shape of the modified phase impedance oscillations, as shown in Figs. 3.35 and 3.36.

Finally, a small delay in both measured signals can be pointed out. This delay comes from the phase shift introduced by the analogical treatment of the U_{out} signal, such as the high-pass filter and the amplification stages.

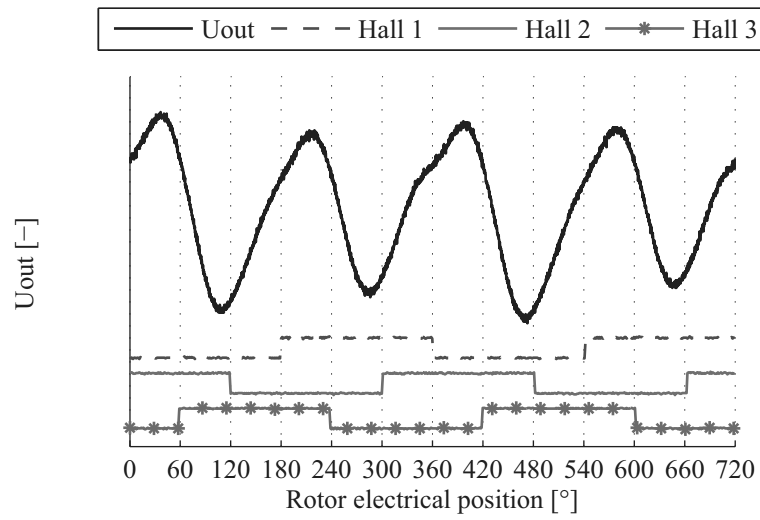


(a)

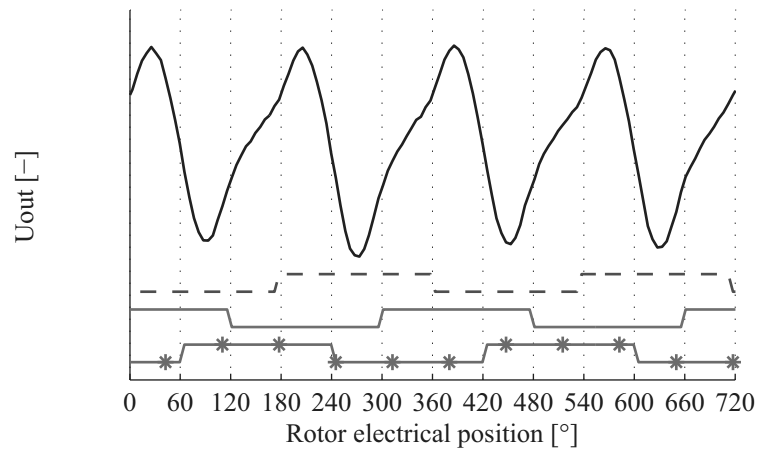


(b)

FIGURE 4.17 – Measured (a) and calculated (b) U_{out} signal, standard motor.



(a)



(b)

FIGURE 4.18 – Measured (a) and calculated (b) U_{out} signal, modified motor.

4.6 Realized drive electronics

A custom drive electronics, shown in Fig. 4.19, is realized for the automatic generation of a train of pulses on U_{in} and the respective measurement of the U_{out} voltage with an AD converter. A train of pulses like the one generated on U_{in} is called Pulse Width Modulation (PWM) signal. Further in this thesis, the power PWM, or PWM only will refer to this U_{in} signal, with fixed frequency f and variable duty cycle d . If not otherwise specified, U_{out} will be referred to the AD sampled value of the U_{out} voltage. U_{out} may be presented in its digital value, extracted directly from the drive electronics, or in an analogical voltage measured on a scope, created from its digital value with an Digital to Analogical (DA) converter.

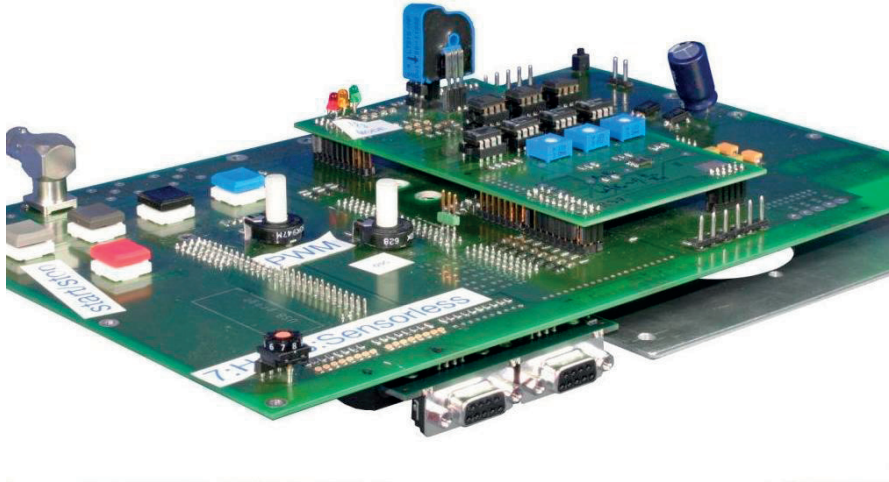


FIGURE 4.19 – Custom drive electronics for technique analysis.

The electronics is composed by three PCBs, connected in a stack. The PCB at the bottom is a commercial development card and holds the microcontroller. The main board, in the middle, is a classical BLDC drive electronics with a drive stage and a six transistor power bridge. On the top of the latter, an interchangeable board contains the analogical treatment for the U_{out} signal filtering and amplification. A simplified schematics of this stage for one phase is shown in Fig. 4.20. First of all the signal $V_{in} = U_{out}|_{\text{before filtering and amplification}}$ passes through a two stage high-pass filter in order to eliminate the low frequency back-EMF that might be present in the U_{out} voltage. The signal is then amplified and an offset of 1.5 V is added. The relation is

$$V_{out} = -V_{in} \frac{10k}{R_g} + 1.5 \quad (4.9)$$

where $V_{out} = U_{out}|_{\text{after filtering and amplification}}$ is the signal measured by the AD converter. This analogical treatment stage is duplicated three times, once for every phase.

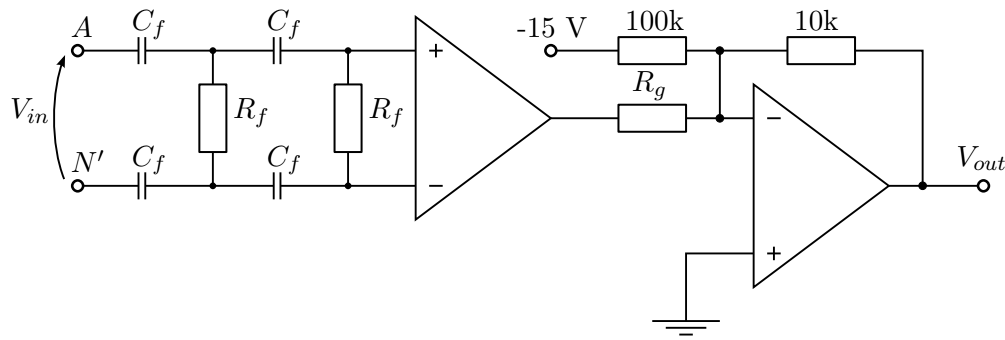


FIGURE 4.20 – Custom electronics for the U_{out} signal filtering and amplification.

Finally, with the realized electronics it is possible to drive a BLDC motor, either using the Hall sensors, either using whatever algorithm based on the measurement of the U_{out} voltage.

4.7 Conclusions

In this chapter, it is successfully shown how to retrieve the position information contained in the L_x and R_x variations created by the iron BH hysteresis. From among three possibilities, the differential circuit 1 is chosen because of its easy implementation. It is also decided to use a square signal for the U_{in} signal, again because of the simplicity of the implementation. This signal is easily generated using the six transistor power bridge present in every BLDC control electronic circuit. The injection of a train of U_{in} pulses creates, thanks to the differential measurement circuit, a position-dependent output signal, U_{out} . The position information contents of U_{out} will be exploited in the next chapters for the development of sensorless position detection drives.

 Sensorless position detection during normal drive

 Contents

5.1	Introduction	78
5.2	Drive schema choice	78
5.2.1	Existing BLDC drive schemas	78
5.2.2	BLDC drive schema choice	79
5.3	U_{out} measurement integration in the two-phases ON supply	79
5.3.1	The two-phases ON supply	79
5.3.2	U_{out} measurements	81
5.4	Sensorless drive implementation	83
5.4.1	Calibration	83
5.4.2	Hall sensors rebuilding at start-up or after a main reset	87
5.4.3	Hall sensors rebuilding starting from a known position	89
5.5	Torque-speed measurements at room temperature	90
5.5.1	Measurement setup	90
5.5.2	Measurements on the modified motor	91
5.5.3	Measurements on the standard motor	95
5.5.4	Comparison between standard and modified motor	96
5.6	Torque-speed measurements at extrema temperature	97
5.6.1	Measurement setup	97
5.6.2	Measurements with the modified motor	98
5.6.3	Measurements with the standard motor	100
5.7	Rotation direction forced by the load torque	102
5.8	Power PWM duty cycle range	103
5.9	Angular resolution	103
5.10	Sensorless position detection of slotless BLDC motors	104
5.11	Conclusions	106

5.1 Introduction

IN this chapter, an innovative low speed and standstill sensorless position detection principle based on the hysteresis phenomenon highlighted in Chapter 3 is introduced. First of all, a drive schema is chosen that actuates the motor and, at the same time, creates the U_{out} signal introduced in Chapter 4 and exploits its position information. A simple position estimation principle is then suggested and a closed loop drive with sensorless position detection is realized.

As many factors, like the external load (and its variation in time) or the environment conditions, like the temperature, may influence the correct operation of the introduced principle, the sensorless schema is deeply analyzed and is successfully proven in many drive operations. Thanks to these measurements the working range and the method limitations are highlighted.

5.2 Drive schema choice

The measurements of U_{out} shown thus far are performed at standstill or at very low speed. The rotor is externally turned and the duty cycle of the U_{in} signal is voluntarily kept low, in order to not create torque.

The objective is now to supply a BLDC motor for making it rotate and, at the same time, measure the U_{out} voltage for the rotor position estimation. Unfortunately, this objective does not correspond to the hypothesis introduced in the previous chapter for the correct U_{out} measurement with the differential circuits. In fact, the need of creating a torque for driving the motor implies that the current should flow through the motor phases. In contrast to the back-EMF that is filtered by the high-pass filter in the analogical treatment of the U_{out} voltage, a current flowing through the sensed phase at the moment in which the U_{in} pulse is injected irremediably corrupts the position information content of the U_{out} voltage.

Thus, for performing a correct measurement of U_{out} , the sensed phase has imperatively to be floating and no current has to circulate through it when the U_{in} pulse is applied.

5.2.1 Existing BLDC drive schemas

Three main BLDC motor drive schemas exist: the sinusoidal supply, the 180° supply and the two-phases ON supply, also called block or 120° supply. These three supply schemas are deeply investigated in [4, 69, 70].

5.3. U_{out} measurement integration in the two-phases ON supply

In a sinusoidal supply drive, the three motor phases are supplied with three sinusoidal voltages, each one shifted by 120° . The phase currents are consequently also sinusoidal, each one shifted by 120° electrical degrees.

In a 180° supply, the electrical period is divided into six sectors of 60° each. In every sector, two phases are connected to the same potential (Vpp or GND) and the third on the opposite.

Finally, in a two-phases ON supply, the electrical period is also divided into six sectors of 60° each, but in every sector, one phase is connected to Vpp, the second to GND and the third is floating.

5.2.2 BLDC drive schema choice

The requirements for a correct U_{out} measurement doubtlessly suggests to drive the motor with the two-phases ON supply. In this drive schema, the motor phases are floating in turn. Moreover, the current in the floating phase naturally vanishes, as it will be shown in the next section, complying both U_{out} measurement specifications.

Clearly, the other drive schemas also permit the integration of the U_{out} measurement, but some artifacts, like windowing, are needed for comply with the specifications. For this reason, the technical simplicity is preferred and the two-phases ON supply is chosen.

5.3 U_{out} measurement integration in the two-phases ON supply

5.3.1 The two-phases ON supply

The two-phases ON supply defines a sequence of six states created with the power bridge shown in Appendix D. These six states are applied following a predefined sequence and they divide the 360° electrical degrees in six sectors of 60° each. These sectors are identified in this thesis with the name of the two supplied phases. The sequence for the forward direction is CA, CB, AB, AC, BC, BA . The transition between two sectors is called commutation. For the backward rotation direction, the commutation table is strictly the same, but the commutations are applied in the opposite way, from right to left. In Fig. 5.1 the power bridge configuration for the AB sector is shown¹. Phase A is connected to Vpp, phase B to GND and phase C is left floating. The current flow through the power bridge and the motor phases is highlighted.

¹ For legibility reasons the resistances R_n and the artificial neutral point N' are not shown.

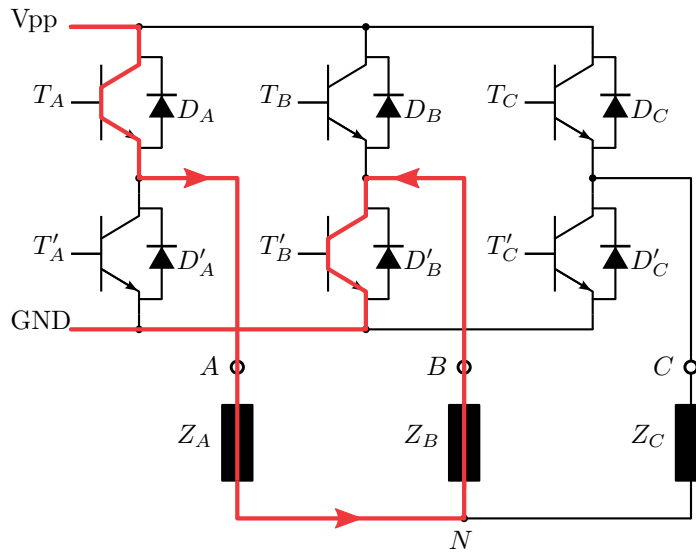


FIGURE 5.1 – Power bridge configuration for the AB sector.

Because of the presence of the phase inductances, when the commutation happens, the current flowing through the supplied phases cannot vanish instantaneously. During this transient state, called current extinction, the current flows not only through the two supplied phases, but also through the extinction diode of the past supplied phase. The transient lasts until the current in the floating phase is extinguished. The current extinction state between the sectors AB and AC is shown in Fig. 5.2 where the current extinction flowing through the diode D_B is highlighted.

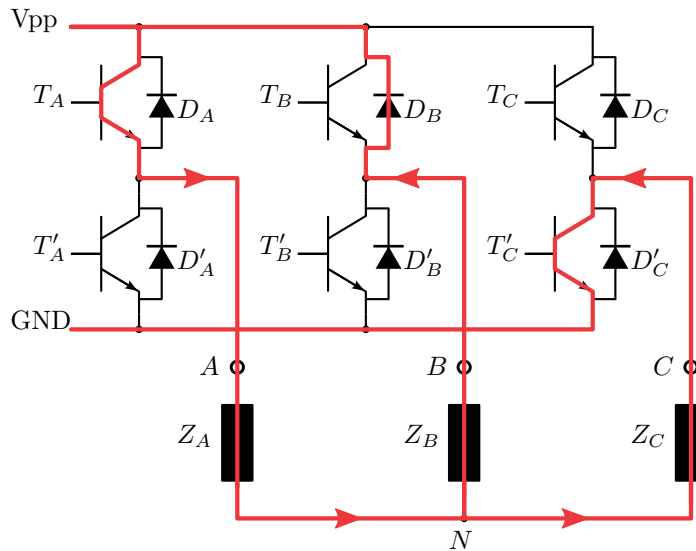


FIGURE 5.2 – Power bridge configuration for the AB - AC commutation transient.

In Fig. 5.3 (adapted from [70]) the classical shapes of the phase voltage u_A , the phase

5.3. U_{out} measurement integration in the two-phases ON supply

current i_A and the back-EMF voltage u_{iA} during a complete electrical period of a BLDC motor with sinusoidal back-EMF driven by block commutation are shown. The sector

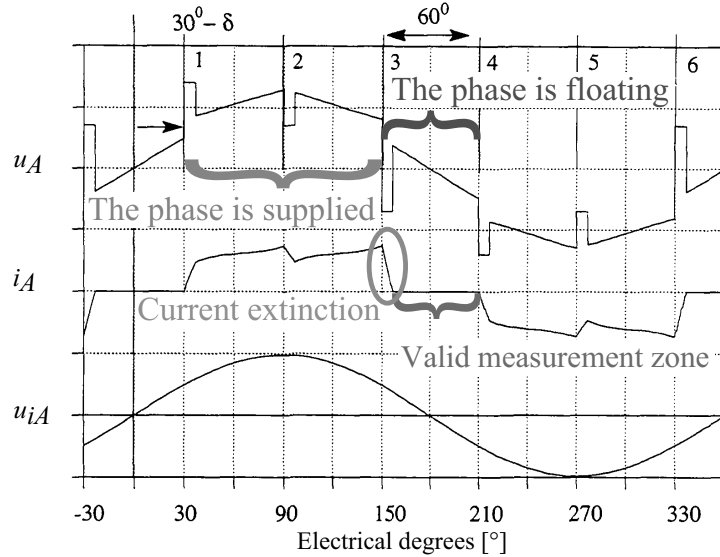


FIGURE 5.3 – Two-phases ON supply signals [70]. u_A , i_A , u_{iA} .

of 60° where the phase A is floating is highlighted. At the beginning of this sector, the current extinction is also highlighted. During this transient state, the U_{out} measurement is corrupted and thus, the zone where the U_{out} measurement is possible is a little less than 60° . It may be noticed, that this valid measurement zone is the same as in the techniques that measure the back-EMF for estimating the rotor position, like in [71]. The big difference here is that the introduced technique is developed for low speed operations and thus the back-EMF on the floating phase is weak. Moreover, in the practical realisation, the back-EMF is eliminated from U_{out} with an high-pass filter and only the U_{out} components created by the high frequency U_{in} signal are measured. Obviously, if the speed increases, the back-EMF increases too and starts to be hard to be filtered out. But, even more obviously, if the back-EMF is high enough, there is no reason for not substituting the introduced sensorless algorithm by the back-EMF one for the position detection.

5.3.2 U_{out} measurements

In this subsection the Hall sensors are still used for the position detection and the different motor phases are supplied following the two-phases ON commutation sequence. The duty cycle of the power PWM is increased in order to create a sufficient torque and make the rotor turning. Remember that the power PWM used for driving the motor is also the U_{in} signal. Hence, at the same time, the created U_{out} signal can be measured.

U_{out} on phase A

The U_{out} signal of phase A is sensed, the measurements after AD sampling are shown in Fig. 5.4. The x-axis coordinate is shifted in order to match the angles shown in Fig. 5.3.

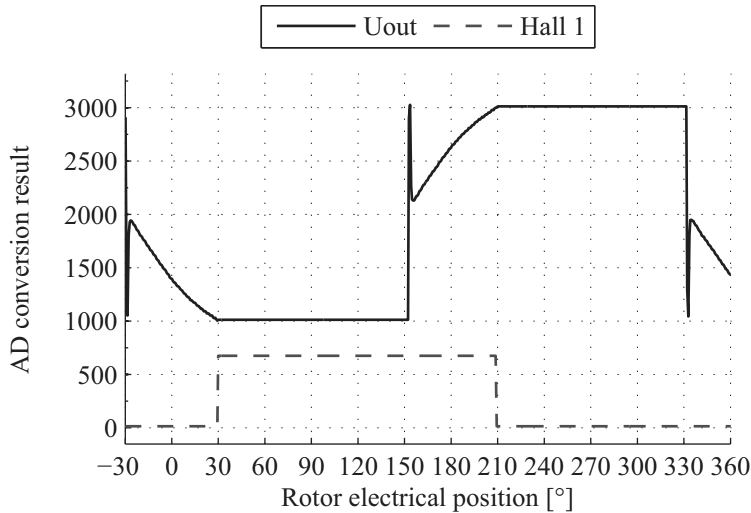


FIGURE 5.4 – AD sampled U_{out} signal and Hall 1 sensor in a two-phases ON supply.

The U_{out} measurement plotted in Fig. 5.4 can be divided in three zones. The flat zones, visible from 30° up to 150° and from 210° up to 330° , appear when the sensed phase is supplied (the leg of the power bridge is set to V_{pp} or GND). During these zones no information can be retrieved on this phase and the U_{out} value is simply hold by software at the last correctly sensed value (here the values at 30° and respectively 210°).

A second pattern that can be seen are the spikes, like at positions 150° and 330° . Spikes appear when the phase is floating, but still in the current extinction zone. Here too, no information about the rotor position can be retrieved because the U_{out} signal is corrupted.

Finally, when the sensed phase is floating and the current is extinguished, from -30° after the spike up to 30° and from 150° after the spike up to 210° , the U_{out} signal can be correctly measured. In the example shown in Fig. 5.4, U_{out} vary significantly from 2'000 to 1'000 during the first 60° , and from 2'200 to 3'000 during the second 60° . This is the position information contained in U_{out} that is available on this phase.

U_{out} on phases A, B and C

During normal drive, the U_{out} voltage is sensed on one of the three motor phases in turn in everyone of the six commutation sectors. The U_{out} voltage sensed on the three phases during an electrical revolution is shown in Fig. 5.5. Excepting the six current extinction zones, corresponding to the spikes in Fig. 5.5 a position information is available at every moment.

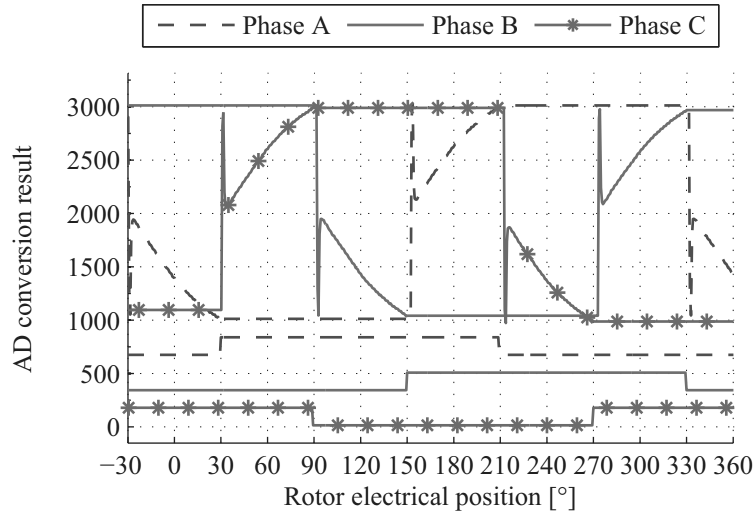


FIGURE 5.5 – AD sampled U_{out} signals and Hall sensors during two-phases ON commutation.

5.4 Sensorless drive implementation

From Fig. 5.5, only the valid U_{out} measurements are extracted and shown in Fig. 5.6. This signal contains all the position information that is available in U_{out} thanks to the iron hysteresis effects on the BLDC motor, and is now exploited for the sensorless position detection.

In the two-phases ON commutation supply, the estimation of the position needs to be refreshed only every 60° , like the Hall sensors. The simplest way for driving the motor is therefore to rebuild the three Hall sensors based on the available U_{out} signal.

5.4.1 Calibration

Observing Fig. 5.6 a first problem related to the U_{out} numerical value appears. The U_{out} voltage is the result of a differential measurement between two varying impedances. Its

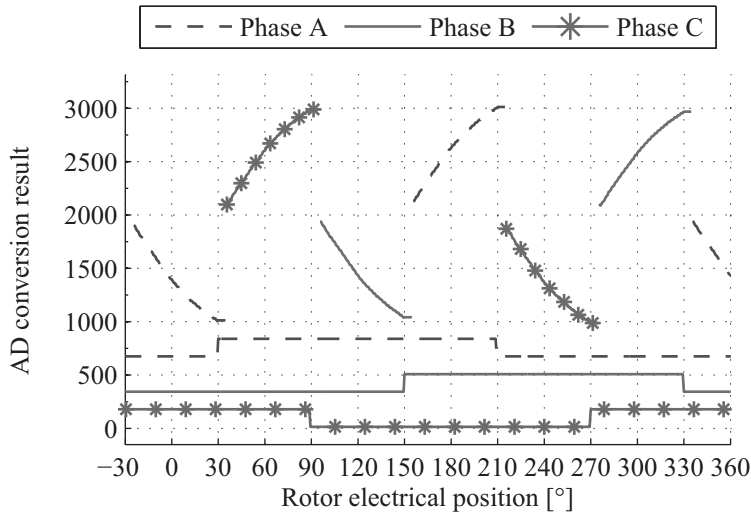


FIGURE 5.6 – Valid AD sampled U_{out} signals and Hall sensors during two-phases ON commutation.

value depends also from the U_{in} amplitude and the analogical amplification before the AD conversion. Hence, because of its origin, the U_{out} signal cannot be used for detecting the rotor position without, at least once, mapping into the software the relation between the rotor electrical position and the U_{out} values.

The start and threshold values

In Fig. 5.7 the start values of every commutation are highlighted with a \triangleright . These values correspond to the first correct U_{out} measurement obtained on every sector when the drive electronics switches from a sector to the following.

Similarly, in Fig. 5.8, the last valid U_{out} values before the new commutation are highlighted with a \diamond . These are the threshold values.

Start values and threshold values may vary from phase to phase because of a non-perfect symmetry in the motor construction. Moreover, if the motor has more than one pole pairs, these start and threshold values are similar but not identical for the different electrical periods. The differences between electrical periods are explained by the imperfections on the rotor symmetry, like eccentricity or varying permanent magnet remanence.

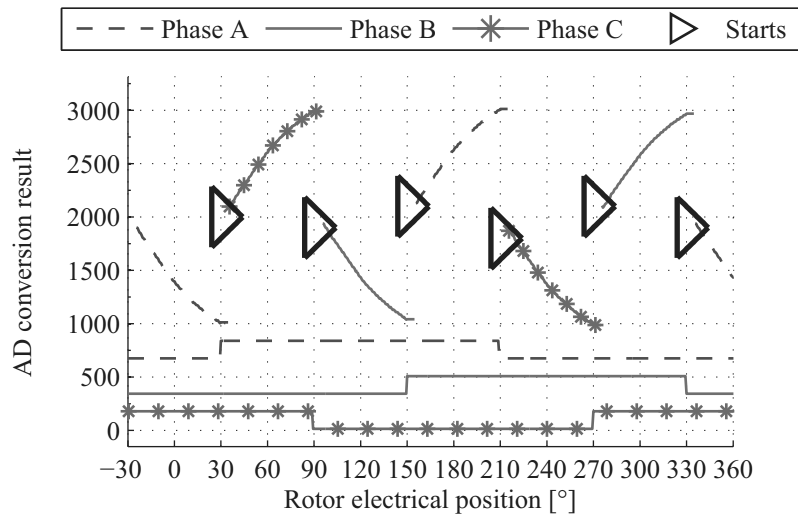


FIGURE 5.7 – Start values on the valid AD sampled U_{out} signals.

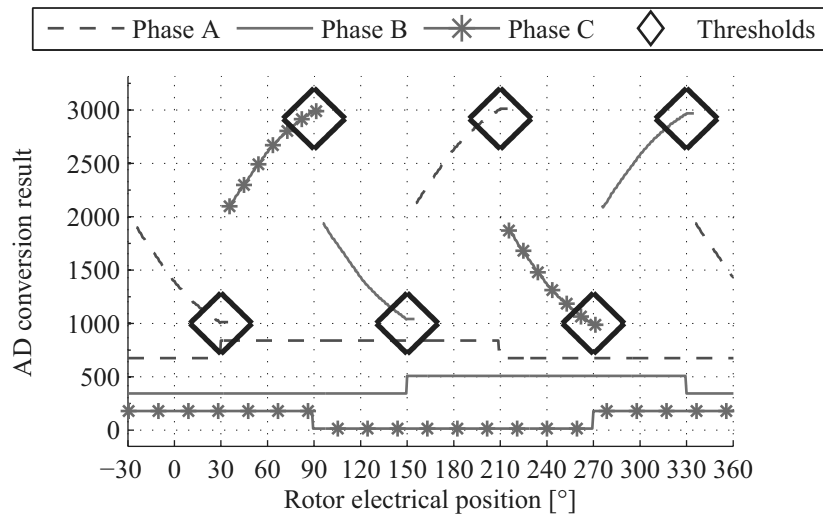


FIGURE 5.8 – Threshold values on the valid AD sampled U_{out} signals.

The calibration maps

By connecting start and thresholds values with a straight line, a linear approximation of the U_{out} value is performed for every 60° electrical sector and a calibration map, like the one shown in Fig. 5.9 can be drawn. Note that the motor used in this subsection is not the same as the one used for the previous figures, which explains the different threshold and start values.

In Fig. 5.9 the thresholds values are identified with a \blacklozenge and the start values are plotted with a \blacktriangleright . The triangle direction indicates the evolution of the U_{out} signal while the motor is driven and thus rotating. Again, on Fig. 5.9 the six sectors are identified with the

name of the supplied phases in that sector.

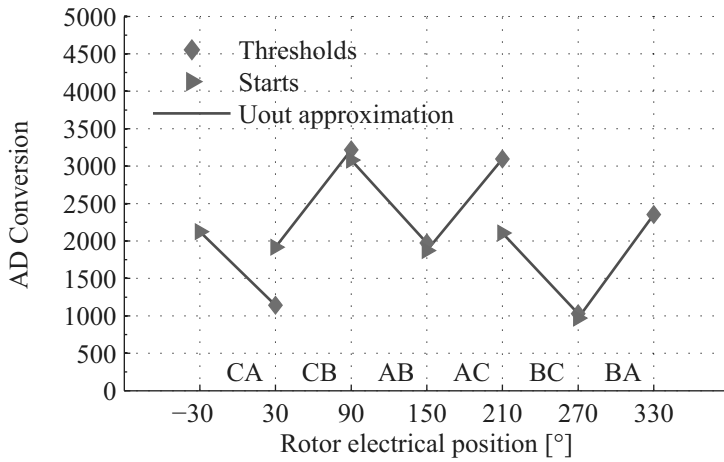


FIGURE 5.9 – Calibration map, forward direction.

If the motor is driven in the opposite direction, another calibration map is drawn. In Fig. 5.10 the backward rotation direction calibration map is plotted. The thresholds values are again identified with a \blacklozenge , but the start values are identified with a \blacktriangleleft . Note that the backward map has to be read from right to left.

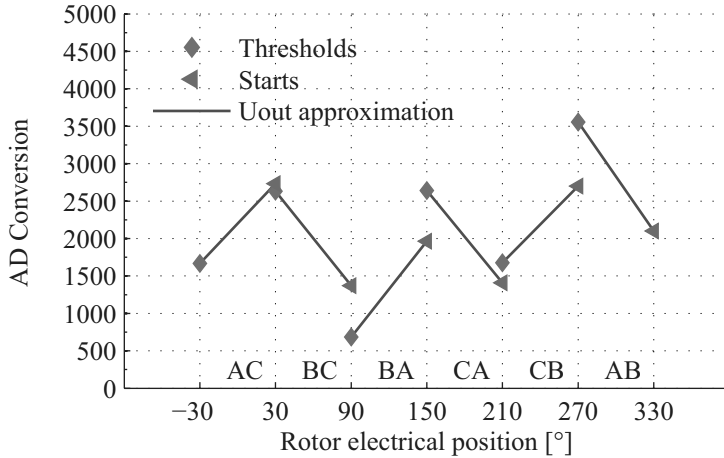


FIGURE 5.10 – Calibration map, backward direction.

The start values of the backward calibration map should theoretically be symmetrical to the thresholds values of the forward calibration map in respect to the middle of the AD range, 2'048, and vice versa. In fact, as it can be noticed by observing the commutation sequence on the two calibration maps, for every rotor position, the motor is supplied between the same phases but with opposite connections in both rotation directions. The phase connected to V_{pp} in the forward direction is connected to GND in the backward

direction, and the phase connected to GND in the forward direction is connected to V_{pp} in the backward direction.

Hence, if the U_{in} voltage is inverted and because the U_{out} measurement is obtained with a differential circuit, its value before filtering and amplification is inverted too. After the analogical treatment, the U_{out} value is then symmetrical in respect to the added offset, 1.5 V that corresponds to the 2'048 bits measured by the AD converter.

In practice, this relation is only approximately respected. Because of the motor asymmetries and the analogical stage imperfections, the symmetry moves slightly away from 2'048, depending on the commutation sector.

5.4.2 Hall sensors rebuilding at start-up or after a main reset

The observation of the available position information contained in U_{out} suggest to analyze two different situations for the Hall sensors rebuilding.

The first analyzed situation is to find the rotor position at start-up or after a main reset of the drive electronics. The problem is that the U_{out} signal is not a bijective function over one electrical period. That means that when the rotor electrical position is lost, the latter can not be retrieved with the U_{out} measurement only, even if the system has previously been calibrated and the maps are available. As already highlighted in Section 4.5, there is no one-to-one correspondence and the same value of U_{out} measured on one phase may correspond to up to four different positions.

For illustrating the problem, a practical example is introduced. A motor is calibrated and its calibration maps for both rotating directions are memorized. Thereafter, a main reset is imposed to the system, the rotor position information is lost but not the calibrations. At that unknown fixed position, the six possible U_{out} measurements are performed. Each measurement is identified with the name of the supplied phases, AB , BA , AC , CA , BC , CB . Table 5.1 shows the measured values for the unknown position. Measurements are sorted from the highest to the lowest value.

Supplied phases	U_{out}
BC	2680
AC	2513
BA	2275
AB	1835
CA	1541
CB	1404

TABLE 5.1 – 6 possibles U_{out} for a fixed rotor position.

With these six measurements, it is now tried to find the rotor position, based on the information contained in the calibration maps. In fact, it is known that, for every sector XY , with $X = A, B, C, Y = A, B, C$ and $X \neq Y$, the possible values of $U_{out}(XY)$ and $U_{out}(YX)$ are within the limits given by the start and threshold values stored in the two calibration maps for that sector. That means that if the six possible measurements are performed, at least one pair of U_{out} measures, $U_{out}(AB)$ and $U_{out}(BA)$, $U_{out}(AC)$ and $U_{out}(CA)$, $U_{out}(BC)$ and $U_{out}(CB)$, are within the limits of the unknown XY sector. If this sector is identified, the rotor position is successfully retrieved.

In Figs. 5.11 and 5.12, the calibration maps of the motor for both rotation directions are shown. Only one electrical period is considered. The electrical position is subdivided in 6 sectors, again identified with the name of the supplied phases in that sector. On both calibration maps, the six U_{out} measurements are superimposed by tracing six black lines. Where a measurement crosses the U_{out} linear approximation in its same sector, a \bullet is plotted at the crossing point and near the measurement legend. A \bullet means that this could be the actual position of the rotor.

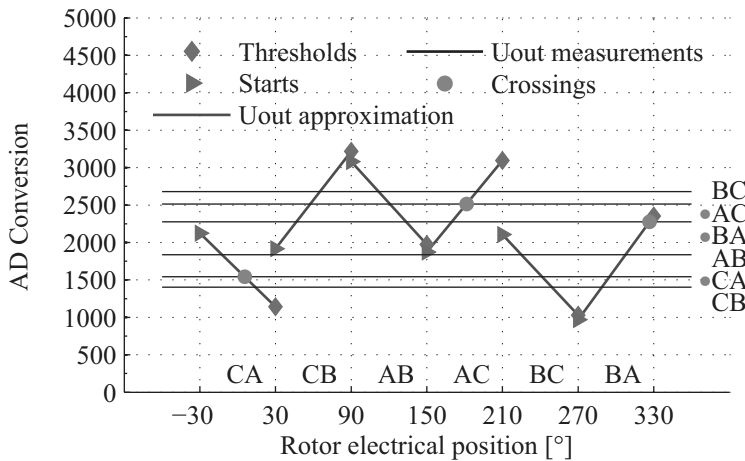


FIGURE 5.11 – Possible electrical rotor position. Forward calibration map.

In Fig. 5.11 three crossing points are detected. The measurement $U_{out}(AC)$ crosses the calibration map around 180° in the AC sector. Moreover, the measurement $U_{out}(BA)$ crosses in the BA sector, around 325° . Finally, also the $U_{out}(CA)$ crosses its respective CA sector, around 5° .

In Fig. 5.12 two crossing points are detected for the $U_{out}(AC)$ and the $U_{out}(CA)$ measurements. Two positions are possible, 15° and respectively 200° .

Merging the information coming from these U_{out} measurements and the motor calibration maps, for this example the rotor can be either in sector AC around position 10° or 180° away in sector CA around position 190° . But unfortunately, because of the symmetrical effect of the North and South permanent magnet poles on the iron hysteresis,

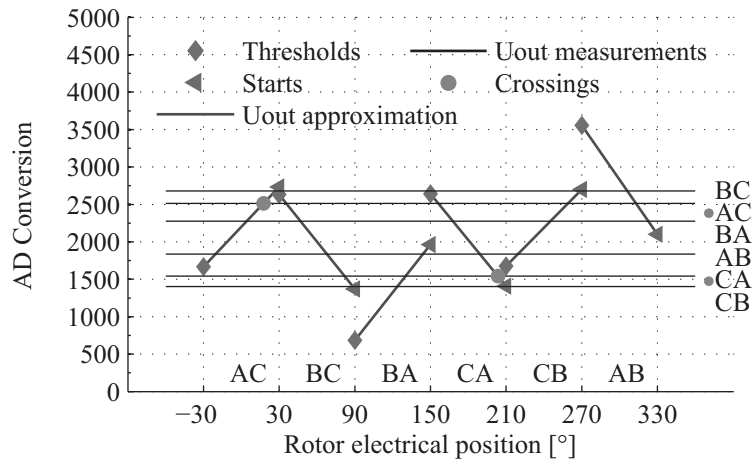


FIGURE 5.12 – Possible electrical rotor position. Backward calibration map.

it is not possible to state which one of the two is the real rotor position.

Finally, it can be concluded that even if the U_{out} signal contains the electrical position of the rotor, the latter is at position 10° in this example, a doubt of 180° remains. For avoiding this ambiguity an additional source of information is therefore needed. A solution to this problem, also based on the iron hysteresis but exploiting another effect, is introduced in Chapter 7.

5.4.3 Hall sensors rebuilding starting from a known position

In the second analyzed situation, it is hypothesized that the actual position is known. Starting from this known position, the goal is to track the rotor position and no more lose it.

In contrast to the position detection at start-up or after a main reset, the actual objective is relatively easily attained. In fact, if the actual position is known and the calibration maps are available, the simplest way for tracking the rotor position is to continuously measure the U_{out} voltage. Then, when the measured U_{out} value passes the respective thresholds \diamond stored in the calibration map, the software knows that the sector has changed. In this way three virtual Hall signals can be created and refreshed.

This sensorless principle is implemented in the realized electronics, Section 4.6, and the motor is driven using the virtual Hall signals. Fig. 5.13 shows U_{out} of the sensed phase, the virtual Hall signal ($\rightarrow*$) used for driving the motor and the Hall sensor signal ($--$) as a reference. The visible spikes due to current extinction in the phase are filtered by software. The motor speed is 220 rpm.

It can be appreciated how the virtual Hall sensor is correctly refreshed, even if a small

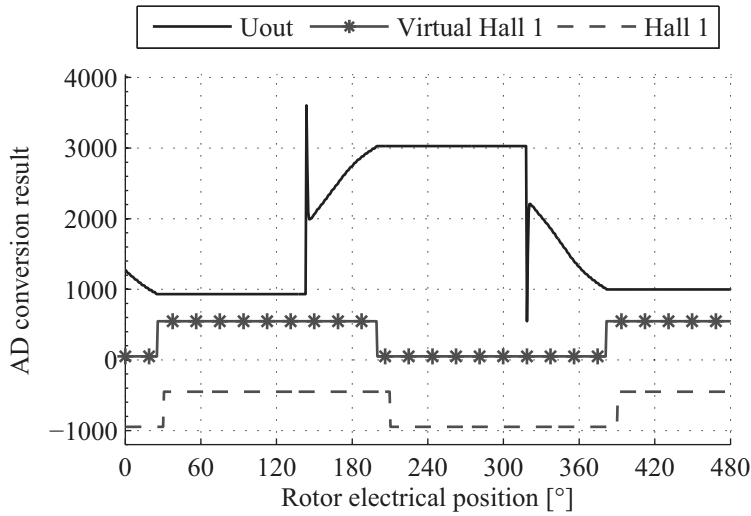


FIGURE 5.13 – Sensorless drive implementation. AD sampled U_{out} , Hall 1 and virtual Hall 1 signals.

time delay exists between the original Hall signal and the virtual one. Nevertheless, the main objective, namely the sensorless autocommutation, is successfully attained.

5.5 Torque-speed measurements at room temperature

In this section, the sensorless position detection starting from a known position, introduced in Subsection 5.4.3 is tested during steady state operations. The motor is driven with different loads at different speeds. A classical torque-speed graph is measured and the behaviour of the position estimation is attentively observed.

5.5.1 Measurement setup

In the realized setup, shown in Fig. 5.14, the developed electronics drives the BLDC motor with a constant supply voltage, neither current nor speed control are implemented. The supply voltage is fixed by a constant PWM duty cycle. It is chosen to supply the power bridge with 24 V, and apply a duty cycle of $d = 64\%$ on the power PWM. The motor is therefore supplied with a mean voltage of ~ 15 V.

The rotor position is retrieved either with the Hall sensors or with the developed sensorless principle. The developed electronics permits to calibrate the sensorless position detection thresholds when desired. For the calibration, the motor is driven with the Hall sensors. The calibration is performed once and the obtained maps are used during the whole trial.

5.5. Torque-speed measurements at room temperature

The BLDC motor is mechanically coupled with a DC motor. The DC motor generates the brake torque and the latter is manually varied with the potentiometer R and the dedicated current supply. The current in the DC motor is measured with an amperemeter A . Between the BLDC and the DC motor, a direct torque measurement is provided with a dynamic torquemeter. Torque and Hall sensors are continuously measured and sent to the PC where a software automatically stores the motor speed, retrieved thanks to the Hall sensors, and the torque, delivered by the torque measurement electronics.

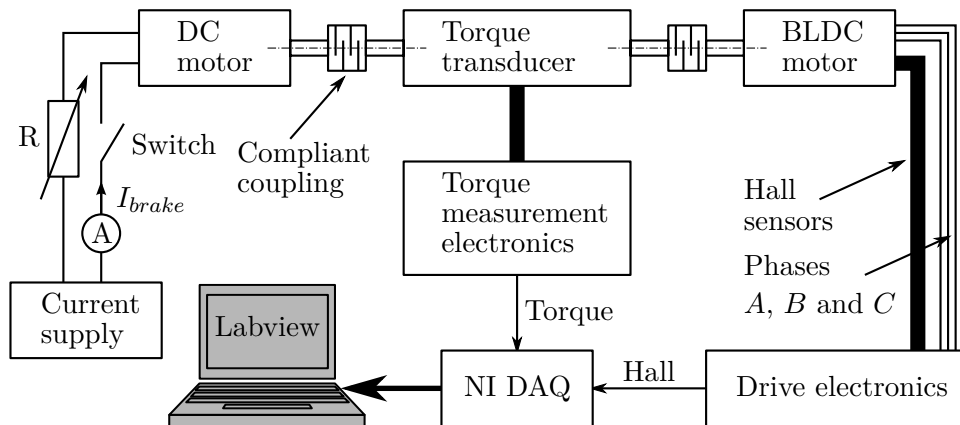


FIGURE 5.14 – Setup of the automatic torque-speed measurements

5.5.2 Measurements on the modified motor

The modified motor is tested at room temperature ($+20^{\circ}\text{C}$) with the shown setup. The thresholds for the sensorless position detection are calibrated at 540 rpm. The torque-speed characteristics are measured twice, first driving the motor with the Hall sensors, then using the virtual Hall sensors created with the developed sensorless method. The obtained torque-speed characteristics are superimposed in Fig. 5.15. The torque bump around the 300 rpm is caused by a mechanical resonance of the coupling element. Unfortunately it has not been possible to eliminate this problem.

In Fig. 5.15 it can be appreciated how the developed sensorless position detection principle is able to drive the motor during the very low speed operations. The minimal speed achievable is ~ 50 rpm, using either the Hall sensors or the sensorless technique. However, it is also important to point out that the introduced method fails at 800 rpm. This measure highlights a first drawback: the amplitude of the U_{out} signal depends on the current level in the supplied phases.

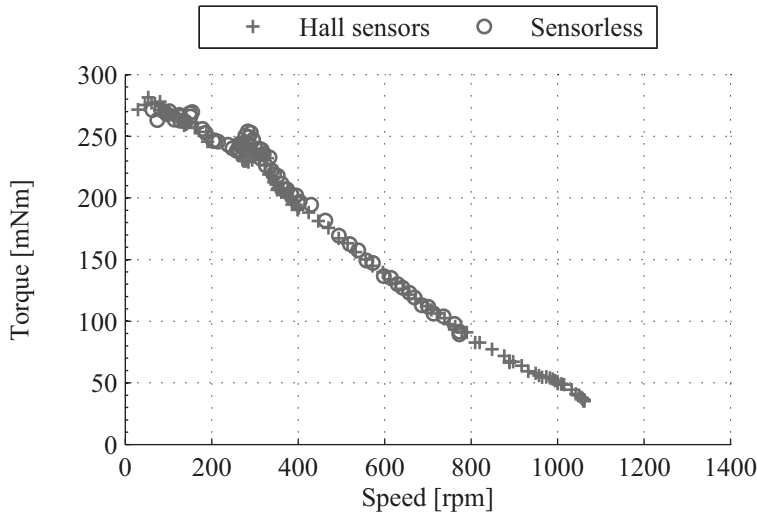


FIGURE 5.15 – Torque-speed measurements, modified motor, calibration at 540 rpm, 20°C

Influence of the phase current on the U_{out} amplitude

Taking into account the origin of U_{out} , it is easy to intuitively understand the influence of the phase current I_{in} on the signal. In fact, if $I_{in} \neq 0$ A when the U_{in} pulse is injected, the magnetic flux created by the two supplied coils add itself to the one created by the permanent magnets and thus moves the iron working point of both teeth on the BH plane. Therefore, for the same electrical position, the local hysteresis loop that will be followed if $I_{in} \neq 0$ A when the impulsion U_{in} is injected, is not the same as if $I_{in} = 0$. As a consequence, the higher I_{in} when the U_{in} pulse is injected, the higher the U_{out} amplitude.

In Fig. 5.16, a modified motor is driven in two-phases ON supply with two different loads. The current of phase B for the two trials is shown. In Fig. 5.17, the U_{out} voltage of phase A is shown for the same two loads. As expected, it can be appreciated how during the valid measurement zones, $[-30^\circ \ 30^\circ]$ and $[150^\circ \ 210^\circ]$, U_{out} lowers and respectively grows more for the second trial. This is a simple proof that the phase current influences the U_{out} signal amplitude.

The consequence of this dependence on the sensorless principle is that the thresholds saved during the calibration correspond exactly to the Hall sensors commutations only at the load at which the calibration is done. If the load decreases, the U_{out} amplitude decreases too, and if the load increases, the U_{out} amplitude increases too. So, at a torque higher than the calibration one, the commutation happens in advance, and at a torque level lower than the calibration one, the commutation arrives late, both compared to the referent case.

5.5. Torque-speed measurements at room temperature

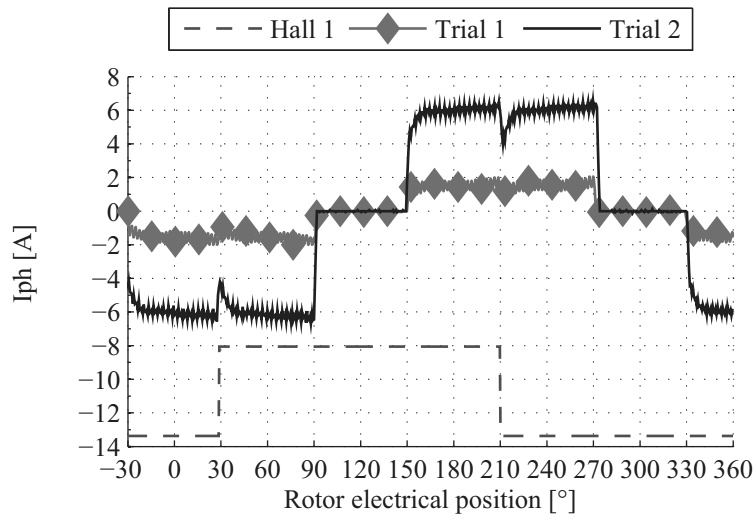


FIGURE 5.16 – Phase current for two different loads

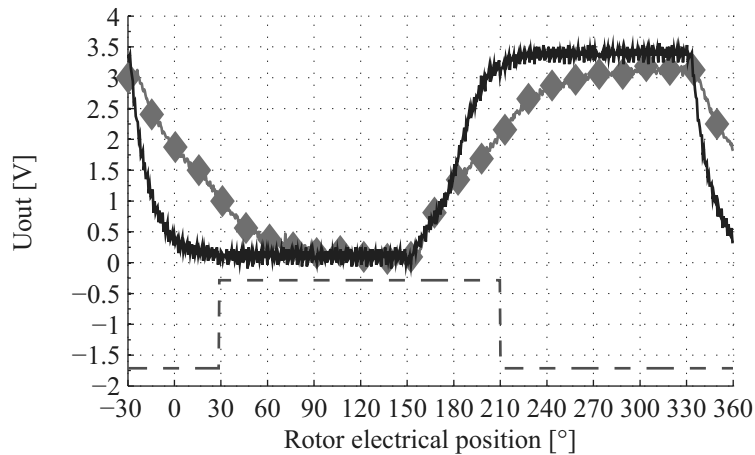


FIGURE 5.17 – U_{out} voltage for two different loads

Thanks to this explications, the behaviour of the sensorless position detection method shown in Fig. 5.15 is understood. In fact, for the high torques, the commutation occurs in advance, but not enough for altering the motor torque output. On the other hand, for a torque lower than 100 mNm, the virtual Hall signals are so late in comparison to the Hall sensors that the motor stops rotating.

Measurements with calibration at 990 rpm

The measurements are now done on the same modified motor, but the calibration is done at 990 rpm, 50 Nm. This trial is shown in Fig. 5.18. It can be appreciated how the sensorless principle works perfectly for the low torques, but starts to fail for the high

ones. In fact, below 300 rpm the commutation occurs with such an advance that the motor performances are degraded.

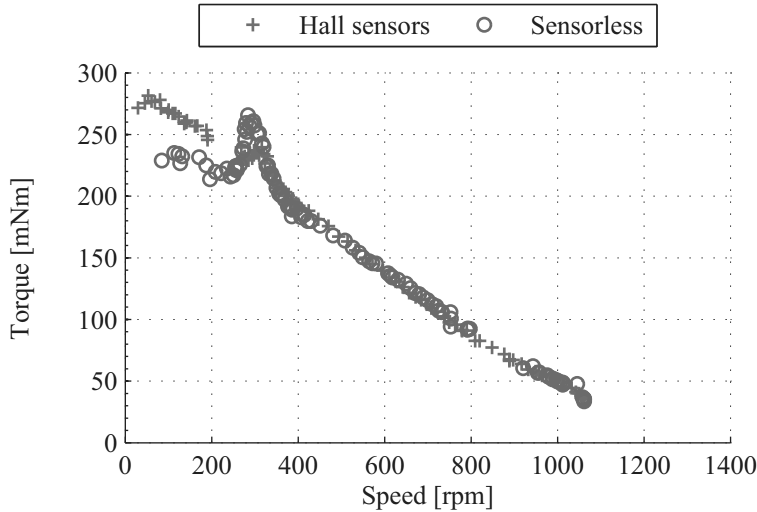


FIGURE 5.18 – Torque-speed measurements, modified motor, calibration at 990 rpm, 20°C

Influence of the calibration on the virtual Hall sensors

In order to recapitulate the situation, in Figs. 5.19 and 5.20 the Hall sensor 1 and the virtual Hall sensor 1 are superimposed for three different working points on the torque-speed characteristic of the modified motor. Fig. 5.19 shows the measurements for the trial with calibration at 540 rpm. As stated, the commutation is perfect at the calibration working point, is in advance for higher and late for lower torques. Fig. 5.20 shows the measurements for the trial with calibration at 990 rpm. For higher torques the commutation is more and more in advance. At 270 rpm the commutation advance exceeds 30° and the drive performances are highly degraded.

Conclusions

At the end of this analysis, it can be stated that the technique works well around the calibration zone and that the latter is defined by the phase current level. In order to ensure the motor commutation for every load, the calibration at low torque is suggested. In addition, an improvement of the quality of the virtual Hall reconstruction can be easily obtained by compensating the current influence on the U_{out} signal by software. In fact, starting from the calibration maps stored at low torque, the commutation thresholds can be easily adapted as a function of the phase current. This purpose is unfortunately

5.5. Torque-speed measurements at room temperature

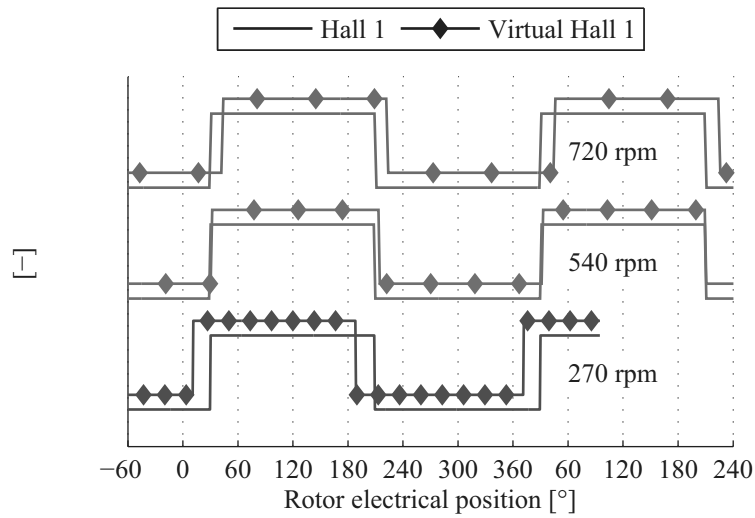


FIGURE 5.19 – Hall and virtual Hall sensor 1 for different working points. Calibration at 540 rpm.

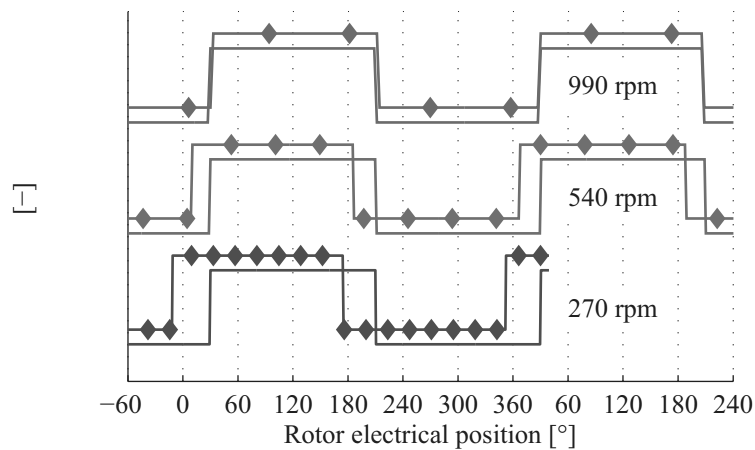


FIGURE 5.20 – Hall and virtual Hall sensor 1 for different working points. Calibration at 990 rpm.

not implemented on the realized electronics because of a very poor quality of the phase currents measurements.

5.5.3 Measurements on the standard motor

The same torque-speed measurements are now done with a standard motor and plotted in Fig. 5.15. Again, the calibration is done around 540 rpm, 160 mNm.

In the measurements performed on the standard motor shown in Fig. 5.21, below 100 rpm, or more precisely when the load exceeds 280 mNm, the sensorless position

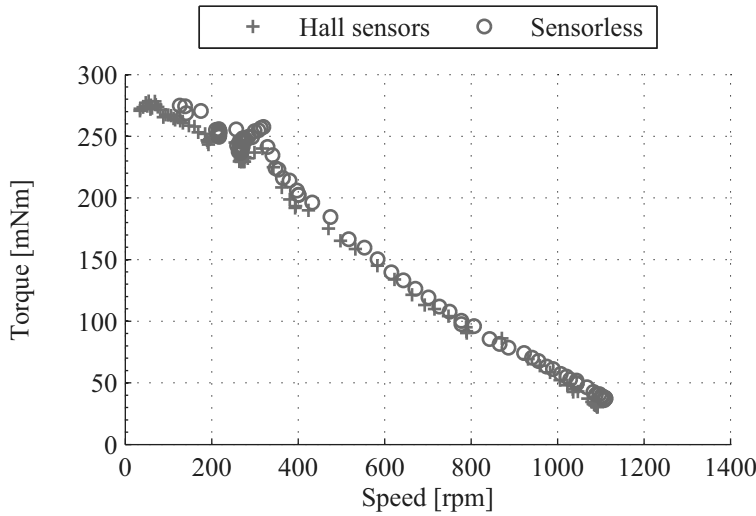


FIGURE 5.21 – Torque-speed measurements, standard motor, calibration at 540 rpm, 20°C

detection fails. In fact, because of its higher teeth iron section, the U_{out} amplitude in the standard motor is less affected by the phase current than in the modified one. Hence, for higher and lower torques than the calibration one, the U_{out} amplitude does not significantly neither grow nor lower. At high torques the U_{out} signal has therefore not a higher amplitude, which could facilitate its measurement. And in addition, because of the high currents circulating in the drive, the electronic noise increases and perturbs the U_{out} measurement so that the drive electronics is no more able to retrieve the rotor position.

Finally, despite the technical difficulties, the measurement shows again the effectiveness of the sensorless position detection.

5.5.4 Comparison between standard and modified motor

Using the performed measurements, it is also possible to compare the motor characteristics between the standard and the modified motor. Measurements done at room temperature for both motors driven with the Hall sensors, i.e. when the commutation angle is ensured without any doubt, are plotted in the same graph, Fig. 5.22. As it can be noticed, no difference appears between the two curves, the modified motor performance (\times) is at the same level than the standard motor ($+$).

If the motor performances are the same, this is not the case for the sensorless position detection. Even if its sensitivity to the injected current is increased, thanks to its higher U_{out} amplitude, the modified motor is much easier to drive with the developed sensorless principle, which confirms the pertinence of the done modifications.

5.6. Torque-speed measurements at extrema temperature

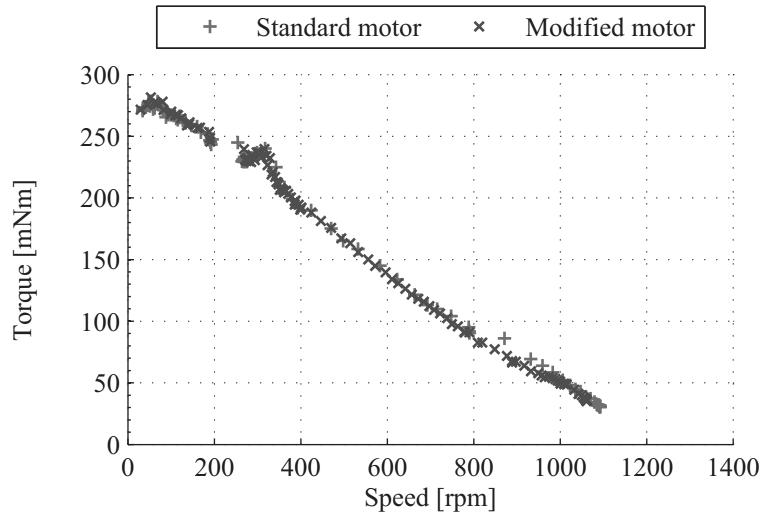


FIGURE 5.22 – Torque-speed comparison between standard and modified motor, 20°C

5.6 Torque-speed measurements at extrema temperature

In order to prove the robustness of the position estimation, the torque-speed measurement is also performed for both motors, standard and modified, in a steam room, at two extrema temperatures, very cold and very hot. In fact, temperature changes many characteristics of a motor, and thus it has to be verified that the technique is still effective away from the ambient temperature.

5.6.1 Measurement setup

The setup for the measurements in the steam room is slightly different than the one introduced in Fig. 5.14. Because of the temperature constraints, the torquemeter cannot be placed in the steam room and thus, the torque measurement has to be done indirectly. The brake torque is therefore calculated based on the DC motor characteristics and the measurement of the current I_{brake} done with the amperemeter A. The desired temperature is imposed to the steam room and at least two hours are elapsed before starting the measurements, for ensuring a homogeneous temperature in the motor. Torque-speed points are manually stored in an Excel sheet. This setup is schematised in Fig. 5.23.

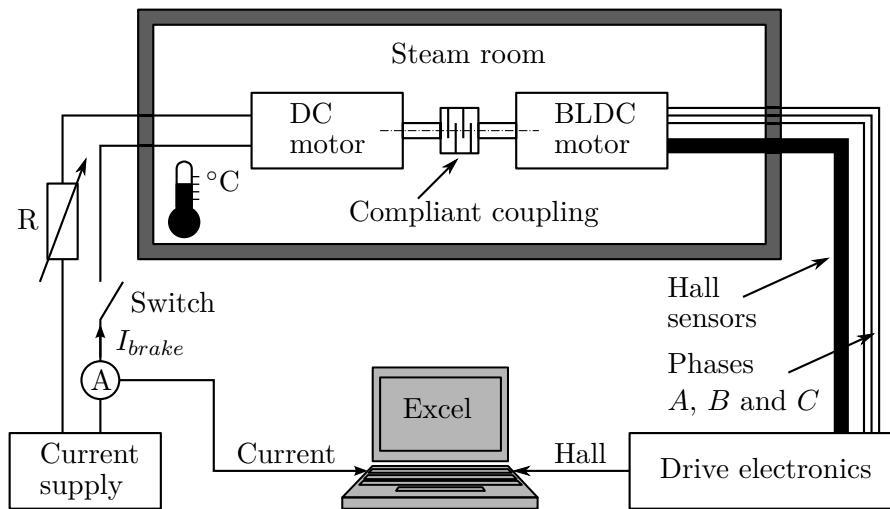


FIGURE 5.23 – Setup of the torque-speed measurements in the steam room.

5.6.2 Measurements with the modified motor

Measurement at +20°C, setup validation

First of all, a measurement with the new setup is performed at room temperature. This measurement is shown in Fig. 5.24. On the same graph, the measurement obtained with the first setup is also plotted with the purpose of comparing the effectiveness of the indirect torque measurement. The automatic setup curve is obtained using the Hall sensors, and the steam room setup curve is obtained using the developed sensorless method.

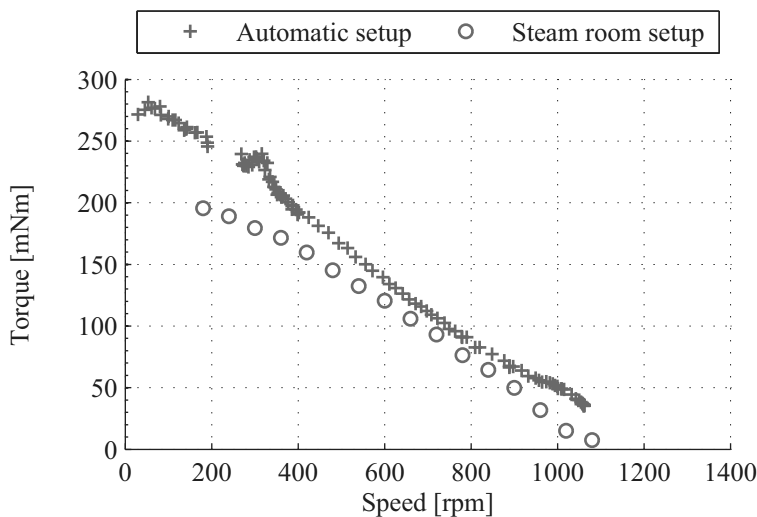


FIGURE 5.24 – Torque-speed measurements with both setups, modified motor, +20°C.

5.6. Torque-speed measurements at extrema temperature

The results introduced in Fig. 5.24 prove that the measurements of the two setups are coherent. The slope of the torque-speed characteristic is quite the same from 1'100 rpm down to 400 rpm. At slower speed, the steam room setup curve bends because of the sensorless position detection, as explained in the previous section.

A small torque offset between the two measurements is also present. This offset is explained because with the steam room setup it is not possible to measure the frictions of the mechanical construction. These frictions do not influence the I_{brake} current circulating through the DC motor but are on the other hand measured with the first setup, as the torque is directly measured with the torquemeter. In addition, the latter has a manual zero-torque calibration that also explain the measured offset.

Measurement at -20°C and $+80^{\circ}\text{C}$

The steam room is now activated and two torque-speed characteristics are measured, at very cold, -20°C , and very hot $+80^{\circ}\text{C}$ temperature. The first measurement is shown in Fig. 5.25 and the second in Fig. 5.26. The drive electronics is calibrated only once at room temperature at the beginning of the measurements, at 1'060 rpm with no load.

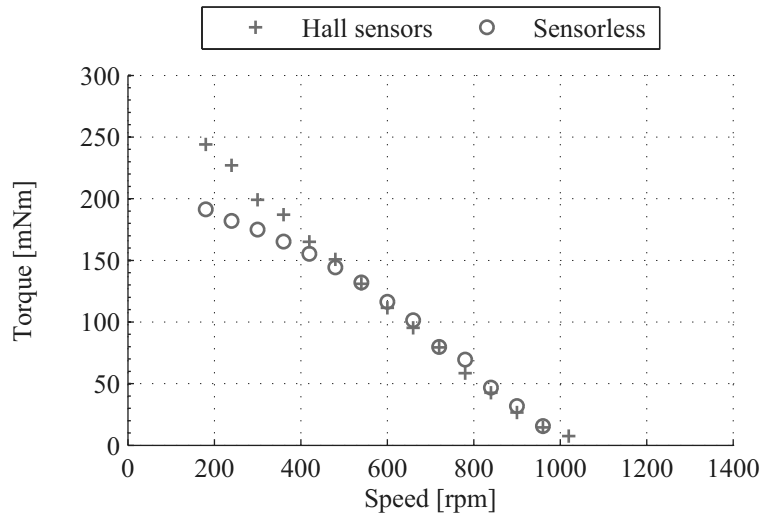


FIGURE 5.25 – Torque-speed measurements at -20°C , modified motor, calibration at 1060 rpm $+20^{\circ}\text{C}$.

As is can be appreciated in Figs. 5.25 and 5.26 the sensorless position detection works in both extreme conditions. The curves realized with the developed sensorless position detection principle (\circ) are superimposed to the ones realized with the Hall sensors ($+$) from 1'1000 rpm down to 400 rpm. At lower speed, with a high torque and high current in the phases, U_{out} amplitude increases considerably. Coherently with the measurement shown in Fig. 5.18, because of the fixed thresholds, the commutations happen more and

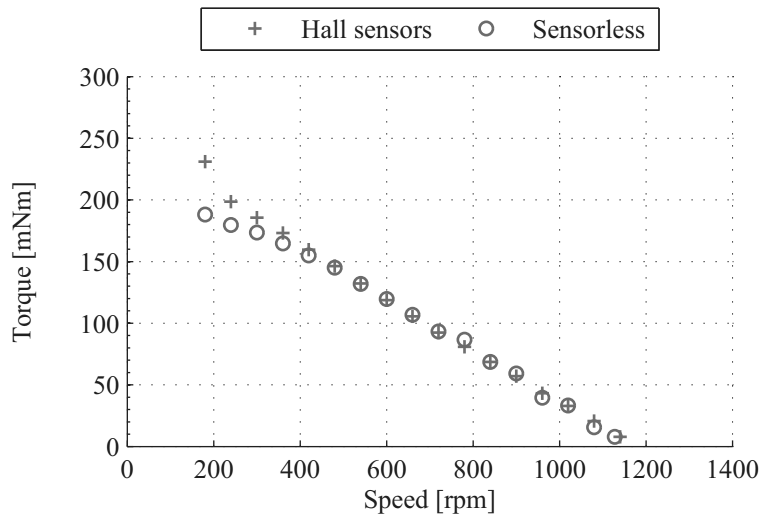


FIGURE 5.26 – Torque-speed measurements at $+80^{\circ}\text{C}$, modified motor, calibration at 1060 rpm $+20^{\circ}\text{C}$.

more in advance compared to the Hall sensors, reducing finally the torque delivered by the motor. This phenomenon is clearly visible on Figs. 5.25 and 5.26 when the two measurements, with Hall sensors (+) and without (o) start to diverge at 400 rpm, 150 mNm.

5.6.3 Measurements with the standard motor

Measurement at $+20^{\circ}\text{C}$, setup validation

Again, the first measurement is performed at room temperature with the aim of verify the accuracy of the setup. The measurement performed with the new setup, superimposed to the one obtained with the automatic setup is shown in Fig. 5.27.

As for the modified motor, the slope of the torque-speed characteristic is the same for the two measurements, and only a small torque offset is present. In this case, the points obtained with the steam room setup are around 20 mNm lower than the ones obtained with the automatic measurement setup.

Measurement at -40°C and $+120^{\circ}\text{C}$

The steam room is now activated and two torque-speed characteristics are measured, at very cold, -40°C , and very hot $+120^{\circ}\text{C}$ temperature. Both temperatures are more extreme than the ones imposed to the modified motor. For the latter, the temperatures

5.6. Torque-speed measurements at extrema temperature

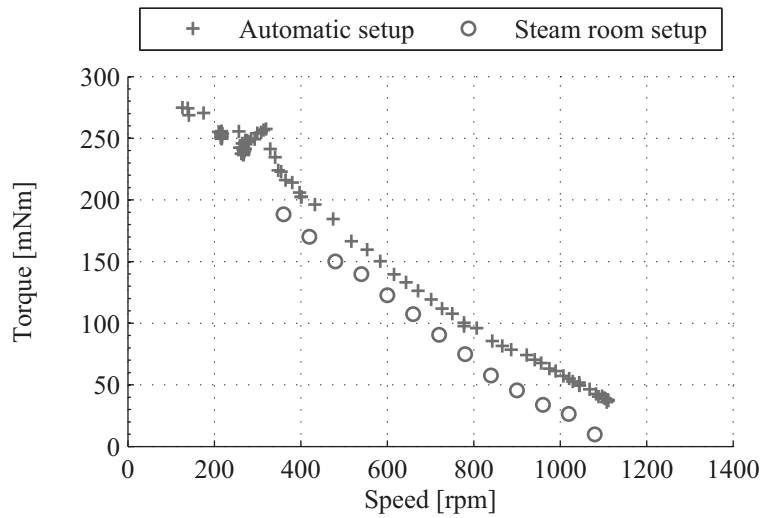


FIGURE 5.27 – Torque-speed measurements with both setups, standard motor, $+20^{\circ}\text{C}$.

have in fact not been brought to these extrema for avoiding a mechanical failure, as only two prototypes have been realized. The first measurement is shown in Fig. 5.28 and the second in Fig. 5.29.

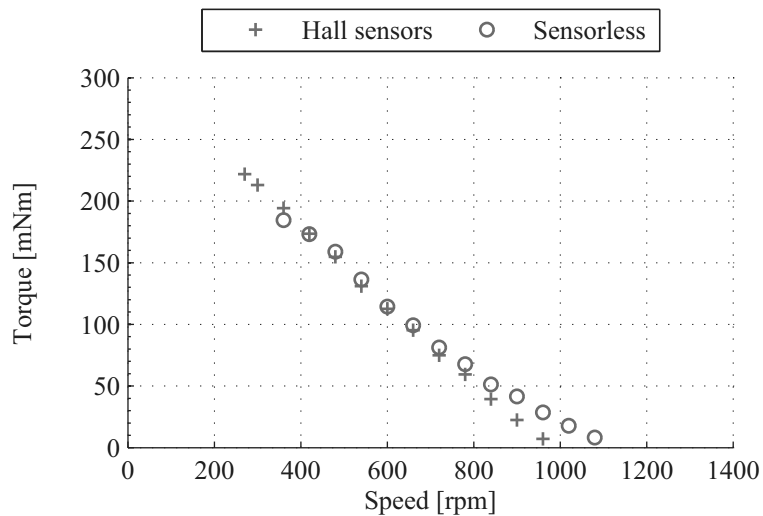


FIGURE 5.28 – Torque-speed measurements at -40°C , standard motor, calibration at 540 rpm -40°C .

The measurements done at -40°C $+120^{\circ}\text{C}$ prove once more the effectiveness of the developed position detection principle. However, for these measurements, the calibration done at room temperature did not work in the extreme environments. For both trials, the calibration is performed at 540 rpm at the temperature of the steam room, -40°C and respectively $+120^{\circ}\text{C}$. Moreover, a slope change for the high speed operations, as

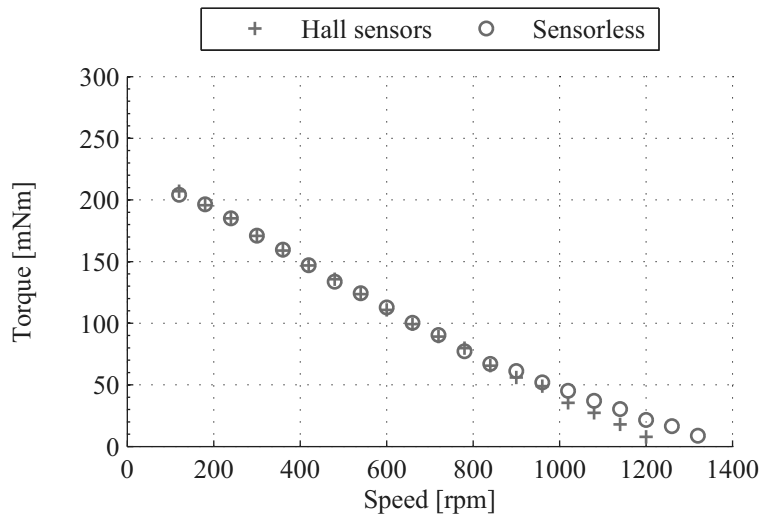


FIGURE 5.29 – Torque-speed measurements at $+120^{\circ}\text{C}$, standard motor, calibration at 540 rpm $+120^{\circ}\text{C}$.

well as the failure of the sensorless position detection for the speed operations lower than 350 rpm in the cold environment trial are noticed. Again, these problems are only related to the small amplitude of the U_{out} signal produced by the used drive electronics and do not compromise the effectiveness of the technique.

5.7 Rotation direction forced by the load torque

Until now, the motor driven with the introduced position estimation technique has always been loaded with a passive “constant” brake. That means that the motor has always rotated in the direction imposed by the drive electronics.

In case of an active external load with direction opposed to the one imposed by the software and a torque higher than the one delivered by the motor, the rotor may start rotating in the opposite way. For avoiding the loss of the position estimation, it is therefore necessary to detect the change in the rotation direction, and use other thresholds in order to travel along the U_{out} curve in the opposite direction. Fig. 5.30 shows these thresholds used for estimating the rotor position in case of externally forced rotation direction. These thresholds are already introduced in Fig. 5.7 for the realization of the calibration maps. The proposed solution is implemented and gives good results at low speed operations.

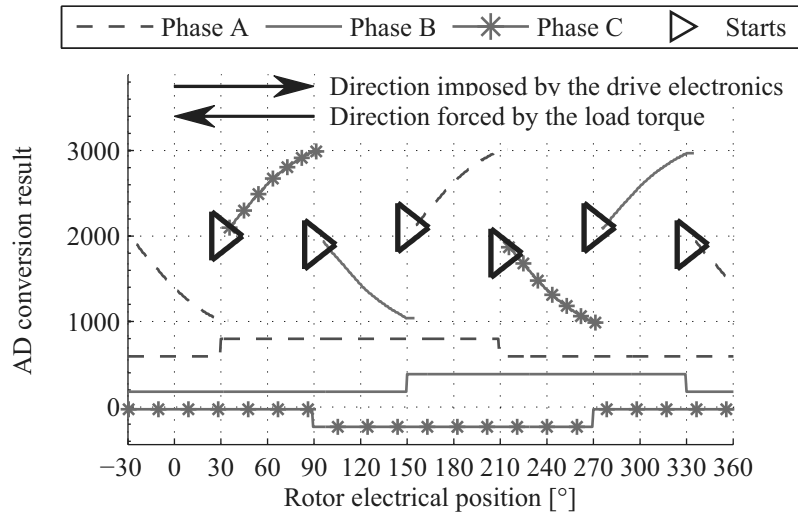


FIGURE 5.30 – Thresholds in case of forced opposite rotation direction.

5.8 Power PWM duty cycle range

As explained in Section 5.3, the signal U_{in} that creates the position dependent U_{out} signal is also the power PWM that drives the motor.

Because of this double function, the duty cycle of the power PWM has to be within some limits. First of all, experience has shown that measurements are noisy and not reliable during the first $7 \mu\text{s}$ after the U_{in} edge. Therefore the t_{ON} time should last at least $10 \mu\text{s}$ (for the analyzed motors) in order to create enough information to be detected without errors. Typically, for a PWM carrier frequency $f = 20 \text{ kHz}$ the duty cycle should not be lower than $d = 0.2$.

An upper limit also exist because the proposed technique needs a regular injection of a rising (or falling) edge between two phases. Hence, the motor can not be driven at full wave, $d = 1$. In the realized drive, the maximum admitted duty cycle is $d = 0.9$.

5.9 Angular resolution

In the actual configuration the software refreshes the estimated position every 60° . This is the minimum resolution needed for driving the motor in block commutation.

It can however be pointed out that the measured value of U_{out} contains much more information on the rotor position. As for example, a rapid calculation is performed on the U_{out} measurement shown in Fig. 5.4. In that measurement, it is clearly visible how the U_{out} signal varies of $\sim 1'000$ bits during 60° . That means that, in this particular

case, if a linear approximation is assumed, the electrical angular resolution $\Delta\theta_e$ of the introduced technique is:

$$\Delta\theta_e = \frac{60^\circ}{1'000} = 0.06^\circ/\text{bit} \quad (5.1)$$

For the BLDC motor used until now that has 5 pole pairs this corresponds to

$$\Delta\theta_m = \frac{\Delta\theta_e}{5} = 0.012^\circ/\text{bit} \quad (5.2)$$

where $\Delta\theta_m$ is the mechanical angular resolution. This is equivalent to an angular encoder with a huge number of 30'000 increments. Obviously, the angular resolution of the introduced technique depends on many factors: the motor itself, the U_{in} amplitude, the gain of the analogical amplification of U_{out} and so on. Moreover, depending on the motor characteristics, the U_{out} amplitude may not vary linearly during the 60° where it is measured. Nevertheless, if the system is known and calibrated, this information is easily available and could be used for a precise positioning of the rotor.

5.10 Sensorless position detection of slotless BLDC motors

The addressed sensorless principle has also been applied to another BLDC motor, shown in Fig. 5.31. It is a slotless BLDC motor, perfectly symmetric by its construction, 120 W, 3 phases, 1 pole pairs. Its datasheet is given in Appendix B.2.

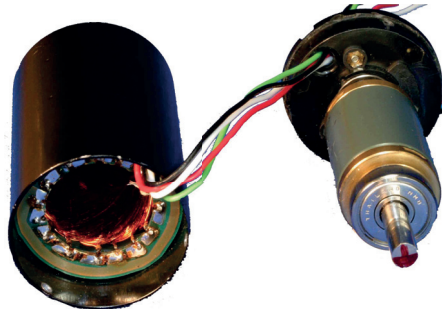


FIGURE 5.31 – Tested slotless BLDC motor. Opened.

Fig. 5.32 shows the U_{out} signal for two different positions created when a step is imposed on the U_{in} voltage. As expected, also for this motor the U_{out} signal varies significantly between two different rotor positions.

The motor is now externally turned and a power PWM small enough to not generate torque is injected between the phases 1 and 2. U_{out} is measured on the floating phase 3. Fig. 5.33 shows the U_{out} signal sampled with an AD for two complete mechanical

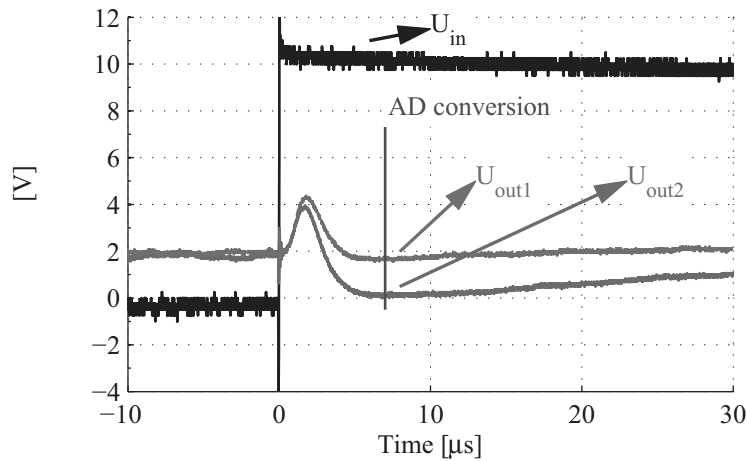


FIGURE 5.32 – U_{out} after filtering and amplification for two different positions created by a step on U_{in} . Slotless motor.

rotations. As for the other motors used until now, the signal is highly position dependent

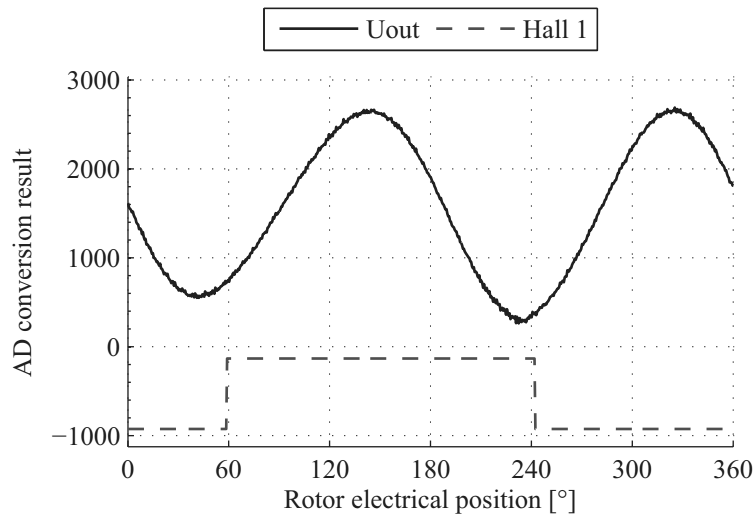


FIGURE 5.33 – U_{out} after the AD sampling for two electrical revolutions. Slotless motor.

and can be used for the rotor position detection.

In order to prove the effectiveness of the technique on this motor configuration, a torque-speed measurement is performed at room temperature using the setup shown in Fig. 5.14. Two trials are shown in Fig. 5.34. First of all, the motor is driven with the position measured with the Hall sensors, (+). The measurement is then repeated with the motor driven with the reconstructed Hall signals, based on the U_{out} measurements, (○). The calibration is performed at 1'240 rpm.

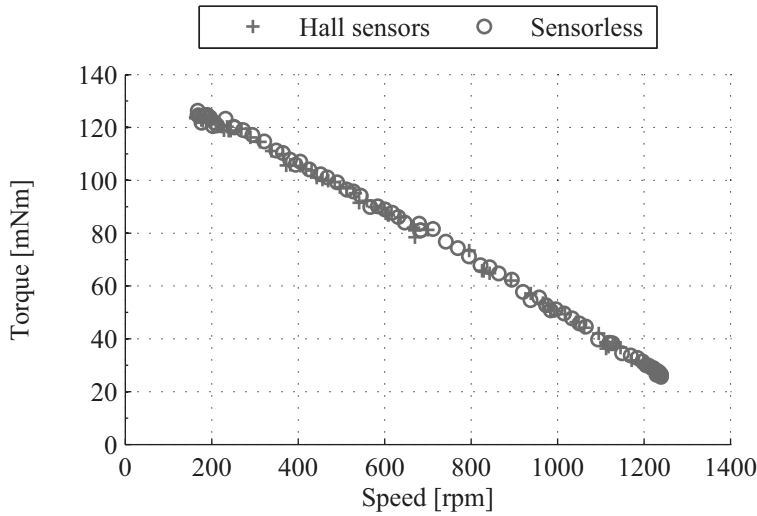


FIGURE 5.34 – Torque-speed measurements, slotless motor, calibration at 1240 rpm.

From Fig. 5.34 it can be appreciated that the measurements obtained with the developed technique are perfectly superimposed to the ones obtained using the Hall sensors.

5.11 Conclusions

In this chapter, a proposition for integrating the position-dependent U_{out} signal measurement into a BLDC motor drive electronics is introduced.

The motor is driven by block-commutation and the power PWM needed for the motor driving is also used as U_{in} signal. Hence, no special signals are injected into the phases and the hardware integration of the proposed measurement principle in a motor drive requires only a few additional components for the analogical treatment of U_{out} . For each commutation sector, U_{out} is measured on the floating phase. Based on the measured U_{out} , a simple schema that consist in creating three virtual Hall signals is introduced for the sensorless drive of a BLDC motor.

It is shown that, with the U_{out} signal only, it is not possible to univocally detect the rotor position, but just to estimate the next position based on the actual one. Moreover, it is shown that the introduced implementation needs a calibration stage in order to permit a correct Hall sensor reconstruction. For this reason, in Chapter 6 an algorithm based on Kalman filtering is introduced for estimating on-line the parameters needed for the exploitation of the U_{out} signal.

The effectiveness of the principle is demonstrated thanks to torque-speed characteri-

sations performed at room and extrema temperatures, on both standard and modified motors. It can be stated that the developed sensorless position detection principle is not influenced by the temperature variations. At ambient temperature as well as in a very hot and in a very cold environment the position detection principle drives the motor correctly. The reason of this good performance is found in the type of the measurements. In fact, the temperature affect the whole motor. Measurements performed in the introduced method are not influenced by variations that involve the entire system because they do not count on absolute values but only differences between the phase impedances.

Based on these measurements, it is also shown that the current in the motor phases influences the U_{out} signal and consequently, that the best performances are obtained around the calibration zone.

In addition, the comparison between the standard and the modified motor shows that the provided motor modification greatly simplifies the sensorless position detection without affecting the motor performance.

Finally, it can be stated that the measurement of the impedance variations due to the iron BH hysteresis is very promising for the sensorless position detection at standstill and during very low speed operations, even if the introduced implementation may still suffer of a lack of robustness because of the relatively simple use of the U_{out} measurements. In order to compensate this drawback, in Chapter 6 the U_{out} signal is used in a Kalman filtering based drive. The additional position information brought by the U_{out} signal lead to a more robust sensorless position detection technique.

Enhanced Kalman filtering

Contents

6.1	Introduction	110
6.2	Synchronous motor model	110
6.2.1	The mechanical equation	112
6.3	Kalman filtering with parameters estimation	114
6.3.1	Implementation	116
6.3.2	Parameters observability	117
6.3.3	Simulation results	118
6.3.4	Experimental setup	124
6.3.5	Experimental results without parameter estimation	125
6.3.6	Experimental results with parameter estimation	127
6.3.7	Parameters estimation proof	131
6.3.8	Practical considerations on the parameter estimation algorithm	133
6.3.9	Comments	134
6.4	Kalman filtering with U_{out} measurement	134
6.4.1	State-space model observability theory	134
6.4.2	Local observability extension	135
6.4.3	Kalman filter on a two-phases ON supply	136
6.4.4	U_{out} measurement	140
6.4.5	U_{out} calibration	142
6.4.6	Comments	143
6.5	Kalman filtering with U_{out} and parameters estimation	144
6.6	Conclusions	147

6.1 Introduction

THE present chapter is a result of a visionary objective: create a sensorless position detection principle, functioning over the whole speed range, robust, adapted to steady-state and dynamic operations, suitable for all kind of BLDC motors and without the need for any kind of off-line calibration.

In order to achieve this elevated goal, it is chosen to merge the exploitation of the U_{out} signal introduced in Chapter 4 and Chapter 5 into a sensorless position detection schema, based on Kalman filtering.

Kalman filtering applied to the sensorless position detection of synchronous motors is a powerful and robust tool. However, Kalman filtering has also some drawbacks. The two major limitations are the motor operations at low speed and the need for accurate model parameters.

The fusion of a Kalman filtering drive with the principle developed in Chapter 5 solves automatically the problem of the motor operations at low speed thanks to the U_{out} signal, which contains the rotor position information and is available over the whole speed range. For the correct U_{out} signal measurement, the development of a a Kalman filtering drive with two-phases ON supply, already introduced in [61]¹, is needed.

In order to avoid any off-line calibration, the second drawback has to be solved with the realization of a Kalman filtering drive able to estimate not only the motor state but also the model parameters. This step is crucial for the overall development and thus it is treated first in Section 6.3.

Once demonstrated the feasibility and correct functioning of the estimation algorithm, the Kalman filtering drive with two-phases ON supply is introduced in Section 6.4.

Finally, in Section 6.5, the merging of these two implementations leads to the wanted robust sensorless drive, with a large speed range and without the need of off-line calibration.

6.2 Synchronous motor model

A general nonlinear model used in a Kalman filter can be described by the two equations listed below:

$$\begin{cases} \dot{\mathbf{x}} = \mathbf{g}(\mathbf{x}) + \mathbf{B} \mathbf{u} & (6.1) \\ \mathbf{y} = \mathbf{C} \mathbf{x} & (6.2) \end{cases}$$

¹In the paper it is however not clear if a speed and/or position encoder is used or not.

6.2. Synchronous motor model

where (6.1) is the non-linear state equation and (6.2) the measurement equation. The term $\mathbf{x} = (x_1, x_2, \dots, x_m)^T$ represents the state vector and x_n are the state variables. $\mathbf{y} = (y_1, y_2, \dots, y_m)^T$ is the measurement vector and $\mathbf{u} = (u_1, u_2, \dots, u_m)^T$ is the external control (or input) vector. Uppercase bold letters like \mathbf{C} are used for representing matrices.

For the physical model of the synchronous motor it is chosen to map the three motor phase currents through a Park transformation to a new reference frame (α, β) , fixed to the stator [39]. The state vector $\mathbf{x} = (i_\alpha, i_\beta, \omega, \theta, \Gamma_{load})^T$ is therefore composed by the state variables listed in Table 6.1.

TABLE 6.1
Synchronous motor model state variables

i_α	Phase α current	[A]
i_β	Phase β current	[A]
ω	Rotor speed	[rad/s]
θ	Rotor position	[rad]
Γ_{load}	Load torque	[Nm]

The non-linear state equations composing (6.1), with

$$\mathbf{B} = \begin{pmatrix} \frac{1}{L} & 0 & 0 & 0 & 0 \\ 0 & \frac{1}{L} & 0 & 0 & 0 \end{pmatrix}^T \quad (6.3)$$

and

$$\mathbf{u} = \begin{pmatrix} u_\alpha & u_\beta \end{pmatrix}^T \quad (6.4)$$

are:

$$\frac{di_\alpha}{dt} = \frac{1}{L} \left(-Ri_\alpha - K_m\omega \sin(p\theta) + u_\alpha \right) \quad (6.5)$$

$$\frac{di_\beta}{dt} = \frac{1}{L} \left(-Ri_\beta + K_m\omega \cos(p\theta) + u_\beta \right) \quad (6.6)$$

$$\frac{d\omega}{dt} = -\frac{3K_m}{2I_{mot}} \left(i_\beta \cos(p\theta) - i_\alpha \sin(p\theta) \right) - \frac{K_{f,mot}}{I_{mot}}\omega + \frac{1}{I_{mot}}\Gamma_{load} \quad (6.7)$$

$$\frac{d\theta}{dt} = \omega \quad (6.8)$$

$$\frac{d\Gamma_{load}}{dt} = 0 \quad (6.9)$$

u_α, u_β are the phase voltages mapped into (α, β) frame. The model parameters are listed in Table 6.2. For the motor model it is assumed that the phase impedances $L_A = L_B = L_C = L$ and the phase resistances $R_A = R_B = R_C = R$ do not vary with the rotor position.

TABLE 6.2
Synchronous motor model parameters

R	Phase resistance	$[\Omega]$
L	Phase inductance	$[\text{H}]$
K_m	Torque constant	$[\text{Nm/A}]$
$K_{f,mot}$	Friction constant	$[\text{Nm/rad/s}]$
I_{mot}	Rotor inertia	$[\text{kg/m}^2]$
p	Pole pairs	$[-]$

Finally, the measurement vector \mathbf{y} is composed by the two phase currents:

$$\mathbf{y} = \begin{pmatrix} i_\alpha & i_\beta \end{pmatrix}^T \quad (6.10)$$

and therefore

$$\mathbf{C} = \begin{pmatrix} 1 & 0 & 0 & 0 & 0 \\ 0 & 1 & 0 & 0 & 0 \end{pmatrix} \quad (6.11)$$

6.2.1 The mechanical equation

As stated in [39], if the motor torque constant K_m and the motor mechanical parameters, inertia I_{mot} and friction constant $K_{f,mot}$, are not accurately known, the mechanical equation (6.7) in the Kalman filter is useless. Moreover, even in case of good accuracy parameters, (6.7) contains the free and unknown term Γ_{load} . Why should one calculate the other contributions if finally the last term, Γ_{load} can have any value? Two approaches are suggested.

Approach with hypothesis $I_{mot} = \infty$

In this first approach, the hypothesis $I_{mot} = \infty$ is adopted. Consequently, (6.7) is simplified to

$$\frac{d\omega}{dt} = 0 \quad (6.12)$$

and (6.9) is eliminated. The motor model is therefore rewritten as follows:

$$\frac{di_\alpha}{dt} = \frac{1}{L} \left(-Ri_\alpha - K_m\omega \sin(p\theta) + u_\alpha \right) \quad (6.13)$$

$$\frac{di_\beta}{dt} = \frac{1}{L} \left(-Ri_\beta + K_m\omega \cos(p\theta) + u_\beta \right) \quad (6.14)$$

$$\frac{d\omega}{dt} = 0 \quad (6.15)$$

$$\frac{d\theta}{dt} = \omega \quad (6.16)$$

This approach, adopted in [39] for the first time, has been used many times. It is the right way for implementing the Kalman filter if the knowledge of the drive model is inaccurate. The price to pay is nevertheless a slow dynamic response that can be seen in the speed estimation and measurement comparison figures in [39].

Approach with load modelling

The second approach, introduced in this thesis, is to model the load torque. Let the load torque, Γ_{load} , be modeled with a sum of a friction torque, $\Gamma_{fr} = K_{f,load} \omega$, an inertial torque, $\Gamma_I = I_{load} \frac{d\omega}{dt}$, and an additional variable torque, Γ_{rest} , which contains all the other load contributions. The following load model

$$\Gamma_{Load} = K_{f,load} \omega + I_{load} \frac{d\omega}{dt} + \Gamma_{rest} \quad (6.17)$$

is inserted into (6.7), which becomes:

$$\begin{aligned} \frac{d\omega}{dt} = & -\frac{3K_m}{2I_{mot}} \left(i_\beta \cos(p\theta) - i_\alpha \sin(p\theta) \right) - \frac{K_{f,mot}}{I_{mot}} \omega \\ & + \frac{1}{I_{mot}} \left(K_{f,load} \omega + I_{load} \frac{d\omega}{dt} + \Gamma_{rest} \right) \end{aligned} \quad (6.18)$$

Rearranging this last equation, it is obtained:

$$\frac{d\omega}{dt} = -\frac{3K_m}{2I_{tot}} [i_\beta \cos(p\theta) - i_\alpha \sin(p\theta)] - \frac{K_{f,tot}}{I_{tot}} \omega - \frac{1}{I_{tot}} \Gamma_{rest} \quad (6.19)$$

with $I_{tot} = I_{mot} + I_{load}$ and $K_{f,tot} = K_{f,mot} + K_{f,load}$. The form of (6.19) corresponds exactly to (6.7), but now the parameters are the total drive inertia, I_{tot} , the total drive friction constant, $K_{f,tot}$, and the fifth state variable Γ_{rest} contains only the load that is related neither to an inertial load nor to a viscous friction. These two contributions to the total load are now included into the motor mechanical equation thanks to the

parameters $K_{f,tot}$ and I_{tot} . The motor model is therefore rewritten as follows:

$$\frac{di_\alpha}{dt} = \frac{1}{L} \left(-Ri_\alpha - K_m\omega \sin(p\theta) + u_\alpha \right) \quad (6.20)$$

$$\frac{di_\beta}{dt} = \frac{1}{L} \left(-Ri_\beta + K_m\omega \cos(p\theta) + u_\beta \right) \quad (6.21)$$

$$\frac{d\omega}{dt} = -\frac{3K_m}{2I_{tot}} \left(i_\beta \cos(p\theta) - i_\alpha \sin(p\theta) \right) - \frac{K_{f,tot}}{I_{tot}}\omega + \frac{1}{I_{tot}}\Gamma_{rest} \quad (6.22)$$

$$\frac{d\theta}{dt} = \omega \quad (6.23)$$

$$\frac{d\Gamma_{rest}}{dt} = 0 \quad (6.24)$$

If a high dynamic response is wanted with the Kalman filter speed and position estimation, (6.19) has to be used. More than that, it is necessary to know not only the motor mechanical parameters, but the ones of the entire drive.

6.3 Kalman filtering with parameters estimation

The idea introduced in this thesis is to estimate the motor parameters by a second Kalman filter that works in parallel with the first one that is used to estimate the motor state. The use of two Kalman filters for both state variables and parameters estimation was firstly proposed in [72] and has already been implemented in [73] in the field of parameter estimation of an autoregressive process from noisy observations, or in [74], in the field of vehicle control, for example. In [75] the use of Kalman filtering for parameter estimation is widely discussed.

The basic operation of the algorithm is drawn in Fig. 6.1, where $\Theta = (\Theta_1, \Theta_2, \dots, \Theta_m)^T$ is the parameter vector and Θ_n are the parameters of the model. The suffix t denotes the instant, in the discrete time, at which the vectors are considered and the hat indicates estimated values, like $\hat{\mathbf{x}}$ and $\hat{\Theta}$.

The Kalman filter for the state variables estimation (KF1) estimates $\hat{\mathbf{x}}_{t+1}$ by integration of $\hat{\mathbf{x}}_t$ based on the synchronous motor model, with parameters $\hat{\Theta}_t$, and thanks to the measurements on the real system \mathbf{y}_t . The second Kalman filter (KF2) works in parallel to KF1, and is dedicated to the parameter estimation. KF2 estimates the parameters $\hat{\Theta}_{t+1}$, based on their previous values and on the state estimations $\hat{\mathbf{x}}_t$ and $\hat{\mathbf{x}}_{t+1}$ obtained by KF1.

Thanks to the scheme in Fig. 6.2 it appears clear that KF2 takes advantage of the ability of KF1 to correct its state vector estimation from the *a priori*, $\hat{\mathbf{x}}_t(-)$, to the *a posteriori* estimation, $\hat{\mathbf{x}}_t(+)$, with the measurements \mathbf{y}_t . These corrections are ab-

6.3. Kalman filtering with parameters estimation

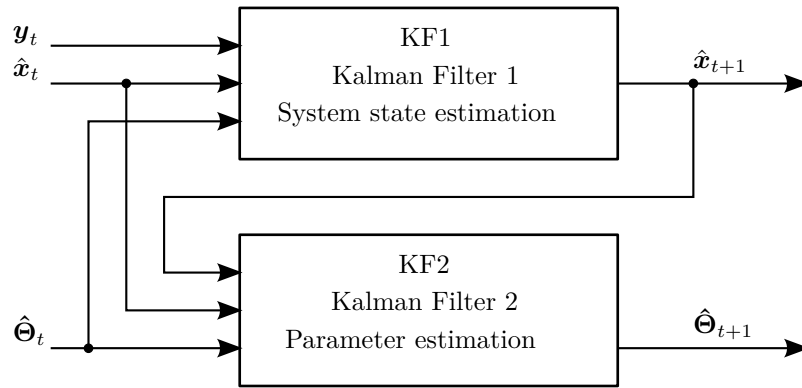


FIGURE 6.1 – The two interacting Kalman filters.

sorbed by KF2 into the new parameter estimation $\hat{\Theta}_{t+1}$ and therefore re-injected into the motor model itself.

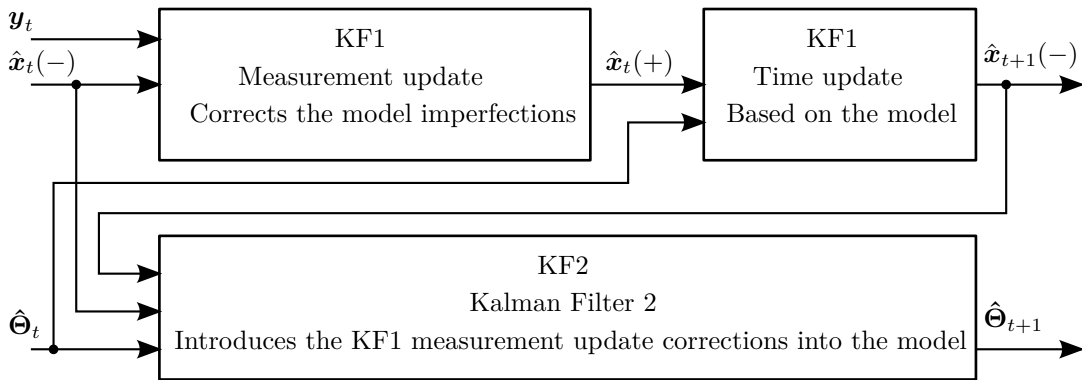


FIGURE 6.2 – Intuitive functioning scheme of the two interacting Kalman filters.

The functioning of this algorithm is intuitively explained in the example shown in Fig. 6.3. Starting from the estimation \hat{x}_{t0} , KF1 first calculates $\hat{x}_{t1}(-)$ using the time update (\longrightarrow) and then corrects this estimation to $\hat{x}_{t1}(+)$ with the measurement update ($- - \rightarrow$). In Fig. 6.3 the dotted arrow ($\cdots \rightarrow$) stands for the time update that has been corrected. The KF2 calculates the parameters $\hat{\Theta}_{t0}$ that characterize the dotted arrow and provides them to KF1. In this 2D example the parameters are reduced to the arrow slope only. As it can be noticed in Fig. 6.3, for the next time update step, KF1 uses this new parameter (the slope of the dotted arrow $\hat{x}_{t0} \cdots \rightarrow \hat{x}_{t1}(+)$), for calculating $\hat{x}_{t2}(-)$. Consequently the measurement update correction at $t = t_2$ is less important. The new parameters $\hat{\Theta}_{t1}$ are again calculated by KF2 and then given to KF1 for the next iteration.

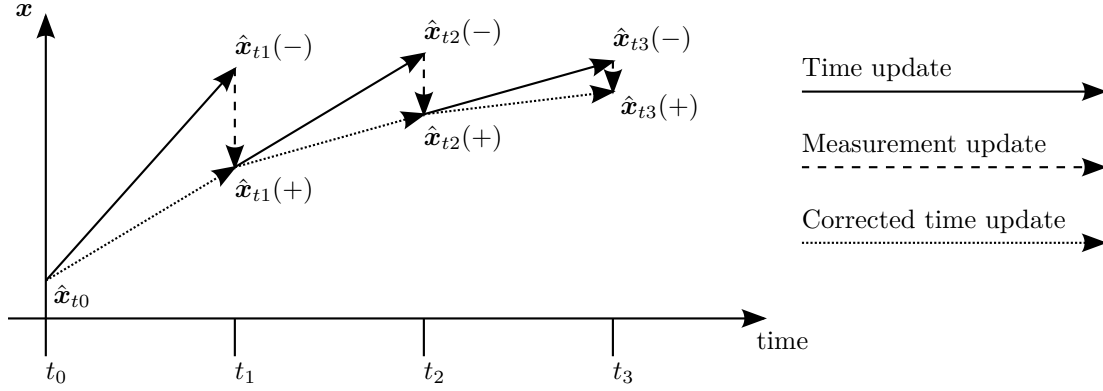


FIGURE 6.3 – Intuitive functioning of the parameter identification algorithm.

6.3.1 Implementation

The introduced technique is easy to implement. First of all, the measurement equation of KF2 is obtained by the rearrangement of the linearized discrete version of the state equation. An example for a 2-state variables model is:

$$\begin{aligned} \mathbf{x}_{t+1} &= \mathbf{x}_t + (\mathbf{A}\mathbf{x}_t + \mathbf{B}u_t) T_s \\ \begin{pmatrix} x_{1,t+1} \\ x_{2,t+1} \end{pmatrix} &= \begin{pmatrix} x_{1,t} \\ x_{2,t} \end{pmatrix} + \begin{pmatrix} a_1 & a_2 \\ a_3 & a_4 \end{pmatrix} \begin{pmatrix} x_{1,t} \\ x_{2,t} \end{pmatrix} T_s + \begin{pmatrix} b_1 \\ b_2 \end{pmatrix} \begin{pmatrix} u_{1,t} \\ u_{2,t} \end{pmatrix} T_s \end{aligned} \quad (6.25)$$

Let (6.25) be a general linear discrete state equation where T_s is the sampling period, in which the parameter matrix \mathbf{A} is to be determined. All other terms of (6.25) are known. Equation (6.25) is now rewritten with the purpose of isolating the parameter vector $\Theta = (a_1, a_2, a_3, a_4)^T$ and becomes:

$$\begin{cases} x_{1,t+1} - x_{1,t} - b_1 u_{1,t} T_s = a_1 x_{1,t} T_s + a_2 x_{2,t} T_s \\ x_{2,t+1} - x_{2,t} - b_2 u_{2,t} T_s = a_3 x_{1,t} T_s + a_4 x_{2,t} T_s \end{cases} \quad (6.26)$$

$$\begin{cases} x_{1,t+1} - x_{1,t} - b_1 u_{1,t} T_s = \begin{pmatrix} x_{1,t} T_s & x_{2,t} T_s \end{pmatrix} \begin{pmatrix} a_1 \\ a_2 \end{pmatrix} \\ x_{2,t+1} - x_{2,t} - b_2 u_{2,t} T_s = \begin{pmatrix} x_{1,t} T_s & x_{2,t} T_s \end{pmatrix} \begin{pmatrix} a_3 \\ a_4 \end{pmatrix} \end{cases} \quad (6.27)$$

$$\underbrace{\begin{pmatrix} x_{1,t+1} - x_{1,t} - b_1 u_{1,t} T_s \\ x_{2,t+1} - x_{2,t} - b_2 u_{2,t} T_s \end{pmatrix}}_{\mathbf{y}_\Theta} = \underbrace{\begin{pmatrix} x_{1,t} T_s & x_{2,t} T_s & 0 & 0 \\ 0 & 0 & x_{1,t} T_s & x_{2,t} T_s \end{pmatrix}}_{\mathbf{C}_\Theta} \underbrace{\begin{pmatrix} a_1 \\ a_2 \\ a_3 \\ a_4 \end{pmatrix}}_{\Theta} \quad (6.28)$$

6.3. Kalman filtering with parameters estimation

This manipulation is simple and always possible as no matrix inversion is needed. Finally, the state and the measurement equations for KF2 are:

$$\begin{cases} \dot{\Theta} = 0 & (6.29) \\ \mathbf{y}_{\Theta} = \mathbf{C}_{\Theta} \Theta & (6.30) \end{cases}$$

Two options for estimating the motor parameters are investigated: in the first one, all parameters are estimated at the same time, creating a 5-state variables Kalman filter. This option is however burden for the on-line realization. Another option is more interesting: the parameters are estimated one by one, with 5 single variable filters. Results are as good as with the first option, but less time consuming 2x2 matrix operations are needed for the electrical parameter estimation, and no matrix operation is needed for the mechanical parameters estimation.

Based on the functioning principle, some conclusions can be drawn:

1. KF1 does not need to be modified for the implementation of the parameter estimation
2. Results from KF2 can be used by KF1 or not, as wished.
3. In opposition to KF1, in KF2 there are no state equations for the estimation of $\hat{\Theta}_{t+1}$. The parameter estimation is based only on the measurement update.
4. The KF2 accuracy depends on that of KF1 and therefore, if KF1 does not work properly, KF2 will neither.

6.3.2 Parameters observability

Electrical parameters

Using the theory from [54, 76, 77], the observability of the electrical parameters can be analyzed. The analysis shows that it is possible to estimate the three electrical parameters R , L , K_m at the same time only during dynamic transients. In case of steady-state operation with a constant speed $\omega = \omega_0$, only two parameters are identifiable, and this only in the case if the third one is accurately known.

Simulations show that at steady-state the three electrical parameters converge quickly towards an incorrect solution. The three parameter estimations that are found correspond to a local solution of (6.20) and (6.21) at the given $\omega = \omega_0$. Another value of ω_0 leads to another parameters estimation that will once again only locally satisfy the system of equations.

Moreover, it has been noticed that the parameter estimation found at steady-state is not stable in time and may diverge after a while.

Mechanical parameters

It is easy to understand that at steady-state it is not possible to find the total inertia, I_{tot} , because in (6.22) $\frac{d\omega}{dt} = 0$ and therefore I_{tot} is non-influential.

On the other hand, the total friction constant $K_{f,tot}$ can be estimated at steady-state. But if the other terms involved in (6.22), like K_m , have not converged to the correct value, the $K_{f,tot}$ value is wrong too.

All these drawbacks are confirmed in the simulations and with the experimental setup. Because of them, the algorithm is activated only during speed transients and the last estimated values are kept constant during the steady-state operations.

6.3.3 Simulation results

An example of the algorithm results is shown in Figs. 6.4 - 6.9. Start parameter errors are R : -10% , L : $+10\%$ and K_m : -10% . Inertia and friction constants are initialized to the motor-only datasheet values. Total drive values are: $I_{tot} = 2I_{mot}$ and $K_{f,tot} = 4K_{f,mot}$. The motor is driven in a sewing machine mode, imposing a speed of $\pm 1'000$ rpm every 90° mechanical degrees, as shown in Fig. 6.4. The initial position is $\hat{\theta}_0 = \theta_0 = 0^\circ$ and the initial speed is $\hat{\omega}_0 = \omega_0 = 0$ rpm.

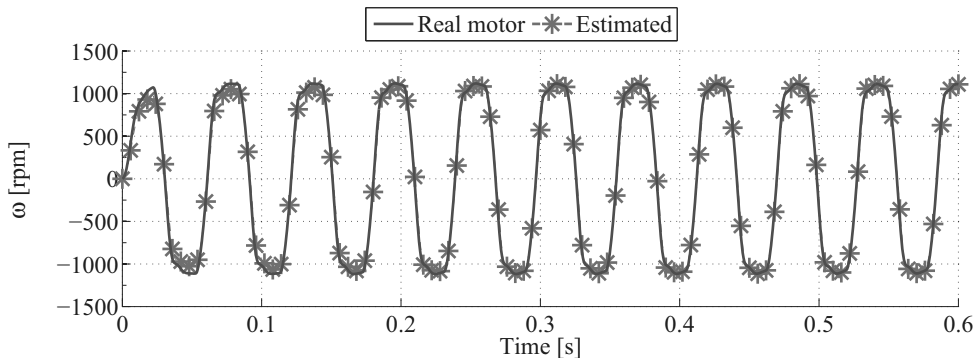


FIGURE 6.4 – KF1 speed estimation. Sewing machine mode. First 0.6 s.

Motor electrical parameters

The convergence of the motor electrical parameters estimation can be observed in Figs. 6.5 and 6.6.

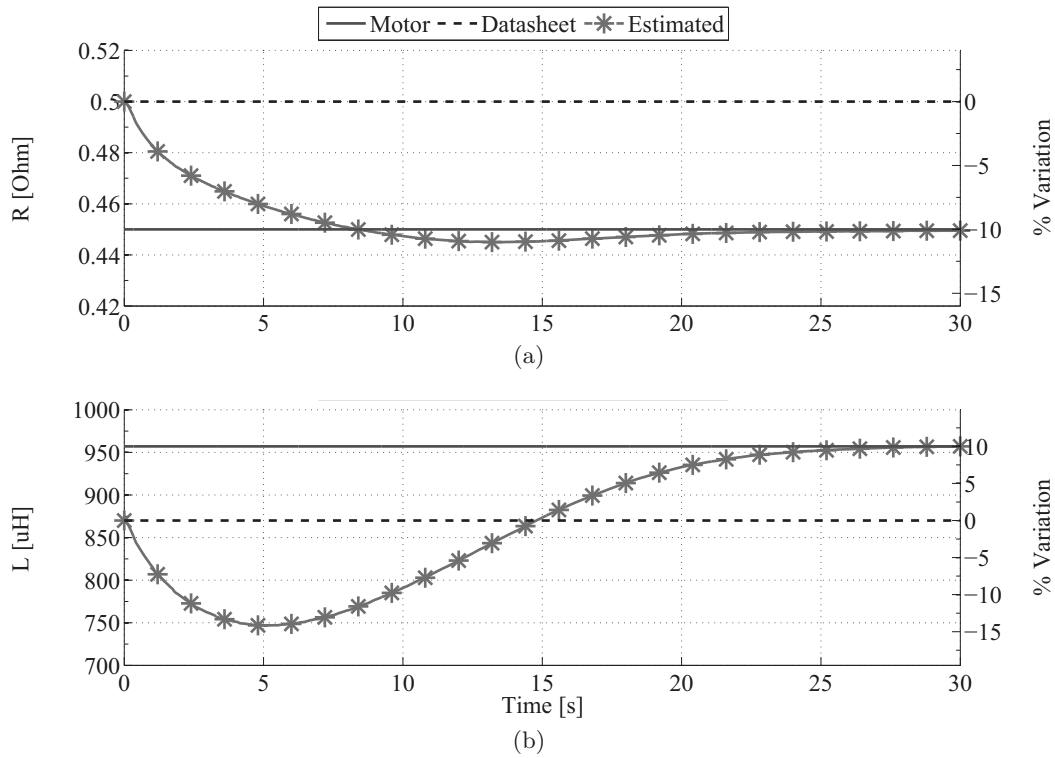


FIGURE 6.5 – KF2 phase resistance R (a) and inductance L (b) estimation. Sewing machine mode.

It can be noticed that the algorithm needs some time before to converge. In fact, at the beginning, the estimation of the inductance \hat{L} starts in the wrong direction. This is because of the wrong values of \hat{R} and \hat{K}_m that are used by the algorithm for measuring \hat{L} . On the other hand, it is interesting to point out how during the first 0.6 s, zoom in Fig. 6.6a, \hat{K}_m moves very quickly towards the motor value. But principally because the \hat{L} estimation starts first in the wrong direction, \hat{K}_m converges only when the estimations of \hat{L} and \hat{R} tend towards the real values. Finally, in this example, after 30 s the three electrical parameter estimations have correctly converged to the real values.

Mechanical parameters

The estimations of the mechanical drive parameters are shown in Fig. 6.7. In both cases, the zoom of the first 0.6 s only is shown because the convergence is very quick. This is possible because the Kalman weighting matrices are tuned for improving the convergence

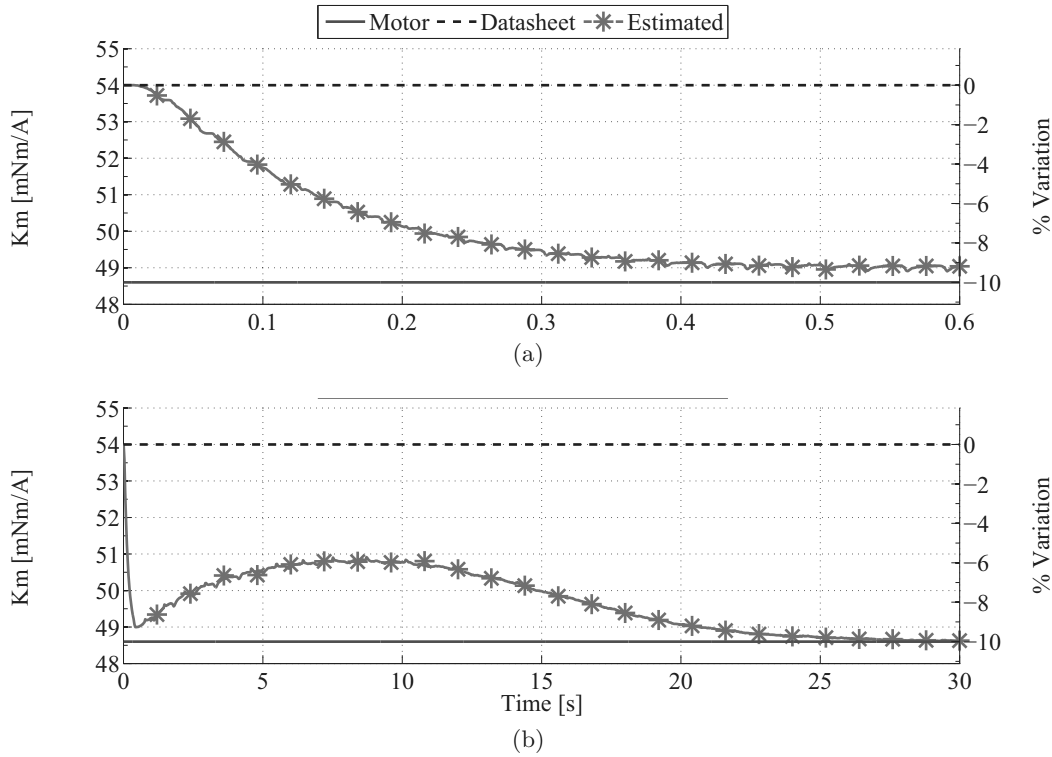


FIGURE 6.6 – KF2 torque constant K_m estimation. Sewing machine mode. First 0.6 s (a) and whole simulation (b).

rate. In fact, the results of these estimations are less critical because the equality between the LHS and RHS of (6.22) is achieved by the additional term Γ_{rest} . For this reason the convergence rate can increase without necessarily affecting the filter stability. This cannot be done with the electrical parameter estimations, as the electrical equations (6.20) and (6.21) become too “nervous” with high convergence rates and consequently degrade the KF1 currents estimation.

State variables

Finally, Figs. 6.8 and 6.9 show, as expected, that the KF1 speed and position estimation errors significantly decrease. The sensorless position detection is highly improved. In order to increase the readability of the simulation results, in both figures, the zooms of the first and the last 0.6 s are shown in the (a), respectively (c). The speed estimation error is shown in Fig. 6.8. The estimation error during the dynamic phase, when the speed reference changes from 1'000 to -1'000 rpm and vice versa, decreases from the initial ~ 200 rpm to a few rpm only. The electrical position estimation error is shown in Fig. 6.9. The position estimation error starts at $\sim 10^\circ$ electrical degrees, and after a transition, it vanishes as soon as the electrical parameter estimations converge to the real values.

6.3. Kalman filtering with parameters estimation

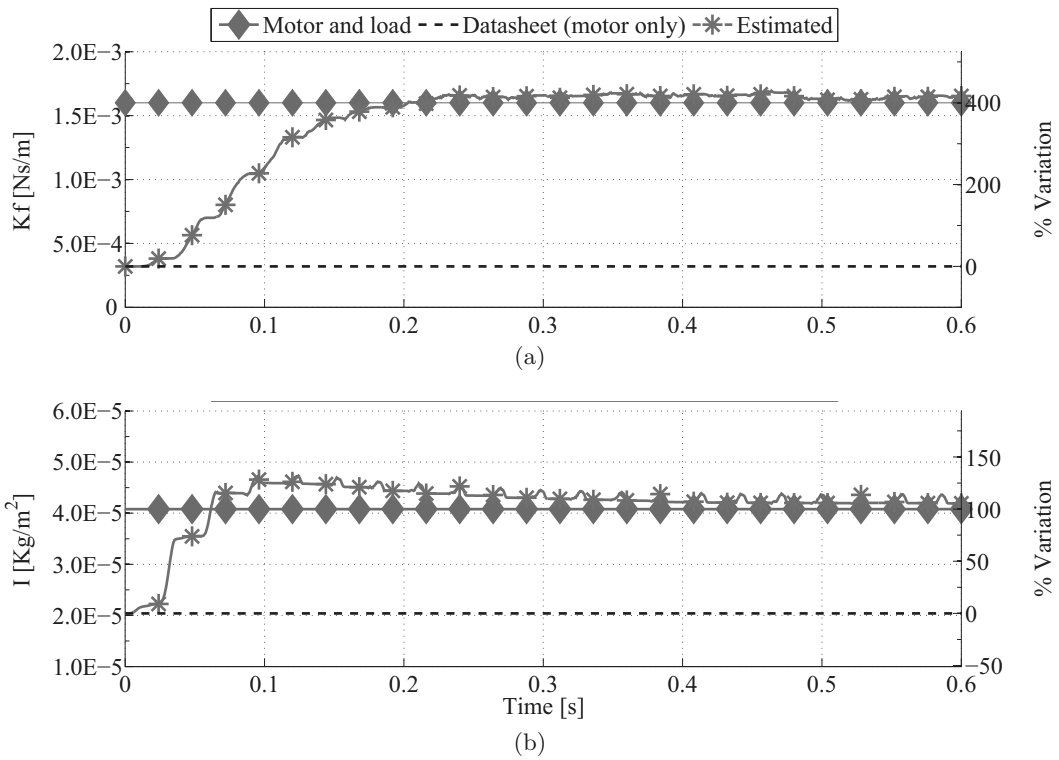


FIGURE 6.7 – KF2 friction constant $K_{f,tot}$ (a) and total inertia I_{tot} (b) estimation. Sewing machine mode. First 0.6 s.

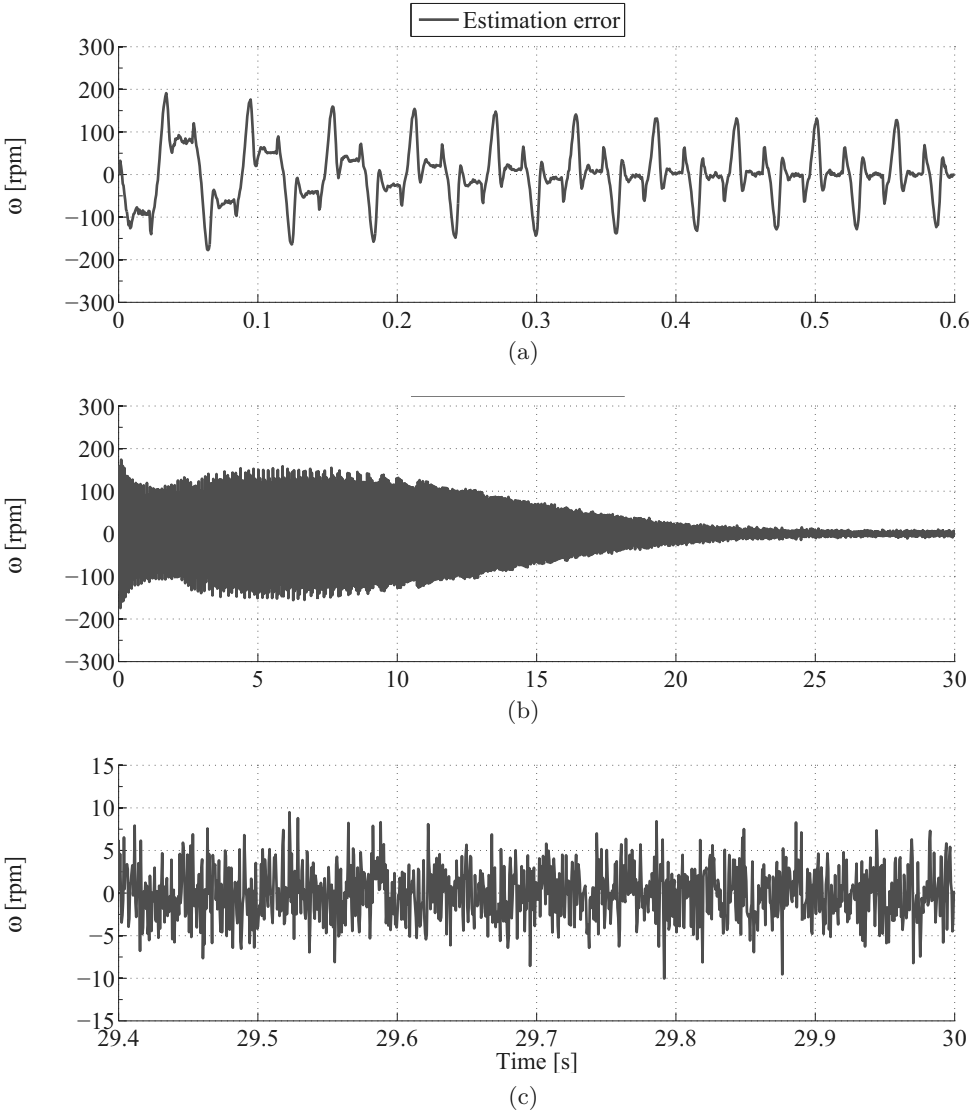


FIGURE 6.8 – KF1 speed estimation error. Sewing machine mode. First 0.6 s (a), whole simulation (b) and last 0.6 s (c).

6.3. Kalman filtering with parameters estimation

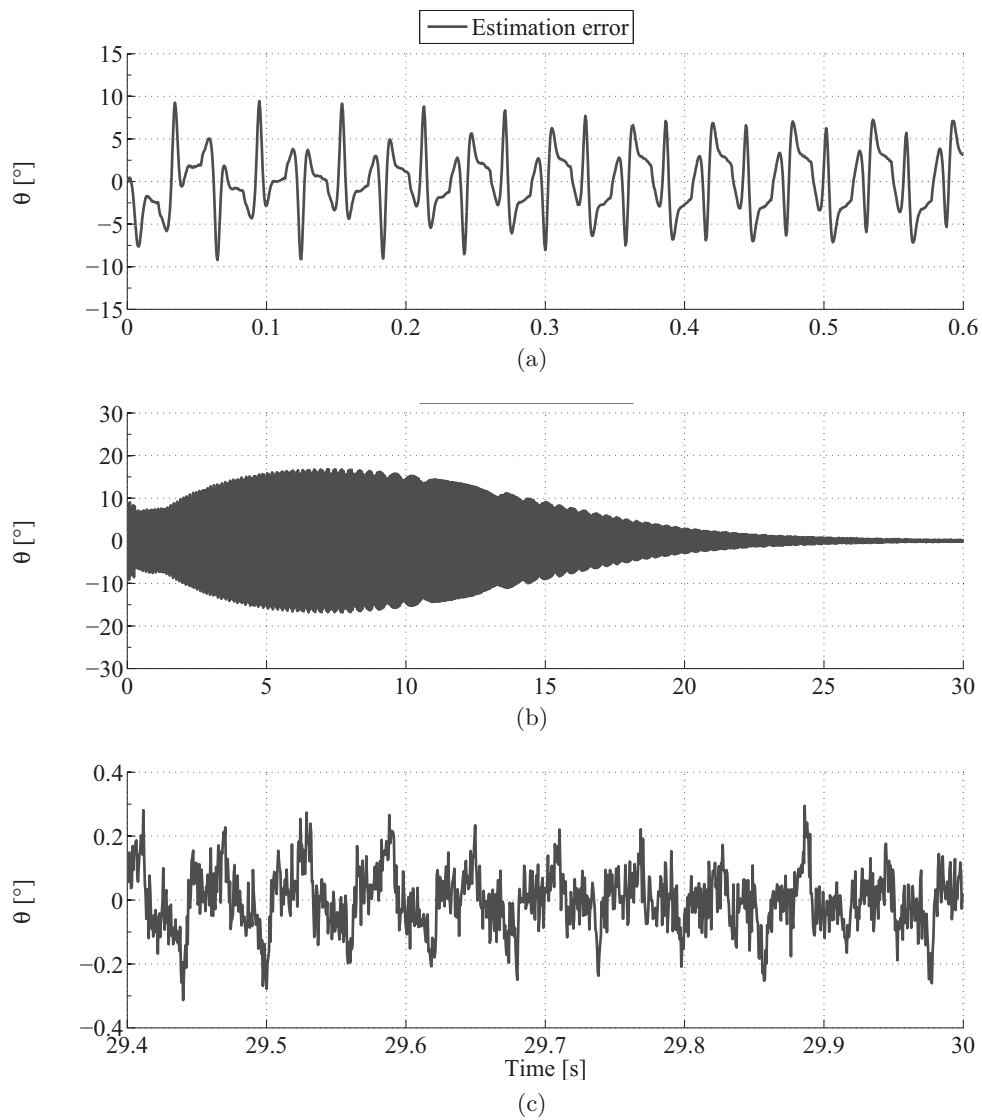


FIGURE 6.9 – KF1 position estimation error. Sewing machine mode. First 0.6 s (a), whole simulation (b) and last 0.6 s (c).

6.3.4 Experimental setup

In order to confirm the validity of the simulation results, the technique is applied on a 5 pole pairs BLDC motor used in automotive industry, coupled with its reduction stage. For debug and illustration purpose, an optical encoder is added on the back of the drive. The DSP used is a TMS320F28335, 150 MHz clock, from Texas Instruments. The drive and the developed electronics are shown in Appendix A.2.

The drive datasheet values are listed in Table 6.3. Note that the mechanical parameter values are given for the motor only. Friction constant is evaluated on the motor bearings datasheet and the inertia is that of the rotor only. Friction constant and inertia of the reduction stage are unknown. For all the shown results, the drive model parameters at start-up are the datasheet ones, if not otherwise indicated.

TABLE 6.3
Experimental setup model datasheet values.

R	Phase resistance	0.22 Ω
L	Phase inductance	770 μH
K_m	Torque constant	29.7 mNm/A
$K_{f,mot}$	Friction constant	$32 \cdot 10^{-5}$ Nm/rad/s
I_{mot}	Rotor inertia	$5.74 \cdot 10^{-6}$ kg/m ²
p	Pole pairs	5

The results shown in the next subsections are obtained during the transient when the speed reference changes suddenly from +2'400 rpm to -2'400 rpm. The position estimations obtained with different configurations of the Kalman filter are compared with the position measured with the optical encoder. The measurement covariance matrix R_n of the Kalman filter used in all the trials is set to:

$$R_n = \begin{pmatrix} 1 & 0 \\ 0 & 1 \end{pmatrix} \quad (6.31)$$

The speed direction change is executed at time $t = 0$ ms and is indicated on the following figures with a vertical black line.

6.3.5 Experimental results without parameter estimation

Results with hypothesis $I = \infty$

The parameters estimation algorithm is first applied on the Kalman filter implemented with the hypothesis $I = \infty$, introduced in Subsection 6.2.1. It is a classical implementation of the Kalman filter: there is no parameter estimation, KF2 is not activated at any time. The system covariance matrix used for this trial is:

$$Q_n = \begin{pmatrix} 0.1 & 0 & 0 & 0 \\ 0 & 0.1 & 0 & 0 \\ 0 & 0 & 10 & 0 \\ 0 & 0 & 0 & 10^{-6} \end{pmatrix} \quad (6.32)$$

where $Q_n(3,3)$ is voluntary relatively high in order to let the speed vary freely.

As it can be appreciated in Fig. 6.10, the classical implementation of the Kalman filter gives very good results for the position estimation during steady-state operations, even just using poor quality datasheet values. This conclusion is also valid for the other state variables not shown here.

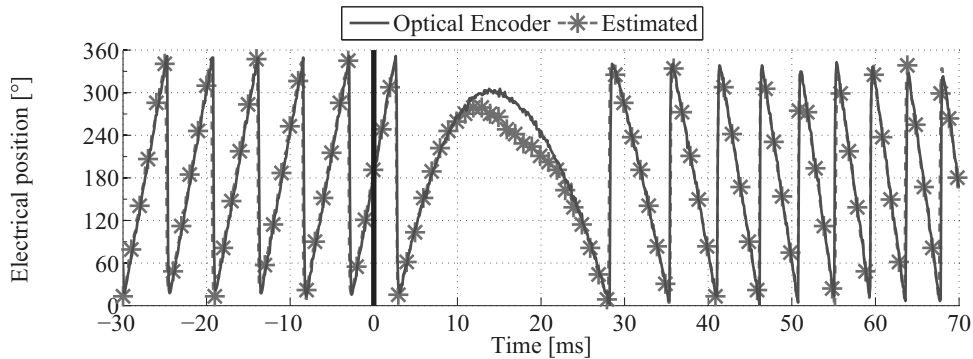


FIGURE 6.10 – Position estimation with hypothesis $I = \infty$.

On the other hand, during the transient, a small position estimation error appears, but the performance of the filter is acceptable. This result is nevertheless highly dependent on the system covariance matrix, and on the accuracy of the model electrical parameters. Small variations on the latter lead to unpredictable results.

In Fig. 6.11, three more trials are shown. The first trial, (a), shows the result of the position estimation during the speed reference change if the datasheet value of R is decreased by 5%. For the second trial, (b), the inductance L is this time decreased by 5%. Finally, the third trial, (c), the datasheet value of K_m is increased by 5%. Again, the position estimation during steady-state is very good, but compared to Fig. 6.10, in these last three trials the position estimation error during the speed transient starts to be important.

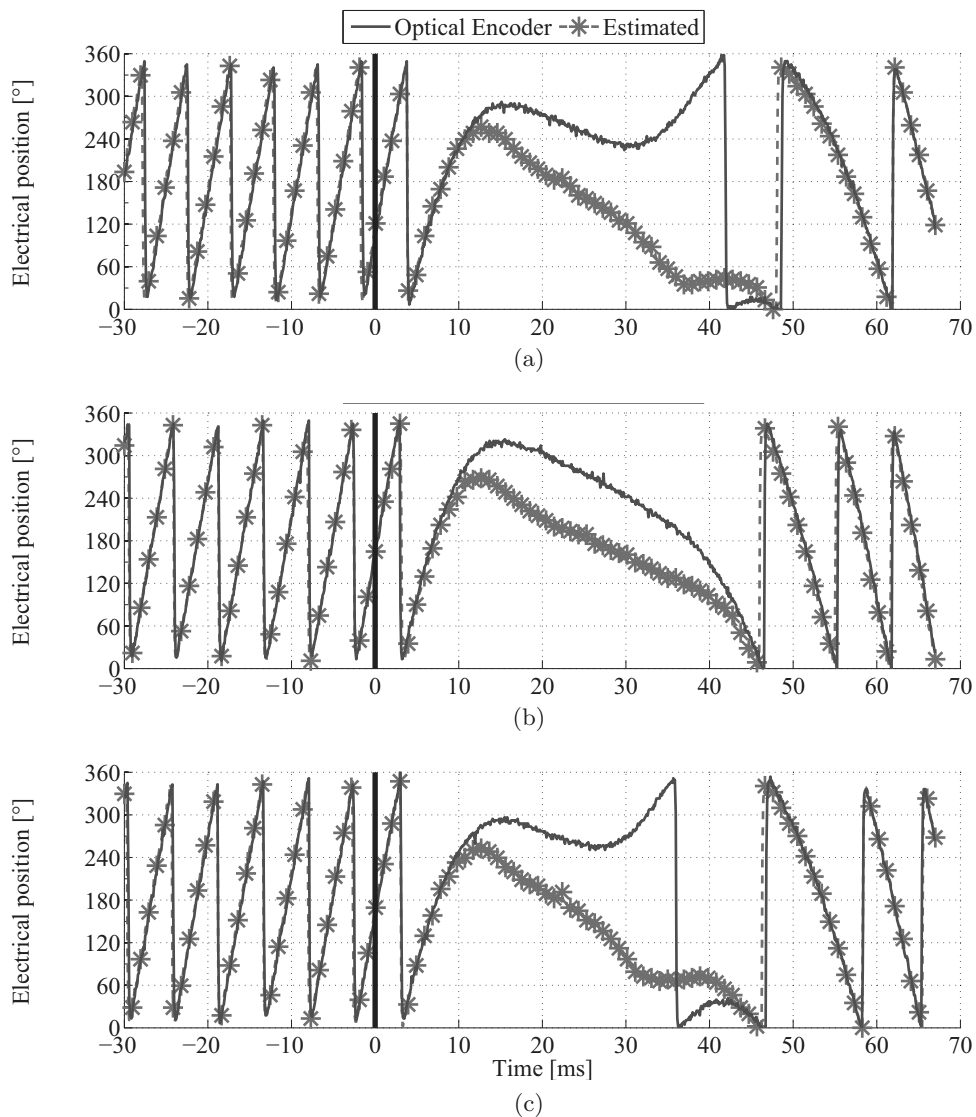


FIGURE 6.11 – Position estimation with hypothesis $I = \infty$.
 (a): R decreased by 5%,
 (b): L decreased by 5%,
 (c): K_m increased by 5%.

Finally, it can be concluded that this implementation of the Kalman filter is definitively very sensitive to the datasheet parameter value accuracy.

Results with mechanical equation

The step further is now to remove the simplification $I = \infty$ and consequently to insert the mechanical equation (6.7) into the motor model. Once again, there is no parameter

6.3. Kalman filtering with parameters estimation

estimation, KF2 is still switched off. The system covariance matrix used for this trial is:

$$Q_n = \begin{pmatrix} 0.1 & 0 & 0 & 0 & 0 \\ 0 & 0.1 & 0 & 0 & 0 \\ 0 & 0 & 10^{-7} & 0 & 0 \\ 0 & 0 & 0 & 10^{-6} & 0 \\ 0 & 0 & 0 & 0 & 1 \end{pmatrix} \quad (6.33)$$

In Fig. 6.12 it can be observed that, as for the previous trials, the position estimation is good during the steady-state operations. But here, the position estimation error during the speed transient is evident and unacceptable. Nearly 35 ms are spent before the Kalman filter is able to find the correct position estimation of the rotor again.

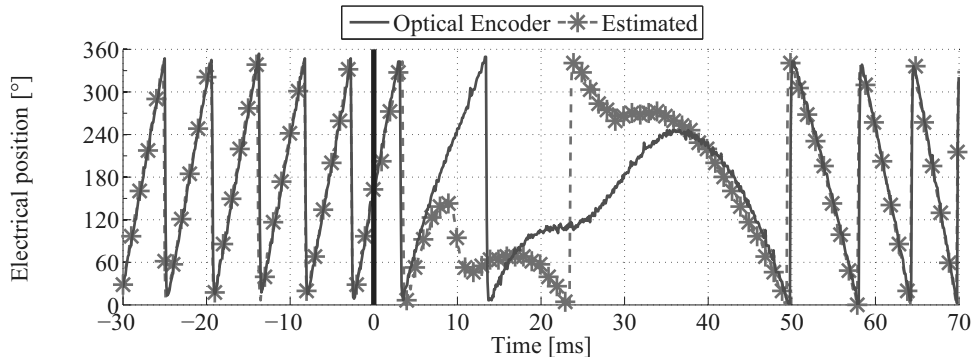


FIGURE 6.12 – Position estimation with mechanical equation, but no parameter estimation.

Without a good knowledge of the drive parameters, there is no improving of the position estimation during transients. In comparison with the trials shown in Figs. 6.10 and 6.11 the results are even less accurate. The only advantage is that the Kalman filter is less sensible on the accuracy of the model parameters and on the matrix Q_n (6.33).

6.3.6 Experimental results with parameter estimation

Results with hypothesis $I = \infty$

The introduced technique is now applied to the Kalman filter implemented with the hypothesis $I = \infty$. Q_n is kept the same as in (6.32). As (6.7) is simplified to $\frac{d\omega}{dt} = 0$, only the estimations of the three electrical parameters are needed. In Table 6.4 the evolution of the estimated values is shown. The evolution is represented in % compared to the respective datasheet values.

TABLE 6.4
Electrical parameters estimated values.

	Variation compared to the datasheet values		
	after start-up	after 1 st speed change	after 2 nd or more
R	+4%	+11%	+21%
L	+26%	+30%	+30%
K_m	-6%	-15%	-12%

In Table 6.4, it can be seen that already during the start-up, all three electrical parameters move considerably and that after a first transient, the parameters are practically estimated. The estimated parameters are significantly different from the datasheet values: the estimated resistance \hat{R} is up to 20% higher than the datasheet value. The estimated inductance is even more higher, the correction reaches +30%. Finally, the estimated torque constant is about 12% lower than the datasheet value.

In Fig. 6.13 on the left hand side, the measurements of K_m (\times) and the evolution of the estimation (—) during the first 14 ms after start-up are plotted. On the right hand side the distribution of these measurements is shown. Measurements are normalized to the datasheet value and the y-axis is logarithmic. From Fig. 6.13 it can be appreciated how the algorithm is able to use a really noisy information for estimating the parameter K_m .

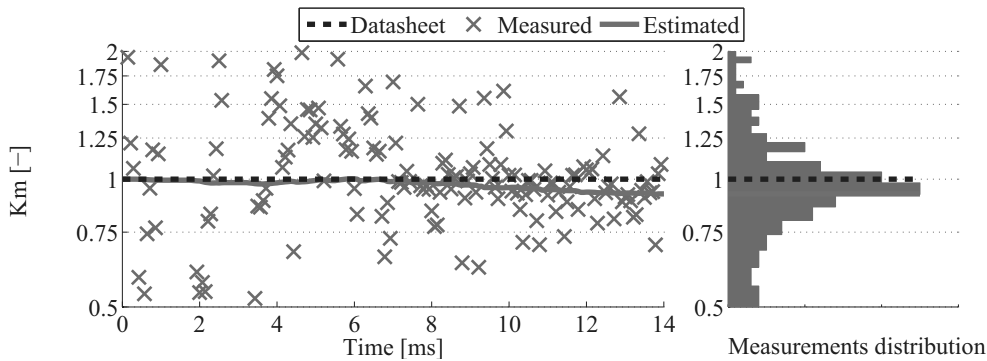


FIGURE 6.13 – K_m estimation.

In Fig. 6.14 the first transient after start-up is plotted. The position estimation is not perfect, but the quality may be acceptable, depending on the performances needed by the final application. As stated in the previous section, the implementation of the Kalman filter with the hypothesis $I = \infty$ highly depends on the accuracy of the model parameters. But, thanks to the introduced technique, immediately after start-up the electrical parameters are already roughly estimated and the position estimation is effective.

6.3. Kalman filtering with parameters estimation

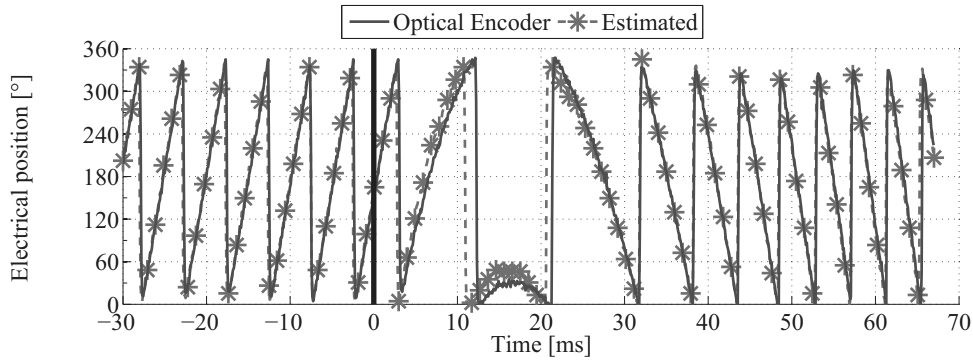


FIGURE 6.14 – Position estimation with hypothesis $I = \infty$ and parameter estimation.

Results with mechanical equation and load modelling

As the last trial, the introduced technique, using the mechanical equation with load modelling (6.19) and the model parameters estimation is finally implemented. The system covariance matrix used for this trial is:

$$Q_n = \begin{pmatrix} 0.1 & 0 & 0 & 0 & 0 \\ 0 & 0.1 & 0 & 0 & 0 \\ 0 & 0 & 10^{-7} & 0 & 0 \\ 0 & 0 & 0 & 10^{-6} & 0 \\ 0 & 0 & 0 & 0 & 10^{-6} \end{pmatrix} \quad (6.34)$$

The first fact to point out is that the electrical parameter estimations are the same as in the previous subsection, shown in Table 6.4. The addition of the mechanical equation obviously does not influence the electrical parameters estimation. The estimated model mechanical parameter values are given in Table 6.5.

TABLE 6.5
Mechanical parameters estimated values.

	Variation compared to the datasheet values		
	after start-up	after 1 st speed change	after 2 nd or more
$K_{f,tot}$	+1%	+5%	+6%
I_{tot}	+19%	+125%	+120%

An important difference between the electrical and mechanical parameter estimation is highlighted in Table 6.5. In contrast to Table 6.4, the mechanical parameters need at least two speed transients for converging to the motor real values. This is easily explained. During the first speed transient, the start-up, the electrical parameters estimations are in evolution and are far away from they converged value. It appears

obvious, that if the electrical parameters estimations have not reached the real motor values, the algorithm can not correctly estimate the external load with precision. On the other hand, at the beginning of the following transient, the first speed change in the shown trial, the electrical parameters are already close to their real motor values. As a consequence, KF2 can finally correctly estimate the external load.

As an example, in Fig. 6.15 the evolution of I_{tot} estimation is plotted. Start-up and speed direction changes are highlighted with vertical black lines. It can be appreciated how, after the start-up, only a small correction is brought by KF2 to the I_{tot} estimation. On the other hand, during the second transient, the first speed change, the total inertia estimation has a huge variation and finally converges.

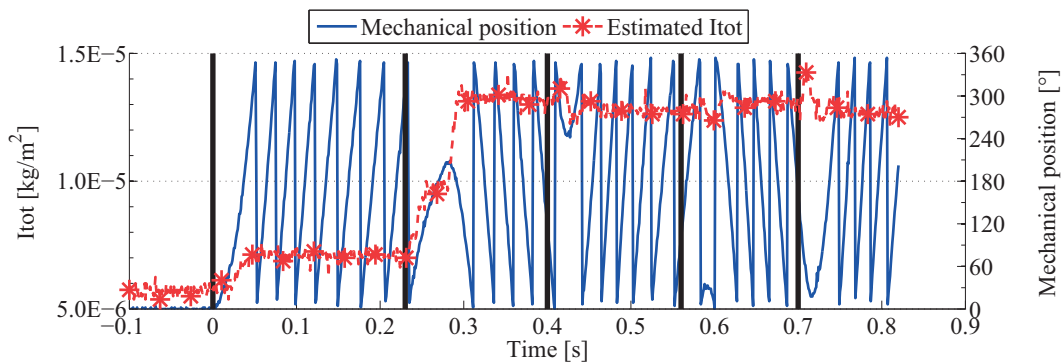


FIGURE 6.15 – I_{tot} estimation.

After two transients, the start-up and a first direction change, the position estimation obtained is plotted in Fig. 6.16. The Kalman filter has no more difficulties in following the abrupt speed change and the accuracy of the position and speed estimation has increased compared to Fig. 6.14. A visible consequence of the better position estimation is the shorter time needed for the speed inversion. In Fig. 6.14, the speed inversion occurs after 17 ms and 114° mechanical degrees. In the same conditions, thanks to the load modelling and estimation the speed inversion occurs after only 14 ms and 97° mechanical degrees.

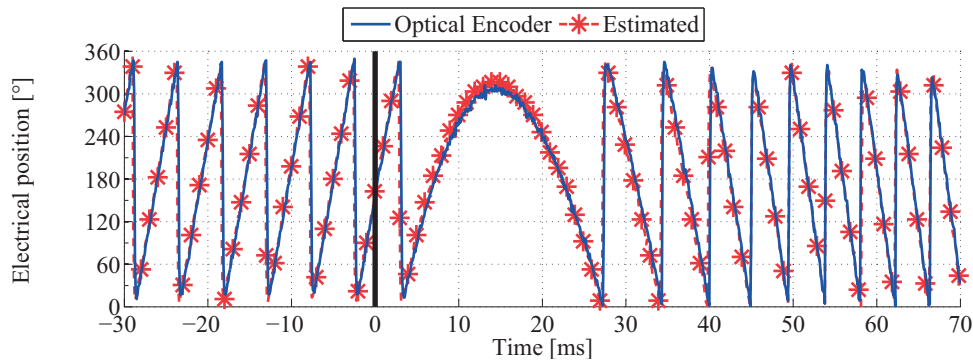


FIGURE 6.16 – Position estimation with load modelling and parameter estimation.

6.3.7 Parameters estimation proof

Thanks to the performed parameter estimations, in the previous subsections it is shown that the accuracy of the KF1 estimations is increased. Even if the result is already very satisfying, the goal now is to prove that the estimated parameters correspond to the real motor values.

Unfortunately, concerning the phase resistance R and inductance L , it is not possible to compare the estimated values with some measurements, because of their dependence on various factors, as the temperature, the measurement frequency, the measurement technique and so on. On the other hand, the torque constant K_m is uniquely defined and thus analyzed hereafter.

Concerning the mechanical parameters, they are usually hard to measure. An alternative solution for proving the pertinence of the algorithm results is to estimate with KF2 a value which is well known in advance. This can be easily done for the total inertia I_{tot} estimation, with the use of a set of discs with calibrated inertia.

Torque constant K_m

The torque constant is easy to measure off-line with a scope picture of the back-EMF of the motor, like the one plotted in Fig. 6.17. The amplitude of the back-EMF is $u_i = 5$ V at $\omega_0 = 3'476$ rpm. The back-EMF constant K_e is calculated as follows:

$$K_e = \frac{u_i}{\omega_0} = \frac{5 \text{ V}}{364 \text{ rad/s}} = 13.82 \frac{\text{mV}}{\text{rad/s}} \quad (6.35)$$

From [4, 69], the torque constant is defined as:

$$K_m = \frac{3}{2} K_e = 20.73 \frac{\text{mNm}}{\text{A}} \quad (6.36)$$

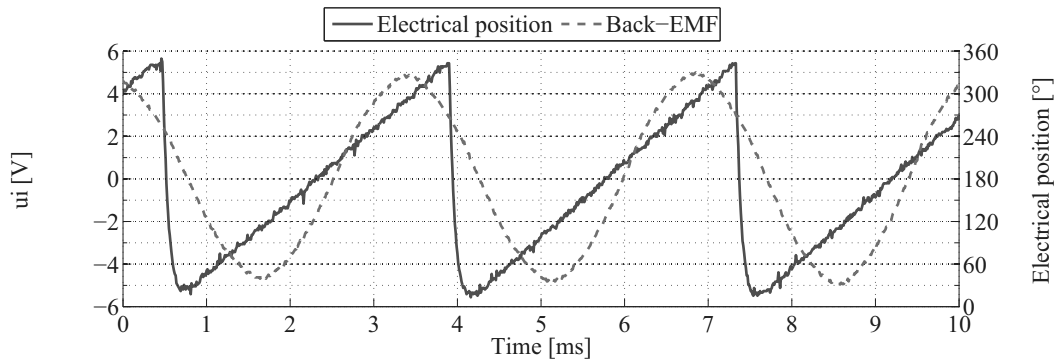


FIGURE 6.17 – Motor back-EMF for K_m measurement.

Chapter 6. Enhanced Kalman filtering

The measured $K_m = 20.73$ mNm/A is far away from the datasheet value 29.7 mNm/A. After two transients, KF2 estimates $\hat{K}_m = 22.2$ mNm/A which confirms the pertinence of the estimation.

Total inertia I_{tot}

The standard motor used in the previous chapters is driven in sewing machine mode, $\omega_0 = \pm 1'500$ rpm, and all its parameters are estimated. The first trial is done with the rotor only, and the estimated value of the rotor inertia only is $\hat{I}_{mot} = 22.2 \cdot 10^{-6}$ Kgm², which is near the datasheet value $I_{mot} = 20.4 \cdot 10^{-6}$ Kgm². Then, the different discs are in turn directly coupled to the output axis and for every trial the total inertia \hat{I}_{tot} is estimated and memorized. A picture of the calibrated inertia coupled to the used motor is shown in Fig. 6.18.

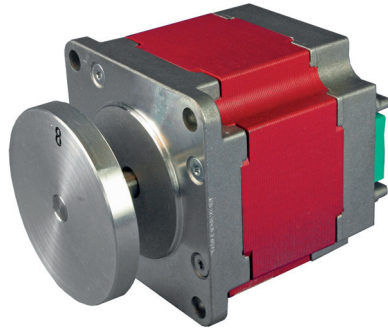


FIGURE 6.18 – Standard motor and coupled calibrated inertia.

By subtracting the rotor-only inertia \hat{I}_{mot} from the total inertia \hat{I}_{tot} estimated at every trial, the estimated inertia of the discs only is calculated. In Fig. 6.19 the estimated inertia of the different discs are compared to their calibrated value. It can be appreciated that the estimation is perfect for the small inertias. Starting from disc N° 4, $I = 4 \cdot 10^{-6}$ Kgm², the estimation is slightly degraded but still pertinent.

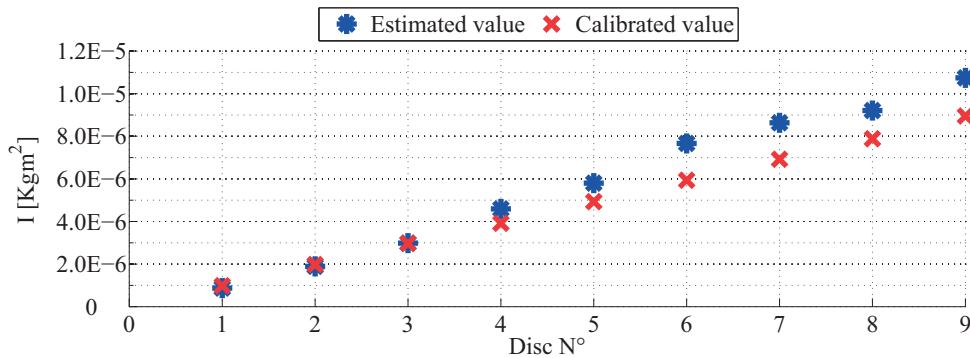


FIGURE 6.19 – Comparison between estimated and calibrated inertias.

6.3.8 Practical considerations on the parameter estimation algorithm

Convergence range

The drive is extremely robust against poor quality model parameters. Variations of about $\pm 30\%$ on each initial model electrical parameter are not a problem.

For the mechanical parameters, as they are normally not known in advance, it is possible to proceed as follows. The initial friction coefficient K_f can always be initially set to 0 Nm/rad/s if no better value is known. On the other hand, the initial inertia I_{tot} may be fixed, for example, to 80% of the motor value. Its real value, obviously, can only be higher.

It is here important to point out that the stability of the overall system, which is composed by KF1, KF2 and the speed control implemented in the drive electronics, depends on every one of these components. In the introduced results, the parameters of the speed control are kept constant during all the trials and the covariance matrices of KF1 and KF2 are chosen by hand tuning. The mathematical demonstration of the stability of an overall system like the one introduced is too complicated and is not treated here. The tools for this analysis are given in [78, 79].

Convergence speed

The convergence speed is highly dependent on the covariance matrices Q_n and R_n of every parameter estimation Kalman filter. For the electrical parameters, despite the incorrect results obtained in the simulations, where a high gain lead to instabilities, in the shown trials the values of Q_n are high at start-up and slightly lowered afterwards without affecting the entire system stability. On the other hand, Q_n of the two mechanical parameters estimation filters are elevated and kept constant during the trial.

Computation time

In the shown experimental results, all parameters are estimated one by one, with 3 or 5 single-variable Kalman filters. Moreover, for development reasons related to the reduction of the computation time, the electrical parameters are estimated with one equation only, (6.5) or (6.6) and not both as done in the simulations. In this configuration, no matrix operations are needed for the parameters estimation and thus the computation time is kept down to about 6.3 μs for the electrical parameters. Additional 4.2 μs are needed for the two mechanical parameters estimation. This time can be reduced by a better low-level software coding, which is actually not optimized. The computation

time needed for the 4-state variables Kalman filter with simplification $I = \infty$ used for the motor position and speed estimation is $24.6 \mu\text{s}$. The computation time needed for the 5-state variables Kalman filter used for the motor position and speed estimation is $38.1 \mu\text{s}$. That same computation time is needed if the parameter estimation is done with a 5-state variables Kalman filter too. The choice of a 5 single-variable Kalman filters implementation appears therefore clearly more judicious. With these computation times, the frequency of the Kalman filter update has been fixed to $f = 15 \text{ kHz}$.

Steady-state

As written in Subsection 6.3.2, the full parameters estimation at steady-state is not possible. Experimental trials confirm that parameter estimation at steady-state leads to divergence. For this reason, it is suggested to estimate the parameters only during speed transients. It is important however to point out that the Kalman filter performs the position estimation at $\omega = \omega_0$ without difficulty even in case of inaccurate electrical parameter values.

6.3.9 Comments

The introduced algorithm shows very promising results for the synchronous motor parameter estimation even with poor accuracy of the initial values of the electrical parameters. The first major challenge is therefore attained: the Kalman filtering based drive is able to tune its own parameters and thus avoid any off-line calibration.

The experimental results confirm the effectiveness of the technique either using the hypothesis $I = \infty$ or not. The best results are however obtained with the mechanical equation and the load modelling. Moreover, it is shown that due to the accurate parameter estimation and the load modelling, the accuracy of KF1 state estimation increases.

Thanks to these results, it is now possible to develop a new sensorless drive based on a Kalman filter that uses the U_{out} signal for the low speed operations.

6.4 Kalman filtering with U_{out} measurement

6.4.1 State-space model observability theory

The measurement of the U_{out} signal is needed for filling in one big drawback of the Kalman filtering based drives: motor operation at low speed. This drawback is mathematically described by the state-space model observability theory. Consider a general

non linear system:

$$\begin{cases} \dot{\mathbf{x}} = \mathbf{f}(\mathbf{x}, \mathbf{u}) \\ \mathbf{y} = \mathbf{h}(\mathbf{x}) \end{cases} \quad (6.37)$$

where $\mathbf{x} \in \mathfrak{R}^n$ represents the system state, $\mathbf{y} \in \mathfrak{R}^q$ the observable parameters and $\mathbf{u} \in \mathfrak{R}^m$ the externally applied controls. \mathbf{f} and \mathbf{h} are real functions. In order to exploit this model for a Kalman filtering application, the local observability of (6.37) has to be determined. A criterion for the local observability of non-linear systems is given in [45, 76]. The criterion states that a space-state model in the form of (6.37) is locally observable if the rank of its observability matrix O is full. The O matrix is given by:

$$O = [\nabla L_f^0 h \quad \nabla L_f^1 h \quad \cdots \quad \nabla L_f^{n-1} h]^T \quad (6.38)$$

where $L_f = \frac{\partial h}{\partial \mathbf{x}} f$ indicates the Lie derivative of h along the vector field f .

BLDC motor state-space model observability

The criterion (6.38) is now applied to the BLDC motor state-space model (6.20) - (6.24). The observability matrix O is:

$$O = \begin{bmatrix} 1 & 0 & 0 & 0 \\ 0 & 1 & 0 & 0 \\ -\frac{R}{L} & 0 & -\frac{K_m \sin(p\theta)}{L} & -\frac{K_m \omega \cos(p\theta)p}{L} \\ 0 & -\frac{R}{L} & \frac{K_m \cos(p\theta)}{L} & -\frac{K_m \omega \sin(p\theta)p}{L} \end{bmatrix} \quad (6.39)$$

Matrix (6.39) has full rank, i.e. is locally observable, only if $\omega \neq 0$. In fact, for $\omega = 0$, the last column of O contains only zeros. As a consequence of this theory, the model is not observable at standstill. In practice, it is known that the observer-based drives do not work not only at standstill, but also during low speed operations.

6.4.2 Local observability extension

In order to extend the local observability of the Kalman filter, the basic idea is to add an additional source of information, $y_3 = g(\theta)$, to the available measurements listed in (6.10). The new measurement vector becomes:

$$\mathbf{y} = \begin{pmatrix} i_\alpha & i_\beta & g(\theta) \end{pmatrix}^T \quad (6.40)$$

Applying the locally observability criterion (6.38) with the new measurement vector (6.40), the observability matrix O is calculated as follows:

$$O = \begin{bmatrix} 1 & 0 & 0 & 0 \\ 0 & 1 & 0 & 0 \\ 0 & 0 & 0 & \frac{\partial}{\partial \theta} g(\theta) \\ -\frac{R}{L} & 0 & -\frac{K_m \sin(p\theta)}{L} & -\frac{K_m \omega \cos(p\theta)p}{L} \\ 0 & -\frac{R}{L} & \frac{K_m \cos(p\theta)}{L} & -\frac{K_m \omega \sin(p\theta)p}{L} \\ 0 & 0 & \frac{\partial}{\partial \theta} g(\theta) & \omega \left(\frac{\partial^2}{\partial^2 \theta} g(\theta) \right) \end{bmatrix} \quad (6.41)$$

In (6.41) it appears that the system will be locally observable even at $\omega = 0$ if $\frac{\partial}{\partial \theta} g(\theta) \neq 0$.

The introduced approach is already implemented in [49], where a Hall sensor is used as a low resolution sensor and its signal entered in the measurement equations. The innovation in this thesis is that, instead of an additional sensor, the U_{out} signal introduced in Chapter 4 is used as $g(\theta)$ function. In this way, the drive is still fully sensorless according to the definition given in the introduction.

6.4.3 Kalman filter on a two-phases ON supply

In a classical implementation of the Kalman filter, the BLDC motor is driven with a sinusoidal supply. Unfortunately this supply is not suitable for a correct measurement of the U_{out} signal. Therefore, a Kalman filter that drives the BLDC motor with the well known two-phases ON supply introduced in Chapter 5 has to be developed.

The big differences between these two supplies are that the two-phases ON supply introduces discontinuities in the phase currents and voltages, and that the latter are not completely imposed by the power bridge. Each phase in turn is floating, and the other two are influenced by the phase current extinctions and the back-EMF. Consequently, in this supply, the input vector \mathbf{u} (6.4) is not completely controlled by the power bridge and a model of the latter is needed.

Simulations of a BLDC motor in a two-phases ON supply have been done for example in [80] under Matlab/simulink environment, or in [70, 81, 82] where phase voltages and currents are analytically determined. In these models, each one of the six sectors of the two-phases ON supply is divided in a transient state, the current extinction, as introduced in Section 5.3, and in a normal state. The phase voltage equations used in this thesis are taken from [82]. For example, in the AB sector shown in Fig. 5.1 these

are:

$$u_A = \frac{U_{dc}}{2} - \frac{u_{iC}}{2} \quad (6.42)$$

$$u_B = -\frac{U_{dc}}{2} - \frac{u_{iC}}{2} \quad (6.43)$$

$$u_C = u_{iC} \quad (6.44)$$

where $U_{dc} = d V_{pp}$. Remember that d is the PWM duty cycle, V_{pp} the power supply of the power bridge and u_{iC} is the back-EMF on phase C . The phase voltage equations for the AB - AC commutation shown in Fig. 5.2 are:

$$u_A = \frac{U_{dc}}{3} \quad (6.45)$$

$$u_B = \frac{U_{dc}}{3} \quad (6.46)$$

$$u_C = -\frac{2U_{dc}}{3} \quad (6.47)$$

Implementation with space-state model

For the Kalman filter implementation, a state-space model of the motor is required, like the set of equations (6.20) - (6.24). These state equations of the BLDC motor introduced in Section 6.2 are clearly valid for every supply, and thus, for a two-phases ON supply too.

A simulation is performed, the motor is driven from 0 rpm up to 1'500 rpm with KF1 only. In Fig. 6.20 the phase current $i_\alpha = i_a$ at steady-state, $\omega_0 = 1'500$ rpm, is shown.

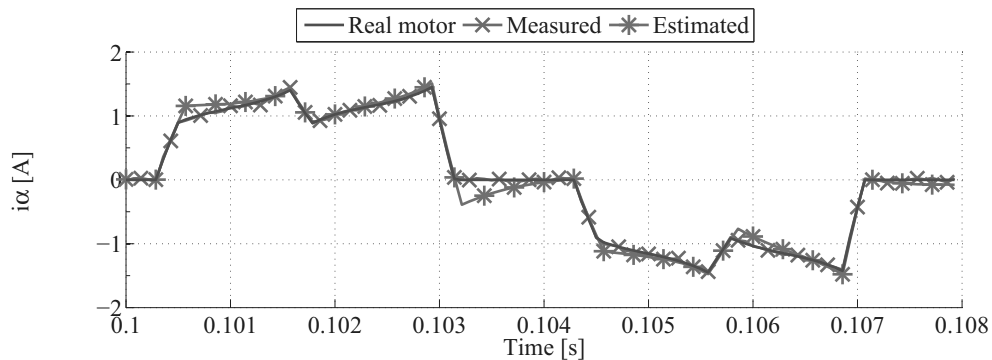


FIGURE 6.20 – i_α estimation with space-state model.

In Fig. 6.20 it can be noticed that the estimation is correct during the normal states, but not at the end of the current extinction transients, as at $t = 0.1032$ s for example. This problem is related with the sampling period T_s . In fact, during the transients, the

current dynamic is much higher than during the normal states. As a consequence, with the chosen T_s there are very few iterations of the Kalman filter during the transient. Hence, the last time-update may largely exceed the real transient time, and thus the currents are erroneously estimated.

A solution to this problem is to increase the number of samples, i.e. decrease the sampling period T_s . This approach is unfortunately not effective for a real time implementation, as the sampling period T_s lower limit is imposed by the hardware and the computational time.

Implementation with space-state model and current correction

A first effective solution is to detect the end of the current extinction after the calculation of the time-update, and consequently correct the estimated currents. A simulation with this implementation is performed and in Fig. 6.21 the phase current $i_\alpha = i_a$ at steady-state, $\omega_0 = 1'500$ rpm, is shown.

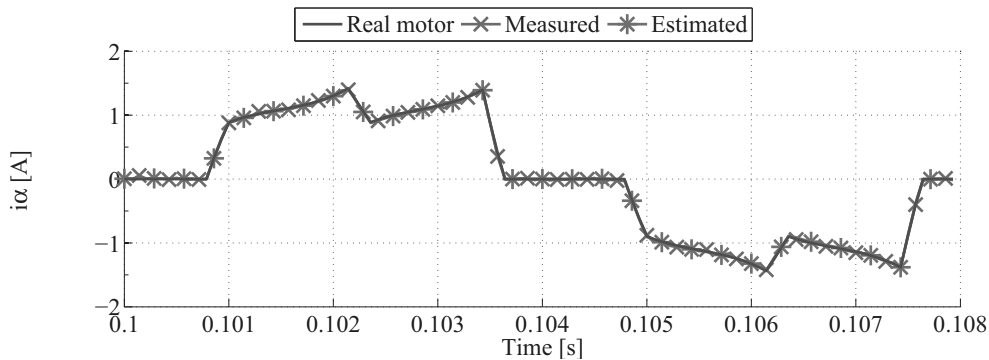


FIGURE 6.21 – i_α estimation with space-state model with current correction.

The accuracy of the estimation of the phase current i_α is increased, and consequently that of the overall filter, without any need to change the sampling period T_s and without consequences on the computational time.

Implementation with space-state model and analytical model

A second solution to the highlighted problem is to merge the state-space and the analytical model during the Kalman filter implementation. In this implementation, the Kalman filter also discriminates between the current extinction and the normal state.

During the normal state, the space-state model is used and the Kalman filter is applied as usual.

On the other hand, during the current extinction, the measurement update of the Kalman filter is deactivated. The time update of the motor state is still done with the space-state equations, but the currents i_α and i_β are calculated with the analytical equations taken from [70].

For the transient AB - AC shown in Fig. 5.2, the phase A current i_A for a BLDC motor with sinusoidal back-EMF is given by:

$$i_A = \frac{u_A}{R_A} + \left(I_0 - \frac{u_A}{R_A} \right) e^{-t \frac{R_A}{L_A}} - \frac{K_m \frac{\omega}{p}}{|Z_A|} \left(\sin(\omega t + \varphi - \gamma_A) - \sin(\varphi - \gamma_A) e^{-t \frac{R_A}{L_A}} \right) \quad (6.48)$$

where I_0 is the initial current at the commutation instant, $|Z_A| = \sqrt{R_A^2 + (\omega L_A)^2}$, $\gamma_A = \arctan\left(\frac{\omega L_A}{R_A}\right)$ and t is the time since the commutation instant. $\varphi = \frac{3\pi}{6} - \delta$ for this commutation transient. As φ varies depending on the commutation, its values are given in Table 6.6.

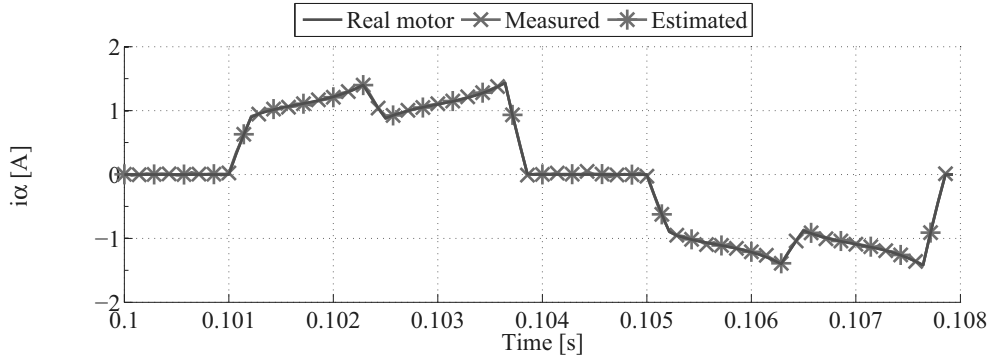
TABLE 6.6
 φ values for the six commutations

$CB - AB$	$AB - AC$	$AC - BC$	$BC - BA$	$BA - CA$	$CA - CB$
$\frac{\pi}{6} - \delta$	$\frac{3\pi}{6} - \delta$	$\frac{5\pi}{6} - \delta$	$\frac{7\pi}{6} - \delta$	$\frac{9\pi}{6} - \delta$	$\frac{11\pi}{6} - \delta$

δ is the commutation phase advance angle. It is chosen to fix this angle to $\delta = 0^\circ$ in this thesis. However, it must be pointed out that this angle can unfortunately not exactly be known, as the rotor position is not measured but estimated by the Kalman filter. In fact, the estimation error on the rotor position is seen by the motor as a phase advance (or delay) and thus most of times $\delta \neq 0^\circ$.

Theoretically, (6.48) is defined for steady-state operations only, at constant speed and constant load torque. This hypothesis is normally not satisfied in an electrical drive as dynamic operations and load variations are frequent. However, as the current extinction period is very short, the steady-state assumption can be used.

A simulation with this last implementation is performed and in Fig. 6.22 the $i_\alpha = i_a$ current at steady-state, $\omega_0 = 1'500$ rpm, is shown. As it can be appreciated in Fig. 6.22, the i_α current is correctly estimated in this last implementation and the overall performance of the Kalman filter is comparable to the implementation with space-state model and current correction.


 FIGURE 6.22 – i_α estimation with space-state and analytical model.

Implementation choice

In this thesis it is chosen to use the last implementation, where the space-state and analytical model are used in turn, during the normal and transient state respectively. With the simulations, it has not been possible to highlight a significant difference between this implementation and the one based on the space-state model with corrected currents. However, as the U_{out} signal is not available during the current extinction transients, the chosen implementation is more adapted because the Kalman filter is already deactivated during that same time.

6.4.4 U_{out} measurement

In Fig. 6.23, the characteristic shape of the U_{out} signal available during an electrical period is shown. As for the creation of the calibration maps introduced in Subsection 5.4.1, every segment of the U_{out} signal is interpreted in the Kalman filter with a linear approximation

$$U_{out} = a_i \theta + b_i \quad (6.49)$$

where the index $i = CA, CB, AB, AC, BC, BA$ indicates the respective sector. Thus, the position signal measured by the Kalman filter is calculated as follows

$$g(\theta) = \theta_{U_{out}} = \frac{U_{out} - b_i}{a_i} \quad (6.50)$$

It is important to point out that the result of (6.50) is highly relied on the estimated position. In fact, depending on the latter, a sector of the two-phases ON is activated and the respective a_i and b_i parameters are selected. As a consequence, if the position $\hat{\theta}$ is wrongly estimated, the measured position $\theta_{U_{out}}$ does not contain the correct information. In order to highlight this problem, two simulations are performed with the motor at

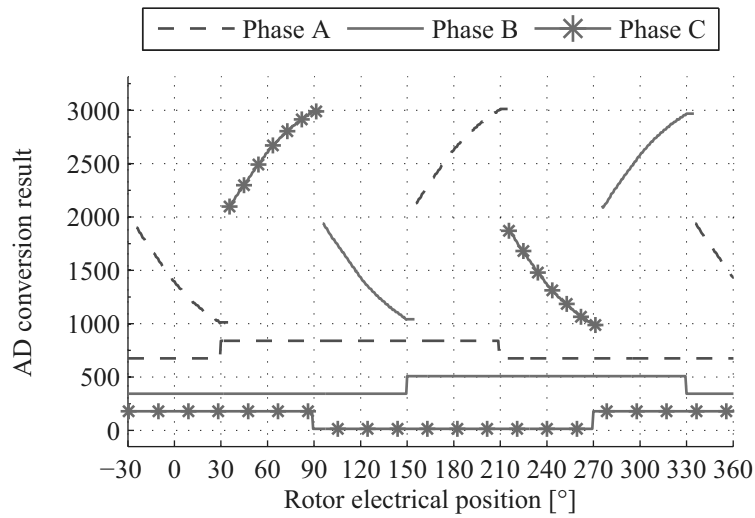


FIGURE 6.23 – AD sampled U_{out} signals and Hall sensors in a two-phases ON supply.

standstill. The $\theta_{U_{out}}$ measurement is performed using (6.50). The U_{out} signal is created based on the measurement shown in Fig. 6.23, and a random noise is voluntary added.

In the first trial, an initial position error of 40° electrical degrees is imposed. In Fig. 6.24 the evolution of the position estimation is shown.

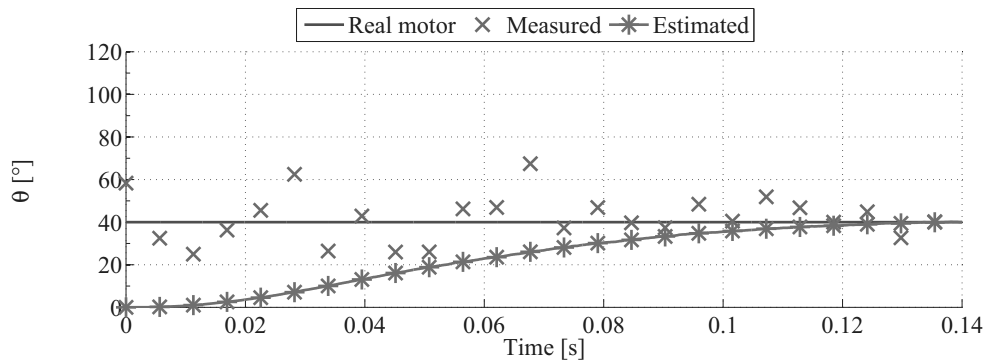
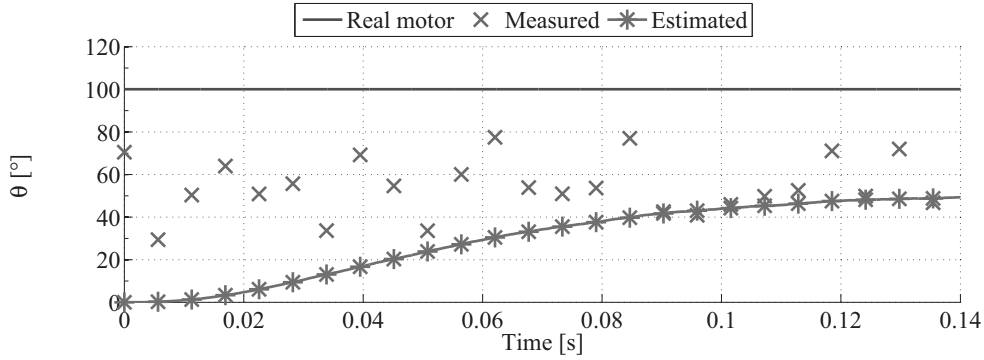


FIGURE 6.24 – Estimated position $\hat{\theta}$ at standstill, initial error 40° .

As it can be appreciated, with the additional $\theta_{U_{out}}$ measurements (not all the measurements are shown), even if very noisy, the Kalman filter is able to correctly retrieve the rotor position at standstill.

A second simulation with an initial error of 100° on the position estimation is performed. In Fig. 6.25 the evolution of the position estimation is shown.

In this second simulation, it can be noticed how the Kalman filter does not converge to


 FIGURE 6.25 – Estimated position $\hat{\theta}$ at standstill, initial error 100° .

the correct position, but to the wrong measured position θ_{Uout} . In fact, the two-phases ON sector is different for the estimated position $\hat{\theta} = 0^\circ$ than for the motor position $\theta = 100^\circ$ and because of that, (6.50) is calculated with the wrong a_i and b_i parameters.

This last situation can however happen only at standstill if the rotor position is lost. During normal operations, the position estimation error is not big enough for creating the problem.

6.4.5 U_{out} calibration

In order to attain the final objective, one last task has to be performed. The latter is to calibrate the a_i and b_i parameters of the measurement equation (6.50). The parameters are estimated using the technique introduced in Section 6.3. The two following additional equations are simply added to the KF2 block:

$$\underbrace{U_{out} - b_i}_{y_\Theta} = \underbrace{\theta}_{C_\Theta} \underbrace{a_i}_\Theta \quad (6.51)$$

$$\underbrace{U_{out} - a_i \theta}_{y_\Theta} = \underbrace{1}_{C_\Theta} \underbrace{b_i}_\Theta \quad (6.52)$$

In opposition to the constraints on the electrical and mechanical parameter observability, for the estimation of the θ_{Uout} measurement parameters there is no need of dynamic transients. a_i and b_i can be estimated at every time and thus, also during steady-state operations.

A simulation is performed, the motor is driven at 2'000 rpm, and wrong values are voluntary given to a_i and b_i . In Figs. 6.26 and 6.27 the estimation of a pair of these parameters is shown.

In Figs. 6.26 and 6.27 it can be appreciated how, even in presence of very noisy measurements, the algorithm is able to converge toward the real values.

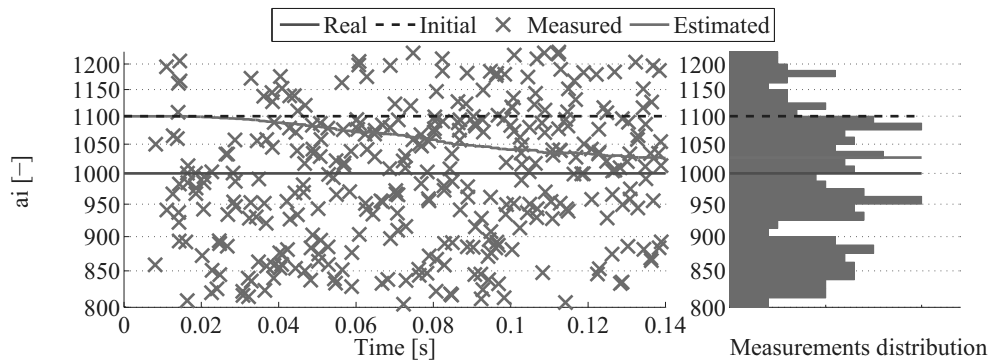


FIGURE 6.26 – Estimated parameter a_i .

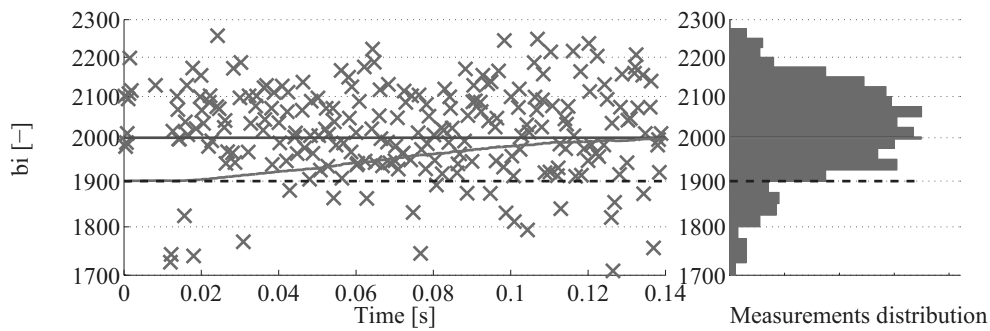


FIGURE 6.27 – Estimated parameter b_i .

6.4.6 Comments

In this section the integration of the U_{out} signal into a Kalman filtering based drive is introduced. The Kalman filter implementation is adapted for a two-phases ON supply for permitting the correct measurement of the U_{out} signal. The U_{out} signal is interpreted by the Kalman filter as a linear function of the rotor position θ . The parameters of this representation are estimated in the same way as the other model parameters, using KF2.

Thanks to the additional position measurement, the working range of the Kalman filter is extended down to low speed operations.

It is however important to point out that this advantage is unfortunately not obtained without compensation. In fact, the introduced implementation requires a higher computational effort because of the higher matrices size. This drawback is quite restrictive with the actual calculation power available in a microcontroller. However, it is doubtless that, thanks to the improvement of the microcontrollers, this constraints will disappear in the future.

6.5 Kalman filtering with U_{out} and parameters estimation

In this section a simulation of the complete Kalman filter drive is introduced. The motor is driven in a sewing machine mode, the speed reference is changed every 90° mechanical degrees from +1'000 rpm to -1'000 rpm. The initial errors on the electrical parameters values are R : -10%, L : +10% and K_m : -10%. Inertia and friction constants are initialized to the motor-only datasheet values. Total drive values are: $I_{tot} = 2I_{mot}$ and $K_{f,tot} = 4K_{f,mot}$. Finally, an error of +5% and -10% is initially given to the shown pair of a_i and b_i parameters.

The simulation shows first of all that KF1 is able to drive the motor with a two-phases ON supply. The phase current i_α and the phase voltage u_α are shown in Fig. 6.28, the electrical position θ and the speed ω are shown in Fig. 6.29.

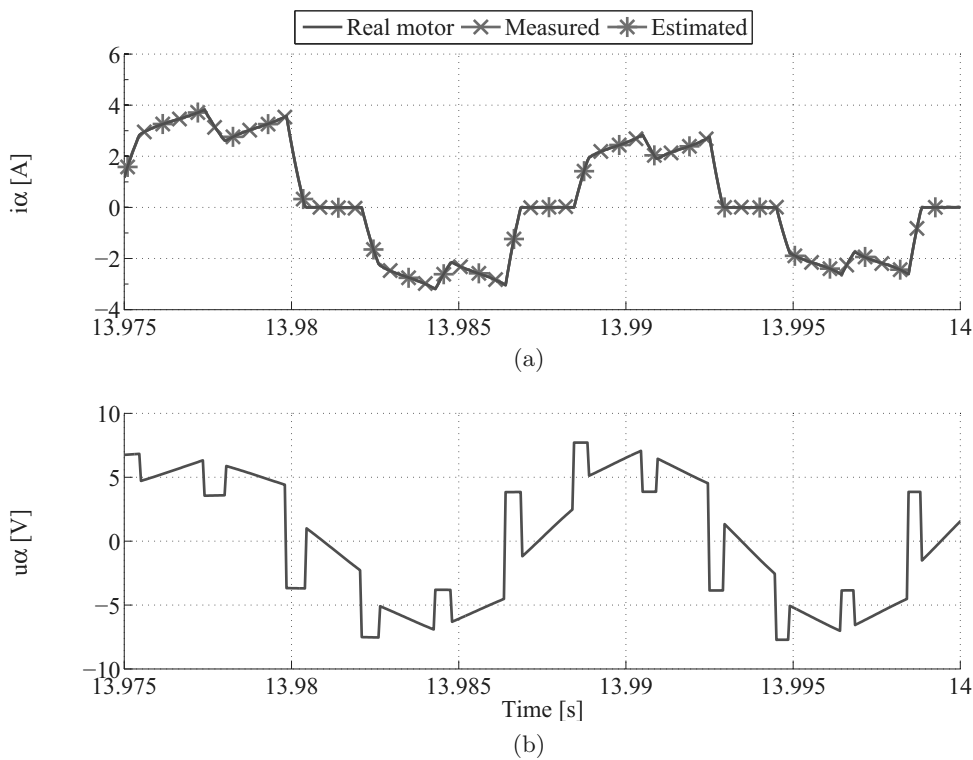


FIGURE 6.28 – i_α (a) and u_α (b).

On the other hand, KF2 is able to estimate the parameters a_i and b_i of the additional position measurement $\theta_{U_{out}}$. The convergence of a pair of these parameters is shown in Fig. 6.30. It can be appreciated how the algorithm quickly converges towards the real values.

6.5. Kalman filtering with U_{out} and parameters estimation

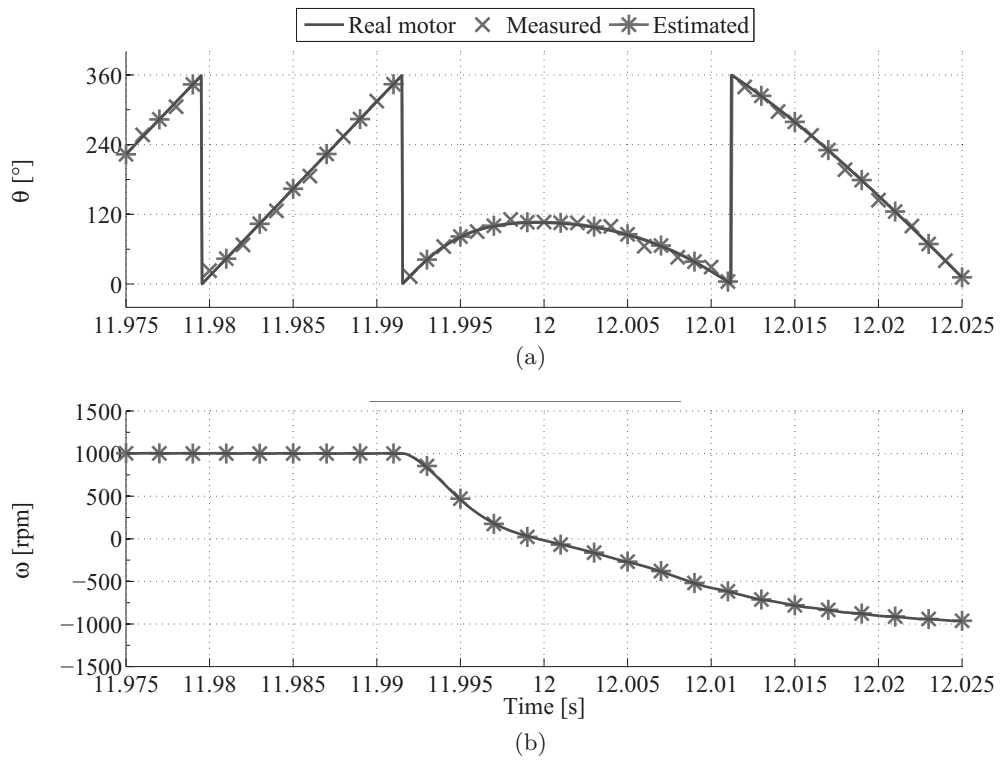


FIGURE 6.29 – θ (a) and ω (b).

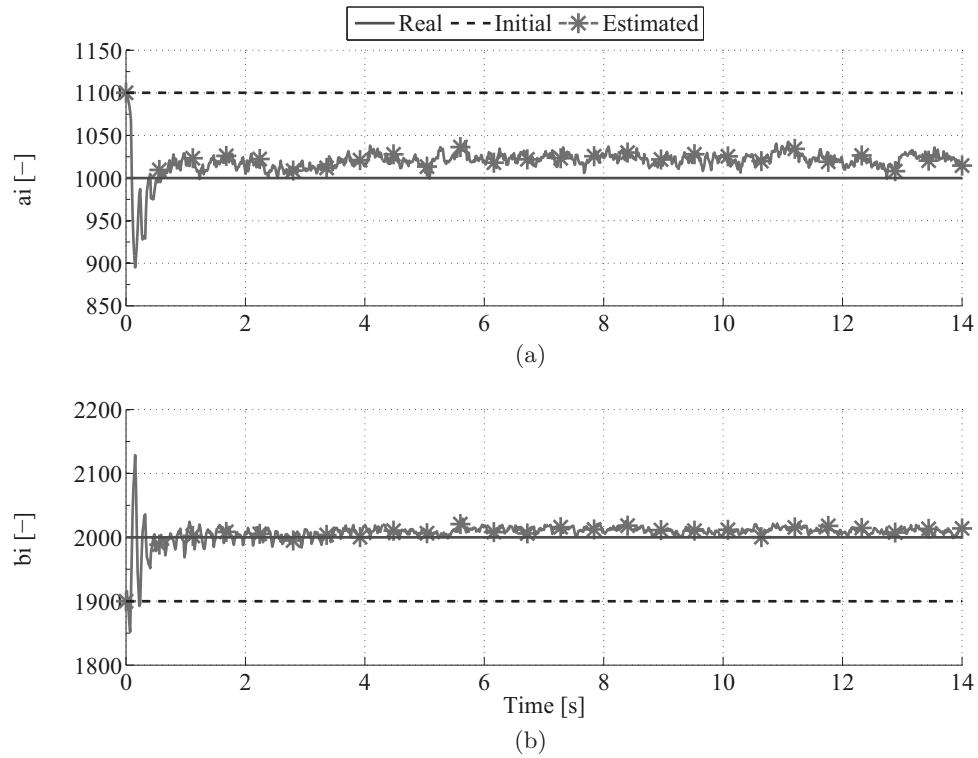


FIGURE 6.30 – Estimated parameter a_i (a) and b_i (b).

At the same time, KF2 estimates also the electrical parameters of the motor model, R , L and K_m , that are shown in Fig. 6.31, and the mechanical parameters, the total inertia I_{tot} and total friction coefficient $K_{f,tot}$, that depend on the motor and on the external load. These last estimations are shown in Fig. 6.32.

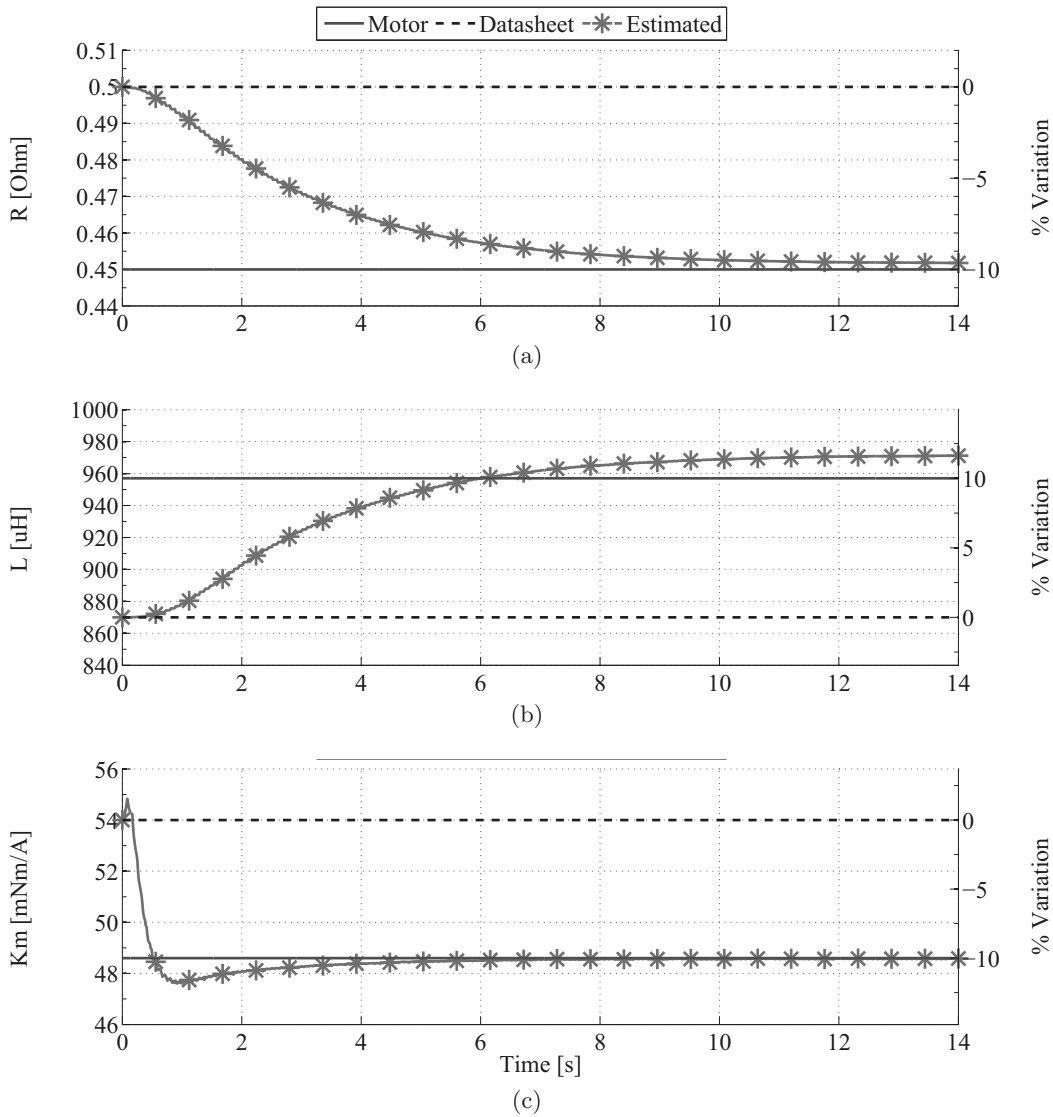


FIGURE 6.31 – Estimated parameter R (a), L (b) and K_m (c).

This simulation proves that the realization of a sensorless position detection principle, working over the whole speed range, robust, adapted to steady-state and dynamic operations, that does not need any kind of off-line calibration is made possible.

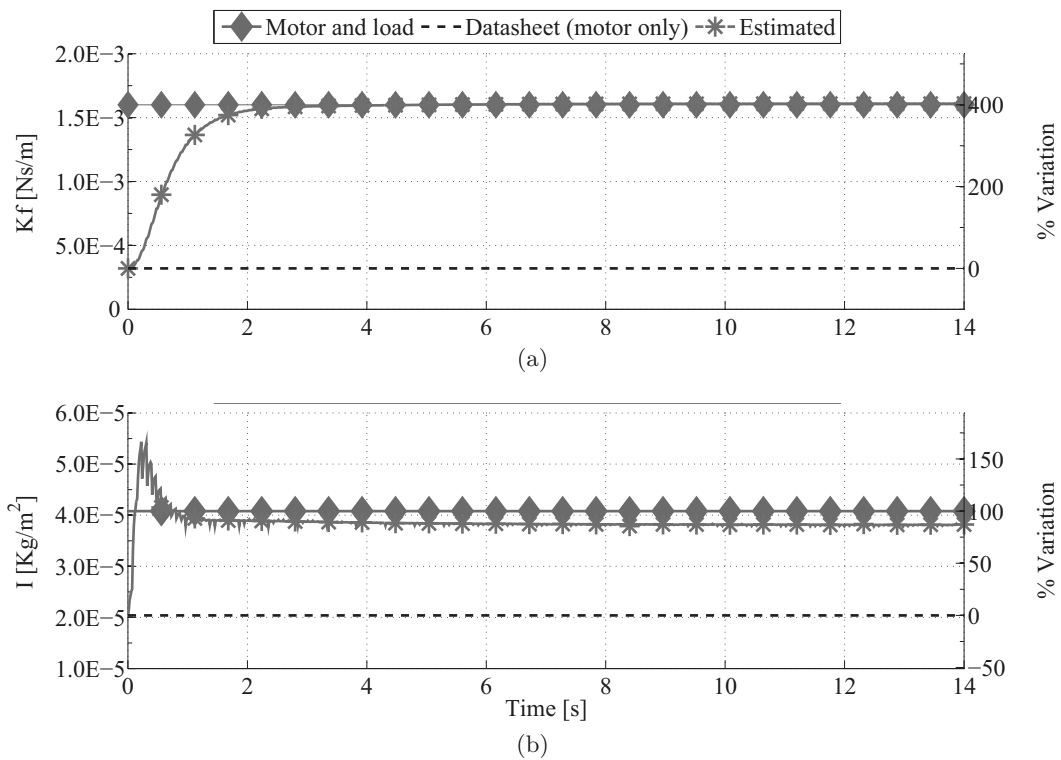


FIGURE 6.32 – Estimated parameter $K_{f,tot}$ (a) and I_{tot} (b).

6.6 Conclusions

In this chapter an innovative Kalman filtering implementation for the rotor position detection of BLDC motors is introduced.

The position dependent U_{out} signal is integrated into a Kalman filter that drives a BLDC motor with a two-phases ON supply. The U_{out} signal provides an additional input to the Kalman filter and by this way, the observability of the latter is extended to the low speed operations and even down to standstill.

With the purpose of providing a complete solution, an algorithm for the on-line parameter estimation of the models used in the Kalman filter is introduced. The algorithm is able to estimate the electrical parameters of the motor, the mechanical parameters of the entire drive (motor and load) and finally, also the parameters needed for the U_{out} signal exploitation. The entire algorithm is successfully tested in simulations and a part of it is moreover successfully tested on a realized prototype.

First pulse principle

Contents

7.1	Introduction	150
7.1.1	Position detection objective	150
7.2	Measurement theory	151
7.2.1	Phases iron BH working point	152
7.2.2	Position NSN physical interpretation	153
7.2.3	Position NNS physical interpretation	156
7.3	Simplified model	158
7.3.1	Prediction of the first pulse effect on the phase impedances	159
7.3.2	Prediction of the first pulse effect on U_{out}	160
7.3.3	Interpretation	160
7.4	Measurements	163
7.4.1	Setup	163
7.4.2	Measurements	164
7.4.3	Interpretation	168
7.5	Practical implementation issues	169
7.6	Conclusions	169

7.1 Introduction

THE position detection of a BLDC motor at zero speed when the position estimation is lost is very difficult to achieve if no saliencies are present on the rotor. Very few techniques, as [83] where the magnetic anisotropy of the permanent magnet is sensed, or techniques based on saturation [66, 84, 85], work for that particular case. Alternatively, some rotor modification have been introduced, like mechanical saliencies [20] or mechanical artifacts in order to spatially constrain the eddy currents [8, 9, 11 – 13].

In this chapter a new and innovative measurement principle, called first pulse, able to detect the rotor position at standstill of a non-salient motor is introduced. The first pulse measurement principle finds its physical origins in the iron BH hysteresis. It is strongly related to the BH hysteresis exploitation introduced in Chapters 4, 5 and 6, but it exploits the hysteresis in an even more subtle way.

First of all, the theory of the first pulse measurement principle is introduced, and, for simplifying the explanation, two examples are deeply analyzed. A simplified model of the principle theory is then introduced. This model is used for predicting the results of the measurement over an entire electrical revolution of the motor. Thereafter, the first pulse measurement is implemented in a realized electronics and the theory is experimentally verified. Some practical issues of the principle are discussed and finally, advantages and drawbacks are commented, some conclusions are drawn and future challenges are introduced.

7.1.1 Position detection objective

For starting up a BLDC motor without oscillations it is necessary to know its rotor position at standstill, in order to directly impose the right rotation direction. This position has to be determined even after a main reset of the drive electronics, i.e. in the case when there is no information available about the past rotor position.

For this task, the necessary minimal position estimation resolution is nevertheless really low. For example, it is enough to know the corresponding Hall state of the actual rotor position. Fig. 7.1 shows the Hall sensor states of a complete electrical period of the standard test BLDC motor used in this chapter. Based on them, the period of 360° electrical degrees is subdivided in 6 sections of 60° each. These different sectors are identified further in this chapter by the acronyms (north or south pole) of the three Hall sensor states, as indicated in Fig. 7.1 on the top.

In Chapter 5 it is shown that the differential U_{out} voltage contains some rotor position information. However, in Section 5.4.2 it is highlighted that, even if this position infor-

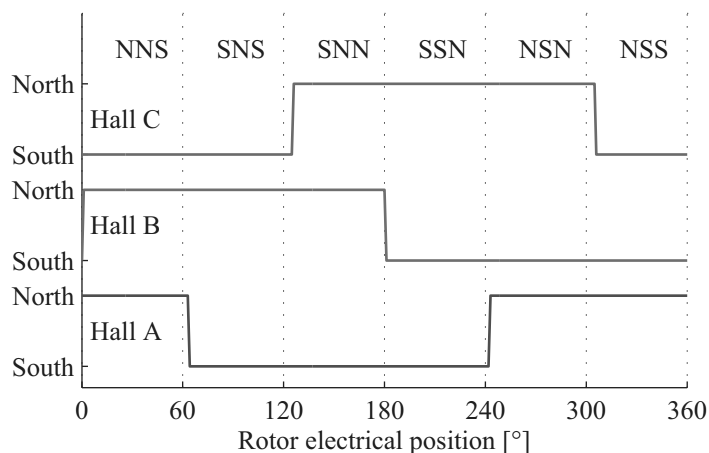


FIGURE 7.1 – Hall sensor states for a complete electrical period.

mation has a resolution of only some electrical degrees, the same U_{out} value is obtained for up to four different electrical rotor positions in four different sectors and thus, that the rotor position can not be retrieved after a main reset of the drive electronics with the U_{out} signal only.

In order to eliminate this ambiguity, the objective of the introduced measurement principle is hence limited to determine in which of these sectors is the actual rotor position.

7.2 Measurement theory

The physical basis of the first pulse measurement principle for estimating the rotor position at standstill after a main reset of the drive electronics is related to the stator teeth iron BH hysteresis.

The first pulse measurement consists in the injection of two successive pulses of U_{in} and the measurement of U_{out} , exactly as it is already done in the previous chapters. An important fact is that the position information is not retrieved by the absolute value of U_{out} as in Chapter 5, but by the comparison between the U_{out} signals created by the first and the second U_{in} pulses.

In fact, it will be shown that depending on the rotor position, if two or more successive U_{in} pulses are injected, the U_{out} corresponding to the first pulse may be different from all the following ones (2, 3, 4, ...), and that all the following pulses (2, 3, 4, ...) always create the same U_{out} .

7.2.1 Phases iron BH working point

For understanding the first pulse measurement principle, it is necessary to go back to the iron BH global and local hysteresis introduced in Chapter 3. In Chapter 3 every motor phase is analyzed separately. It is shown that the teeth iron of each phase moves in the BH plane following a global hysteresis created by the rotor permanent magnets. During a complete electrical revolution, one motor tooth faces a complete permanent magnet north-south period. The iron BH working point of the tooth follows therefore an entire global hysteresis loop. Considering the geometry of the BLDC motor, the iron BH working points of the three phases are placed on the same global hysteresis, each phase separated by 120° .

As shown in Fig. 7.2, it is arbitrarily chosen to fix the rotor position origin at the beginning of the iron north polarisation, and to place the motor phase B at 0° , with $B = 0$ T. This position corresponds to the q position of phase B , as shown in Fig. 7.3(a). On that same figure on the right hand side, the position d of phase B is shown. This position corresponds to the electrical position 90° , that on the main hysteresis, Fig. 7.2, is located in the upper right corner. Finally, on that same BH hysteresis, it is chosen to place the motor phase A at 120° and phase C at 240° .

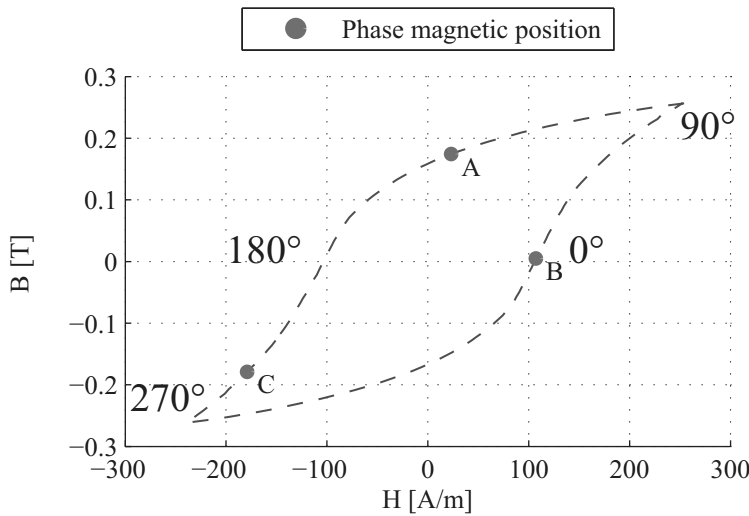


FIGURE 7.2 – Iron BH hysteresis loop, chosen angular origin.

This placement unfortunately also depends on the rotation direction of the rotor, i.e. depending on the past position, the iron BH working point for a given position may not be the same. In Fig. 7.4 it is shown how, for the same rotor position of 0° (NNS), the phases A and B can have another location on the BH hysteresis.

Nevertheless, the theory and all the measurements and examples in this chapter are based on the angular origin shown in Fig. 7.2.

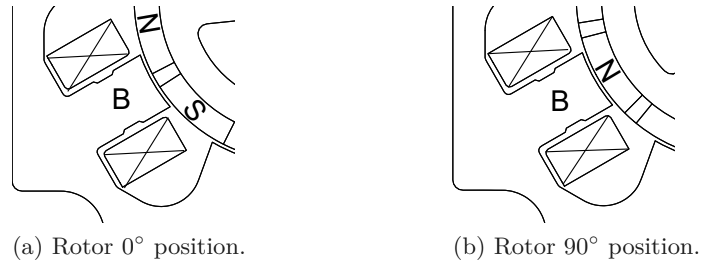


FIGURE 7.3 – Rotor q (a) and d (b) positions for the phase B .

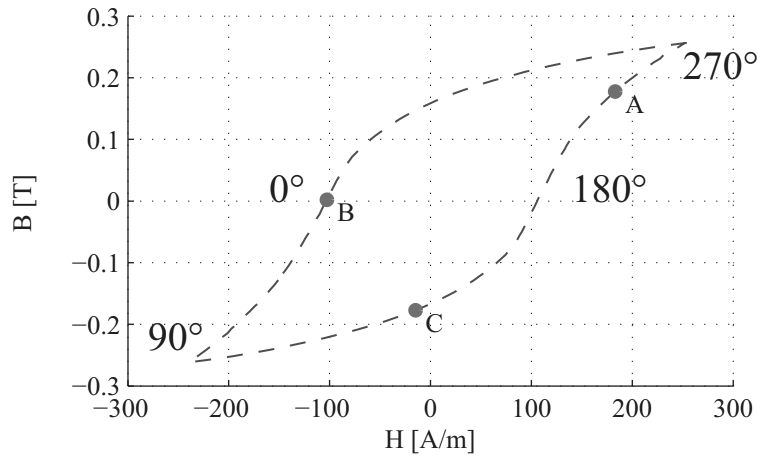


FIGURE 7.4 – Iron BH hysteresis loop, other possible angular origin.

7.2.2 Position NSN physical interpretation

For simplifying the phenomenon description, two particular rotor positions, NSN and NNS, are analyzed.

At position NSN, the initial working points of the iron in three phases teeth are shown with a \bullet and identified by A , B , C in Fig. 7.5.

Now, a U_{in} pulse is injected between phases A and B and the U_{out} voltage is observed with a scope. Fig. 7.6 shows an example of the U_{in} voltage with $t_{on} = 20 \mu s$, the current I_{in} and voltage U_{out} after filtering and amplification.

The arrows in Fig. 7.5 show how the working points of the teeth A and B move when this first pulse of U_{in} is applied. In the phase A , the current creates a positive magnetic field and in the phase B a negative one, as the two phases are connected in series. The first arrow (the one starting from A and B) indicates the movement due to the growing current in that phase; the second arrow indicates the movement due to the decreasing current. It can be clearly seen in Fig. 7.5 that the working point of the phase A tooth has changed after the first pulse of U_{in} and becomes A' , identified with an \blacklozenge . On the

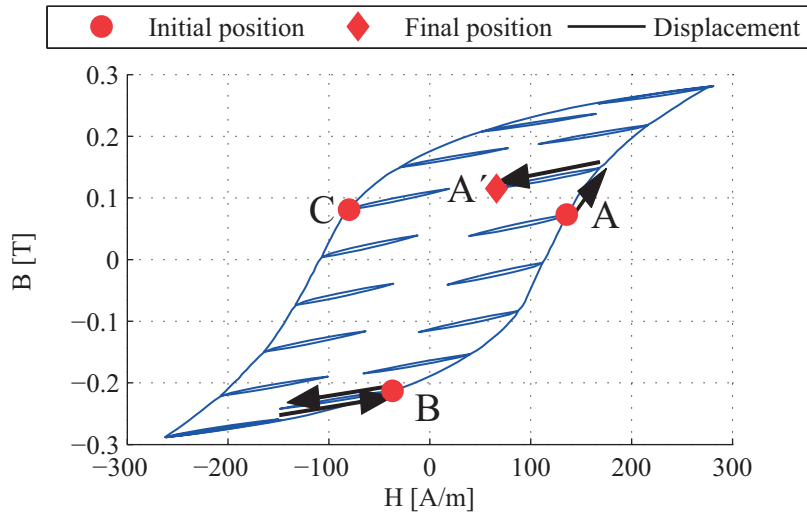


FIGURE 7.5 – Iron BH hysteresis loops, NSN rotor position. 1st pulse.

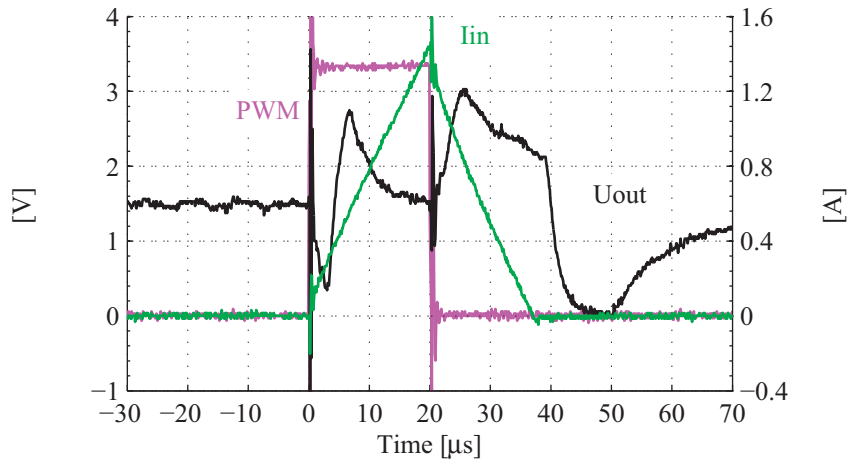
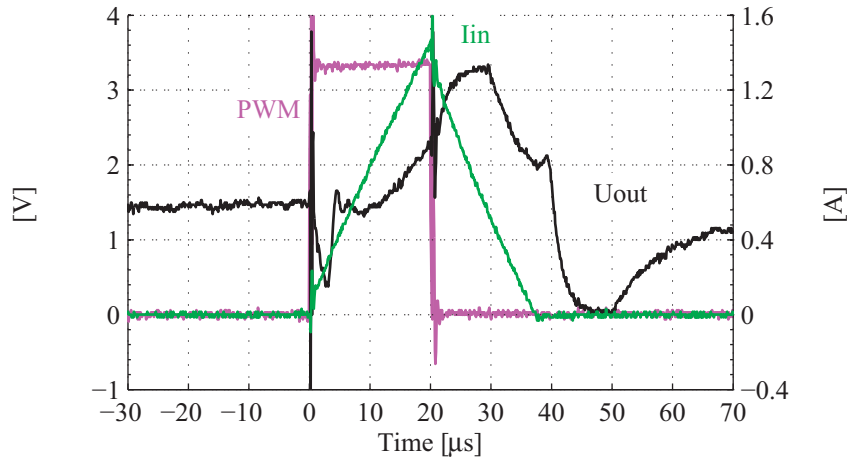
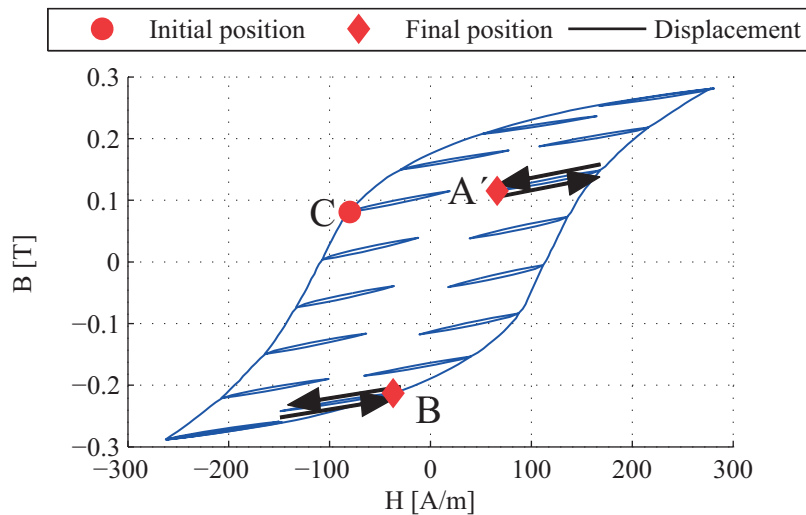


FIGURE 7.6 – PWM pulse of U_{in} , and corresponding U_{out} and I_{in} . 1st pulse.

other hand, the working point of the phase B moves back to its initial position, and the working point of the phase C tooth does not move at all as no current flows through that coil.

A second U_{in} pulse is applied and the U_{out} voltage visualized in Fig. 7.7 The first conclusion, is that U_{out} is significantly different from before, even if the rotor position has absolutely not changed.

For understanding this interesting conclusion it is necessary to observe the the displacement of the working points of the three phases in this second situation. In Fig. 7.8 these displacements are shown. As it can be noticed, in that situation, both phases A and B move and but go back to the position they had before this second pulse, A' and respectively B . As the iron BH working point of phase A has a different trajectory in

FIGURE 7.7 – PWM pulse of U_{in} , and corresponding U_{out} and I_{in} . 2^{nd} pulse.FIGURE 7.8 – Iron BH hysteresis loops, NSN rotor position. 2^{nd} pulse.

the plane than before, the phase A impedance changes and U_{out} differs.

A third U_{in} pulse is finally injected. Not surprisingly, the measured U_{out} voltage, Fig. 7.9, corresponds to the one obtained with the second pulse. In fact, the second pulse does not change the iron working point of any phase, as the operating point starts and finishes in A' and B respectively. As a consequence, the phase impedances do not vary for this third pulse and the U_{out} signal is the same. Hence, for all the following pulses the working points of both phases A and B do not change anymore.

It can therefore be stated that there is a magnetic difference in the stator iron between the first pulse and all the following ones for this position. In this example, this difference influences the phase impedance Z_A , and can therefore be measured in the U_{out} voltage. Notice moreover that no visible changes appear on the current evolution for all the three

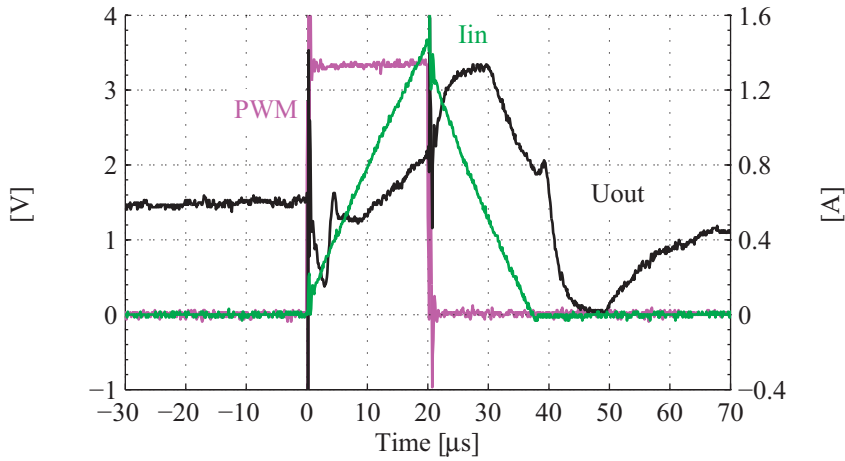


FIGURE 7.9 – PWM pulse of U_{in} , and corresponding U_{out} and I_{in} . 3rd pulse.

pulses. In fact, the variation on the phase impedance Z_A is too small to significantly influence the latter.

7.2.3 Position NNS physical interpretation

The previous interpretation is now employed in the position NNS. The working points of the three phase teeth before a pulse are shown with a \bullet and identified by A , B , C in Fig. 7.10.

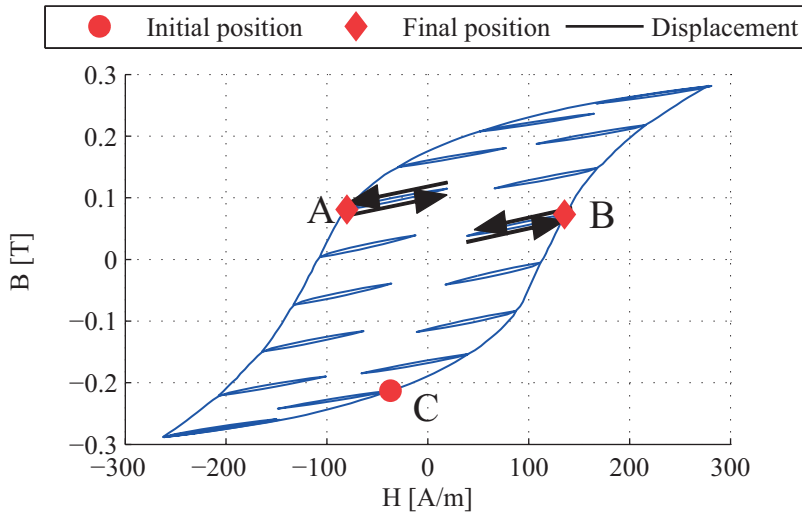


FIGURE 7.10 – Iron BH hysteresis loops, NNS rotor position. 1st pulse.

Contrary to the position NSN, in position NNS the working points of both phases A and B teeth do not change after the first U_{in} pulse. As a consequence, every pulse of U_{in} applied in this position has the same effect on the stator iron and no difference in

the magnetic path appears between the first pulse and the following ones. Hence, no difference is measured between the first U_{out} signal and the following ones, Fig. 7.11.

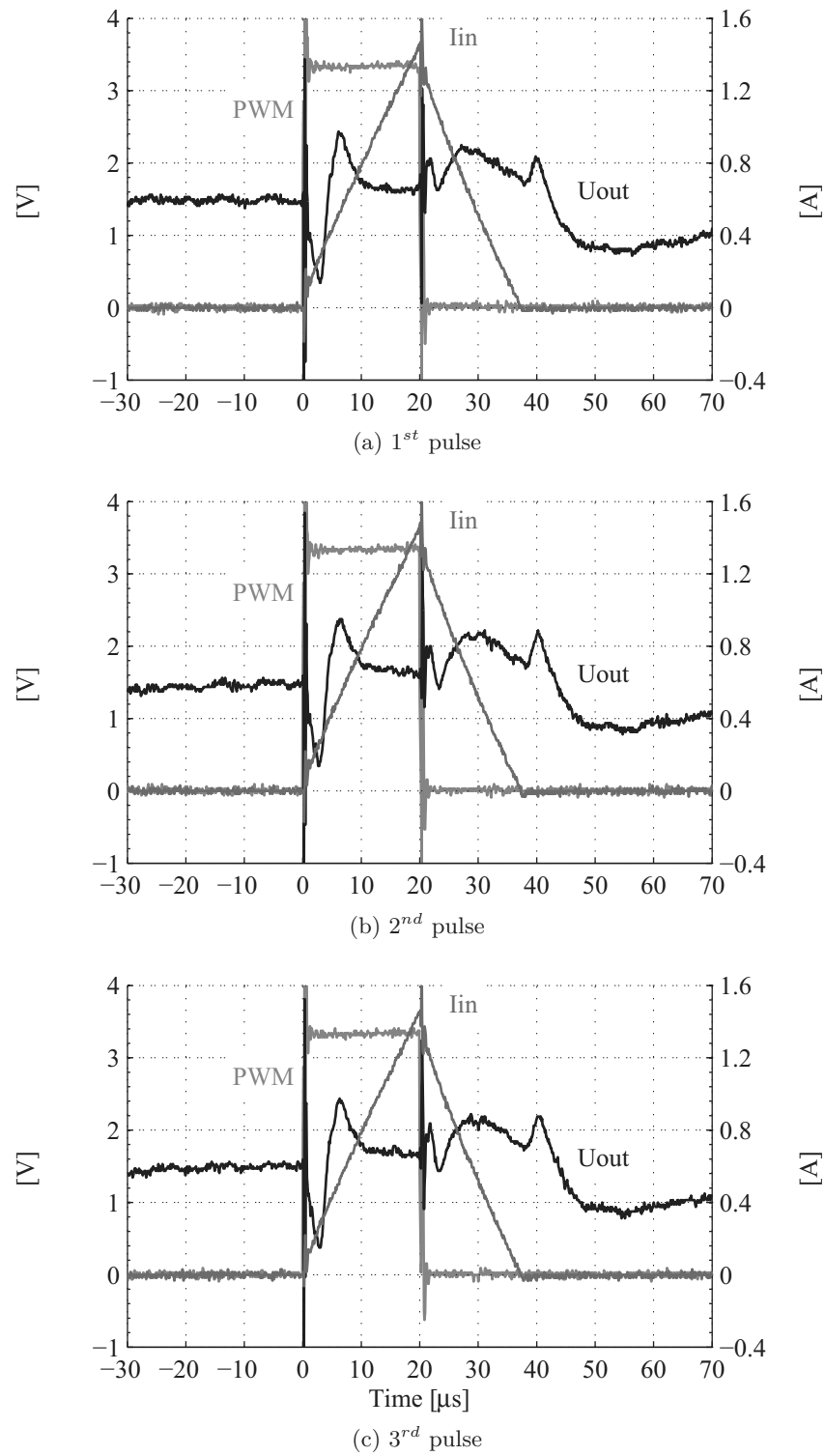


FIGURE 7.11 – PWM pulse of U_{in} , and corresponding U_{out} and I_{in} .

7.3 Simplified model

Starting from the shown examples, it is now possible to extend the concept to the whole electrical revolution of the motor.

A simplified model for predicting the first pulse effect is introduced. It is considered that the first pulse effect exists in the case when the iron BH working point of any phase does not come back to its initial position after the first U_{in} pulse.

This can be rapidly determined graphically, as shown in the previous section. Based on this simple model, in Fig. 7.12 it is shown where on the BH hysteresis, a positive or a negative current flowing in a motor phase creates the first pulse effect. An additional distinction is done between “small” and “big” effect. The zones where a “big” effect appear are identified with an *. The limit of this distinction is arbitrarily chosen, depending on the slope of the BH hysteresis loop. It is supposed that where the slope is small, there is only a small difference between the initial and the final position of the iron working point after the first U_{in} pulse. Consequently, the magnetic path for the first pulse is similar to the magnetic path of all the followings ones and therefore only a small difference on Z_x between of the first pulse and the followings is expected (small effect).

On the other hand, where the slope is higher, the magnetic path between the first pulse and the following ones varies considerably, and therefore the variation on the phase impedance Z_x is important. In this case, a big difference is expected (big effect).

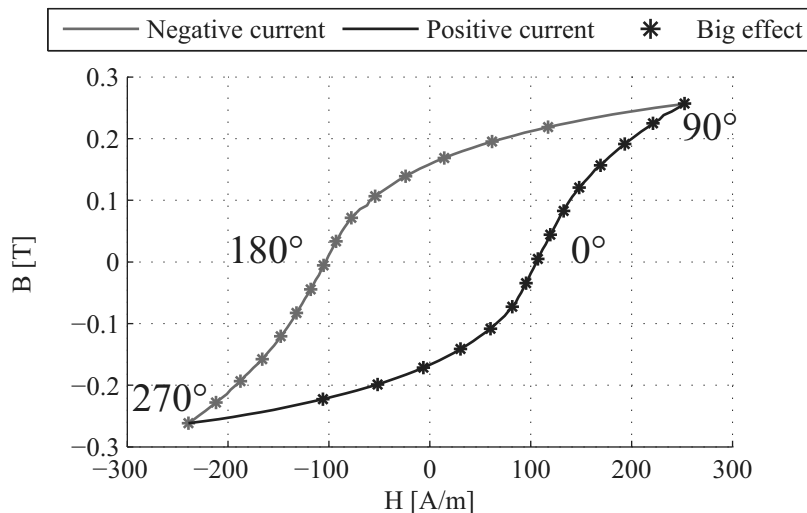


FIGURE 7.12 – Iron BH hysteresis loop, chosen angular reference.

The aim is now to describe which pulses create the effect, and which not, for every rotor position.

7.3.1 Prediction of the first pulse effect on the phase impedances

Starting from the angular reference introduced in Fig. 7.2 the working point of the three phases is automatically rotated counterclockwise every 15° on the BH loop.

For every position, the appearance or not of the effect on the different phases for both positive or negative currents is graphically predicted.

As for example, Fig. 7.13 shows the prediction for the position 195° (SSN), for the pulse AB . Pulses are identified with number that indicates which phases are supplied. Pulse AB means that U_{in} is applied between phase A and phase B , and therefore that phase A receives a positive current and phase B a negative one. In Fig. 7.13 it can be

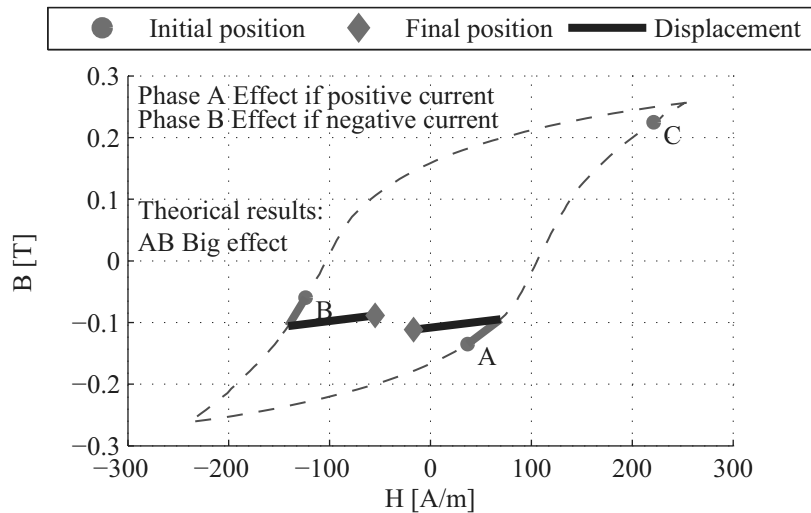


FIGURE 7.13 – Iron BH hysteresis loop, theoretical effect prediction of pulse AB on U_{out} based on the simplified model. Position 195° .

seen how the positive current in the phase A creates the first pulse effect on Z_A , and how the negative current in the phase B creates the effect too, on Z_B . It can be therefore easily predicted that for this position pulse AB creates the first pulse effect on U_{out} .

All the predictions are summarized in Table 7.1. As the effect appears independently on each coil, the three phases are analyzed separately. In the row 2, a “+/-” means that a positive/negative current flows through the phase. For example, the pulse AB corresponds to $A+$ and $B-$. Table 7.1 is made according to Fig. 7.12: a \checkmark corresponds to the big effect and a \sim to the small. Finally, if there is no difference predicted between the first iron magnetic path and the following ones, i.e. no effect at all, a blank ($_$) is left because no difference is expected between the phase impedances Z_x after the first U_{in} pulse.

Table 7.1 is horizontally subdivided in the six different Hall sectors. The electrical

position that correspond to a Hall sensor transition are duplicated for legibility reasons. For example, position 60° appears twice, once in the NNS position group and once in the SNS group.

7.3.2 Prediction of the first pulse effect on U_{out}

As already stated, the iron working point of every phase influences the respective phase impedance Z_x . It can furthermore be seen from (4.5) that the contributions of two phases are merged in the U_{out} voltage for every possible U_{in} pulse.

From Table 7.1 it is therefore now possible to extract a new table, Table 7.2, that summarizes where the phenomenon appears on U_{out} , for each angular position and for each of the 6 possible pulses that can be imposed to a star-connected BLDC motor.

For every pulse and every position, an effect on U_{out} is predicted. If in both supplied phases the first pulse generates a Z_x different in comparison with the following ones, which means that a ✓ is written in both phases in Table 7.1, a major difference on U_{out} is expected and a ✓✓ symbol is written in Table 7.2. A single ✓ means that just one of the supplied phases creates a difference between Z_x of the first pulse and the following ones. The other phase may not create the effect or may create only a small one. In this case a difference on U_{out} is also expected. The \sim symbol is used if one phase creates a small effect and the other does not. In this case the expected difference on U_{out} is minor. Finally, if there is no difference between the first Z_x and the following ones for both phases, a blank is left (—) because no difference will appear on U_{out} .

7.3.3 Interpretation

The first remark to point out on the theoretical results presented in Table 7.2 is that the phenomenon does not have the same borders as the Hall sectors. This is rapidly understood from the observation of Fig. 7.12 in which clearly appears that the phenomenon is related to the phase position on the BH hysteresis loop, without influence of the magnetic polarity. With the first pulse measurement principle, the rotor position can be identified within a range of 60° with a shift of 22.5° in respect to the Hall sectors. This position estimation is sufficient for starting a BLDC motor without oscillations. In fact, with a 60° resolution this shift is non-influential for that task.

TABLE 7.1
Theoretical results on the single phases Z_x every 15° .

Position		Phases					
		A+	A-	B+	B-	C+	C-
0°	NNS		✓	✓			✓
15°	NNS		✓	✓			✓
30°	NNS		✓	✓		~	
45°	NNS		✓	✓		✓	
60°	NNS		✓	✓		✓	
60°	SNS		✓	✓		✓	
75°	SNS		✓	✓		✓	
90°	SNS		✓		~	✓	
105°	SNS		✓		✓	✓	
120°	SNS		✓		✓	✓	
120°	SNN		✓		✓	✓	
135°	SNN		✓		✓	✓	
150°	SNN	~			✓	✓	
165°	SNN	✓			✓	✓	
180°	SNN	✓			✓	✓	
180°	SSN	✓			✓	✓	
195°	SSN	✓			✓	✓	
210°	SSN	✓			✓		~
225°	SSN	✓			✓		~
240°	SSN	✓			✓		✓
240°	NSN	✓			✓		✓
255°	NSN	✓			✓		✓
270°	NSN	✓		~			✓
285°	NSN	✓		✓			✓
300°	NSN	✓		✓			✓
300°	NSN	✓		✓			✓
315°	NSS	✓		✓			✓
330°	NSS		~	✓			✓
345°	NSS		✓	✓			✓
360°	NSS		✓	✓			✓

TABLE 7.2
Theoretical results on U_{out} for every pulse every 15° .

Position		Impulsions					
		AB	AC	BA	BC	CA	CB
0°	NNS		✓	✓✓	✓✓	✓	
15°	NNS		✓	✓✓	✓✓	✓	
30°	NNS			✓✓	✓	✓	~
45°	NNS			✓✓	✓	✓✓	✓
60°	NNS			✓✓	✓	✓✓	✓
60°	SNS			✓✓	✓	✓✓	✓
75°	SNS			✓✓	✓	✓✓	✓
90°	SNS	~		✓		✓✓	✓
105°	SNS	✓		✓		✓✓	✓✓
120°	SNS	✓		✓		✓✓	✓✓
120°	SNN	✓		✓		✓✓	✓✓
135°	SNN	✓		✓		✓✓	✓✓
150°	SNN	✓	~			✓	✓✓
165°	SNN	✓✓	✓			✓	✓✓
180°	SNN	✓✓	✓			✓	✓✓
180°	SSN	✓✓	✓			✓	✓✓
195°	SSN	✓✓	✓			✓	✓✓
210°	SSN	✓✓	✓		~		✓
225°	SSN	✓✓	✓		~		✓
240°	SSN	✓✓	✓✓		✓		✓
240°	NSN	✓✓	✓✓		✓		✓
255°	NSN	✓✓	✓✓		✓		✓
270°	NSN	✓	✓✓	~	✓		
285°	NSN	✓	✓✓	✓	✓✓		
300°	NSN	✓	✓✓	✓	✓✓		
300°	NSS	✓	✓✓	✓	✓✓		
315°	NSS	✓	✓✓	✓	✓✓		
330°	NSS		✓	✓	✓✓	~	
345°	NSS		✓	✓✓	✓✓	✓	
360°	NSS		✓	✓✓	✓✓	✓	

7.4 Measurements

7.4.1 Setup

In order to verify the described theory, a series of measurements are introduced below. The measurements are performed using the setup shown in Appendix C.4. Measurements are obtained as follows: three U_{in} pulses are injected by a custom electronics into the motor phases. Between every pulse a $t_{off} = 130 \mu s$ is waited, so that U_{out} goes back to its steady-state before the next pulse. Signals U_{in} , I_{in} and U_{out} of the three pulses are measured with a scope and then saved on a PC. These signals are shown in the first row of Fig. 7.14.

The saved signals are then manipulated by software. They are shifted to the left by $t_{shift} = 150 \mu s$, the second row of Fig. 7.14. Finally, the original and the shifted signals are plotted on the same axis, the third row of Fig. 7.14. Thanks to this manipulation, the first and the second pulse signals are superimposed at time $t = 0 \mu s$ and the second and the third ones are superimposed at time $t = 150 \mu s$. In this way, it is directly observable if there are any differences in the U_{in} , I_{in} and U_{out} signals between the first and the second pulses, as well as between the second and the third ones.

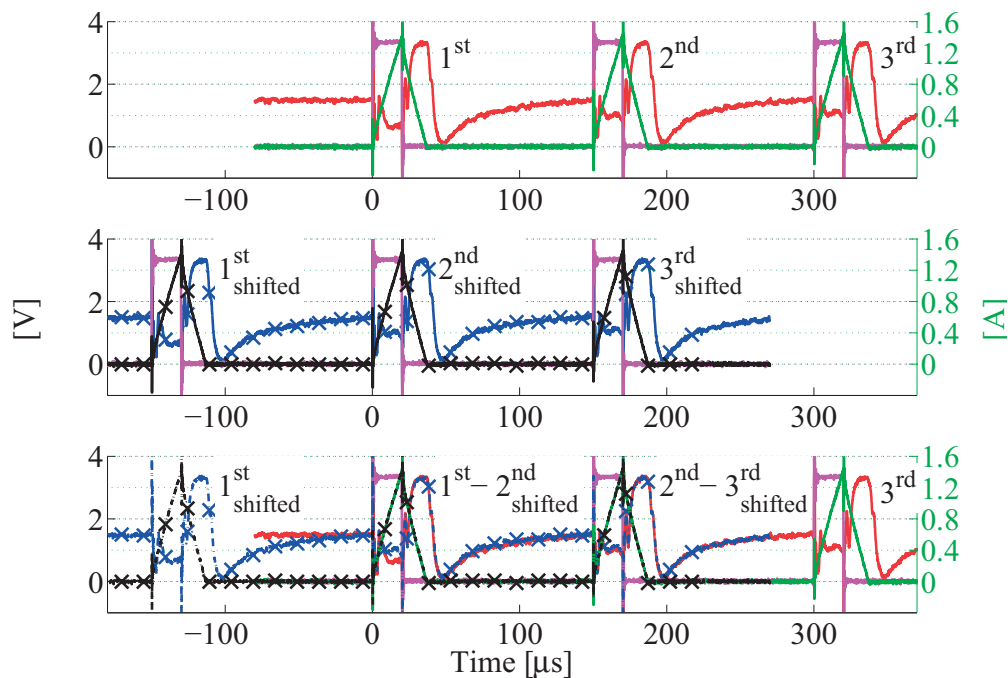


FIGURE 7.14 – 1st row: original signals.
 2nd row: shifted signals.
 3rd row: 1st and 2nd rows superimposed.

During the experiment, the rotor position of the BLDC motor is ensured by an ac-

tuator controlled by a PC, with a position encoder coupled to the motor, as shown in Appendix C.4.

7.4.2 Measurements

Measurements are performed for many positions on a complete rotor electrical revolution, maintaining the same U_{in} signal, pulse AB , for all the trials. Fig. 7.15 shows the electrical angular position of the performed measurements.

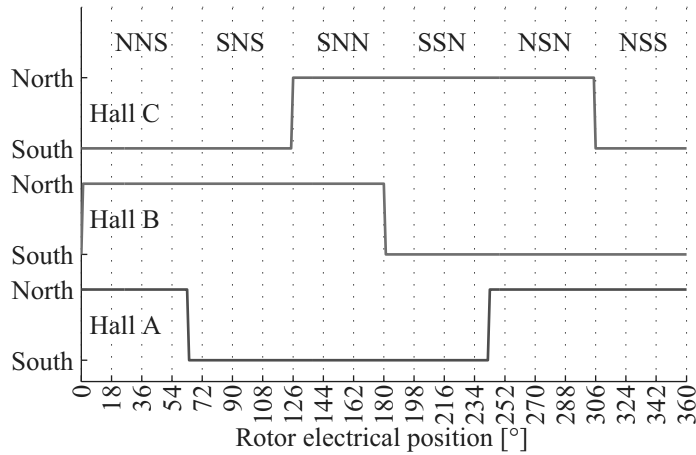


FIGURE 7.15 – Hall sensor states for a complete electrical period.

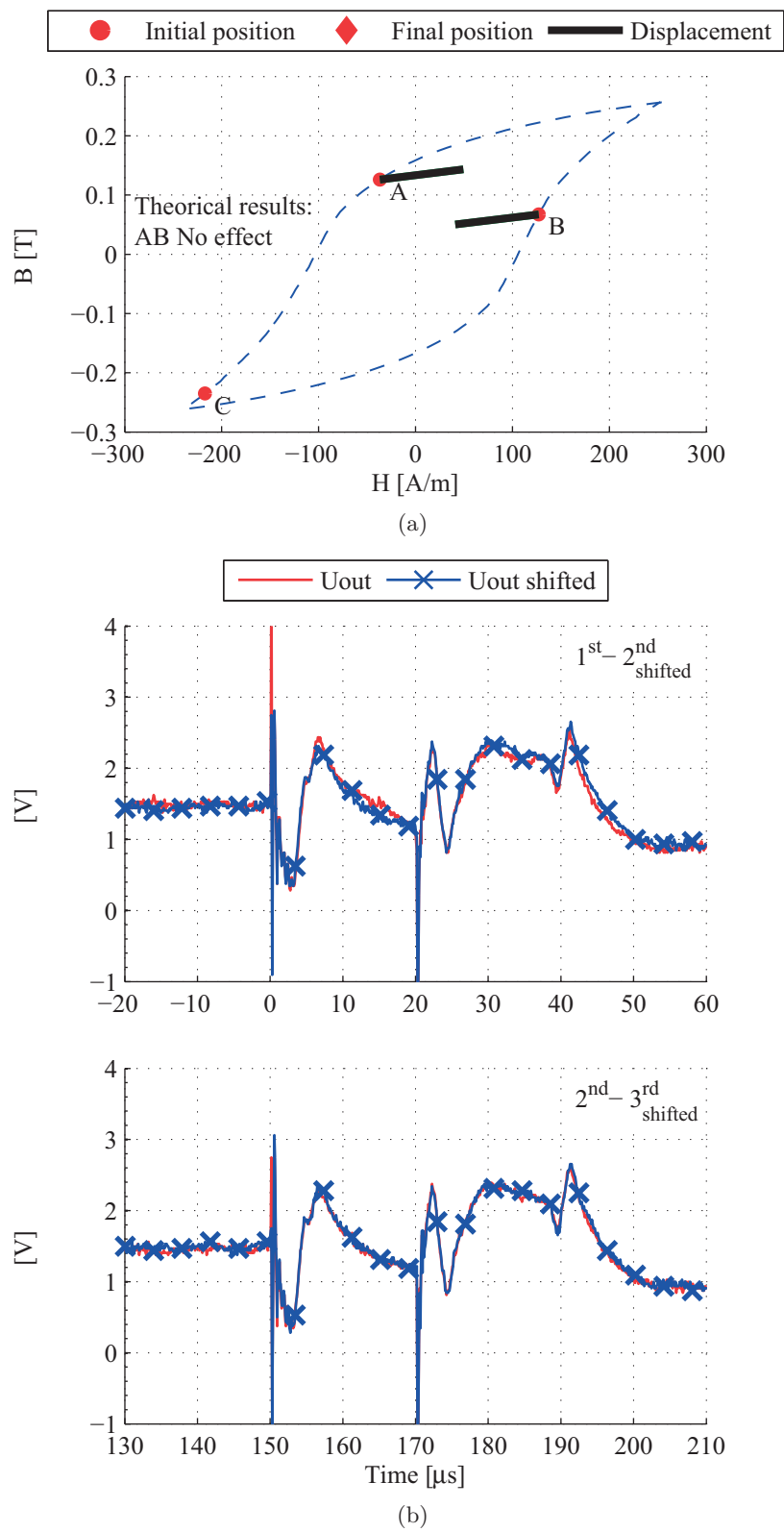
Measurements scope snapshots and theoretical results for three rotor positions are plotted in Figs. 7.16-7.18. Measurements scope snapshots are presented as in the third row of Fig. 7.14, from time $t = -50 \mu s$ to $t = 200 \mu s$.

In Fig. 7.16, for the position 18° (NNS), no effect is predicted by the theory because both phases A and B iron working points come back to the initial position after the first pulse. Measurements confirm the prediction: it can be clearly seen that U_{out} of the first and second pulses are the same.

In Fig. 7.17, for the position 108° (SNS), a small effect is predicted by the theory because the iron working point of phase B does not come back to the initial position after the first pulse. Measurements confirm the prediction: it can be seen that U_{out} of the first and second pulses are different during t_{ON} .

In Fig. 7.18, for the position 234° (SSN), a big effect is predicted by the theory because the iron working point of both phases A and B does not come back to the initial position after the first pulse. Measurements confirm the prediction: it can be clearly seen that U_{out} of the first and second pulses are different during t_{ON} and also after.

Finally, based on the theory, U_{out} of the second and the third pulses must always be the same, and this is the case for all the three positions.

FIGURE 7.16 – Impulsion AB , position 18° . Theory (a), measurement (b).

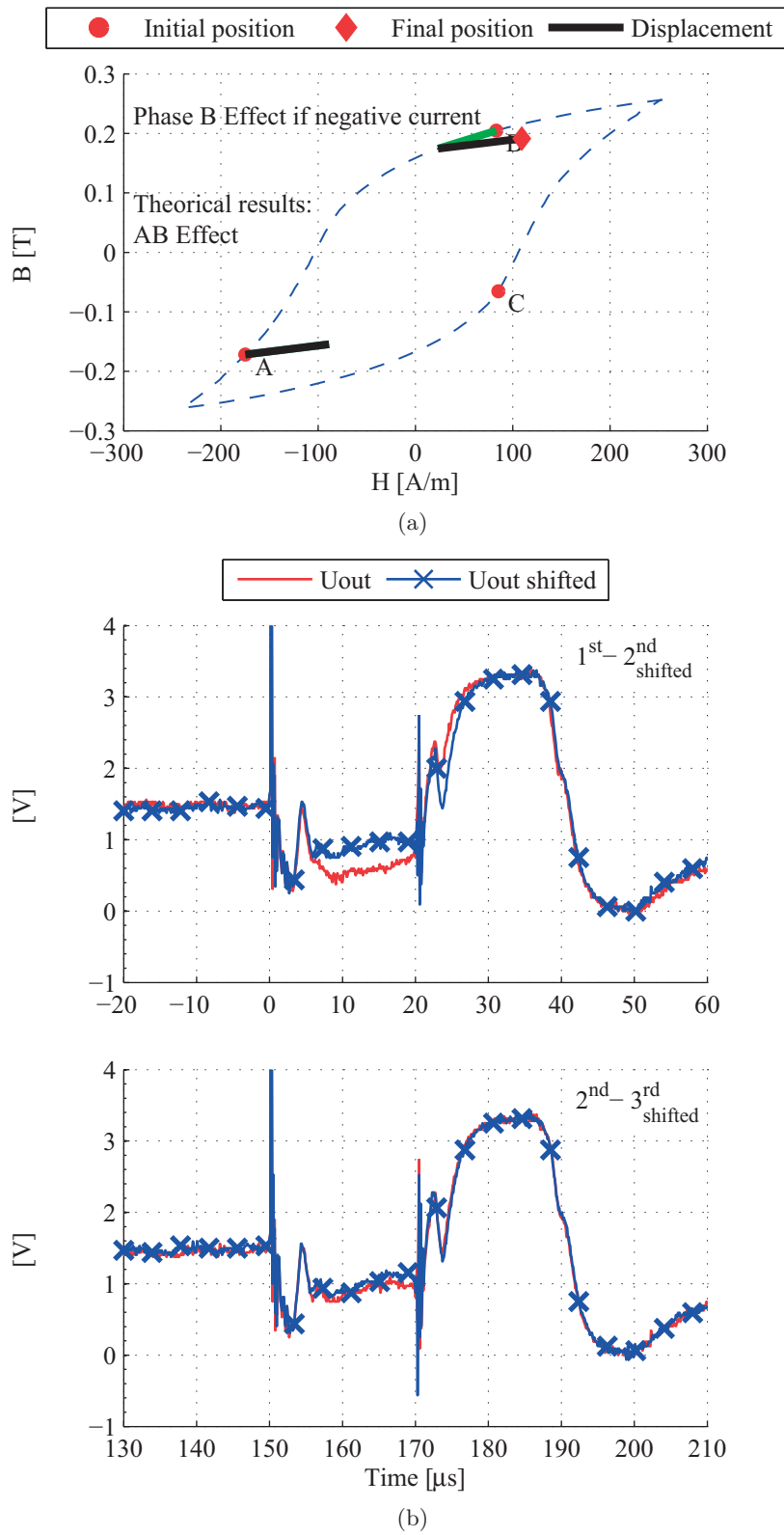
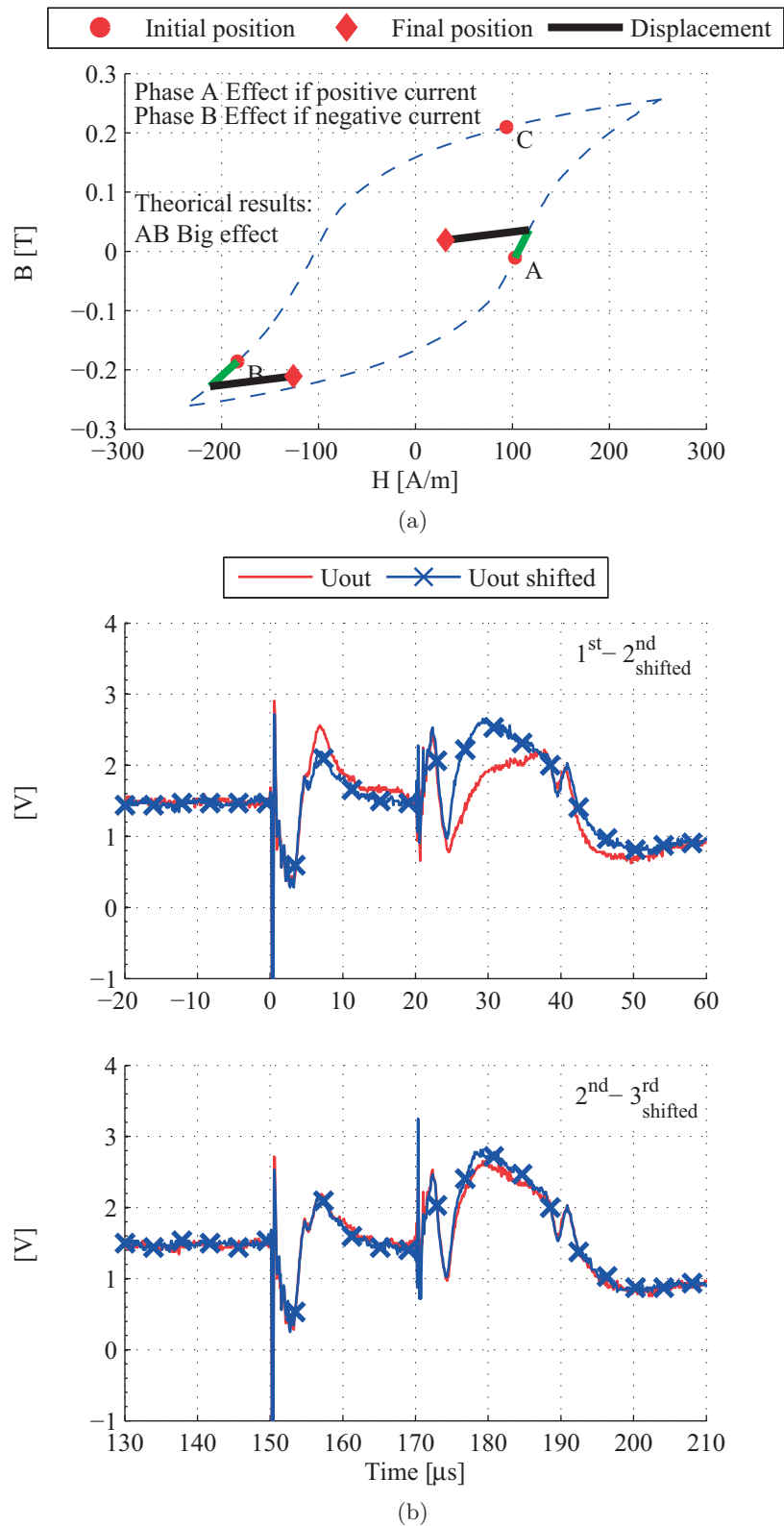


FIGURE 7.17 – Impulsion AB , position 108° . Theory (a), measurement (b).

FIGURE 7.18 – Impulsion AB , position 234° . Theory (a), measurement (b).

7.4.3 Interpretation

In the left column of Table 7.3, a qualitative interpretation of the results of all the performed measurements is done. Only three levels (\checkmark , \sim , $_$) are used for interpreting the measurements. A \checkmark is written where the first pulse phenomenon clearly appears, which corresponds to both $\checkmark\checkmark$ and \checkmark in the theory, as we are not able to distinguish these two levels in the measurements. A \sim is written when just a small difference exists. If no difference appears between the first U_{out} and the following ones, a blank ($_$) is left.

Theoretical results are predicted thanks to the qualitative representation of the three phases iron working points on the BH main loop, as explained in the previous section. Theoretical results are shown along with the measurements in Table 7.3 for permitting a rapid comparison.

From Table 7.3 it can be noticed that the measurements match well the results predicted by the simplified theory, especially where the phenomenon appears. On the other hand, where the proposed theory predicts no effect, some minor differences between the first U_{out} and the following ones are nevertheless measured. Unfortunately, actually there is not a precise explication to these minor differences.

TABLE 7.3
Measurement results for many positions, pulse AB .

Position	Effect	
	Measurements	Theory
0°	\sim	
18°	NNS	
36°		
54°		\sim
72°	SNS	\sim
90°		\sim
108°		\checkmark
126°	SNN	\checkmark
144°		\checkmark
162°		$\checkmark\checkmark$
180°		$\checkmark\checkmark$
198°	SSN	$\checkmark\checkmark$
216°		$\checkmark\checkmark$
234°		$\checkmark\checkmark$
252°	NSN	$\checkmark\checkmark$
270°		\checkmark
288°		\checkmark
306°		\checkmark
324°	NSS	\sim
342°		\sim
360°		\sim

7.5 Practical implementation issues

In the previous sections, the measurement analysis are done graphically in order to better explain the measurement principle. But the implementation of the first pulse measurement on an electronics with a microcontroller present few difficulties.

The U_{in} signal is created as for the BH exploitation introduced in Chapters 4, 5 and 6 with a classical six-transistor bridge used for driving almost every BLDC motor. Again, the power PWM signal used for driving the motor is at the same time used for the measurements. Hence, no special signals are injected into the phases.

Only the t_{ON} parameter has to be tuned: it has to be sufficiently long for permitting the correct U_{out} measurement after the transistors commutation noise. On the other hand, it should not be too long, in order to not generate torque, but this is easy to achieve because there is no need to saturate the motor teeth by injecting high currents.

The U_{out} signal can then be measured with an AD converter triggered at a determinate time after the U_{in} slopes, as shown in Fig. 7.19. The comparison between the measurement taken during the first and the second pulse can be finally easily done by software.

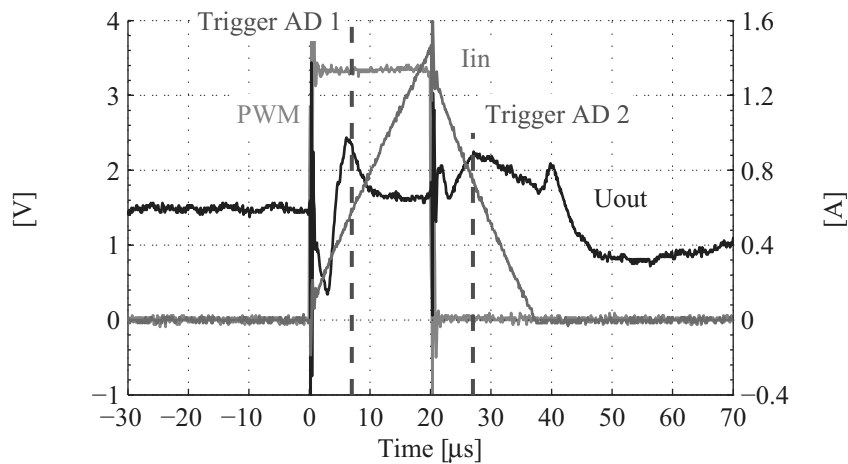


FIGURE 7.19 – AD trigger on a first pulse measurement.

7.6 Conclusions

In this chapter, the innovative first pulse measurement principle for the position detection at standstill is introduced. The principle exploits a very particular effect created by the iron BH hysteresis. The position is not estimated using an absolute value but

by the comparison between two measurements. The position resolution is 60° , which is enough for starting a BLDC motor in the wanted direction without any oscillations.

The first pulse principle is very promising: almost every PM motor has an iron stator and the measurement does not need any previous calibration. Furthermore, the measurement does not need to saturate the motor and does not have any impact on the motor control. The first pulse measurement principle is applicable and works only at standstill, for determining the rotor electrical position. Once the position is estimated, any motor sensorless drive system may be used.

Used in combination with the BH hysteresis exploitation introduced in Chapters 5 or 6, the first pulse measurement principle could lead to sensorless control in closed loop of BLDC motors, even the ones with non-salient rotor, from standstill to nominal speed.

A major drawback of the introduced first pulse measurement principle comes from its ephemerality. The measurement depends on the previous magnetic state of the motor iron and, as only the first pulse with respect to the following ones contains information, it is necessary to reset the iron BH state before any new pulse series injected into two other phases. By reset it is meant to bring the BH working point on the external main hysteresis. At this moment a reset of the BH iron state can be achieved by externally moving the rotor, but this is not suitable for automation. High priority should be placed on a way for resetting the stator iron to a known position on the BH characteristic, in order to ensure repeatability of the measurements and independence from the past.

CHAPTER 8

Conclusions

Contents

8.1	Original contributions	173
8.2	Contributions for other applications	174
8.3	Research outlook	175
8.4	Industrial outlook	175

THIS thesis permits a better knowledge of the magnetic phenomena that influence the BLDC motors phase inductances and resistances, and in particular the iron BH hysteresis. It is shown how, in any BLDC motor with a stator made of iron, the phase inductance and resistance vary as a function of the rotor position. The origin of these variations is found in the non-linearity of the BH hysteresis of the stator iron. Thanks to the understanding of the phenomenon, a standard motor is modified in order to increase the influence of the BH hysteresis on the phase inductance and resistance variations.

A very simple measurement principle, based on a differential voltage detection is introduced, so that a new ready-to-use position-dependent signal is provided. With this signal, an innovative sensorless position detection principle for the low speed operations is introduced. The implementation of the sensorless position detection principle is simple and naturally integrated in the widely used two-phases ON supply. The principle is deeply tested with a realized prototype and its effectiveness is demonstrated. Three main drawbacks are nevertheless highlighted: first of all, it is shown that a calibration of the system is needed. Moreover, it is found that the phase currents influence the position measurement. These two problems added to the simple and fragile interpretation of the position-dependent signal accentuate the need of a more powerful exploitation of the presented principle.

In order to solve the drawback of the mandatory off-line calibration, needed not only for the introduced principle but also for most sensorless position detection techniques, an on-line parameter estimation algorithm based on Kalman filtering is developed in this thesis. The algorithm is able to estimate the parameters needed for the exploitation of the position-dependent signal. The latter is then used as an additional input in a Kalman filtering based sensorless drive. With this innovative implementation of the Kalman filter, the position-dependent signal is robustly exploited and the working range of the filter is extended to the motor operations at low speed, without any need of off-line calibration. In addition, thanks to the introduced motor and load model parameter estimation, it is proven by simulations and confirmed by a practical realization, that the developed sensorless position detection principle is extremely performable during steady-state as well as during high dynamical operations. The functioning of the entire Kalman filter, with the additional position-dependent input and all-parameters estimation, is proven by simulation. A practical realization of the latter, unfortunately not yet realized, is therefore needed for confirming the effectiveness and the completeness of the innovative sensorless position detection principle exposed in this thesis.

Based again on the BH hysteresis characteristics of the stator iron, this thesis introduces an innovative and promising principle for the rotor position detection of BLDC motors at standstill. Depending on the rotor position, a very particular phenomenon related to BH hysteresis appears. It is shown that the effects measured by a first voltage pulse injected into the motor phases can be different from the effects created by the

following pulses, depending on the rotor position. The principle is hence not based on an absolute measurement, but on the comparison between the effects created by the first pulse and the following ones. A theoretical model of the phenomenon is introduced and confirmed by measurements. A solution for resetting the iron BH working point is however still to be found. This development is imperative for permitting the position detection at standstill with the introduced “first pulse” principle.

8.1 Original contributions

The main original contributions and innovations provided in this thesis are listed hereafter:

- *Iron BH hysteresis influence on the phase inductance and resistance.* It is highlighted that the movement of the permanent magnets on the rotor lead the stator iron to follow an hysteresis in the BH plane. If an additional AC current is injected, the magnetic working point of the stator iron follows local hysteresis that influences the motor phase inductances and resistances, even far away from saturation.
- *Differential measurement principle.* In order to retrieve the small variations in the phase inductances and resistances, a simple differential measurement is introduced. The measurement principle provides a ready-to-use position-dependent signal, exploitable in many ways.
- *Sensorless position detection principle for low speed operations.* The position-dependent signal is exploited in a simple way for creating a sensorless position detection method working over the whole speed range, including low speed operations. The hardware integration of the proposed principle in a typical two-phase ON motor drive requires only a few additional components. The power signal used for driving the motor is at the same time used for the position measurements, no changes are needed on the standard 3-leg transistor bridge normally used.
- *Sensorless position detection principle at standstill.* Thanks to the iron BH hysteresis influence on the motor phase inductance and resistance, the “first pulse” principle that permits the rotor position discrimination at standstill is introduced.
- *Motor and load model on-line parameter estimation for Kalman filtering applications.* An easy-to-implement algorithm, already used in other applications, is for the first time employed in the field of sensorless position detection. The algorithm is based on two interacting Kalman filters, one for the state estimation and one for the parameter estimation. Thanks to the introduced motor and load model parameter estimation, the overall performances of the position detection are increased, especially during high dynamic transients.

- *Extension down to the low speed operations of the observability of the Kalman filter.* Thanks to the additional source provided by the position-dependent signal, the Kalman filter is able to correctly estimate the rotor position even during low speed operations.

The combination of this innovative implementation with the algorithm for the parameters estimation leads to a full sensorless position detection principle, working over the whole speed range, suitable for steady-state and dynamic operations, without any need of off-line calibration.

8.2 Contributions for other applications

It is important to point out that some principles introduced in this thesis can be used in more general cases and are not restricted to the introduced applications. The contributions that may be used in other ways are listed here.

- *The differential measurement principle* works with any inductance or resistance variations. As a consequence, the measurement of the position-dependent signal introduced in this thesis is applicable on every three-phase motor that has any kind of saliency, like interior permanent magnet motors for example, and can be exploited along with all the proposed sensorless position detection principles.
- *The algorithm for the motor and load model parameter estimation:*
 - is implemented in this thesis with two interacting Kalman filters. Clearly, the filter dedicated to the parameter estimation can be used without the Kalman filter dedicated to the motor state estimation as long as the motor state variables are precisely known during the motor operation. In case of use of direct position sensors, like optical encoders or resolvers, and accurate current measurement, the parameter estimation algorithm is still effective.
 - can be used for other motors geometries, like hybrid stepper, and not just for BLDC motors.
 - can moreover be used as indicator of the health of the electric drive. The estimation of the phase resistance may be used for monitoring the motor temperature. The estimation of the total friction coefficient contains information on the bearings wear and tear. A sudden change in the latter or in the total inertia estimation may indicate a rupture of the gear chain, and so on.

8.3 Research outlook

In this thesis the iron hysteresis phenomenon is analyzed qualitatively. An interesting field of research which opens is to analytically model the iron hysteresis phenomenon in a BLDC motor, and in particular the local hysteresis loops, as a function of the magnetic characteristic of the stator iron, the permanent magnet position and the current circulating through the motor coils. Taking into account this model in the design of future motors, the hysteresis effects could be predicted, leading to the control of the inductance and resistance variations.

Moreover, a deeper knowledge of the behaviour of the local hysteresis loops will help to find a solution for the exploitation of the very promising magnetic position discrimination based on the first pulse principle.

8.4 Industrial outlook

Even if the domain of sensorless position detection of BLDC motors is studied since many years, there is still a gap to fill for permitting the technological transfer from academic research to industrial applications.

In contrast with the existing techniques for the sensorless position detection, the introduced principles shows many advantages:

- No additional signal injection into the motor phases is needed, only the power PWM is used.
- Very simple dedicated electronics.
- Insensibility to the environmental conditions, like motor temperature, thanks to the differential measurement principle.
- Suited for any motor geometry. No mechanical artifacts on the rotor are necessary. If needed, simple modifications of the stator can be applied on existing motors for increasing the hysteresis effect.
- No more off-line calibration is needed, the parameters are estimated on-line.
- Extended-speed working range thanks to the fusion of a position information based on impedance variations and another information based on the back-EMF.

Hence, because of its simple implementation, low electronic complexity and wide application, the industrialization of the differential voltage measurement principle and its exploitation for the sensorless position detection during low speed operations is possible.

Chapter 8. Conclusions

I believe that it is necessary to keep on developing simple sensorless position detection principles in order to facilitate the acceptance of the industrial partners. A right track to follow for attain this objective is to introduce in the motor design process a criterion that quantifies the applicability for the sensorless position detection, as it is done for a linear actuator in [86]. The modifications on these motors, designed for self-sensing, need to be industry-oriented, avoiding excessive machining, additional material and too important power losses.

Finally, in my opinion, the future developments of drive electronics should also focus on the use of algorithms like the one introduced in this thesis for the parameters estimation, in order to add new functionalities to the electrical motors, like monitoring and diagnosis. This development is a key for transforming the electrical drive from a motor only into a sensor of its own state and its environment.

Appendix

Demonstrators of the developed sensorless principles

A.1 Two phases-ON drive

The BLDC motor is fixed to the electronics itself and, thanks to a series of LEDs, the estimated position is superimposed to a angular position indicator fixed on the motor output axis. A small rope is wound the motor output axis, and with the small mechanics visible on the lower right corner of Fig. A.2, a variable brake is provided.

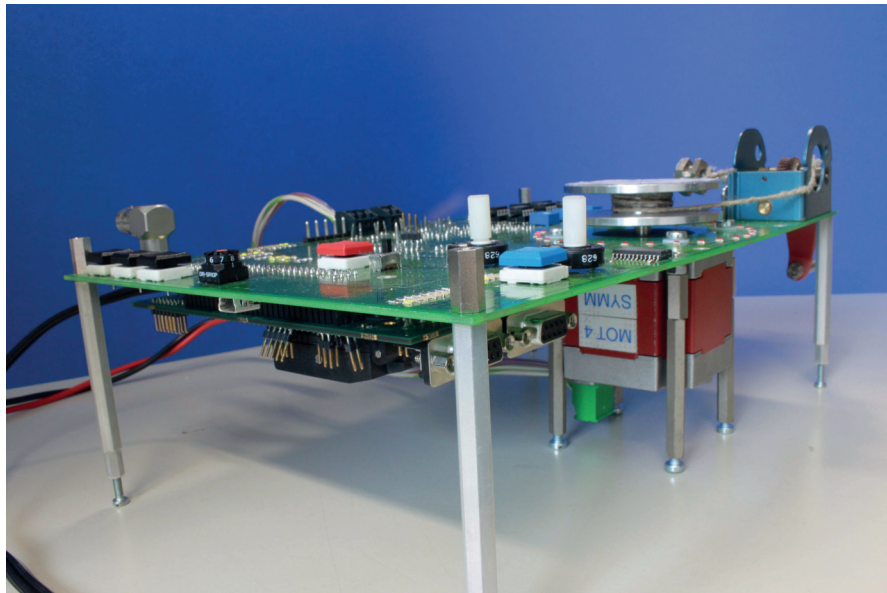


FIGURE A.1 – Two phases-ON demonstrator. Custom drive electronics.

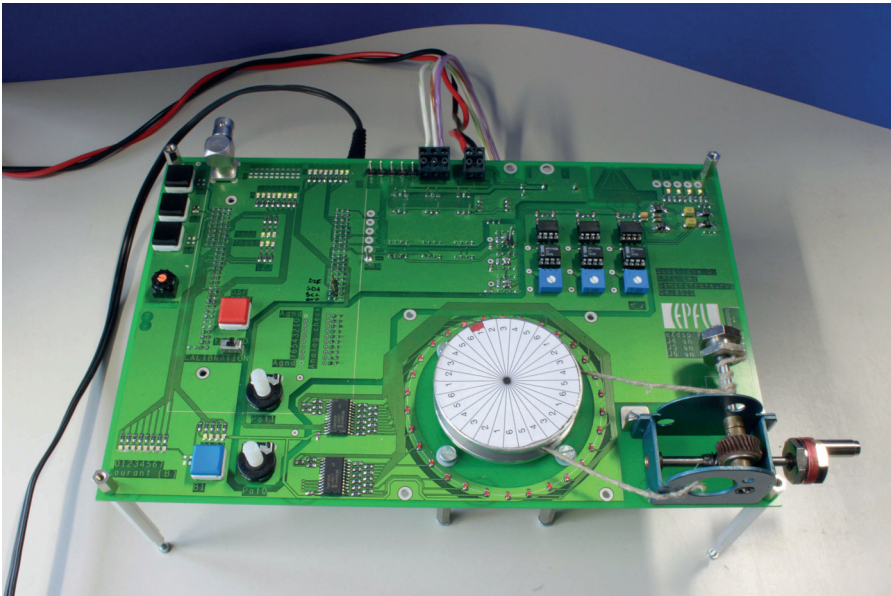


FIGURE A.2 – Two phases-ON demonstrator. Custom drive electronics.

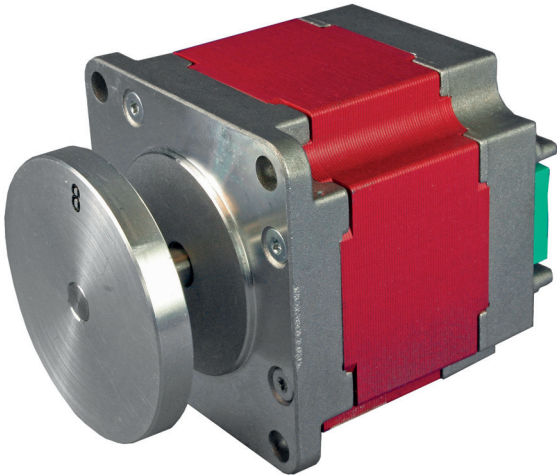


FIGURE A.3 – Two phases-ON demonstrator. The used Sonceboz 5455-20 motor.

A.2 Kalman filtering drive

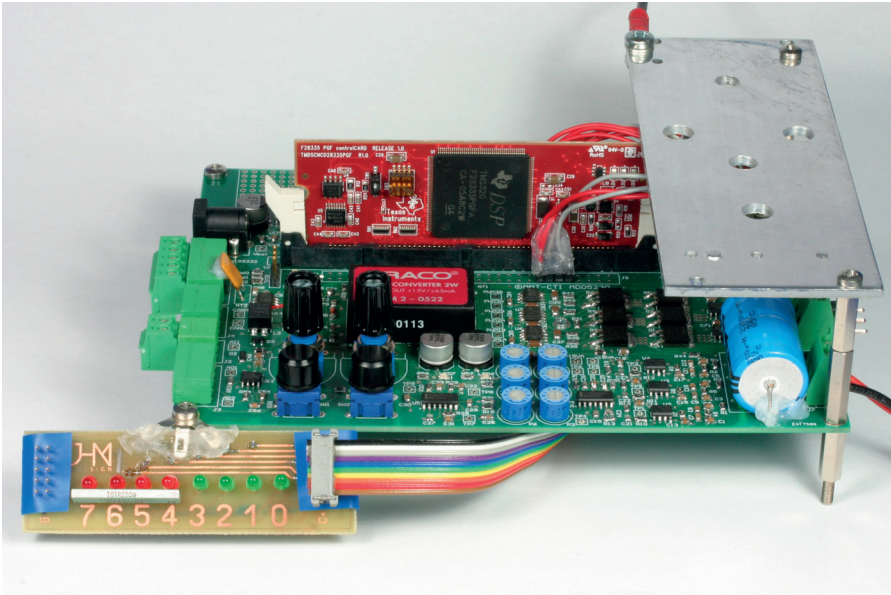


FIGURE A.4 – Kalman filtering demonstrator. Developed drive electronics.

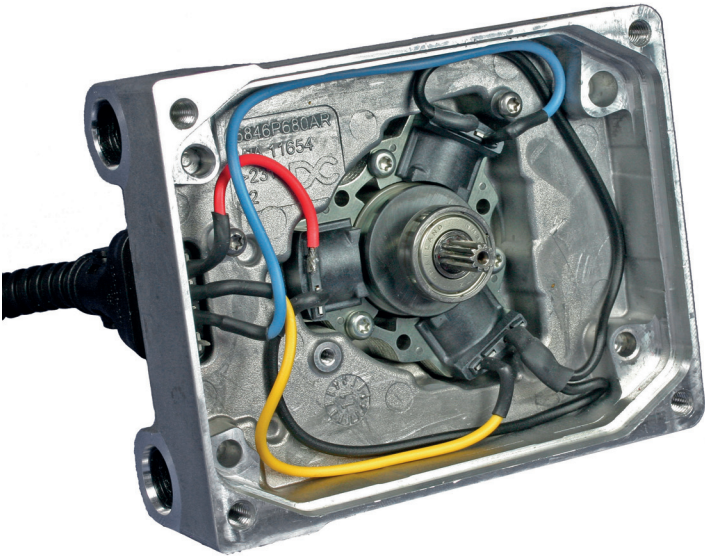


FIGURE A.5 – Kalman filtering demonstrator. Open drive, motor detail.

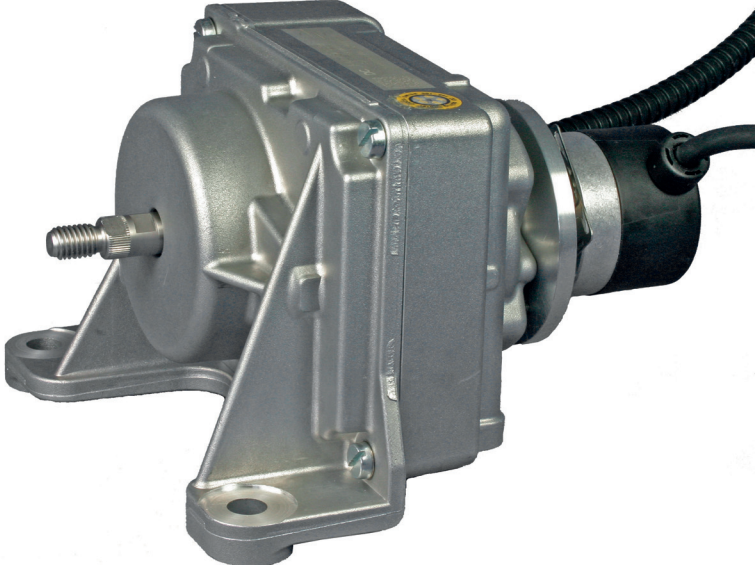


FIGURE A.6 – Kalman filtering demonstrator. Entire drive.

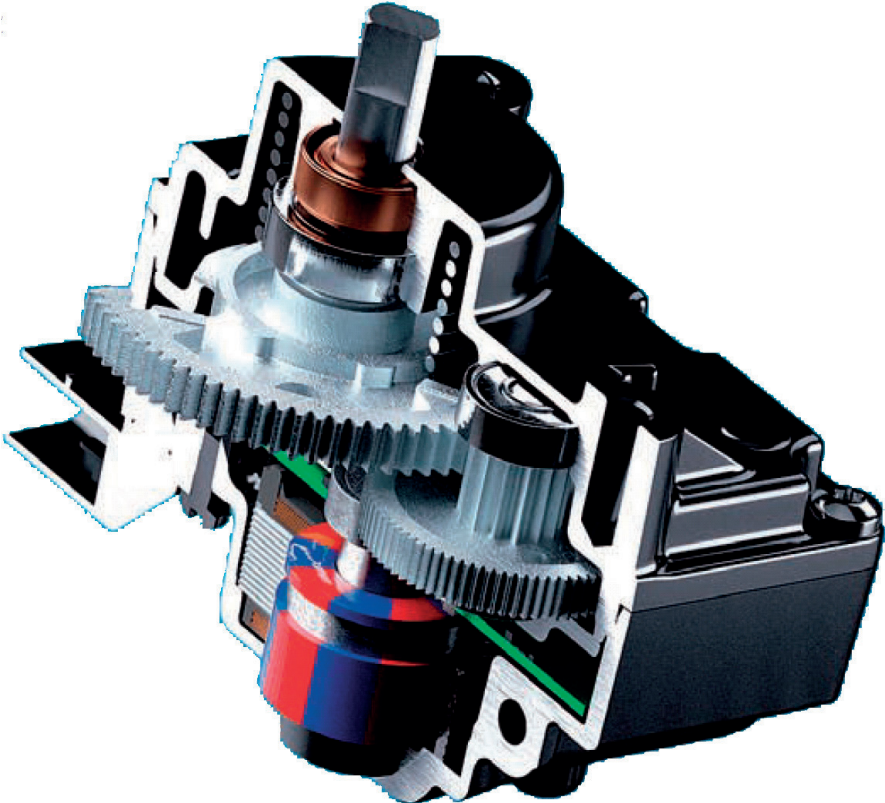


FIGURE A.7 – Kalman filtering demonstrator. Cut of the drive.
Source: *75 years Sonceboz*, MTZ journal, 2011, www.sonceboz.com

APPENDIX B

Motor datasheets

B.1 Sonceboz SA, Brushless DC motor, 5455-20

B.2 Maxon motor AG, Brushless EC motor, 118899





SONCEBOZ

▶ **Brushless - DC motors**

5455-20

- Size 57.2 x 57.2 x 50.8 mm
- Continuous output power:
110 W
(165 mNm, 6500 rpm)
- Steps/rev. 30

Dynamic, speed, and accuracy are the keywords of BLDC technology. Used when positioning or speed regulation are critical.

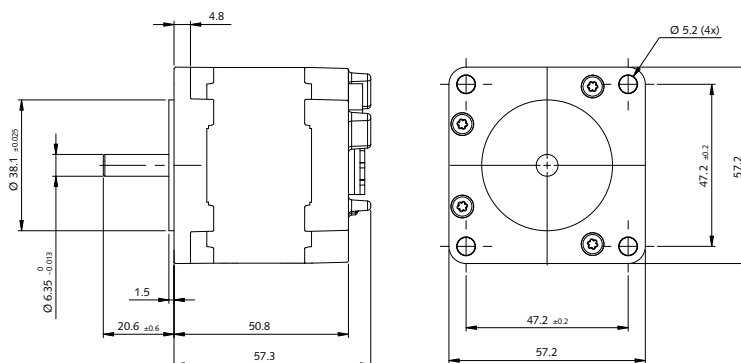
▶ **Technical data**

Weight	630 g	Motor constant (min. value)	66 mNm/ \sqrt{W}	Torque constant (max. value)	54 mNm/A
Phase number	3-Y	Nominal voltage	60 V	Max. continuous current	6.2 A
Continuous stall torque	335 mNm*	No load speed	10 000 rpm	Terminal inductance	0.87 mH
Max. stall torque	670 mNm**	Rotor inertia	204 g.cm ²	Protection	IP 30
Detent torque	30 mNm	Terminal resistance	0.50 Ω		

*Continuous values based on 25° C ambient temperature, motor mounted to a 150 x 150 x 10 mm aluminium heat sink.
**Max. 10 sec. at 25° C ambient temperature.

▶ **Dimensions**

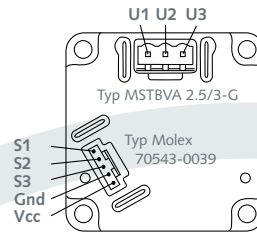
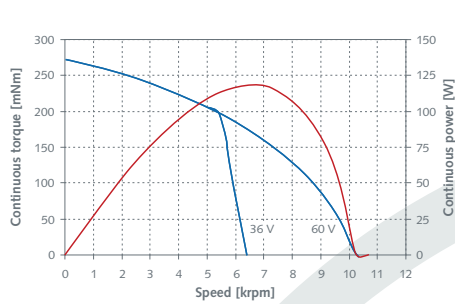
Drawing not to scale. All dimensions in mm.



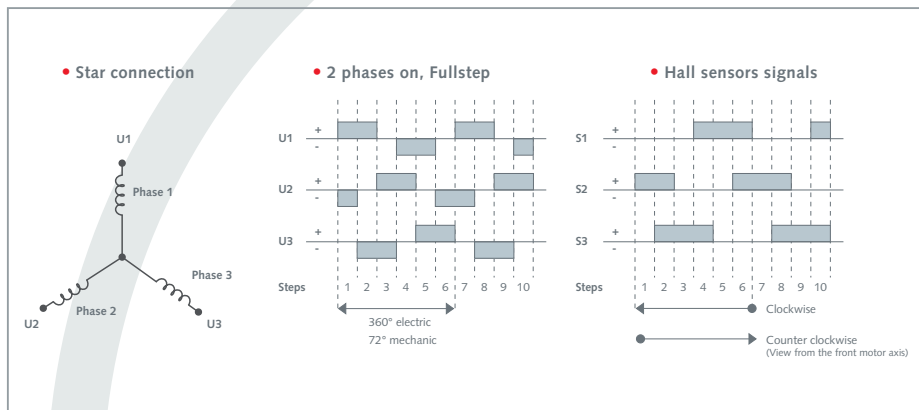
B.2. Maxon motor AG, Brushless EC motor, 118899

[Brushless - DC motors 5455-20 - 2/2]

Dynamic characteristics



Counter connector (Windings) MSTB 2.5/3-ST
 Counter connector (Hall sensors) 50-57-9405
 Tin plated contacts 16-02-0102



Options

- Motors with adapted windings
- Integrated high resolution position sensor
- Driver and control electronics

Special requirements upon customer specifications. Right to change reserved.

< 1.0 >

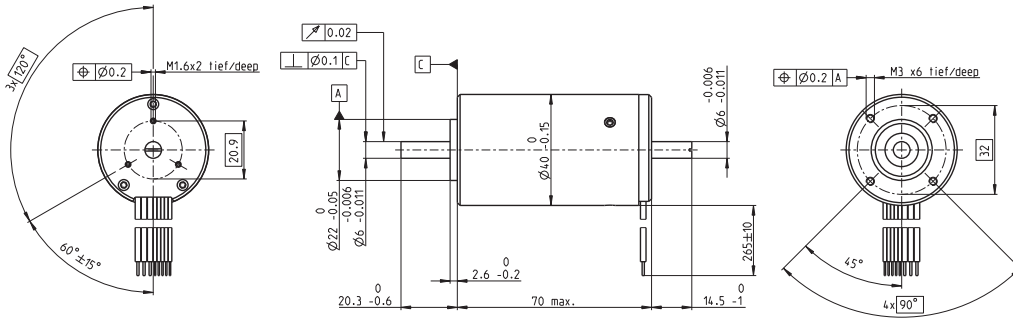
SONCEBOZ SA
 2605 Sonceboz - Switzerland
 Tel. +41(0) 32 488 11 11
 Fax +41(0) 32 488 11 00
 E-mail : info@sonceboz.com
 Internet : www.sonceboz.com



Appendix B. Motor datasheets

EC 40 Ø40 mm, brushless, 120 Watt, CE approved

maxon EC motor

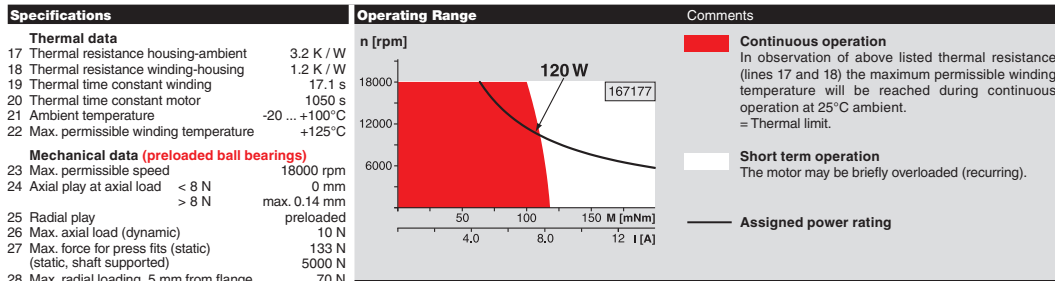


M 1:2

- Stock program
- Standard program
- Special program (on request)

Order Number													
167176	167177	118894	118895	167178	167179	118896	118897	167180	118898	167181	167183	118899	118901

Motor Data													
Values at nominal voltage													
1 Nominal voltage	V	12.0	18.0	21.0	30.0	24.0	36.0	42.0	48.0	48.0	48.0	48.0	48.0
2 No load speed	rpm	10300	12000	10400	11600	10300	9830	10400	7560	10300	5930	5420	3530
3 No load current	mA	886	754	515	426	443	275	258	139	222	97.8	86.2	41.3
4 Nominal speed	rpm	9050	10900	9240	10500	9160	8710	9290	6450	9190	4830	4290	2400
5 Nominal torque (max. continuous torque)	mNm	107	113	116	120	120	123	122	127	123	130	126	127
6 Nominal current (max. continuous current)	A	10.4	8.62	6.46	5.24	5.78	3.76	3.40	2.22	2.96	1.77	1.57	1.03
7 Stall torque	mNm	985	1340	1150	1420	1210	1200	1280	940	1270	743	639	410
8 Starting current	A	89.2	94.4	60.1	57.9	55.0	34.6	33.5	15.7	28.8	9.72	7.65	3.21
9 Max. efficiency	%	81	83	83	83	84	83	84	82	84	81	80	77
Characteristics													
10 Terminal resistance phase to phase	Ω	0.134	0.191	0.349	0.518	0.436	1.04	1.25	3.07	1.66	4.94	6.28	14.9
11 Terminal inductance phase to phase	mH	0.0266	0.0439	0.0797	0.132	0.106	0.263	0.319	0.788	0.425	1.28	1.52	3.56
12 Torque constant	mNm / A	11.0	14.2	19.1	24.6	22.1	34.7	38.2	60.1	44.1	76.4	83.5	128
13 Speed constant	rpm / V	865	673	500	389	433	275	250	159	216	125	114	74.8
14 Speed / torque gradient	rpm / mNm	10.5	9.05	9.13	8.20	8.55	8.26	8.20	8.12	8.16	8.07	8.59	8.76
15 Mechanical time constant	ms	9.39	8.06	8.13	7.30	7.61	7.35	7.30	7.22	7.26	7.18	7.64	7.79
16 Rotor inertia	gcm ²	85.0	85.0	85.0	85.0	85.0	85.0	85.0	85.0	85.0	85.0	85.0	85.0



maxon Modular System		Overview on page 16 - 21	
29 Number of pole pairs 1	30 Number of phases 3	Planetary Gearhead Ø42 mm 3 - 15 Nm Page 238	Encoder HED_5540 500 Imp., 3 channels Page 267 / 269
31 Weight of motor 390 g	Values listed in the table are nominal. Explanation of the figures on page 137	Planetary Gearhead Ø52 mm 4 - 30 Nm Page 241	Resolver Res 26 Ø26 mm 10 V Page 277
Connection Motor (Cable AWG 22) red Motor winding 1 black Motor winding 2 white Motor winding 3		Recommended Electronics: DECS 50/5 Page 289 DEC 50/5 291 DEC Module 50/5 291 DEC V 50/5, DEC 70/10 297 DES 50/5, DES 70/10 298 EPOS2 24/5 305 EPOS2 50/5 305 EPOS2 70/10 305 EPOS P 24/5 308 Notes 20	
Connection sensors (Cable AWG 26)¹⁾ green V-Hall 4.5 ... 24 VDC blue GND red / grey Hall sensor 1 black / grey Hall sensor 2 white / grey Hall sensor 3 Wiring diagram for Hall sensors see p. 27		Brake AB 28 24 VDC 0.4 Nm Page 318	

Automatic measurement setups

C.1 BH measurement setup

A current I is injected into a winding which is wound around the torus, and a gaussmeter is placed in the airgap for measuring the induction field \mathbf{B} . The current injection and the gaussmeter measurements are handled by a Matlab script.

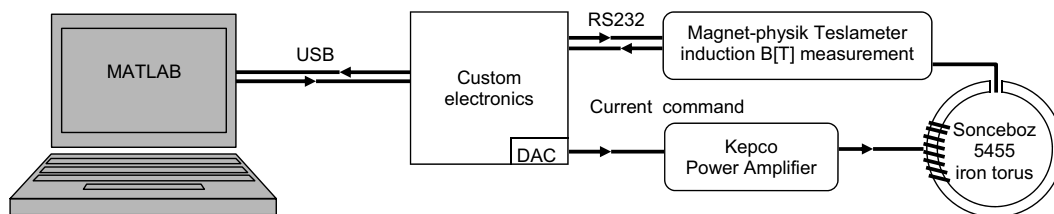


FIGURE C.1 – BH measurements setup.

C.2 L_{xx} and R_x measurement setup

The self inductance L_{xx} and phase resistance R_x of each motor phase is measured at standstill in function of the rotor angular position. Measurement is performed by injecting a sinusoidal voltage and detecting the current, using a precision impedance analyzer. The rotor is coupled with an actuator controlled from the PC, that imposes the angular position. The three Hall sensors of the motor are used for having an information about the rotor position.

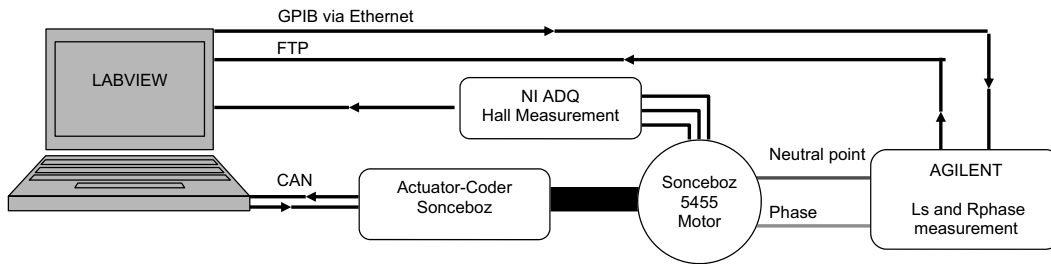


FIGURE C.2 – L_{xx} and R_x measurement setup.

C.3 Rotor eccentricity measurement setup

The eccentricity of the rotor is measured in function of its angular position. Measurement is performed using a precision interferometer. The measurement is performed three times, on the top, in the middle and on the bottom of the rotor. The rotor is coupled with an actuator controlled from the PC, that imposes the angular position.

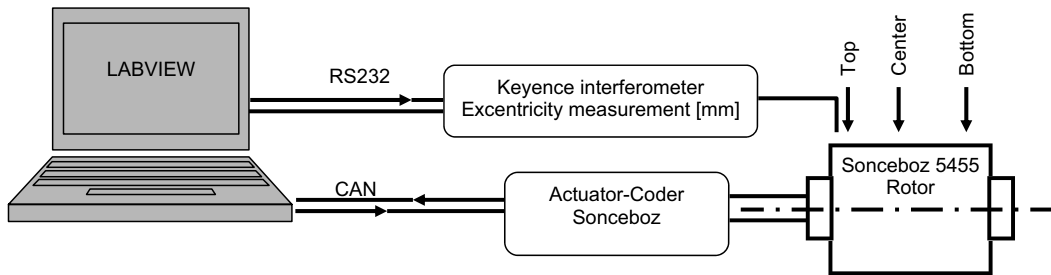


FIGURE C.3 – Eccentricity measurements setup.

C.4 First pulse measurement setup

The first pulse measurement principle is applied to the motor at standstill with the realized custom electronics, as function of the rotor angular position. The rotor is coupled with an actuator controlled from the PC, that imposes the angular position. Scope images are automatically triggered by the custom electronics, retrieved on the PC and treated with a Matlab script.

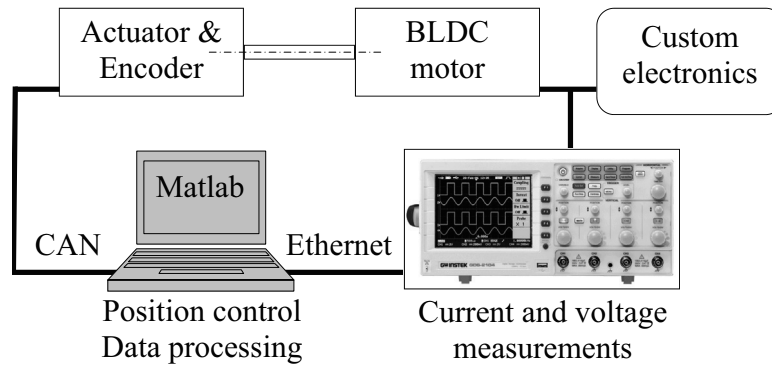


FIGURE C.4 – First pulse measurement setup.

Power bridge for BLDC motor drives

A power bridge for a BLDC drive is schematically represented in Fig. D.1. The bridge is composed by three legs, each one composed by a pair of power transistors, $T_A - T'_A$, $T_B - T'_B$, $T_C - T'_C$, with their own extinction diodes, $D_A, D'_A, D_B, D'_B, D_C, D'_C$. Every leg is connected to its respective motor phase A, B and C . The transistors are used as switches, their state can be open or closed. For avoiding a short circuit, the transistors of the same leg are not allowed to be both in the closed state. Hence, every phase terminal can be either connected to V_{pp} , either connected to GND or not connected neither to V_{pp} nor GND. In this last case, the phase is defined as floating.

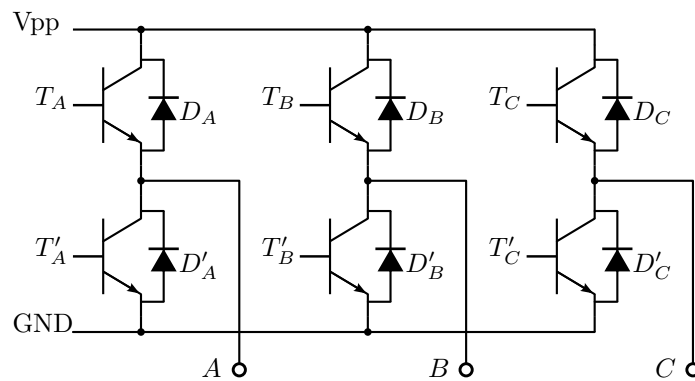


FIGURE D.1 – Power bridge schematics.

List of Symbols and Acronyms

Latin alphabet

A	-	Motor phase A
AC	-	Alternative current
AD	-	Analogical to Digital (converter)
B	-	Motor phase B
\mathbf{B}	[T]	Magnetic induction
Back-EMF	-	Back electromotive force (voltage)
BLDC	-	Brushless DC (motor)
BW	-	Backward (rotation direction)
C	-	Motor phase C
CAN	-	Controller Area Network, standard bus protocol
d	-	Duty cycle (of a PWM signal)
d	-	Direct position
DA	-	Digital to Analogical (converter)
DC	-	Direct current
EKF	-	Extended Kalman Filter
f	[Hz]	Frequency
FEM	-	Finite Elements Method
FW	-	Forward (rotation direction)
GND	-	Ground voltage
\mathbf{H}	[A/m]	Magnetic field
IPM	-	Interior Permanent Magnet (motor)
i_x	[A]	Phase current, $x = A, B, C$
i_{in}	[A]	Current flowing through a motor phase when U_{in} is applied

List of Symbols and Acronyms

I	[A]	Current
I	[Kg/m ²]	Inertia
K_e	[V/rad/s]	Back-EMF constant
K_f	[Nm/rad/s]	Friction constant
K_m	[Nm/A]	Torque constant
KF1	-	Kalman filter dedicated to the state estimation
KF2	-	Kalman filter dedicated to the parameter estimation
LHS	-	Left Hand Side (of the equation)
L	[H]	Phase inductance
L_x	[H]	Phase inductance, $x = A, B, C$
L_{xx}	[H]	Phase self-inductance, $x = A, B, C$
L_{xy}	[H]	Phase mutual-inductance, $x = A, B, C, y = A, B, C$
L_m	[H]	Phase mutual-inductance
MEMS	-	Microelectromechanical systems
N	-	North pole of a permanent magnet
N	-	Neutral point of a star connected BLDC motor
N'	-	Artificial neutral point
p	-	Pole pairs
P	[W]	Power
PWM	-	Pulse Width Modulation
q	-	Quadrature position
\mathbf{Q}_n	-	system covariance matrix
RHS	-	Right Hand Side (of the equation)
R	[Ω]	Phase resistance
R_x	[Ω]	Phase resistance, $x = A, B, C$
R_n	[Ω]	Resistance used for creating the artificial neutral point N'
\mathbf{R}_n	-	Measurement covariance matrix
S	-	South pole of a permanent magnet
t	[s]	Time
t_{ON}	[s]	Duration of the U_{in} impulsion
t_{OFF}	[s]	Interval between two U_{in} impulsions
T	[s]	Period
T_s	[s]	Sampling period
T_x	[s]	Transistor $x = A, B, C$
\mathbf{u}	-	Control vector
u_x	[V]	Phase voltage, $x = A, B, C$
u_{ix}	[V]	Phase back-EMF, $x = A, B, C$
U_{in}	[V]	Signal applied to the BLDC motor for the sensorless position detection
U_{out}	[V]	Position dependent signal measured on the BLDC motor

List of Symbols and Acronyms

Vcc	[V]	Positive digital voltage
Vpp	[V]	Positive power voltage
w_h	[J/m ³]	Energy per volume unit lost in an hysteresis loop
\mathbf{x}	-	State vector
\mathbf{y}	-	Measurement vector
Z_x	[Ω]	Phase impedance, $x = A, B, C$

Greek alphabet

θ	[rad]	Angular position
ω	[rad/s]	Angular speed or pulsation, $\omega = 2\pi f$
Γ	[Nm]	Torque
μC	-	Microcontroller
μ_0	[Vs/Am]	Vacuum permeability, $\mu_0 = 4\pi \cdot 10^{-7}$ Vs/Am
μ_r	-	Relative permeability
Θ	-	Parameter vector
ρ	[(J/m ³)/A ²]	Resistivity parameter

Bibliography

- [1] B. C. Kuo and K. Butts, “Closed-loop control of a 3.6° floppy disk drive PM motor by back EMF sensing,” *11th Annual Symposium on Incremental Motion Control Systems and Devices (IMCSD)*, pp. 295 –308, 1982.
- [2] L. Cardoletti, *Commande et réglage de moteurs synchrones auto-commutés par des capteurs indirects de position*. PhD thesis, no 1118, Ecole Polytechnique Fédérale de Lausanne, EPFL, 1993.
- [3] S. Merzaghi, *Analyse et mise en oeuvre d’un moteur électromagnétique microfabriqué*. PhD thesis, no 4801, Ecole Polytechnique Fédérale de Lausanne, EPFL, 2010.
- [4] M. Jufer, *Traité d’Electricité Volume IX*. Presses Polytechniques et Universitaires Romandes, 2004.
- [5] F. Genduso, R. Miceli, C. Rando, and G. Galluzzo, “Back EMF sensorless-control algorithm for high-dynamic performance PMSM,” *IEEE Transactions on Industrial Electronics*, vol. 57, no. 6, pp. 2092 –2100, 2010.
- [6] C. Bianchini, C. Concari, and A. Toscani, “Low-cost sensorless BLDC for organic fluids treatment in sterile environments,” in *18th International Conference on Electrical Machines (ICEM)*, pp. 1 –5, sept. 2008.
- [7] S. Bujacz, A. Cichowski, P. Szczepankowski, and J. Nieznanski, “Sensorless control of high speed permanent-magnet synchronous motor,” in *18th International Conference on Electrical Machines (ICEM)*, pp. 1 –5, sept. 2008.
- [8] M. Tomita, M. Satoh, H. Yamaguchi, S. Doki, and S. Okuma, “Sensorless estimation of rotor position of cylindrical brushless DC motors using eddy current,” in *4th*

Bibliography

- International Workshop on Advanced Motion Control (AMC/MIE)*, vol. 1, pp. 24–28, 1996.
- [9] M. Tomita, S. Doki, S. Okuma, and H. Yamaguchi, “Sensorless rotor position estimation at standstill of cylindrical brushless dc motors using opened phase voltage change caused by eddy currents,” *Electrical Engineering in Japan*, vol. 126, no. 1, pp. 52–60, 1999.
- [10] N. Bianchi and S. Bolognani, “Sensorless-oriented design of PM motors,” *IEEE Transactions on Industry Applications*, vol. 45, no. 4, pp. 1249–1257, 2009.
- [11] A. Faggion, N. Bianchi, and S. Bolognani, “Ringed-pole permanent-magnet synchronous motor for position sensorless drives,” *IEEE Transactions on Industry Applications*, vol. 47, pp. 1759–1766, july-august 2011.
- [12] N. Bianchi, S. Bolognani, and A. Faggion, “Rotor design arrangement of SPM motors for the sensorless control at low speed and standstill,” in *14th International Power Electronics and Motion Control Conference (EPE/PEMC)*, pp. S1–23–S1–28, 2010.
- [13] M. Morandini, S. Bolognani, and A. Faggion, “Outer-rotor ringed-pole SPM starter-alternator suited for sensorless drives,” in *Sensorless Control for Electrical Drives (SLED)*, 2011.
- [14] Y. Kano, T. Kosaka, N. Matsui, and T. Nakanishi, “Sensorless-oriented design of IPM motors for general industrial applications,” in *18th International Conference on Electrical Machines (ICEM)*, pp. 1–6, sept. 2008.
- [15] Y. Kano, T. Kosaka, N. Matsui, and T. Nakanishi, “Design and experimental verification of a sensorless-oriented concentrated-winding ipmsm,” in *XIX International Conference on Electrical Machines (ICEM)*, pp. 1–6, sept. 2010.
- [16] P. Sergeant, F. De Belie, and J. Melkebeek, “Rotor geometry design of an interior permanent-magnet synchronous machine for more accurate sensorless control,” in *XIX International Conference on Electrical Machines (ICEM)*, pp. 1–6, sept. 2010.
- [17] L. Alberti, N. Bianchi, S. Bolognani, and E. Fornasiero, “IM rotor parameters analysis with an intentionally created saliency,” in *First Symposium on Sensorless Control for Electrical Drives (SLED)*, pp. 120–126, 2010.
- [18] J. Johnson, M. Ehsani, and Y. Guzelgunler, “Review of sensorless methods for brushless DC,” in *IEEE Industry Applications Conference (IAS)*, vol. 1, pp. 143–150 vol.1, 1999.
- [19] T. Sato and Y. Sakaki, “Physical meaning of equivalent loss resistance of magnetic cores,” *IEEE Transactions on Magnetics*, vol. 26, no. 5, pp. 2894–2897, 1990.

-
- [20] P. Jansen and R. Lorenz, "Transducerless position and velocity estimation in induction and salient AC machines," *IEEE Transactions on Industry Applications*, vol. 31, no. 2, pp. 240–247, 1995.
- [21] M. Corley and R. Lorenz, "Rotor position and velocity estimation for a salient-pole permanent magnet synchronous machine at standstill and high speeds," *IEEE Transactions on Industry Applications*, vol. 34, no. 4, pp. 784–789, 1998.
- [22] N. Bianchi, S. Bolognani, J.-H. Jang, and S.-K. Sul, "Comparison of PM motor structures and sensorless control techniques for zero-speed rotor position detection," *IEEE Transactions on Power Electronics*, vol. 22, no. 6, pp. 2466–2475, 2007.
- [23] N. Bianchi and S. Bolognani, "Influence of rotor geometry of an IPM motor on sensorless control feasibility," *IEEE Transactions on Industry Applications*, vol. 43, pp. 87–96, jan.-feb. 2007.
- [24] N. Bianchi, S. Bolognani, J.-H. Jang, and S.-K. Sul, "Advantages of inset PM machines for zero-speed sensorless position detection," *IEEE Transactions on Industry Applications*, vol. 44, no. 4, pp. 1190–1198, 2008.
- [25] S. Bolognani, S. Calligaro, R. Petrella, and M. Tursini, "Sensorless control of IPM motors in the low-speed range and at standstill by HF injection and DFT processing," *IEEE Transactions on Industry Applications*, vol. 47, no. 1, pp. 96–104, 2011.
- [26] S. Sayeef, G. Foo, and M. Rahman, "Very low speed operation of a variable structure direct torque controlled IPM synchronous motor drive using combined hf signal injection and sliding observer," in *18th International Conference on Electrical Machines (ICEM)*, pp. 1–6, sept. 2008.
- [27] S. Sayeef, G. Foo, and M. Rahman, "Rotor position and speed estimation of a variable structure direct-torque-controlled IPM synchronous motor drive at very low speeds including standstill," *IEEE Transactions on Industrial Electronics*, vol. 57, no. 11, pp. 3715–3723, 2010.
- [28] G. Foo and M. Rahman, "Sensorless direct torque and flux-controlled IPM synchronous motor drive at very low speed without signal injection," *IEEE Transactions on Industrial Electronics*, vol. 57, no. 1, pp. 395–403, 2010.
- [29] G. Foo and M. Rahman, "Sensorless sliding-mode MTPA control of an IPM synchronous motor drive using a sliding-mode observer and HF signal injection," *IEEE Transactions on Industrial Electronics*, vol. 57, no. 4, pp. 1270–1278, 2010.
- [30] K. Hanamura and H. Dohmeki, "Position sensorless control for interior permanent magnet synchronous motor using adaptive flux observer," in *XIX International Conference on Electrical Machines (ICEM)*, pp. 1–6, sept. 2010.

Bibliography

- [31] X. Fei, W. Hao-xiong, C. Min-liang, and L. Yong, "A novel sensorless control of PMSG based on sliding mode observer," in *XIX International Conference on Electrical Machines (ICEM)*, pp. 1–4, sept. 2010.
- [32] G. Scelba, G. De Donato, F. Capponi, A. Consoli, and O. Honorati, "A co-simulation platform for evaluation of sensorless control techniques for IPMSMs," in *International Conference on Electrical Machines (ICEM)*, 2010.
- [33] O. Benjak and D. Gerling, "Review of position estimation methods for IPMSM drives without a position sensor part I: Nonadaptive methods," in *International Conference on Electrical Machines (ICEM)*, pp. 1–6, sept. 2010.
- [34] O. Benjak and D. Gerling, "Review of position estimation methods for IPMSM drives without a position sensor part II: Adaptive methods," in *International Conference on Electrical Machines (ICEM)*, pp. 1–6, sept. 2010.
- [35] J. Persson, M. Markovic, and Y. Perriard, "A new standstill position detection technique for non-salient PMSM's using the magnetic anisotropy method (MAM)," *IEEE Industry Applications Conference (IAS)*, vol. 1, pp. 238–244 Vol. 1, 2005.
- [36] S. M. Grewal and P. A. Andrews, *Kalman Filtering: Theory and Practice Using MATLAB*. John Wiley and Sons, 2nd ed., 2008.
- [37] L. Jones and J. Lang, "A state observer for the permanent-magnet synchronous motor," *IEEE Transactions on Industrial Electronics*, vol. 36, no. 3, pp. 374–382, 1989.
- [38] R. Dhaouadi, N. Mohan, and L. Norum, "Design and implementation of an extended Kalman filter for the state estimation of a permanent magnet synchronous motor," *IEEE Transactions on Power Electronics*, vol. 6, pp. 491–497, jul 1991.
- [39] A. Bado, S. Bolognani, and M. Zigliotto, "Effective estimation of speed and rotor position of a PM synchronous motor drive by a Kalman filtering technique," in *23rd Annual IEEE Power Electronics Specialists Conference (PESC)*, vol. 2, pp. 951–957, 1992.
- [40] S. Bolognani, M. Zigliotto, and K. Unterkofler, "On-line parameter commissioning in sensorless PMSM drives," in *Proceedings of the IEEE International Symposium on Industrial Electronics (ISIE)*, vol. 2, pp. 480–484, 1997.
- [41] S. Bolognani, M. Zigliotto, and M. Zordan, "High performance PMSM sensorless drive based on stochastic filtering," in *Proceedings of the International Conference on Power Electronic Drives and Energy Systems for Industrial Growth*, vol. 2, pp. 562–567, 1998.
- [42] S. Bolognani, R. Oboe, and M. Zigliotto, "Sensorless full-digital PMSM drive with EKF estimation of speed and rotor position," *IEEE Transactions on Industrial Electronics*, vol. 46, no. 1, pp. 184–191, 1999.

-
- [43] S. Bolognani, M. Zigliotto, and M. Zordan, "Extended-range PMSM sensorless speed drive based on stochastic filtering," *IEEE Transactions on Power Electronics*, vol. 16, no. 1, pp. 110–117, 2001.
- [44] S. Bolognani, L. Tubiana, and M. Zigliotto, "Extended Kalman filter tuning in sensorless PMSM drives," *IEEE Transactions on Industry Applications*, vol. 39, no. 6, pp. 1741–1747, 2003.
- [45] G. Zhu, A. Kaddouri, L. Dessaint, and O. Akhrif, "A nonlinear state observer for the sensorless control of a permanent-magnet AC machine," *IEEE Transactions on Industrial Electronics*, vol. 48, no. 6, pp. 1098–1108, 2001.
- [46] J. Persson and Y. Perriard, "An optimized extended Kalman filter algorithm for hybrid stepper motors," in *29th Annual Conference of the IEEE Industrial Electronics Society (IECON)*, vol. 1, pp. 297–300, 2003.
- [47] J. Persson, *Innovative standstill position detection combined with sensorless control of synchronous motors*. PhD thesis, no 3221, Ecole Polytechnique Fédérale de Lausanne, EPFL, 2005.
- [48] R. Wu and G. Slemon, "A permanent magnet motor drive without a shaft sensor," in *IEEE Industry Applications Society Annual Meeting*, vol. 1, pp. 553–558, 1990.
- [49] Y. Buchnik and R. Rabinovici, "Speed and position estimation of brushless DC motor in very low speeds," in *23rd IEEE Convention of Electrical and Electronics Engineers in Israel*, pp. 317 – 320, sept. 2004.
- [50] S. Bolognani and M. Zigliotto, "Parameter sensitivity of the Kalman filter applied to a sensorless synchronous motor drive," in *6th European Conference on Power Electronic Applications*, 1995.
- [51] K. Rahman and S. Hiti, "Identification of machine parameters of a synchronous motor," *IEEE Transactions on Industry Applications*, vol. 41, no. 2, pp. 557–565, 2005.
- [52] H. Kim, J. Hartwig, and R. Lorenz, "Using on-line parameter estimation to improve efficiency of IPM machine drives," in *33rd Annual IEEE Power Electronics Specialists Conference (PESC)*, vol. 2, pp. 815–820, 2002.
- [53] S. Underwood and I. Husain, "Online parameter estimation and adaptive control of permanent-magnet synchronous machines," *IEEE Transactions on Industrial Electronics*, vol. 57, no. 7, pp. 2435–2443, 2010.
- [54] T. Boileau, N. Leboeuf, B. Nahid-Mobarakeh, and F. Meibody-Tabar, "Online identification of PMSM parameters: Parameter identifiability and estimator comparative study," *IEEE Transactions on Industry Applications*, vol. 47, no. 4, pp. 1944–1957, 2011.

Bibliography

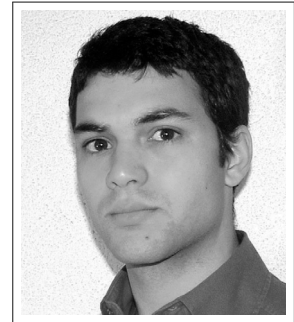
- [55] B. Nahid-Mobarakeh, F. Meibody-Tabar, and F. Sargos, "On-line identification of PMSM electrical parameters based on decoupling control," in *IEEE Industry Applications Conference (IAS)*, vol. 1, pp. 266–273, 2001.
- [56] B. Nahid-Mobarakeh, F. Meibody-Tabar, and F. Sargos, "Mechanical sensorless control of PMSM with online estimation of stator resistance," *IEEE Transactions on Industry Applications*, vol. 40, no. 2, pp. 457–471, 2004.
- [57] N. Matsui, "Sensorless PM brushless DC motor drives," *IEEE Transactions on Industrial Electronics*, vol. 43, pp. 300–308, apr 1996.
- [58] K.-W. Lee, D.-H. Jung, and I.-J. Ha, "An online identification method for both stator resistance and back-EMF coefficient of PMSMs without rotational transducers," *IEEE Transactions on Industrial Electronics*, vol. 51, no. 2, pp. 507–510, 2004.
- [59] S. Ichikawa, M. Tomita, S. Doki, and S. Okuma, "Sensorless control of permanent-magnet synchronous motors using online parameter identification based on system identification theory," *IEEE Transactions on Industrial Electronics*, vol. 53, no. 2, pp. 363–372, 2006.
- [60] S. Morimoto, M. Sanada, and Y. Takeda, "Mechanical sensorless drives of IPMSM with online parameter identification," in *IEEE Industry Applications Conference (IAS)*, vol. 1, pp. 297–303, 2005.
- [61] B. Terzic and M. Jadric, "Design and implementation of the extended Kalman filter for the speed and rotor position estimation of brushless DC motor," *IEEE Transactions on Industrial Electronics*, vol. 48, pp. 1065–1073, dec 2001.
- [62] G. Bertotti, F. Fiorillo, and M. Pasquale, "Measurement and prediction of dynamic loop shapes and power losses in soft magnetic materials," *IEEE Transactions on Magnetics*, vol. 29, pp. 3496–3498, Nov. 1993.
- [63] G. Bertotti and V. Basso, "Hysteresis models for the description of domain wall motion," *IEEE Transactions on Magnetics*, vol. 32, N°5, pp. 4210–4212, 1996.
- [64] G. Bertotti, *Hysteresis in magnetism - For physicists, material scientists and engineers*. Academic Press, New York, 1998.
- [65] R. M. Bozorth, *Ferromagnetism*. IEEE Press, 1993.
- [66] M. Schroedl, "Detection of the rotor position of a permanent magnet synchronous machine at standstill," *Proceedings of international conference in electrical machines (ICEM), Pisa, Italy*, 1988.
- [67] www.cedrat.com, *Flux2D User Guide*.
- [68] www.keithley.com, *Low level measurements handbook*.

-
- [69] J. H. Jr and T. Miller, *Design of Brushless Permanent-Magnet Motors*. Magna Physics Publishing, 1994.
- [70] C. Fleury, *Modélisation de l'entraînement électrique synchrone auto-commuté*. PhD thesis, no 1428, Ecole Polytechnique Fédérale de Lausanne, EPFL, 1995.
- [71] F. Bonvin, *Analyse et mise en oeuvre de méthodes de commande sans capteur pour moteurs synchrones à aimants permanents*. PhD thesis, no 2354, Ecole Polytechnique Fédérale de Lausanne, EPFL, 2001.
- [72] L. Nelson and E. Stear, "The simultaneous on-line estimation of parameters and states in linear systems," *IEEE Transactions on Automatic Control*, vol. 21, no. 1, pp. 94–98, 1976.
- [73] D. Labarre, E. Grivel, Y. Berthoumieu, E. Todini, and M. Najim, "Consistent estimation of autoregressive parameters from noisy observations based on two interacting Kalman filters," *Signal Processing*, vol. 86, no. 10, pp. 2863–2876, 2006.
- [74] T. A. Wenzel, K. J. Burnham, M. V. Blundell, and R. A. Williams, "Dual extended Kalman filter for vehicle state and parameter estimation," *Vehicle System Dynamics*, vol. 44, no. 2, pp. 153–171, 2006.
- [75] C. M. Trudinger, M. R. Raupach, P. J. Rayner, and I. G. Enting, "Using the Kalman filter for parameter estimation in biogeochemical models," *Environmetrics*, vol. 19, pp. 849–870, 2008.
- [76] R. Hermann and A. Krener, "Nonlinear controllability and observability," *IEEE Transactions on Automatic Control*, vol. 22, no. 5, pp. 728–740, 1977.
- [77] S. Diop and M. Fliess, "Nonlinear observability, identifiability, and persistent trajectories," in *IEEE Conference on Decision and Control*, pp. 714–719 Vol.1, dec 1991.
- [78] E. D. Seborg, A. D. Mellichamp, F. T. Edgar, and J. F. Doyle, *Process Dynamics and Control*. John Wiley and Sons, 2010.
- [79] R. Longchamp, *Commande numérique de systèmes dynamiques*. PPUR Presses Polytechniques Universitaires Romandes, 2006.
- [80] W. Hong, W. Lee, and B.-K. Lee, "Dynamic simulation of brushless dc motor drives considering phase commutation for automotive applications," in *IEEE International Electric Machines Drives Conference (IEMDC)*, vol. 2, pp. 1377–1383, may 2007.
- [81] R. Nucera, S. Sudhoff, and P. Krause, "Computation of steady-state performance of an electronically commutated motor," *IEEE Transactions on Industry Applications*, vol. 25, pp. 1110–1117, nov/dec 1989.

Bibliography

- [82] M. Markovic, A. Hodder, and Y. Perriard, “An analytical determination of the torque-speed and efficiency-speed characteristics of a BLDC motor,” in *Energy Conversion Congress and Exposition (ECCE)*, 2009.
- [83] J. Persson, M. Markovic, and Y. Perriard, “A new standstill position detection technique for nonsalient permanent-magnet synchronous motors using the magnetic anisotropy method,” *IEEE Transactions on Magnetics*, vol. 43, no. 2, pp. 554–560, 2007.
- [84] F. Demmelmayr, A. Eilenberger, and M. Schroedl, “Sensorless electric traction drive with 500 Nm outer rotor permanent magnet synchronous machine,” in *XIX International Conference on Electrical Machines (ICEM)*, pp. 1–7, 2010.
- [85] L. Cardoletti, A. Cassat, and M. Jufer, “Indirect position detection at standstill for brushless DC and step motors,” *European Conference on Power Electronics and Applications (EPE), Aachen, West Germany*, vol. 3, pp. 1219–1222, 1989.
- [86] J. Maridor, *Design, Optimization, and Sensorless Control of a Linear Actuator*. PhD thesis, no 5187, Ecole Polytechnique Fédérale de Lausanne, EPFL, 2011.

SCAGLIONE OMAR
1982, Switzerland
omar.scaglione@a3.epfl.ch



Formation

2012 “Iron hysteresis and enhanced Kalman filtering for sensorless position detection of synchronous motors”, PhD ès Sciences, Ecole Polytechnique Fédérale de Lausanne (EPFL), Integrated Actuators Laboratory (LAI).

2007 Master in microengineering, EPFL.

2005 Erasmus exchange, Universitat Politècnica de Catalunya (UPC), Barcelona, Spain.

2001 Scientific High School, Liceo Lugano 1, Switzerland.

Publications

Journal articles

O. Scaglione, M. Markovic, and Y. Perriard, “First-pulse technique for brushless DC motor standstill position detection based on iron B-H hysteresis,” *IEEE Transactions on Industrial Electronics*, vol. 59, pp. 2319 - 2328, may 2012.

Conference papers

O. Scaglione, M. Markovic, and Y. Perriard, “On-line parameter estimation for improved sensorless control of synchronous motors,” *International Conference on Electrical Machines, ICEM, Marseille*, 2012.

O. Scaglione, M. Markovic, and Y. Perriard, “Extension of the local observability down to zero speed of BLDC motor state-space models using iron B-H local hysteresis,” *International Conference on Electrical Machines and Systems, ICEMS, Beijing*, 2011.

O. Scaglione, M. Markovic, and Y. Perriard, “Exploitation of a new iron B-H phenomenon for the standstill position detection of PM motors,” *International Conferences on Electrical Machines, ICEM, Rome*, 2010.

Y. Perriard, O. Scaglione, and M. Markovic, “Self-sensing methods for PM motors in mechatronic applications,” *IEEE International Conference on Advanced Intelligent Mechatronics, AIM, Montreal*, 2010.

Curriculum Vitae

O. Scaglione, M. Markovic, and Y. Perriard, "Exploitation of iron B-H local hysteresis for the rotor position detection of a PM motor," *International Electric Machines and Drives Conference, IEMDC, Miami*, 2009.

O. Scaglione, M. Markovic, and Y. Perriard, "PM motor sensorless position detection based on iron B-H local hysteresis," *International Conference on Electrical Machines and Systems, ICEMS, Tokio*, 2009.

Y. Perriard, M. Markovic, and O. Scaglione, "Self-sensing methods from MEMS to solar aircraft motors," *International Conference on Electrical Machines and Systems, ICEMS, Wuhan*, 2008.

G. Bozovic, O. Scaglione, C. Koechli, and M. Noca, "Swisscube: Development of an ultra-light and efficient inertia wheel for the attitude control and stabilization of cubesat class satellites," *International Astronautical Congress, IAC, Glasgow*, 2008.

Y. Perriard, O. Scaglione, C. Koechli, and J. Persson, "Self-sensing methods to drive micro-machines," *International Workshop on Physics of Semiconductor Devices, IW-PSD, Mumbai*, 2007.

